Differential Ultrasonic Calorimeter for Accurate Measurement of Thermal Losses in Machinery

by Anas Hashmi, BEng (Hons), MSc

Thesis submitted to The University of Nottingham for the degree of Doctor of Philosophy

May 2017



Abstract

Ultrasonic sensors can rapidly respond to changes in the average temperature across a complete ultrasonic pathway. However, these response rates are difficult to achieve using conventional temperature-sensing technologies. This research investigates ultrasound calorimetry and its advantages over the calorimetry implemented using conventional temperature sensors in order to estimate heat losses accurately in electrical motors. The ultrasonic calorimeter is based upon ultrasonic oscillating temperature sensors, which have previously been demonstrated in temperatures that change only in a single direction.

A hysteresis effect was observed in the results of the analysis of the temperature-frequency relationship recorded for temperature changes that occurred in both directions. Data sensor fusion was applied to reduce the hysteresis effect and to achieve faster estimates of the temperature inflection point with a standard uncertainty of around 1.34 mK and a measurement resolution of 0.1 mK, comparing to 62.5 mK for inexpensive conventional temperature sensors. The outcomes of the data sensor fusion were tested to evaluate the heat loss in a water-cooled electric motor. The developed instrument costs less than £15 and is capable of evaluating losses up to 7 kW.

The major electronic development part of this project is the design of a low-cost electronic modular driver that supports the reliable operation of oscillating ultrasonic sensors. Automatic gain control (AGC) was investigated with the view to prevent the output of the amplifier being driven to saturation. This development resulted in a reduction of 26% in the frequency scatter of the ultrasonic output. An evaluation of different arrangements of ultrasonic oscillating sensors was conducted to study the optimal arrangements of both the transducers and the electronic specifications. Several hundred hours of overnight measurements were completed to establish the best arrangements and operational parameters in order to ensure the repeatability and reproducibility of the system.

Declaration

I hereby certify that the work described in this document is done without collaboration of anyone, except as indicated, the work described is entirely original.

Nottingham, May 26, 2017

Anas Hashmi

Acknowledgements

Firstly, I would like to express my sincere gratitude to my supervisor Dr Roger Light for the continuous support of my PhD study and related research, for his patience, motivation, and immense knowledge. His guidance helped me in all the time of research. I would like to thank Dr Steve Sharples for his help, support and motivation.

I would like to express my special appreciation and thanks to my supervisor for the first two years of my PhD study at Nottingham University Dr Alexander Kalashnikov, you have been a tremendous mentor for me. I would like to thank you for encouraging my research and for allowing me to grow as a research scientist. Your advice on both research as well as on my career have been priceless.

It would not have been possible to write this thesis without the help and support of the kind people around me, only some of whom is it possible to mention here. Above all, I would like to thank my mother, father, brothers and friends for their unequivocal support, for which my mere expression of thanks does not suffice.

Publications & Presentations

Publications

P. Popejoy et al., "Comparison of implementations of driving electronics for ultrasonic oscillating sensors," *2012 IEEE International Ultrasonics Symposium*, Dresden, 2012, pp. 2427-2430. doi: 10.1109/ULTSYM.2012.0607

A. Hashmi, A. N. Kalashnikov "Measuring thermal losses of water cooled motors using oscillating ultrasonic temperature sensors," *The 3rd International Conference on Advanced Information Systems and Technologies*, AIST 2014, 130-132. 10-14 May 2014

A. Hashmi, A. N. Kalashnikov, R. A. Light "Inexpensive Differential Ultrasonic Calorimeter for Accurate Measurement of Heat Loss," *The 8th Saudi Students Conference in the UK*, 2015. ISBN: 978-1-78326-914-3

A. Hashmi, A. N. Kalashnikov, R. A. Light, M. Malakouthekhah "Embedded supervisory control and output reporting for the oscillating ultrasonic temperature sensors," *Intelligent Systems in Cybernetics and Automation Theory*, Springer, pp. 138-150.

A. Hashmi, A. N. Kalashnikov and R. A. Light, "Experimental evaluation of ultrasonic oscillating temperature sensors (UOTS) under cyclically changing temperatures," *2015 IEEE International Ultrasonics Symposium (IUS)*, Taipei, 2015, pp. 1-4. doi: 10.1109/ULTSYM.2015.0249

A. Hashmi, R. A. Light, A. N. Kalashnikov and M. Malakoutikhah, "Accurate heat loss evaluation of water-cooled electric motors using a differential ultrasonic calorimeter," *2016 International Conference for Students on Applied Engineering (ICSAE)*, Newcastle upon Tyne, 2016, pp. 42-47. doi: 10.1109/ICSAE.2016.7810158

A. Hashmi, A. N. Kalashnikov "Sensor Data Fusion for Responsive High Resolution Ultrasonic Temperature Measurement Using Piezoelectric Transducers" *The IEEE Transactions on Ultrasonics, Ferroelectrics, and Frequency Control*; under review

A.Hashmi and A.N.Kalashnikov, "Comparison of the responsiveness of ultrasonic oscillating temperature sensors (UOTSes) and conventional sensors to temperature inflection points", *The 5rd International Conference on Advanced Information Systems and Technologies* (AIST), Sumy, 2017, 4p.; accepted

Presentations

"Measuring thermal losses of water cooled motors using oscillating ultrasonic temperature sensors," 3rd International Conference on Advanced Information Systems and Technologies.
Thursday 15/05/2014 [webinar: Sumy, Ukraine]

"Inexpensive Differential Ultrasonic Calorimeter for Accurate Measurement of Heat Losses," the Eighth Saudi Students Conference in the UK.
Saturday 31/01/2015 [London, UK]

"Embedded Supervisory Control and Output Reporting for the Oscillating Ultrasonic Temperature Sensors," Applied Optics Group Seminar.
Wednesday 29/04/2015 [Nottingham, UK]

"Embedded supervisory control and output reporting for the oscillating ultrasonic temperature sensors," Intelligent Systems in Cybernetics and Automation Theory conference.
Thursday 30/04/2015 [online conference]

"Experimental evaluation of ultrasonic oscillating temperature sensors (UOTS) under cyclically changing temperatures," 2015 IEEE International Ultrasonics Symposium.
Saturday 24/10/2015 [Taipei, Taiwan]

"Accurate Heat Loss Evaluation of Water-Cooled Electric Motors Using a Differential Ultrasonic Calorimeter," 2016 IEEE The International Conference for Students on Applied Engineering
Friday 21/10/2016 [Newcastle, UK]

Abbreviations

AGC	Automatic Gain Control
GUI	Graphical User Interface
UOTS	Ultrasonic Oscillating Temperature Sensors
CAD	Computer-Aided Design
BPF	Band-Pass Filter
LPF	Low-Pass Filter
CFD	Computational Fluid Dynamic
BOM	Bill of Material
ADC	Analogue-to-Digital Converter
NDT	Non-Destructive Testing
TOF	Time of Flight
SNR	Signal-to-Noise Ratio
PSoC	Programmable System-on-chip
ADC	Analogue to Digital Converter
UART	Universal Asynchronous Receiver/Transmitter
PGA	Programmable Gain Amplifier
LSB	Least Significant Bytes
MSB	Most Significant Bytes
FVC	Frequency to Voltage Conversion
TCXO	Temperature Compensated Crystal Oscillator
OCXO	Oven Controlled Crystal Oscillator
IMO	Internal Main Oscillator
SNR	Signal to Noise Ratio
ppm	Parts per Million
PEA	Piezoelectric Actuators
CFD	Computational Fluid Dynamics
RCSC	Rectangular Cross Section Chamber
SCSC	Square Cross Sectional Chamber
CCSC	Circular Cross Sectional Chamber
CAD	Computer Aided Design

Contents

Abstract iii
Declaration iv
Acknowledgements v
Publications & Presentations vi
Abbreviations viii
Contents ix
List of Figures xv
List of Tables xxii
List of Software xxv
1 Introduction to Ultrasonic Differential Heat Loss Measurements 1
1.1 Aim and objectives of the present research 1
1.1.1 Focus of the present research 1
1.1.2 Motivation 2
1.1.3 Aims and objectives 3
1.1.4 Independent contributions to knowledge 3
1.2 Heat losses in motors 4
1.2.1 Heat measurements and calorimetry 4
1.2.2 Overview of heat losses in electric motors 5
1.3 Temperature measurements 12
1.3.1 Introduction to temperature measurements 12
1.3.2 Types of temperature sensors 13
1.3.3 Selection of conventional inexpensive temperature sensors 19
1.4 High resolution ultrasonic temperature measurements 20
1.4.1 Definition of ultrasound, its history and applications 20

1.4.2 Overview of ultrasonic temperature measurements 28
1.5 Previous developments in ultrasonic oscillating sensors 33
1.5.1 Low-cost oscillating sensor for the ultrasonic testing of liquids 33
1.5.2 Development of an ultrasonic tilt sensor 34
1.5.3 Assessment of power losses in water-cooled electrical machines 34
1.5.4 Data logging instrumentation for UOTS 34
1.6 Thesis structure 35
2 Critical Evaluation of Ultrasonic Transducers, Measurement Arrangements and Electronic Architectures for Ultrasonic Temperature Measurements 38
2.1 Ultrasonic measurement methods 38
2.1.1 Through transmission 40
2.1.2 Pitch-catch 40
2.1.3 Pulse-echo 40
2.1.4 Backscatter 41
2.1.5 Acoustic emission 41
2.1.6 Summary on ultrasonic measurement methods 41
2.2 Ultrasonic transducers 42
2.2.1 Introduction 42
2.2.2 Operating frequency and cost 42
2.2.3 Transducer types 43
2.3 Approaches to ultrasonic measurements of temperature 45
2.3.1 Ultrasonic temperature measurements using an oscillating sensor 45
2.3.2 Ultrasonic temperature measurements in pulse-echo mode 47
2.4 Comparison of electronic architectures for ultrasonic NDE sensors 48
2.4.1 Introduction 48
2.4.2 Electronic architectures for ultrasonic NDE sensors 48
2.4.3 Comparison of ultrasonic architectures 53
3 Development of Supporting Electronics for The Ultrasonic Driver and Frequency Meter 54
3.1 Electronics for the ultrasonic oscillating sensor system 54
3.1.1 Barkhausen stability criteria and system requirements for the supporting electronics 54
3.1.2 Ultrasonic driver circuit 55

3.1.3 Electronics control of oscillating ultrasonic system 56
3.1.4 PSoC1 background, structure and capabilities 56
3.2 Development of the Automatic Gain Control system (AGC) 58
3.2.1 Purpose of AGC 58
3.2.2 Design objectives 58
3.2.3 Development of AGC using a light bulb 59
3.2.4 Developments of discrete gain control 61
3.2.5 Development of AGC using the AGC chip 62
3.2.6 Development of AGC JFET 65
3.2.7 Integration of AGC using JFET and PSoC 71
3.2.8 Performance of the ultrasonic oscillating sensor with AGC 72
3.2.9 Summary 74
3.3 1-Wire temperature sensor reader based on PSoC1 74
3.3.1 Introduction 74
3.3.2 1-Wire temperature sensors 75
3.3.3 Hardware implementation 78
3.3.4 Calibration of sensors 78
3.3.5 Conclusion 79
3.4 Development of the frequency meter 80
3.4.1 Introduction 80
3.4.2 Available options for frequency measurements 80
3.4.3 Firmware of the frequency measurements device 90
3.4.4 Frequency reference source 91
3.4.5 Resolution and accuracy of the developed meter 99
3.5 Summary 99
4 Development of the Modular Driver for The Ultrasonic Oscillating Sensor 101
4.1 Introduction 101
4.2 Hardware development 102
4.2.1 General guidelines for the developed boards 102
4.2.2 Electronic driver module for ultrasound transducers 103
4.2.3 Ultrasonic sensors control and signal multiplexing 106
4.2.4 Frequency meter and data acquisition control 109
4.2.5 Control and connection of modules 111

4.3 Software development 112
4.3.1 Introduction 112
4.3.2 UART communications protocols 113
4.3.3 Firmware for the electronic driver 113
4.3.4 Sensor control firmware 116
4.3.5 Frequency meter and data acquisition protocols 117
4.3.6 Data verification and error management 117
4.3.7 GUI of modular system 118
4.4 Summary 120
5 Establishing the Operating Conditions for the Ultrasound Oscillating Sensor 121
5.1 Introduction 121
5.2 Modelling of ultrasonic oscillating sensors 122
5.2.1 Introduction 122
5.2.2 Circuit configurations of the ultrasonic oscillating sensor 123
5.2.3 Ultrasonic transducer model 123
5.2.4 Transmission line modelling 127
5.2.5 An improved model for the piezoelectric transducers 128
5.3 Gain change effect on ultrasonic operation 129
5.3.1 Introduction 129
5.3.2 The effects of gain change on ultrasonic oscillating sensor 130
5.3.3 Simulation of the effects of the gain change on the ultrasound sensor output frequency 131
5.4 Supply voltage change impact 132
5.5 BPFs for oscillating ultrasonic sensors 133
5.5.1 Introduction 133
5.5.2 Results and discussion 134
5.6 Phase shift inclusion 137
5.7 Distance between transducers 137
5.7.1 Experimental setup 137
5.7.2 Results and discussion 138
5.7.3 Ultrasonic frequency scatter analysis 140
5.7.4 Temperature–frequency sensitivity analysis 141
5.7.5 Hysteresis analysis 142

5.7.6 Overall comparison of different distances between transducers 143
5.7.7 General observations and discussion 145
5.8 Summary 148
6 Thermal Hysteresis in Piezoelectric Transducers and Data Sensor Fusion Processing 151
6.1 Introduction 151
6.2 Overview of hysteresis in piezoelectric devices 152
6.2.1 Introduction to the piezoelectric hysteresis literature 152
6.2.2 Piezoelectric materials 152
6.2.3 Hysteresis in piezoelectric materials 153
6.2.4 Hysteresis mechanisms 154
6.2.5 Examples of hysteresis in piezoelectric materials 155
6.2.6 Ageing and hysteresis 158
6.3 Overview of data sensor fusion 159
6.3.1 Introduction to sensor fusion 159
6.3.2 Sensor fusion architectures 159
6.3.3 Examples of existing applications of sensor fusion 160
6.4 Sensor fusion in ultrasonic oscillating sensors 161
6.4.1 Why use sensor fusion? 161
6.4.2 Acquisition and preliminary processing of the sensor data 163
6.4.3 Estimation of the inflection point 168
6.4.4 Quantification of the observed hysteresis 172
6.4.5 Sensor fusion extrapolation analysis for the correction of temperature–frequency hysteresis 173
6.4.6 Resolution and precision of fused temperature 176
6.5 Summary 179
7 Differential Measurements of Heat Loss in Water-Cooled Electric Motors 181
7.1 Introduction 181
7.2 Investigation of power loss in water-cooled electric motors 182
7.2.1 Power loss measurements 182
7.2.2 Deriving an analytical expression for variations in estimated efficiency 183
7.2.3 Simulation of the effect of temperature measurement resolution on power loss measurements 185

7.2.4 Using ultrasonic temperature sensors to evaluate motor loss 187
7.3 Motor power rating capabilities 188
7.4 Test rig modelling and CFD simulation analysis 189
7.4.1 Introduction 189
7.4.2 CFD simulations 189
7.4.3 Summary 197
7.5 Design and assembly of the test rig 198
7.5.1 3D printing overview 198
7.5.2 Transient thermal flow analysis 203
7.5.3 Parts and test rig structure 206
7.6 Experimental setup and results 208
7.6.1 Experiments in UOTS with flow in a single chamber 208
7.6.2 Experiments using UOTS heat loss differential measurements 219
7.7 Summary 226
8 Summary and Conclusion 228
8.1 Summary of individual chapters 228
8.1.1 Chapter 1 228
8.1.2 Chapter 2 229
8.1.3 Chapter 3 229
8.1.4 Chapter 4 230
8.1.5 Chapter 5 230
8.1.6 Chapter 6 232
8.1.7 Chapter 7 232
8.2 Cost considerations 233
8.3 Recommendations for future research 234
8.4 Overall summary 235
References 236
Appendices 250
Appendix A PCB layouts of modular system 250
Appendix B C programs for modular system control 251

List of Figures

Fig. 1.1 Classification of electric motors according to operating principles 6
Fig. 1.2 Power distribution of the supplied electrical power in a typical induction motor represented in a Sanky diagram 7
Fig. 1.3 Representation of the new IEC efficiency classes [4] 9
Fig. 1.4 Typical material cost and volume distribution in electric motors [4] 10
Fig. 1.5 Key differences between an RTD and a thermocouple in terms of temperature range and linearity 14
Fig. 1.6 Basic structure of a bimetallic strip 16
Fig. 1.7 Typical measurement arrangement in a liquid-in-glass thermometer 17
Fig. 1.8 Sound spectrum and some common applications and technologies for each sound range 20
Fig. 1.9 Historical timeline of the development and advancements of ultrasound technology for different applications 22
Fig. 1.10 Principle of operation of ultrasonic flow measurements using the transit-time technique [61] 24
Fig. 1.11 A typical ultrasonic welding system used to join thermoplastics [68] 25
Fig. 1.12 A typical ultrasonic fluid level measurement device 26
Fig. 1.13 Comparison of different types of temperature sensors, in addition to low-cost ultrasonic oscillating sensors, in terms of sensor accuracy across full range, temperature range and price per unit 30
Fig. 2.1 Experimental arrangements for ultrasonic evaluation methods [97] 39
Fig. 2.2 A typical experimental setup for an oscillating ultrasonic sensor used in ultrasonic temperature sensing [61] 46

Fig. 2.3 (a) A typical experimental setup and reflected waveform for pulse-echo ultrasonic temperature sensing; (b) ultrasound velocity and temperature relationship obtained from the pulse-echo experiment for different solutions [97] 47
Fig. 2.4 Direct TOF measurement architecture 48
Fig. 2.5 Sing-around architecture 50
Fig. 2.6 Phase shift measurement architecture 51
Fig. 2.7 Oscillating architecture 52
Fig. 3.1 Ultrasonic sensor system diagram 56
Fig. 3.2 Schematic of the AGC amplifier with a filament lamp 59
Fig. 3.3 V-R characteristics of filament lamp N9951189 60
Fig. 3.4 A block diagram of the PSoC-based AGC amplifier with a digital supervisory control 61
Fig. 3.5 AGC parameters of the TPA2016 2.8 W AGC stereo audio amplifier [130] 63
Fig. 3.6 Initial configuration of AGC using audio amplifier in ultrasonic oscillating sensors system 64
Fig. 3.7 Modifications of the configuration of AGC using audio amplifier in ultrasonic oscillating sensors 64
Fig. 3.8 JFET1 circuit diagram [131] 66
Fig. 3.9 JFET1 transient simulation results and specifications for a 24-kHz input signal 67
Fig. 3.10 JFET2 circuit diagram [132] 67
Fig. 3.11 JFET2 transient simulation results and specifications for a 24-kHz input signal 68
Fig. 3.12 JFET3 circuit schematic [133] 68
Fig. 3.13 JFET3 transient simulation results and specifications for a 24-kHz input signal 69
Fig. 3.14 Experimental waveforms for the input and output signals of the AGC for input signals with different amplitudes 70
Fig. 3.15 Block diagram of the ultrasonic driver with JFET3 AGC 71
Fig. 3.16 Frequency-temperature relationship for drivers with and without AGC 73
Fig. 3.17 A typical block diagram, register structure and sensor memory map for DS18B20 1-Wire temperature sensors [134] 76

Fig. 3.18 PCB design for the PSoC-based temperature measurement and acquisition system 78
Fig. 3.19 (a) 1-Wire sensors response before processing, (b) temperature data enhanced 79
Fig. 3.20 Frequency measurements using frequency to voltage conversion 82
Fig. 3.21 Diagram of counting cycles for a fixed amount of time [135] 83
Fig. 3.22 Diagram of measuring the time of a single cycle [135] 85
Fig. 3.23 Diagram of the hybrid method [135] 86
Fig. 3.24 Results of the worst case error simulation of a 16-bit counter 88
Fig. 3.25 Flowchart of the frequency measurements firmware 91
Fig. 3.26 Frequency tolerance in different numbers of pulses 95
Fig. 3.27 BJT-based voltage conversion circuit 97
Fig. 3.28 FET-based voltage conversion circuit 98
Fig. 3.29 Digital inverter-based voltage conversion circuit 98
Fig. 4.1 The general layout of modular system PCBs 102
Fig. 4.2 Schematic diagram of the electronic driver for ultrasound transducers 105
Fig. 4.3 The electronic driver module 106
Fig. 4.4 Schematic diagram of the multiplexer moduleJP2 107
Fig. 4.5 Multiplexers connections with PSoC 108
Fig. 4.6 JP2 header configurations for switching between in-circuit programming and normal module operation 108
Fig. 4.7 Signal-multiplexing module 109
Fig. 4.8 PSoC Gainer development board 109
Fig. 4.9 Schematic diagram of the frequency meter module 110
Fig. 4.10 The frequency meter module 111
Fig. 4.11 Assembled modular system that features (a) signal input multiplexer, (b) ultrasonic driver, (c) output multiplexer and (d) frequency meter 112
Fig. 4.12 Software control of modular system 113
Fig. 4.13 The switched capacitor filter block [128] 114
Fig. 4.14 MATLAB graphical user interface (GUI) program 118
Fig. 5.1 A realistic model of ultrasonic transducer 400ET180 123
Fig. 5.2 Frequency and phase response of a pair of submerged ultrasonic transducers 400ET180 124

Fig. 5.3 The transmitter circuit used to derive parameters of the transducer model .. 126
Fig. 5.4 Mason's circuit 126
Fig. 5.5 A complete simulation model system of an ultrasonic oscillating sensor..... 128
Fig. 5.6 Schematic diagram of a complete ultrasonic oscillating sensor system with simulation models of both piezoelectric transducers 129
Fig. 5.7 Output frequency of an oscillating ultrasonic sensor, which was held at a constant temperature, depending on the overall gain in the signal loop and its composition [95] 130
Fig. 5.8 Simulation results of output frequencies for various gains..... 132
Fig. 5.9 Simulation results of frequency variations in different supply voltages..... 133
Fig. 5.10 Temperature from conventional sensors and frequency measurements for ultrasonic oscillating sensor with a BPF (centre frequency 24.4 kHz, bandwidth of 10 kHz)..... 136
Fig. 5.11 SketchUp model of the experimental setup for UOTS distance measurements 138
Fig. 5.12 The programmed temperature profile of thermostat for ultrasonic distance measurements 139
Fig. 5.13 Ultrasonic frequency scatter behaviour for various tested distances 140
Fig. 5.14 Frequency/temperature sensitivity response for various tested distances..... 142
Fig. 5.15 Hysteresis values of various distances observed in UOTS..... 143
Fig. 5.16 Overall analysis of frequency scatter, hysteresis and sensitivity of distance measurements 144
Fig. 5.17 Frequency resonances of various distances between transducers..... 147
Fig. 5.18 The ideal and non-ideal frequencies and phase responses of the ultrasonic oscillating sensor..... 148
Fig. 6.1 A typical piezoelectric actuator and its principle of operation..... 156
Fig. 6.2 Hysteresis effect observed in the relationship between an applied voltage and the resulting displacement of a piezoelectric tube scanner [159] 156
Fig. 6.3 A typical frequency–temperature hysteresis curve in oscillators that mainly operate using crystal elements [148]..... 157
Fig. 6.4 Typical ageing profile of crystal resonators [156]..... 159
Fig. 6.5 The JDL sensor fusion architecture..... 160

Fig. 6.6 Dead reckoning process: (a) Sensor fusion processing using accelerometer and gyroscope (b) Real time results extracted from a smartphone for accelerometer and gyroscope sensors as well as fused sensor results 161
Fig. 6.7 Typical temperature profile from temperature sensors with calibration processing 164
Fig. 6.8 Examples of frequency noise, scatter and jumps in UOTS operations 164
Fig. 6.9 Design of a customised filter for evaluating frequency data 166
Fig. 6.10 Accepted and rejected UOTS readings based on the derived criteria 166
Fig. 6.11 Accepted and rejected UOTS readings based on the static and dynamic acceptance criteria 167
Fig. 6.12 Curves fittings of inflection point for heating and cooling regions of calibrated temperature data from conventional temperature sensors 168
Fig. 6.13 Line fittings for inflection points in the heating and cooling regions of the UOTS readings 171
Fig. 6.14 Experimental data for the UOTS output frequency and average temperature vs. time [172] 172
Fig. 6.15 Accepted UOTS output frequencies vs. temperature difference are shown in black dots, and the curve expected from equation (6.10) is represented by a red line 173
Fig. 6.16 Typical results obtained for ultrasonic oscillating temperature sensors where the processing interval is the duration 174
Fig. 6.17 Superimposed temperature and ultrasonic frequency with magnified 2nd and 3rd intervals 174
Fig. 6.18 Fused temperature estimates (red dots) and stepwise readings of the reference sensor 2 175
Fig. 6.19 Experimental results after the application of data sensor fusion, (a) full experimental and (b) a zoomed region 177
Fig. 6.20 Histograms for (a) fused temperature variations in t = 698 to 868 s and (b) the difference between the fitted curve and the fused temperature for the full experimental duration 178
Fig. 7.1 Experimental setup diagram of power loss for water-cooled electric motors .. 182
Fig. 7.2 Simulation results for 2-, 4- and 6-pole electric motors with rated power of 0.75 kW for various motor efficiencies against the resolution of the temperature measurement device 186

Fig. 7.3 Various chamber models developed for UOTS measurements 190
Fig. 7.4 Turbulence of water flowing at 8 L/min inside the chamber 192
Fig. 7.5 Turbulence performance for all models at different flowrates 193
Fig. 7.6 Comparison of turbulence of all models at the flowrate of 8 L/min 194
Fig. 7.7 Velocity of water flowing at 8 L/min inside the chambers of the three models 195
Fig. 7.8 Velocity in all models at different flowrates 196
Fig. 7.9 Comparison of turbulence in all models at the flowrate of 8 L/min 197
Fig. 7.10 The transducer holder model 201
Fig. 7.11 Images of printed models of the transducer holder using ABS and PLA 202
Fig. 7.12 Models of the printed curved transducer holder and inlet tube using PLA .. 203
Fig. 7.13 Water temperature profile at the inlet generated with user-defined C code. 204
Fig. 7.14 Temperature changes in a horizontal cross-sectional area 204
Fig. 7.15 Temperature calculation lines for each location in the SCSC model. The water flow starts at the inlet that is marked as an orange circle; the figure includes the corresponding line names chosen for each location. 205
Fig. 7.16 Averaged temperature results for each location in the SCSC model with a zoomed region at 5 seconds 205
Fig. 7.17 Printed model parts of the SCSC model 206
Fig. 7.18 Image of the design after the construction and mounting of the ultrasonic and temperature sensors 207
Fig. 7.19 Experimental setup for measuring water temperature with flow in a single chamber 208
Fig. 7.20 Experimental setup for measuring temperature using ultrasonic oscillating sensors for water-cooled electric motors 209
Fig. 7.21 Flowmeters used to measure the flowrate of water 209
Fig. 7.22 Test rig stand and holder 210
Fig. 7.23 The walls of the SCSC design 211
Fig. 7.24 The inlet and outlet connector parts of the SCSC design 211
Fig. 7.25 Rate of increase in water temperature when the aquarium heater was turned on (red line) and turned off (green line) 212
Fig. 7.26 Water temperature response when ice and cold water were added 213
Fig. 7.27 Ultrasonic frequency response to flowrate changes 214

Fig. 7.28 Output frequincies responses at different flowrates 215
Fig. 7.29 Frequency variations (scatter) at different flowrates 215
Fig. 7.30 Temperature and frequency responses versus time (left) and temperature-frequency relationships (right) in different flowrates 218
Fig. 7.31 Experimental setup for taking temperature differential measurements using ultrasonic oscillating sensors for water-cooled electric motors 219
Fig. 7.32 Experimental setup for temperature differential measurements 220
Fig. 7.33 Temperature recorded using conventional sensors and ultrasonic output frequencies versus the time 221
Fig. 7.34 Results of applying data fusion processing to the inlet and the outlet of the electric motor 222
Fig. 7.35 Differential fused temperature measurements 222
Fig. 7.36 Power loss in the simulated motor during the experimental period 223
Fig. 7.37 Power loss estimation using raw data from conventional temperature sensors 224
Fig. 7.38 Power loss calculated from the fused temperature (left) and power loss estimation using raw data from conventional temperature sensors (right) in heaters set at (a) 75%, and (b, c) 50% of the rated power 225

List of Tables

Table 1.1 Comparison between Direct and Indirect Methods of Measuring Electric Motor Power Loss 8
Table 1.2 The Most Common International Motor Efficiency Ratings [4] 9
Table 1.3 Comparison of Water and Air-cooled Electrical Motors 11
Table 1.4 Comparison of Cooling Methods Used in Different Electric Cars [11]. 11
Table 1.5 Advantages and Disadvantages of Thermocouple Sensors 13
Table 1.6 Advantages and Disadvantages of RTDs 15
Table 1.7 Advantages and Disadvantages of IR Sensors 15
Table 1.8 Advantages and disadvantages of bimetallic strip thermometer 16
Table 1.9 Advantages and Disadvantages of Liquid-in-Glass Thermometers 17
Table 1.10 Advantages and Disadvantages of Change-of-state sensors 18
Table 1.11 Advantages and Disadvantages of Silicon Diode Sensors 19
Table 1.12 Comparison among Different Conventional Temperature Sensors that Potentially Operate in Water 19
Table 1.13 A Comparison between Conventional Temperature Measurement Techniques and Ultrasonic Thermometers 29
Table 2.1 Advantages and Disadvantages of the Different Electronic Architectures for Ultrasonic NDE Sensors 53
Table 3.1 Comparison between Different JFET-Based AGC Designs 70
Table 3.2 Amplitude Stability for the Post-Amplifier PGA2 Gains of 48 and 3.2 72
Table 3.3 Available FVC Devices for Frequency Meter Developments 82
Table 3.4 Summary of the Frequency Measurement Techniques 89
Table 3.5 Results of All Four Tested Clock References, Including Standard Deviation and a Histogram. 93

Table 3.6 Selected BJTs with Low-level Threshold Voltages 96
Table 3.7 Selected FETs with Low-level Threshold Voltages 97
Table 4.1 Parameters of Various PSoC1 Parts [128] 104
Table 4.2 Specifications and Prices of the Selected TCXOs 110
Table 4.3 Description of Connectors and Jumpers in the Modular System 112
Table 4.4 GUI Control of the Modular System 119
Table 5.1 Different Values Calculated for L and C when R is Varied 125
Table 5.2 Equivalent Circuit Parameters for the Transducer Model 126
Table 5.3 Structure and Thicknesses of the Simulated Acoustic Part of the Model 128
Table 5.4 Summary of Results of UOTS Measurements with a Fixed BPF Centre Frequency of 22.7 kHz 134
Table 5.5 Summary of Results of the UOTS Measurements with a Fixed BPF Bandwidth of 10 kHz 135
Table 5.6 Distance Limits Considerations for Test Rig Design Specifications 138
Table 5.7 Frequency Deviations in Different Distances between Transducers 141
Table 5.8 Hysteresis Scatter and Sensitivity of UOTS for Different Distances between Transducers 144
Table 5.9 Outcomes of UOTS Parameters 150
Table 6.1 List of the Remaining and Compromised Advantages of Sensor Fusion 163
Table 6.2 Approximation of the Experimental Curves for the Temperature Data 169
Table 6.3 Approximation of the Experimental Curves of the UOTS Data 171
Table 6.4 Different Data Sets and Standard Deviation Values for Precision Measurements 179
Table 6.5 Specifications of the UOTS Fused Temperature 180
Table 7.1 Temperature Sensor Technologies Used in Commercial Liquid-cooled Electric Motors 187
Table 7.2 Maximum Power Ratings (in kW) of Water-cooled Electric Motors can be Evaluated Using Current Developments 188
Table 7.3 Design Specifications and Criteria for UOTS Hardware Configurations 189
Table 7.4 Comparison of Turbulence, Velocity and Thermal Response in the Proposed Chambers 197
Table 7.5 Advantages and Disadvantages of 3D Printing 199
Table 7.6 Comparison of the Ultimaker2 and the Velleman K8200 200

Table 7.7 Comparison of Polylactic Acid (PLA) and Acrylonitrile Butadiene Styrene (ABS) 201
Table 7.8 Number of Jumps Found at Each Flowrate 216
Table 7.9 Frequency and Temperature Sensitivity at Various Flowrates 218
Table 8.1 Total Cost of the Modular System 233
Table 8.2 Total Cost of the Developments, Including the Construction of the Modular System and the Test Rig 234

List of Software

MATLAB	Digital signal processing; data acquisition; system control
PSoC Designer	PSoC programming
LochMaster	Veroboard layout design
Autodesk Autocad	Test rig modelling
EAGLE	PCB circuits layout and developments
SketchUp	3D Modelling
Ansys Fluent	Computational fluid dynamics analysis
DesignSpark Mechanical	3D modelling and generation of 3D-printed models
Slic3r	Converting 3D models to printing instructions
TINA Simulator	Electronic circuit simulator
OrCAD PSpice	Electronic circuit simulator
LTSpice	Electronic circuit simulator

Chapter 1

Introduction to Ultrasonic Differential Heat Loss Measurements

1.1 Aim and objectives of the present research

1.1.1 Focus of the present research

Ultrasonic sensors can rapidly respond to changes in average temperatures across the complete ultrasonic pathway, which is difficult to achieve using conventional temperature-sensing technologies. This research investigates ultrasound calorimetry and

its advantages over calorimeters that are implemented using conventional temperature sensors in order to achieve the accurate estimate of heat losses in electrical motors.

The proposed ultrasonic calorimeter is based on ultrasonic oscillating temperature sensors. However, in the analysis of the temperature-frequency relationship, a hysteresis effect was observed in the temperature changes occurring in both directions. Further research will be conducted to determine the possible reasons for this effect in the piezoelectric transducers that are deployed in the oscillating sensors.

The major electronic development of this project is the design of a low-cost electronic driver that supports the reliable operation of oscillating ultrasonic sensors. A general driver consists of an amplifier, a phase shifter and a Band Pass Filter (BPF). The inclusion of an amplifier with Automatic Gain Control (AGC) was investigated with the aim of preventing the output of the amplifier from being driven to saturation. This development was expected to reduce the hysteresis in the output frequency of the sensor and to improve the consistency and repeatability of its readings. An evaluation of different arrangements of electronic devices for ultrasonic oscillating sensors was conducted. Several hundred hours of measurements were completed overnight to establish the arrangements and parameters for the operations of the Ultrasonic Oscillating Temperature Senor (UOTS). In order to establish reliable and accurate frequency measurements, a low-cost frequency meter was developed. Several clocking and referencing options were examined in order to achieve highly accurate, high-speed measurements of the ultrasonic output frequency under various environmental conditions.

In order to overcome hysteresis, which is observed in the temperature-frequency relationship, sensor fusion processing was applied first to calibrate the frequency measurements and then to correct the temperature readings by conventional sensors. Moreover, sensor fusion compensated the physical effects of hysteresis, such as ageing, on piezoelectric devices.

1.1.2 Motivation

Highly accurate temperature measurement is a requirement of various applications such as estimating power loss of electric motors or determining the amount of energy released through the burning of food; however, devices with accuracy better than ± 0.15 K are

expensive. This gap calls for the development of a low-cost but accurate temperature measurement device. Low-frequency and low-intensity oscillating ultrasonic sensors, with additional data processing and calibration, could potentially achieve high accuracy at a significantly reduced cost.

1.1.3 Aims and objectives

This research aims to develop an experimental setup and an electronic instrumentation that are capable of measuring thermal losses in water-cooled electrical motors with high accuracy at reduced cost. The objectives of the current research are as follows:

- Develop a supervisory gain control system for ultrasonic signal to avoid saturation and preserve ultrasonic transmitted signal.
- Construct and design supporting electronics for UOTS operation, including a temperature logging device and a frequency meter.
- Develop and verify sensor electronics using inexpensive electronics. This objective includes the software and hardware development of the modular system for oscillating ultrasonic sensors.
- Simulate the oscillating sensor arrangements in order to test the system under various conditions.
- Derive the best operational parameters for the system, which include gain setting, filtering requirements and distance between transducers.
- Design a 3D-printed experimental test rig for water-cooled electric motors, including accurate power loss evaluation and assessment of the motor classification process.
- Elaborate and verify the data fusion procedure for the sensor to compensate for different piezoelectric effects, such as temperature-frequency hysteresis and ageing.

1.1.4 Independent contributions to knowledge

A novel UOTS, featuring single-chip, PSoC-based electronics was implemented, tested and tuned. The development of the UOTS included testing the operational parameters, such as the distance between transducers, power setting, feedback oscillating gain and automatic gain control. The results were evaluated using a simulation and experimental testing. The simulation included modelling piezoelectric transducers as well as the electric and acoustic paths of the instrument. A modular system was developed to accommodate

the simultaneous operation of four UOTS pairs. The parameters of the modular system were controlled using a user-friendly GUI, which reduced the cost of the BOM parts to £10.

Hysteresis, which is specific to the thermal properties of piezoelectric transducers, led to ambiguous UOTS readings in our experiment. This effect was mitigated by using data fusion, in which the fused temperature was estimated by extrapolating the ultrasonic frequency and the temperature readings measured by a conventional sensor. The scattering in the ultrasonic frequency was reduced by employing the appropriate filtering criteria.

The experimental setup for measuring the thermal losses of the electrical motor, which featured a UOTS at both the inlet and the outlet, was successfully built and tested. The setup consisted of two chambers that were constructed using 3D printing technology and the electronics connected to the modular system. The resolution of power loss that was measured using the UOTS feature was significantly higher than the resolution of power loss measured by conventional temperature sensors. Moreover, the UOTS allowed for the faster detection of temperature changes and the faster estimation of the inflection points.

1.2 Heat losses in motors

1.2.1 Heat measurements and calorimetry

Calorimetry is a science that involves determining a change within the state variables of an object in order to estimate the heat transfer related to the alteration of its state. A typical calorimeter operates by evaluating the heat exchanged from the system into the surrounding environment [1]. Calorimetry, in both physics and chemistry, involves the measurements of heat reaction, combustion heat and fusion heat, and it can include the derivation of the specific heat capacity of a substance [2].

During the past century, the principle of calorimeters remained unchanged. However, in the present century, the rapid developments of electronics promoted the revolution of calorimetry science and extended the range of its novel applications. Calorimeters are used widely in various sciences, including the life, pharmaceutical and food sciences. Quality control, safety appliances and fuel energy content estimation are the most common applications of calorimeters [3].

1.2.2 Overview of heat losses in electric motors

1.2.2.1 Introduction

Electric motors are designed to transform energy from an electrical to mechanical form with a minimum of energy loss. This loss is dependent on various factors, such as the motor design, the materials involved in manufacturing, the environmental rating of the device and technical classifications. Over the last decade, there has been an increased interest in the efficiency of electric motors because of the increasing demand on reducing energy consumption in machinery [4]. The power of electrical motors is frequently stated in units of horsepower (hp), where 1 hp is equivalent to 746 W [5]. At present, electric motors consume over 40% of the electrical energy supplied globally [4].

The operating principle of electrical motors is based on the interaction between the magnetic field and the electrical current. The flow of electrical current along the motor armature and field winding causes attraction and repulsion forces at the magnetic poles. These forces result in the rotation of the armature, which consequently delivers torque to the mechanical load.

In general, the several types of electric motors are classified based on their size, application type, electrical characteristics, ingress protection rating and means of cooling [5]. The most common classification is based on the type of driving current, that is, AC or DC (Fig. 1.1).

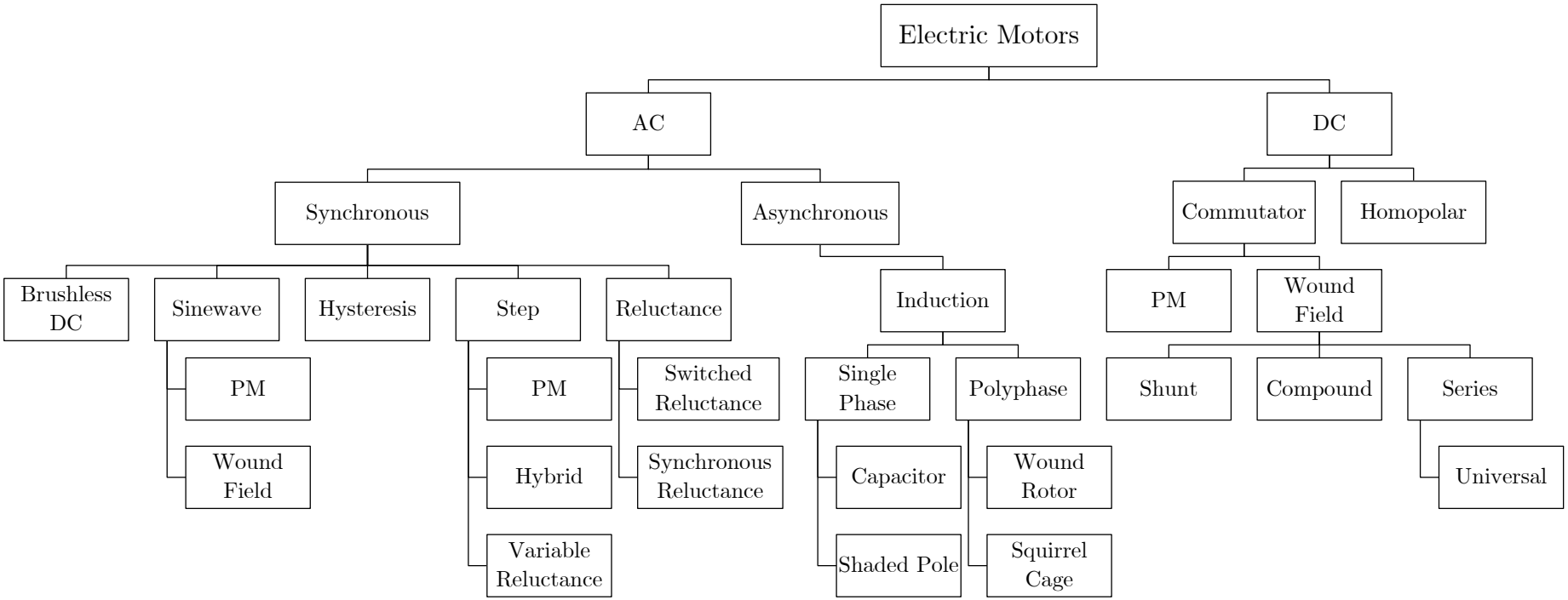


Fig. 1.1 Classification of electric motors according to operating principles

1.2.2.2 Efficiency of electrical motors

Efficiency is considered one of the most important parameters in evaluating any given motor. In order to investigate the efficiency of electrical motors, it is important to understand the sources of power loss. Electric motors can exhibit various types of losses, including losses in the stator winding P_s, losses in the rotor cage P_r, losses in iron (caused by the hysteresis effect) and eddy currents $P_{FE,(s,w)}$, in addition to mechanical losses due to friction and winding losses $P_{fr,w}$, and P_{SLL}, which represent additional losses (i.e. stray load losses).

These losses vary in magnitude. Their relative magnitudes are shown in the Sankey diagram provided in Fig. 1.2, where the thicker arrows indicate larger power losses in both the stator and the rotor. The typical distribution of the supplied electrical power depends on the rated power of the motor. For example, stray load losses constitute only 5% of loss distribution in a 1 kW induction motor, whereas they constitute 15% of the total power loss in a 100 kW motor [4].

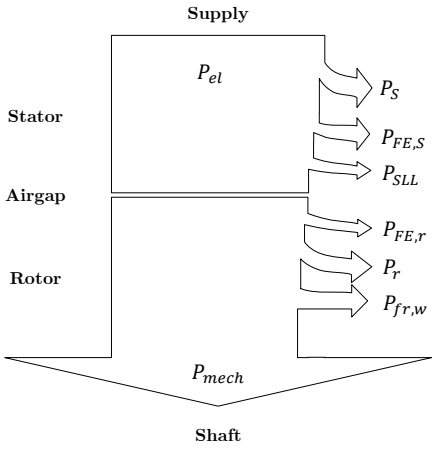


Fig. 1.2 Power distribution of the supplied electrical power in a typical induction motor represented in a Sanky diagram

1.2.2.3 Efficiency measurements

In typical modern industrial electric motors, 85 to 95% of supplied electrical power is converted to mechanical power [5]. By definition, motor efficiency η represents the ratio between the output mechanical power P_{out} (or P_{mech}) and the input electrical powers P_{in} (or P_{el}) as shown in equation (1.1).

$$\eta = \frac{P_{mech}}{P_{el}} \tag{1.1}$$

Equation (1.1) can be rearranged to include the power loss P_{loss}, which is the difference between the electrical input power and mechanical output as shown in equation (1.2).

$$\eta = \frac{P_{el} - P_{loss}}{P_{el}} = 1 - \frac{P_{loss}}{P_{el}} \tag{1.2}$$

Both direct and indirect methods can be used to determine the efficiency of motors. Direct methods require the accurate determination of the input electrical power and the output mechanical power. The calculations involve power, speed and torque measurements. Indirect methods are based on power loss calculations of the individual losses in the motor. A comparison of power loss estimation methods is shown in Table 1.1.

Table 1.1 Comparison between Direct and Indirect Methods of Measuring Electric Motor Power Loss

Measurements approach	Advantages	Disadvantages
Direct	Easier to calculate based on the definition of the efficiency	Poor accuracy in practice High cost of instrumentation required for accurate measurements
Indirect	Typically provides higher accuracy Is applicable for various environmental conditions	It might be difficult or inconvenient to measure losses for all possible sources

1.2.2.4 Standards for determining motor efficiency

Manufactured motors are rated by their efficiency, and they are priced accordingly. Highly efficient motors provide savings in the cost of running the motor. The accurate determination of the efficiency of a motor is important not only to price it but also to optimise its design [4]. There are various versions of national and international initiatives regarding motor efficiency ratings, including the following:

- The European Motor Challenge Program

- European Committee of Manufacturers of Electrical Machines and Power Electronics (CEMEP) voluntary agreement, which established previous classifications of AC motors of EFF1, EFF2 and EFF3
- The 4E Electric Motor System Annex initiative
- IEC 60034-30 IE0 classification standard

Some interrelations among the various motor efficiency ratings are presented in Table 1.2.

Table 1.2 The Most Common International Motor Efficiency Ratings [4]

Efficiency	IEC 60034-30	Europe (CEMEP)	United States
Super premium	IE4		
Premium	IE3		NEMA Premium
High	IE2	EFF1	Epact
Standard	IE1	EFF2	

Fig. 1.3 shows a graph of the rated power–efficiency relationship for IEC 60034-30-rated motors. On the graph, the IE4 rating applies to motors with power-efficiency points above the IE4 curve. The IE3 rating applies to the points between the IE4 and IE3 curves etc.

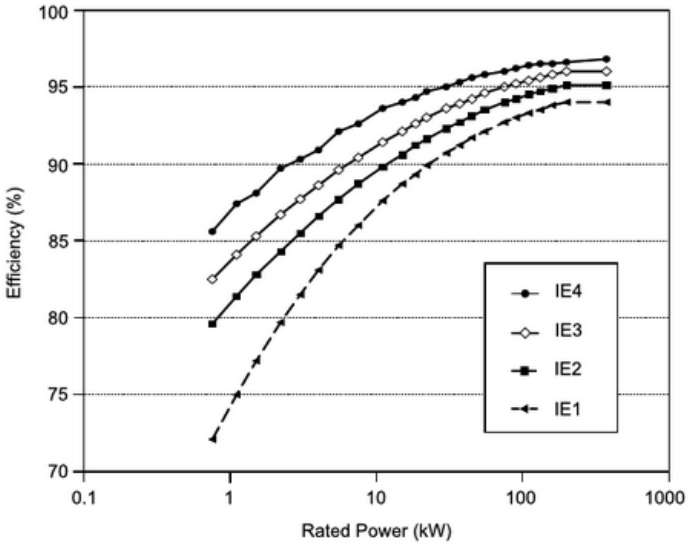


Fig. 1.3 Representation of the new IEC efficiency classes [4]

1.2.2.5 Cooling of electric motors

The motor cooling arrangement is an important design factor because it determines the permissible output power in an electric motor [6, 7]. Modern motors dissipate a

substantial amount of power in the form of heat, which needs to be removed. Cooling units play a significant role in power electronics applications, which is illustrated by the cost and volume share of the typical motor shown in Fig. 1.4.

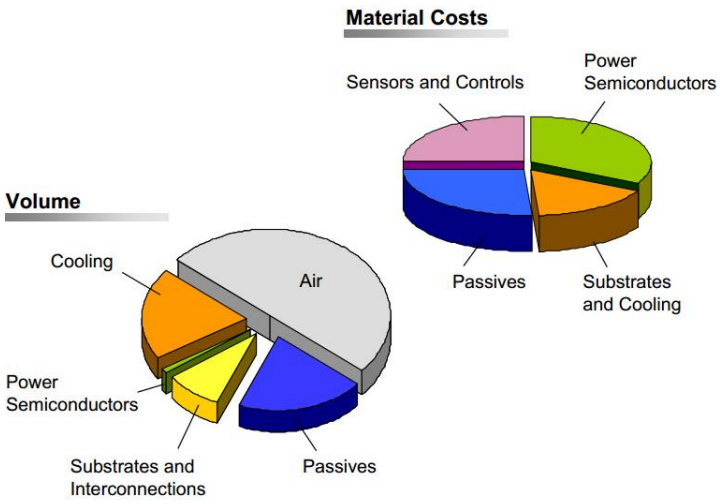


Fig. 1.4 Typical material cost and volume distribution in electric motors [4]

To avoid thermal runaways in electric motors, heat is usually removed by the convection of the coolant, such as air, water and even hydrogen in high-speed motors. Many motors dissipate heat into the ambient air, which is called open-circuit ventilation.

In water-cooled electric motors, heat is transferred to the cooler through an intermediate fluid medium. Because this fluid is circulated in a closed-loop system, this approach is called closed-loop ventilation.

1.2.2.6 Air and water-cooled electric motors

There are both advantages and disadvantages in cooling electric motors that use water or air. Table 1.3 summarises the advantages and disadvantages of both approaches. The choice of the cooling system is dependent on the type and power rating of the application.

Table 1.3 Comparison of Water and Air-cooled Electrical Motors

Coolant type	Advantages	Disadvantages
Water	Higher efficiency Higher output power [6] Lower noise Compact construction [8] Cooling is independent on the speed of the motor [6]	Higher cost Complex design compared to air-cooled motors [8]
Air	Lower cost Less components Lower weight Environmentally friendly	Require extensive maintenance Becoming phased out by water-cooled motors in recent motor designs

1.2.2.7 Motor cooling in electric cars

In hybrid or electric vehicles, one or more cooling loops are used in the electric components and the combustion engine. Different loops are employed for the maintenance of different temperatures in different components. For example, the battery needs to be held at a particular constant temperature in order to extend its lifetime. Sudden increases in this temperature will result in immediate and permanent damage to the battery components [9].

Various types of coolants are used in modern electric and hybrid cars, such as water-ethylene glycol, air and oil. For example, the Toyota Prius uses several cooling loops in the engine and in the electric drive, which is cooled using water-ethylene glycol at 65 °C. Radiators are usually used to dissipate heat into the environment [10]. As shown in Table 1.4, most modern electric and hybrid cars use liquid cooling in their operation. In electric cars, there is an increasing demand for water-cooled motors rather than air-cooled motors.

Table 1.4 Comparison of Cooling Methods Used in Different Electric Cars [11].

Car type	Cooling method
Nissan Leaf	Air
Toyota Prius	Liquid
Tesla Roadster	Liquid
Ford Focus Electric	Liquid

Car type	Cooling method
Lotus Evora	Liquid
Chevrolet Volt	Liquid
Porsche Spyder	Liquid

1.3 Temperature measurements

1.3.1 Introduction to temperature measurements

Temperature can be defined as a single state variable that represents the thermal condition of a system. In physics, temperature is represented by the average kinetic energy generated from molecules movements. Various standard numerical measures are widely used, such as the Celsius, Kelvin and Fahrenheit scales [12]. A maximum theoretical value of temperature that can be reached has not been defined; however, absolute zero (i.e. at 0 K) represents the minimum temperature point at which all molecules stop moving [13].

Techniques used to measure temperature were first discovered by the ancient philosopher, Hero of Alexandria, who established the relationship between the expansion and contraction of air and ambient temperature in the first century BC [14]. During the 16th century, his findings were documented in a book that inspired the scholars during that era to invent the first thermometer. The thermoscope is the first-known device that was built to measure temperature. It was used by Galileo at the beginning of the 17th century. Since then, several scientists have developed their own thermometers and even established their own temperature-sensing scales [14].

Energy can take various forms, such as heat. It is usually transferred if there is some interaction between the system and the surrounding environment. The energy transferred from one medium to another equalizes the temperature between these mediums. This energy represents heat transfer. In a thermal equilibrium, the difference between the temperatures of the environment and the system is zero [13]. The devices used to measure temperature are classified based on many parameters [15], the most common of which include the following:

- Range: the maximum and minimum temperatures recorded by the sensor
- Span: upper and lower temperature limits within the calibrated range
- Turndown: the ratio between the maximum and minimum measurable parameters
- Immersion length: the distance between the edge of the sensor's protective enclosure and the point of contact with the measurer

- Insertion length: the distance between the edge of the sensor's protective enclosure and the external threads

1.3.2 Types of temperature sensors

Three major elements are usually found in a typical temperature measurement system: a primary standard system, a practical measuring system and a measurer. There are seven suggested basic types of temperature measurement devices: thermocouples, Resistive Temperature Devices (RTD), infrared sensors, bimetallic devices, thermometers, change-of-state sensors and silicon diodes [16].

This section briefly summarises each type of sensor and novel sensing technologies, such as distributed temperature sensing.

1.3.2.1 Thermocouples

Thermocouples consist of two different types of conductive materials that are welded together. The junction between the conductors develops a small voltage that is dependent on the temperature change [17]. This type of temperature-sensing device is widely used in industry and home appliances because of their low cost. About 50-60% of all industrial temperature measurement devices are thermocouples [18]. However, they might not be suitable for applications that require high-precision temperature sensing because of the noise developed from parasitic junctions. For example, typical low-cost thermocouples rarely achieve an accuracy of 1 K [19].

Thermocouples are categorized based on their cost, sensitivity to temperature, temperature range, accuracy and combination of conductive manufacturing materials. Because of the large operational temperature range in some thermocouples types, they are a perfect solution for the safe operation of gas-fed devices, where they operate as thermal runaway detectors [20]. The advantages and disadvantages of thermocouples sensors are listed in Table 1.5.

Table 1.5 Advantages and Disadvantages of Thermocouple Sensors

Advantages	Disadvantages
Inexpensive [17] Wide temperature range [17]	Low voltage sensitivity [19] Frequent calibration required [14]

1.3.2.2 Resistive temperature devices

The operating principles of RTDs are similar to those of thermocouples. Temperature is dependent on the characteristics of materials that change their resistivity rather than electromagnetic field. RTDs are also widely used; almost 40% of all sensors used in industry are RTDs [18]. They consist of a coiled wire wrapped around a metallic core that has a large temperature coefficient of resistance [18]. Currently, platinum is the most popular option because of its highly linear resistance versus temperature relationship and its wide temperature range. RTDs have the ability to measure temperature without the direct aid of external temperature references [21].

The relationship between resistance and temperature features greater linearity comparing to thermocouples, as shown in Fig. 1.5. However, narrow-range temperature measurements using RTDs are not recommended because the change in the electromagnetic field in such ranges is notably small.

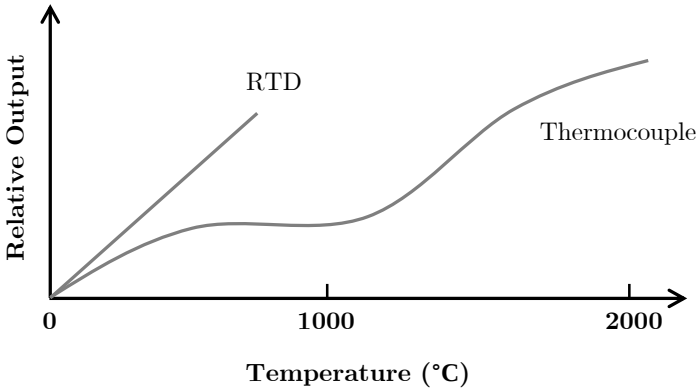


Fig. 1.5 Key differences between an RTD and a thermocouple in terms of temperature range and linearity

One of the most commonly used types of RTDs is the thermistor. This device differs slightly in operation compared to a conventional RTD. The thermistor is made from a semiconductor material rather than the pure metal used in a conventional RTD. Compared with an RTD, the thermistor is able to measure temperature within a narrow temperature range with greater precision and higher resistance versus temperature sensitivity [22]. The advantages and disadvantages of RTD sensors are listed in Table 1.6.

Table 1.6 Advantages and Disadvantages of RTDs

Advantages	Disadvantages
Linear resistance vs. temperature [8] Good stability and repeatability [6] High accuracy [9] Fast response time	High non-linearity in high temperatures Resistive elements usually fragile Self-heating [9]

1.3.2.3 Infrared sensors

Infrared temperature (IR) sensors determine the temperature of the thermal radiation emitted by an object. This infrared radiation is caused by the internal movements of molecules within the object, which are dependent upon the temperature. Infrared radiation has a wavelength ranging from 0.7 μm up to 1000 μm, situated above the red spectrum of light, which makes them invisible to the human eye [23]. IR temperature sensors have become increasingly popular because they feature small sizes and simple operation. IR sensors are widely used in industry because they utilise non-contact measurements [24]. The advantages and disadvantages of IR temperature sensors are listed in Table 1.7.

Table 1.7 Advantages and Disadvantages of IR Sensors

Advantages	Disadvantages
Fast reading time [24] Measure moving targets [23] Ability to operate in hostile conditions [24] Wide temperature range [24]	Only surface temperatures can be measured [24] Accuracy dependent on the operator's experience [23] High cost

1.3.2.4 Bimetallic devices

The operating principle of the bimetallic strip thermometer is that different metals expand and contract at different rates when they are heated or cooled [25]. This principle allows for measuring the temperature based on the displacement exhibited by the metal. Bimetallic devices are considered one of the simplest types of thermal sensors [26]. Bimetallic strip thermometers are commonly used in mechanical clocks to compensate for temperature errors in time keeping [27].

A typical bimetallic device consists of two different types of metals, usually steel and copper, which are welded together in a strip. The combination of metals should feature different values of thermal expansion coefficients [26]. When the strip is heated or cooled, the unclamped end of the device tends to bend (Fig. 1.6).

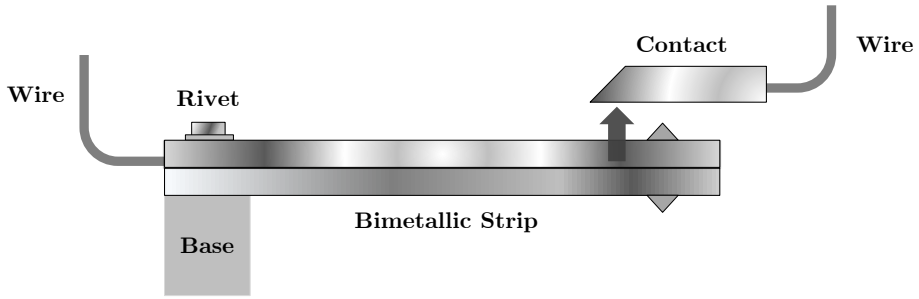


Fig. 1.6 Basic structure of a bimetallic strip

The displacement is measured at the tip of the strip and then is converted to temperature readings by using a table of displacements versus temperatures. Bimetallic devices are widely used as switches in thermostats [28]. The advantages and disadvantages of bimetallic strip thermometer are listed in Table 1.8.

Table 1.8 Advantages and disadvantages of bimetallic strip thermometer

Advantages	Disadvantages
Robustness [28]	Poor accuracy [29]
Simple to operate [28]	Not suitable for low temperature readings [28]
Completely mechanical – no energy required to operate [28]	Hysteresis [29]
Inexpensive [29]	Required calibration [30]

1.3.2.5 Liquid-in-glass thermometers

Thermometers are well-known devices that utilise liquid expansion in order to measure the temperature of a body. A typical thermometer features a temperature sensor and a visible reading scale (Fig. 1.7) that measures the liquid expansion in common temperature scale [31]. These sensors are widely found in medical applications and weather stations [32]. Accurate temperature measurements require the thermal equilibrium between the measurement device and the measurer, which generally consumes more time compared to other types of sensors, such as RTDs.

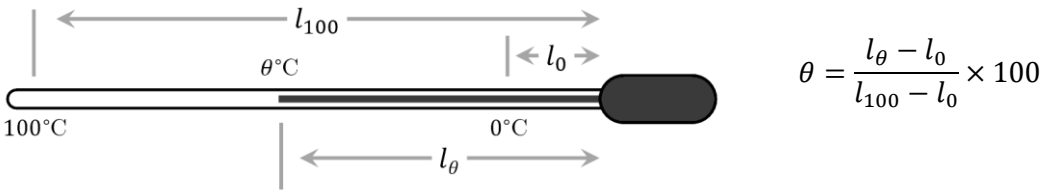


Fig. 1.7 Typical measurement arrangement in a liquid-in-glass thermometer

A common type of thermometers is the liquid-in-glass thermometer, which is usually used to measure the temperature of a room or body temperature. Mercury is the most common fluid used in such sensors because of its high thermal expansion at room temperature [13]. The advantages and disadvantages of thermometers are shown in Table 1.9.

Table 1.9 Advantages and Disadvantages of Liquid-in-Glass Thermometers

Advantages	Disadvantages
Low cost Easy calibration [33]	Errors in readings, glass can expand or contrast [19] Slow reading time [17] Fragile, can be hazardous if broken, mercury vapour is poisonous [33]

1.3.2.6 Change-of-state sensors

Change-of-state temperature sensors measure the change in the material state that is driven by a change in temperature (e.g., ice to water to steam). These devices are offered commercially in many forms, including labels and pellets [16]. They usually operate as an alarm or indicator device, which is triggered when a fixed temperature level is reached [34].

Change-of-state temperature sensor is used in steam traps. When steam traps require maintenance or adjustments, they generate heat. A change-of-state label sensor is attached to the trap, which changes its colour when a threshold temperature is exceeded [30]. These labels may also come in a digital form. The advantages and disadvantages of change-of-state sensors are listed in Table 1.10.

Table 1.10 Advantages and Disadvantages of Change-of-state sensors

Advantages	Disadvantages
No energy required to operate, completely mechanical [30] Small size	Slow response time Poor accuracy [16] Sensor state is irreversible

1.3.2.7 Silicon diodes

Diodes are widely used as temperature-sensing devices in applications where medium-precision temperature readings are required. They feature a relatively linear response across the full operational temperature range [35]. The diode-based measurement electronic circuit is simple to construct and consists of three stages: excitation, offsetting and amplification. Inexpensive microcontrollers measure temperature using an analogue-to-digital converter (ADC) with a precision of ±1 K [36]. Diode sensors are considered one of the cheapest temperature-sensing technologies [36].

Diodes can sense temperature change by monitoring the drop in forward voltage because of its strong dependency on temperature. The diode junction temperature can be given as the Shockley diode equation (1.3):

$$T = \frac{q(V_2 - V_1)}{k\eta . \ln\left(\frac{I_2}{I_1}\right)} \tag{1.3}$$

where V_1 and V_2 are the measured voltages across the diode, I_1 and I_2 are the currents passing through the diode, which can be set using a current source, q is the electron charge, k is Boltzmann's constant and η is the ideality factor [37].

Diode sensors are widely used in integrated circuits to measure junction temperatures (i.e., die temperature) [38]. Table 1.11 shows the advantages and disadvantages of silicon diode sensors.

Table 1.11 Advantages and Disadvantages of Silicon Diode Sensors

Advantages	Disadvantages
Nearly linear voltage vs. temperature relationship [37] Very cheap [35] Reduced self-heating [39] Small size, on-chip integration [38]	Low precision [36]

1.3.2.8 Distributed temperature sensing

Distributed Temperature Sensing (DTS) is a novel technology that was developed to measure the temperature distribution across a fibre optic line [40]. Optic lines can be extended long distances to remote locations, which complicate the process of temperature monitoring. Studies on this novel technology are currently an active research area [41].

The mechanism of temperature measurements using DTS is based on transmitting a signal and monitoring the reflected pulse. As it travels, it collides with the atoms of the transmission line, which in turn slightly changes the frequency shift of the signal. Because the pulse is transmitted continuously, a clear temperature profile of the fibre optic line is formed [42].

This method was also successfully implemented in electrical power lines by tying the power line to a DTS. Many DTS-based ongoing studies focus on agriculture and soil analysis, including soil monitoring [43].

1.3.3 Selection of conventional inexpensive temperature sensors

There is a wide range of commercially available temperature sensors with different specifications. Some of these sensors, which are shown in Table 1.12, may be appropriate for the development of UOTS.

Table 1.12 Comparison among Different Conventional Temperature Sensors that Potentially Operate in Water

Sensor	Package	Temperature Range	Accuracy (± K)	Cost per unit (£)
DS18B20	6mm cylinder	-55 ° C to +150 ° C	0.25	0.99
TSic 301/306	TO92	-50°C to +150°C	0.35	4.70
TST100	5mm cylinder	-40 ° C to +85 ° C	0.30	5.78

Previous research [44] found that 1-Wire sensor technology is the most suitable type of temperature sensor for use in a UOTS. These sensors cost less than £1.00 and are accurate to ±0.25 K, which is very attractive considering their unit price. In addition, these sensors can operate in a wide range of temperatures from -55 °C to +125 °C.

1.4 High resolution ultrasonic temperature measurements

1.4.1 Definition of ultrasound, its history and applications

1.4.1.1 Definition

Ultrasound is a mechanical vibration or sound wave with a frequency above the range of human perception. The velocity of ultrasound is strongly dependent on the temperature and the medium. The typical ultrasonic velocity varies from 1,540 to 1,570 m/s in human tissue. In addition, the velocity of an ultrasound wave can be calculated as a product of the operating frequency and wavelength. The sound spectrum and some common applications and technologies for each sound range are shown in Fig. 1.8.

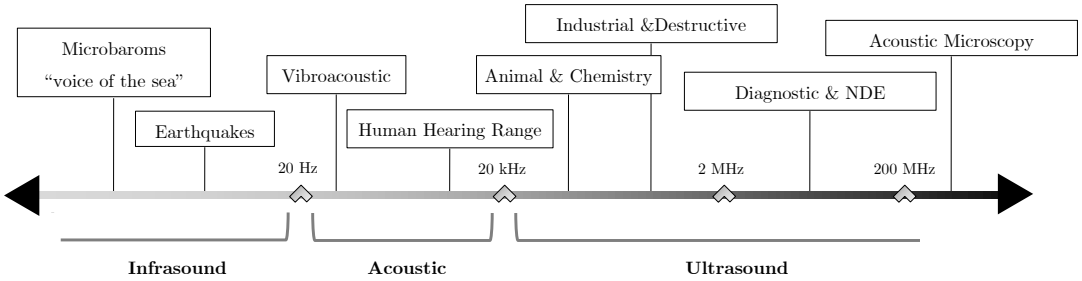


Fig. 1.8 Sound spectrum and some common applications and technologies for each sound range

To measure ultrasound waves, a sound wave with a frequency from 15 kHz to several GHz is transmitted through a medium. The measurer waits for reflected echoes, which are shaped by the internal structure of the reflectors. The specifications of the parameters to be measured are determined by the time of arrival, the pulse shape and other factors. Reflections occur when the medium changes; each medium has a specific acoustic impedance, which is the product of the medium density and speed in that medium. Some notable effects that might occur during evaluation are the refraction and diffraction of the ultrasound. Some factors might limit the performance of ultrasound measurement.

One factor is the attenuation of the wave signal as it travels and its energy is transferred to other forms. In addition, the penetration depth depends on frequency: the higher the frequency, the lower the depth [45].

One of the significant advantages of testing using ultrasonoscopes, that is, devices that operate based on ultrasound principles, is that they use a non-destructive, non-invasive and non-ionizing process. Because of this property, ultrasound technologies are used in a wide range of applications. One of the most common examples of Non-Destructive Testing (NDT) evaluations is in scanning a human body for tumour detection without the need for surgery. In another example, there is no need to break underground pipes to investigate possible leaks. Ultrasound technology has been shown to be superior over other methods for various applications during the last decade [46].

1.4.1.2 History

Some creatures, such as bats, use ultrasound as a navigation tool. In 1794, Lazzaro Spallanzani, an Italian physiologist, studied the sensing organs in creatures such as bats and torpedo fish [47]. Since then, ultrasound has been used intensively in various scientific fields, resulting in numerous applications. For example, ultrasonic-based military equipment was developed prior to the Second World War [48].

Much research was conducted to utilise ultrasound. During the mid-19th century, Jean-Daniel Colladon achieved a major advancement in ultrasonic sonography. He used a church bell under water to measure sound properties in both air and water [48]. Although he used simple equipment, he managed to calculate the speed of sound at 1,435 m/s, which is very close to the current standard of sound velocity [48].

One of the most significant advancements in the ultrasonic field, specifically in transducer fabrication, is the discovery of the piezoelectric effect. In the 1880s, the Curie brothers found a relation between the temperature generated by a piezoelectric material and the strain change. These achievements led to the invention of the piezoelectric quartz electrometer [49].

No official records of using ultrasound existed until the 1910s, when echo-sounder principles were investigated [50]. Following the sinking of the Titanic in 1912, Paul Langevin attempted to develop an instrument that could potentially locate icebergs, thus

reducing the chances of ships colliding with them. With Constantin Chilowsky, he invented a high-frequency, quartz crystal-based ultrasonic machine for the detection of underwater objects, which was subsequently called the hydrophone [51].

In the medical sciences, S.Y. Sokolov achieved some early development of ultrasonic imaging in 1937. In the 1950s, Karl Dussik constructed a medical imaging device that captured internal pictures of the human brain and ventricles using through-transmission techniques [52]. Since then, significant developments in medical ultrasonic led to the introduction of the obstetric ultrasound by Ian Donald in the 1960s. Fig. 1.9 shows a timeline of the developments of different aspects of ultrasound, which is based on the literature.

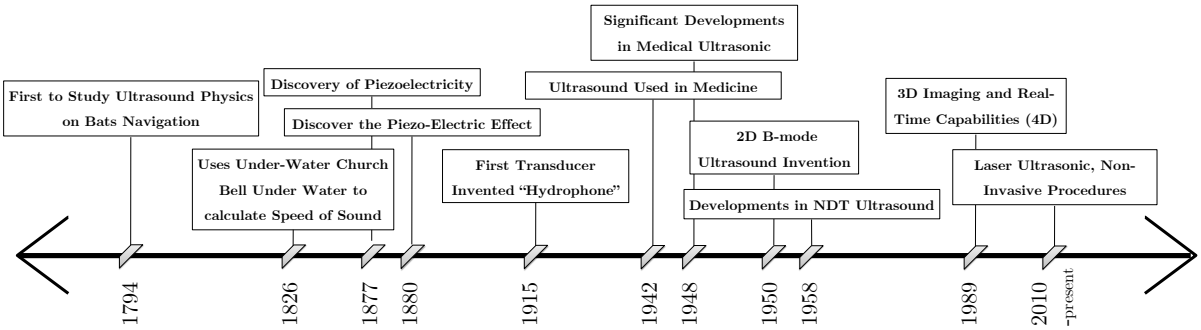


Fig. 1.9 Historical timeline of the development and advancements of ultrasound technology for different applications

1.4.1.3 Ultrasonic applications

The key developments in ultrasonic applications are strongly associated with the discovery of the magnetostrictive effect by Joule and the piezo-electric materials invented by the Curie brothers [53]. In the last 20 years, ultrasonic technology has been widely used in various applications and fields because of its high efficiency, reduced cost and environmentally friendly solutions [54].

The applications of ultrasound can be categorised into two broad areas: low-intensity, high-frequency and high-intensity, and low-frequency applications [55]. The boundary between low- and high-intensity applications is difficult to determine, but they can be approximately classified according their intensity values depending on the testing medium. This boundary was suggested by Gallego-Juarez to accommodate intensity values between 0.1 and 1 W/cm^2 [54].

Low-intensity applications	High frequency (<2 MHz)	Low power (mW range)
High-intensity applications	Low frequency (>1 MHz)	High Power (<10W)

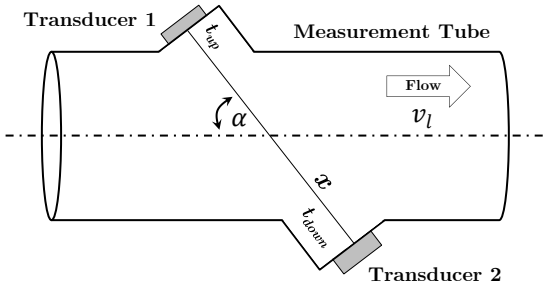
Common examples of low intensity ultrasonic applications include non-destructive testing and imaging, which are primarily used in the medical and electronic fields [55]. Low intensity applications usually focus on the exploration, detection and extraction of information about the tested object [56].

High-intensity ultrasonic applications (referred as to power ultrasonic applications) permanently alter the properties of the tested object. With a few exceptions, high-intensity systems usually exhibit low frequency, especially in chemical and cleaning applications in which the frequency is in the range of a few megahertz [55]. The operation of power ultrasonic applications is based on the effects of nonlinear phenomena, which are heat, diffusion, friction and other associated mechanisms [57].

In addition to its use in measuring temperature (discussed in Chapter 2), ultrasound is used in several industrial applications, such as:

Flowrate

Flowrate is considered an important factor in evaluating systems that include liquid management [58]. A typical ultrasonic flowmeter consists of a pair of ultrasonic transducers that is placed at an inclined angle in a through transmission mode. A transducer pair is placed between the upstream in the direction of the flow and the downstream against the flow of the moving liquid [59]. This placement ensures a change in the velocity vector of the liquid, which in turns changes the velocity of the ultrasonic signal travelling across the path [60]. Flow velocity v_l can be calculated by the length of the ultrasonic pathway and the angle between the transducers. Fig. 1.10 shows the principle of ultrasonic flow measurements using the transit-time technique.



$$v_l = \frac{x}{2\cos\alpha}\left(\frac{1}{t_{down}} - \frac{1}{t_{up}}\right)$$

x is the length of ultrasonic path
α is the angle between transducers
t_{down} downstream transient
t_{up} upstream transient

Fig. 1.10 Principle of operation of ultrasonic flow measurements using the transit-time technique [61]

The second method used to measure flowrate is the Doppler effect approach, which is based on the frequency shift caused by moving objects. This technique requires the presence of scattered particles in moving liquids. The Doppler effect is used to measure the frequency shift caused by these scatters. This technique has been successfully applied to monitor characteristic rheological changes of blood flow [57, 62]. Other methods are used to measure liquid flow using ultrasound, such as cross-correlation, drift ultrasonic and a phase-shift flowmeter [17].

Ultrasonic cleaners

Ultrasonic cleaners have been considered the oldest most useful application of ultrasonic cavitation [63]. The process of cleaning using ultrasound can take many forms. A typical ultrasonic cleaner consists of a tank filled with fluid cleaner; the target object is fully submersed in the fluid. Transducers are usually attached to the base or the walls of the tanks [64].

In the process of ultrasonic cleaning, cavitation bubbles are generated by high-frequency ultrasonic waves to agitate the cleaning solution [65]. High-intensity ultrasonic waves usually resonate at 20-60 kHz with a power in the order of a hundred watts. The agitation creates a high force that is applied to the particles to be cleaned. Ultrasonic cleaners are commercially attractive because they target and clean even small cracks, holes and inaccessible locations [66].

Ultrasonic welding

Ultrasonic welding utilises high-intensity low-frequency ultrasound to create a solid bond between two pieces of materials [67]. The advantages of ultrasonic welding over conventional welding is that less time is required to deform the material (typically less than 1 second), and the process can be automated [68]. Welding can be achieved in low temperature environments with minimal energy consumption, which allows for the easier embedding of electronics, such as in the production of sensors [69]. A typical ultrasonic welding system is shown in Fig. 1.11.

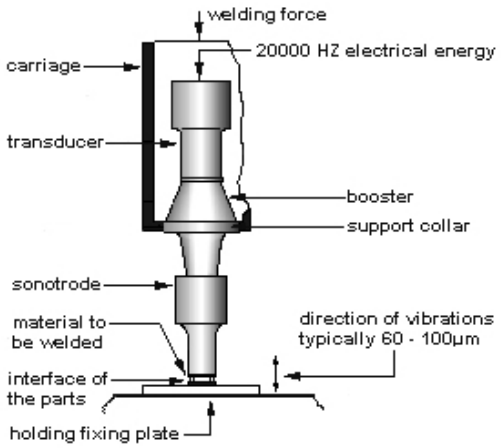


Fig. 1.11 A typical ultrasonic welding system used to join thermoplastics [68]

Ultrasonic welding includes the transmission of ultrasonic energy to a booster, which amplifies the intensity of the ultrasonic wave [70]. The signal is then transmitted to the horn, which applies a wielding pressure after transferring the energy to the targeted object. Finally, friction converts the vibratory energy into heat energy, which softens and melts the joint parts [67].

Level and distance

Ultrasonic level sensors measure the displacement between the transducer and the surface of a material or liquid. The distance is measured by calculating the Time-of-Flight (TOF) required for the ultrasonic wave (up to a few hundred kHz) to travel and reflect back to the transducer [71]. Measurements can be conducted in reflection mode using both a transmitter and a receiver or by using a single transducer in the transmission mode, emission mode or resonance technique [72]. Fig. 1.12 shows a typical fluid level measurement arrangement using an ultrasonic transducer.

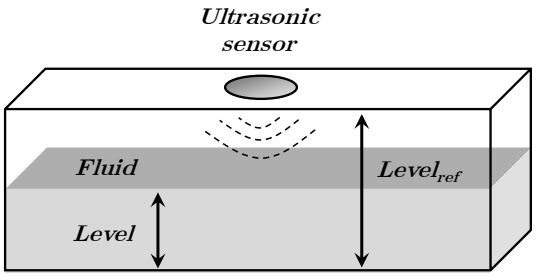


Fig. 1.12 A typical ultrasonic fluid level measurement device

The measurement process can be achieved in hostile environments without any physical contact with the medium. Measurements range can differ from metres to fractions of a millimetre based on the application requirements [73]. Different techniques, such as fuzzy logic, can be used in processes where one or more objects produce multiple echoes [74].

Imaging and health care

Medical ultrasound is the science of diagnostic medical technologies [75]. Ultrasound is often used to capture an internal picture of a moving body organ in addition to blood flow in a real-time profile [76]. In addition to being inexpensive and time saving, ultrasound has many advantages over existing technologies such as the X-ray and MRI. These advantages include the absence of tissue-destructive ionising radiation [77]. The field of medical ultrasound is rapidly developing. Some common ultrasound imaging procedures include abdominal ultrasound, bone sonometry (bone fragility), breast ultrasound, Doppler ultrasound (blood flow assessments), echocardiogram (heart performance) and fetal ultrasound (pregnancy) [77].

Security

Ultrasonic technology is widely used in various security-based systems by employing techniques such as motion detection or gas leakage detection [75]. Recent studies showed that ultrasound could be used as a fingertip scanner at greater depth than standard devices can reach [78].

The ultrasonic motion detector is based on the ability of ultrasound to locate the presence of objects by means similar to conventional radar. When the security system is activated, ultrasonic transducers emit a continuous signal and monitor the reflected signal [79]. Changes in the received signal indicate the presence of an object (or unauthorised entry) which triggers an alarm [80]. High-frequency ultrasonic signals allow the detection of

small objects because of their large wavelength. A commonly used motion detector-based application is the sonar system, which determines the depth of water and locates objects, schools of fish or submarines [81].

Another application of ultrasound in safety is the detection of gas leakage. Transducers used in this application respond to the ultrasonic noise that pressurised gas leakage generates [82]. Available ultrasonic gas leakage devices are widely found in oil processing industries. Most commercial detectors can operate in a 20-m radius [83]. The advantage of employing ultrasound in gas leakage detection is that it ensures an immediate response even in hazardous environments and minimal maintenance is required [84].

Food industry

During the past decade, there has been a developing interest in ultrasonic technology in food processing and preservation [85]. Low-intensity Nondestructive Evaluation (NDE) ultrasound is widely employed in food processing control, particularly in characterising the physicochemical properties of food [86]. Low-intensity ultrasound is used for various purposes, such as the activity stimulation of living cells, surface cleaning of foods, effects on enzymes, ultrasonically assisted extraction, crystallization, emulsification, filtration, drying/freezing processes and tenderising meat [85, 87]. High-intensity, low-frequency ultrasound can be used to degas liquid food, induce oxidation/reduction reactions, extract enzymes and proteins, pasteurise at low temperatures and alter viscosity [88, 89].

Ultrasonic technology is widely use in food processing for many reasons, including energy efficiency, simple installation, competitive cost and relatively low maintenance cost [90].

Further applications

Ultrasonic applications range from industrial applications to medical instrumentation. Previous research showed that a low-cost high-precision ultrasonic tilt sensor could be developed with a sensitivity of 1500 Hz/° and a precision of 1 Hz [91].

In addition, ultrasound is used in humidifiers. High-frequency ultrasound vibrates a diaphragm of material to produce tiny micron-order droplets, which in turn increase humidity [92].

A common application of NDT ultrasound is the detection of defects in objects. Ultrasonic signals from a piece of solid material are analysed to inspect the internal structure. By

calculating ultrasonic TOF, the location of any invisible crack, defect or cavity is estimated [93].

1.4.2 Overview of ultrasonic temperature measurements

1.4.2.1 Introduction

The concept of ultrasonic temperature measurement is derived from the experimentally observed dependency of ultrasonic velocity on the temperature of the object in which the wave propagates [62]. Temperature can be monitored by measuring the propagation velocity of ultrasonic waves because the sound velocity of a material is a function of temperature [60]. The temperature dependence of ultrasound velocity on temperature was first reported in 1873 [94].

The factors of temperature and chemical composition determine the ultrasound propagation. Because ultrasound is dependent on temperature, ignoring temperature-related changes results in inaccurate data acquired from ultrasonic transducers during the evaluation of a specific parameter.

1.4.2.2 Why ultrasonic temperature sensors?

An important feature of ultrasonic sensors, which does not exist in low-cost conventional temperature sensors, is their ability to achieve fast, accurate readings without the need to reach thermal equilibrium between the sensor and the medium of interest.

Employing ultrasonic sensors might result in reducing the cost of measuring instruments if the average temperature needs to be measured, such as across a process tank. Only a single pair of transducers is required instead of a full set of conventional temperature sensors placed at different locations in the tank. Moreover, conventional sensors only provide readings for a single location, whereas ultrasonic sensors provide average temperatures across the operational path [95]. This feature is important when the temperature at the bottom of a tank is lower than the temperature at the top.

The thermal inertia of conventional sensors limits their performance. A few seconds are required for a sensor to reach thermal equilibrium with the medium of interest in the case of temperature changes in the latter. In contrast, only 7 milliseconds are required

for an ultrasonic wave to travel a 10-m path in water. Rapid temperature response is vital in the early detection of possible thermal runaways [96].

Ultrasonic sensors with ultrasound waveguides can operate in very hostile environments at high pressures and temperatures. Most conventional temperature-sensing devices are rarely effective in such environments.

The cost of the transducer is another important consideration that affects the selection of the operating frequency of an ultrasonic sensor. High-frequency ultrasonic transducers (operating at tens of MHz and above) can cost as much as one-thousand pounds each, whereas mass-produced devices operating at 25-40 kHz can be purchased in large quantities for a few pounds [61].

Despite their advantages, ultrasonic sensors have some disadvantages. It was observed that ultrasonic sensors are difficult to calibrate and are very sensitive to contamination [97]. Another significant disadvantage is the occurrence of hysteresis, which was observed in inexpensive ultrasonic sensors, which led to ambiguous readings of the sensors [98]. Table 1.13 shows a comparison between conventional and ultrasonic thermometers.

Table 1.13 A Comparison between Conventional Temperature Measurement Techniques and Ultrasonic Thermometers

Sensor type	Ultrasonic sensors	Conventional sensors
Cost for high precision	Low cost for low frequency transducers	Relatively expensive for high accuracy
Calibration time	Fast	Significantly slower than ultrasound
Measurements location	Average complete ultrasonic pathway	Small scale targeted measurements
Calibration	Complex	Easy
Hysteresis	Exists due to piezoelectric effect	No recorded existence for most types

Calibrated low-cost ultrasonic temperature sensors are capable of producing accurate results compared to conventional types, such as RTDs and thermocouples, but they have a limited range [99]. Fig. 1.13 represents a comparison of different types of temperature sensors and their accuracy across the full range, temperature range and price per unit.

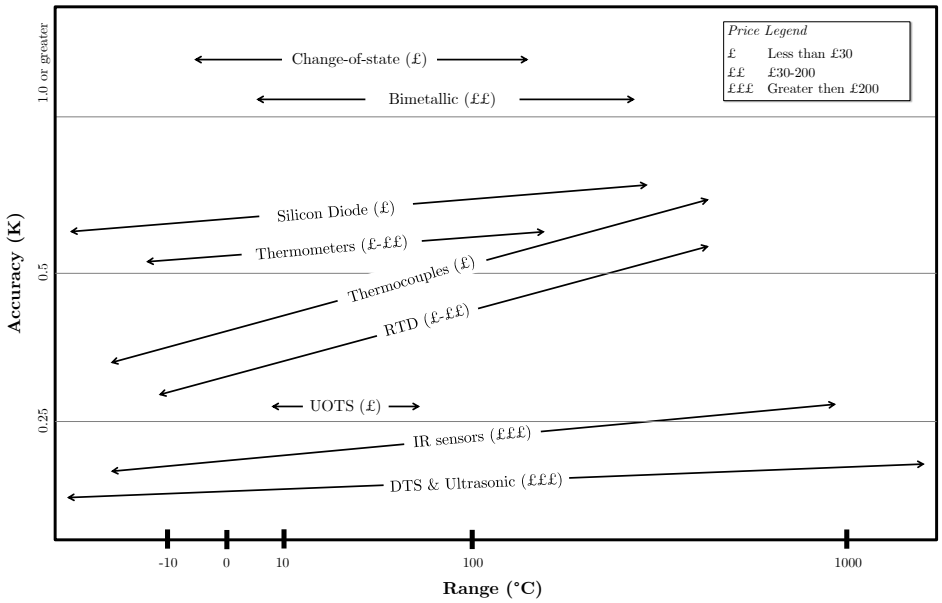


Fig. 1.13 Comparison of different types of temperature sensors, in addition to low-cost ultrasonic oscillating sensors, in terms of sensor accuracy across full range, temperature range and price per unit

1.4.2.3 Temperature dependency of sound in gases and fluids

The acoustic measurement of temperature is possible as sound velocity is highly dependent on temperature. In gases, because sound waves are insensitive to pressure and humidity, temperature is the single variable. In air, the speed of sound is dependent on the square root of temperature. Several laws of physics demonstrate this dependency. Equations (1.4) and (1.5), which are derived from Boyle's Law, Lynnworth and Carnevale, relate the temperature to the speed of gas and fluid in equations (1.4) and (1.5):

$$c_{gas} = \sqrt{\frac{\gamma RT}{M}} \tag{1.4}$$

where γ represents the ratio γ_p/γ_v, which is the specific heat capacity under a constant gas pressure and volume, R is the gas constant, T is the temperature in Kelvins and M is molecular weight.

$$c_{fluid} = \sqrt{\frac{\beta(T)}{\rho(T)}} \tag{1.5}$$

where β is the volumetric modulus of elasticity and ρ is the specific density, both of which are dependent on the fluid temperature.

Additional methods relate the velocity of sound in water to temperature, density, salinity and depth of fluid [100]. Several multi-order equations were derived from experimental data. In 1974, Del Grosso and Mader published a fifth-order equation, (1.6), which approximated the experimentally measured speed of sound in pure water at a precision higher than 4 ppm [100]. The experiment was conducted across a range of temperatures from 0 to 95 °C using an ultrasonic interferometer and the obtained curve was best fitted with the fifth-order polynomial:

$$c = \sum_{i=0}^{5} k_i T^i \tag{1.6}$$

where k_i is the constant calculated for each order, and T is the temperature.

In 1993, Bilaniuk and Wong re-examined Del Grosso and Mader's equations in order to correct the coefficients as well as to allow for compatibility with the 1990 International Temperature Scale (t_{90}) [101]. In 1997, Marczak combined outcomes from previous methods with the approaches introduced by Kroebel and Mahrt (1976) and Fujii and Masui (1993). Then Marczak developed a fifth-order polynomial t_{90}-based scale. Marczak's equations feature fewer k_i decimal places and results that are close to previously derived coefficients [102]. In 1998, Lubbers and Graaff calculated a simple three-order equation with a limited temperature range of validity and an uncertainty value as small as 0.18 m/s compared to Bilaniuk and Wong's equations [102]. These equations were specifically developed for ultrasonic medical applications. The developed expression is stated in equation (1.7):

$$c = 1404.3 + 4.7T - 0.04T^2 \tag{1.7}$$

where c is the speed of sound in pure water with a range of validity between 15-35 °C, and T is the measured temperature of water in degrees Celsius.

1.4.2.4 Examples of ultrasonic acoustic thermometers

Acoustic temperature measurements utilise the dependency of sound velocity on the temperature of the medium by measuring the sound delay that varies with temperature. Acoustic thermometers are usually used in applications where conventional temperature-sensing technologies fail to operate [103].

Because such sensors are sensitive to contamination, airtight enclosures should be fitted for enhanced sensor protection. The downside of such protective packaging is the introduction of a potential delay in sensor response due to the required thermal equilibrium [104]. Various types of acoustic thermometers are used for temperature measurements, including sensors described below.

Bulk Acoustic Wave sensor (BAW)

The basic element of the BAW device is a thin film resonator, which is very similar to a basic quartz crystal, but scaled down in size. A piezoelectric film is placed between two metal films. BAW sensors feature linear operation under extremely high temperatures and pressure. In addition, this type of ultrasonic sensor is considered one of the oldest and simplest acoustic temperature sensors [105].

Surface Acoustic Wave sensor (SAW)

Thermal expansion and propagation delay were used to construct a SAW-based temperature measurements device [106]. The only downside of SAW temperature measurements is their interference with chemical sensors, which causes excessive uncertainty in temperature readings [104].

The Surface Skimming Bulk Waves sensor (SSBW)

SSBW devices were developed as analogue filter devices. It was found that these devices could produce accurate temperature readings of ± 0.2 K over a wide temperature range at low cost and ultra-fine resolution. These devices feature less sensitivity to contamination and faster measurement time compared to SAW sensors [107].

The Torsional Acoustic Waveguide sensor (TAW)

These elastic-based sensors utilise a waveguide with non-uniform cross-section that excites and then receives torsional acoustic waves using the same transducer [106]. Changes in TOF can directly measure temperature and liquid level. TAW sensors are

calibrated and capable of operating at temperatures as high as 1000 K with a resolution of ±0.05 K [106].

Acoustic Temperature Sensor (ATS)

ATS operates because lamb wave propagation across a medium is dependent on temperature [108]. The ATS is not a common temperature evaluation option because of its relatively poor accuracy. However, recent research has focussed on improving the performance of these sensors [109].

Laser ultrasonic sensor

A novel SAW-based propagation delay method was introduced by employing laser ultrasound inversion to measure the temperature distribution of a material. The advantage of laser ultrasound over SAW is that the inversion process does not require surface boundary conditions [108].

1.5 Previous developments in ultrasonic oscillating sensors

1.5.1 Low-cost oscillating sensor for the ultrasonic testing of liquids

This research focused on establishing the feasibility of using inexpensive narrowband ultrasound oscillating sensors to measure temperature and flowrate in broadband sensors [61]. The main objective of this project was to develop a system for measuring the temperature and flowrate of liquids by using ultrasound technologies. The study involved the development of different electronic circuitries: variable gain control, BPF and a phase shift. A microcontroller was used to control the electronics of the sensor circuit parts as well as the measurements of output ultrasonic frequency via the network analyser circuit.

This sensor operated at frequencies of around 330 kHz in deionised water. The system was tested by placing transducers in a 30-mm path, which produced the most stable readings. The test was completed using a range of temperature cycles between 20 and 35 °C in a temperature-controlled environment. The results showed that the sensitivity was around 280 Hz/K in this arrangement.

1.5.2 Development of an ultrasonic tilt sensor

In this project, various designs, development, construction and evaluations of tilt measurements were investigated using an ultrasonic oscillating sensor. The system that was most likely to be classified as a low-cost inclinometer had an overall cost less than £15 [91].

The developments involved testing different transducer arrangements in various capacities and shapes of liquid containers, ranging from a 50 mm^3 cubes to 500 mm pipe cells. Three versions of driver electronics were developed in order to generate the oscillating frequency. These circuits contained variable gain control, BPF and phase shifter, which were controlled by a main board. The sensitivity of the tilt measurements using ultrasound fluctuated between 100 and 200 Hz/° in different volumes of cubic test cells. However, a significantly greater sensitivity of 1500 Hz/° was achieved using a 500 mm pipe test cell. In addition to its high accuracy, this system was able to operate as an accelerograph, that is, a device that measures low frequency vibrations.

1.5.3 Assessment of power losses in water-cooled electrical machines

This assessment involved the development of hardware and software for a test rig that measured the input and output temperatures of water-cooled electrical motors [44]. The test rig included 16 conventional temperature sensors and four pairs of inexpensive narrowband ultrasonic sensors, which were placed in a plastic cylinder.

An electronic ultrasonic driver was developed to sustain the oscillations of ultrasonic transducers. This driver included a high-gain stage and a BPF. Overall, the data on ultrasonic frequency were not consistent with temperature. Because of the poor clocking reference used (±2.5% over the full range of operating temperature [132]), the frequency was scattered along the spectrum.

1.5.4 Data logging instrumentation for UOTS

The work involved an evaluation of UOTS by using different arrangements to achieve the best parameters in the amplifier and filtering stages [110]. Overall, this project aimed to enhance the electronic driver to improve the correlation of frequency and temperature.

Improvements to the clock reference significantly enhanced the frequency readings and the consistency of the data on frequency and temperature data. Different values of gain and filter parameters were tested overnight in experiments that were designed to establish the most stable region in the frequency data.

Ideally, the relationship of temperature versus frequency should be linear. However, the results clearly showed hysteresis. This effect was observed in all the measurements performed.

1.6 Thesis structure

This chapter introduces conventional and ultrasonic technologies used to measure temperature and outlines their historical development. Several types of temperature sensors, including conventional and, most importantly, ultrasonic sensing devices, are briefly discussed and compared. Calorimetry and techniques used to measure differential heat loss in machinery are presented. Ultrasonic oscillating sensors were used in some previous research projects within our group; some of their results are briefly mentioned. The aim and objectives of the project are discussed in the conclusion to this chapter.

Chapter 2 focuses on a critical evaluation of the architectures of ultrasonic transducers and electronic measurements. Several ultrasonic evaluation methods are discussed as well as their advantages and disadvantages. Ultrasonic transducers are the basic elements of any ultrasound-related system; an overview of their types and associated costs is provided. Ultrasonic measurements can be conducted in various configurations, which are discussed by focussing on ultrasonic thermometry. Finally, different electronic architectures used to implement ultrasonic NDE sensors are compared.

Chapter 3 presents the design and testing of the supporting electronics required to operate the ultrasonic oscillating temperature sensor (UOTS) system. The chapter first provides brief description of how to build an ultrasonic driver circuit as well as the system requirements. Several options for achieving an automated gain control (AGC) operation are tried and tested. Software and hardware for the temperature acquisition and processing systems is fully developed and experimentally verified. Finally, in addition to the appropriate selection of the clocking reference, a low-cost and reasonably accurate frequency meter is developed.

Chapter 4 focuses on the developments of an ultrasonic modular driver system. This chapter describes the implementation of hardware in the constructed electronic boards, including an ultrasonic driver, a signal multiplexer and a frequency meter device. The software that was developed for controlling the system operation, the transducer selection process and additional design options are also described in this chapter. The communication protocols used to transmit instructions to the system modules are also discussed. These instructions can be communicated by using either a direct syntax or a customised graphical user interface (GUI).

Chapter 5 describes approaches to derive the parameters of devices that constitute a UOTS. The first parameter to be examined is the optimum overall gain, which ensures the stable operation of the system. In addition, the effects of variations in the power supply voltage on the system operation are studied. Various parameters of the electronic band-pass filter (BPF) are experimentally tested during several overnight experiments. Finally, because the system performance is dependent on the distance between the transducers, several different distances are used during the experiments.

Chapter 6 discusses the methods proposed to reduce the hysteresis effect which is common in piezoelectric based devices. The method proposed to overcome the implications of hysteresis by employing data sensor fusion techniques is described, including its background, architecture and applications. The ability of UOTS to detect temperature inflection points faster than conventional temperature sensors is illustrated.

Chapter 7 focusses on applying the developed system in a real application to accurately determine the power loss in water-cooled electric motors. The background of the development of such motors is introduced, including the fundamental methods by which the efficiency standardisation of electric motors is characterised. The flowrate of the coolant is an important factor in determining motor efficiency, which is illustrated. Several proposed models of the test rig are introduced and compared based on turbulence and velocity using Computational Fluid Dynamic (CFD) simulations. The experimental results are collected in a single chamber, and differential modes are compared based on frequency scatter, frequency-temperature hysteresis and frequency sensitivity. A summary of the experimental setup is also provided.

Chapter 8 summarises the findings of the preceding chapters and comments on the system performance. An overall summary of the entire project is provided. Because the cost of an UOTS is an important factor, this study aims to evaluate temperatures ultrasonically at the lowest possible cost. Hence, a Bill of Material (BOM) for the developments is presented in this chapter. Finally, some recommendations are given for potential future developments in this field.

Chapter 2

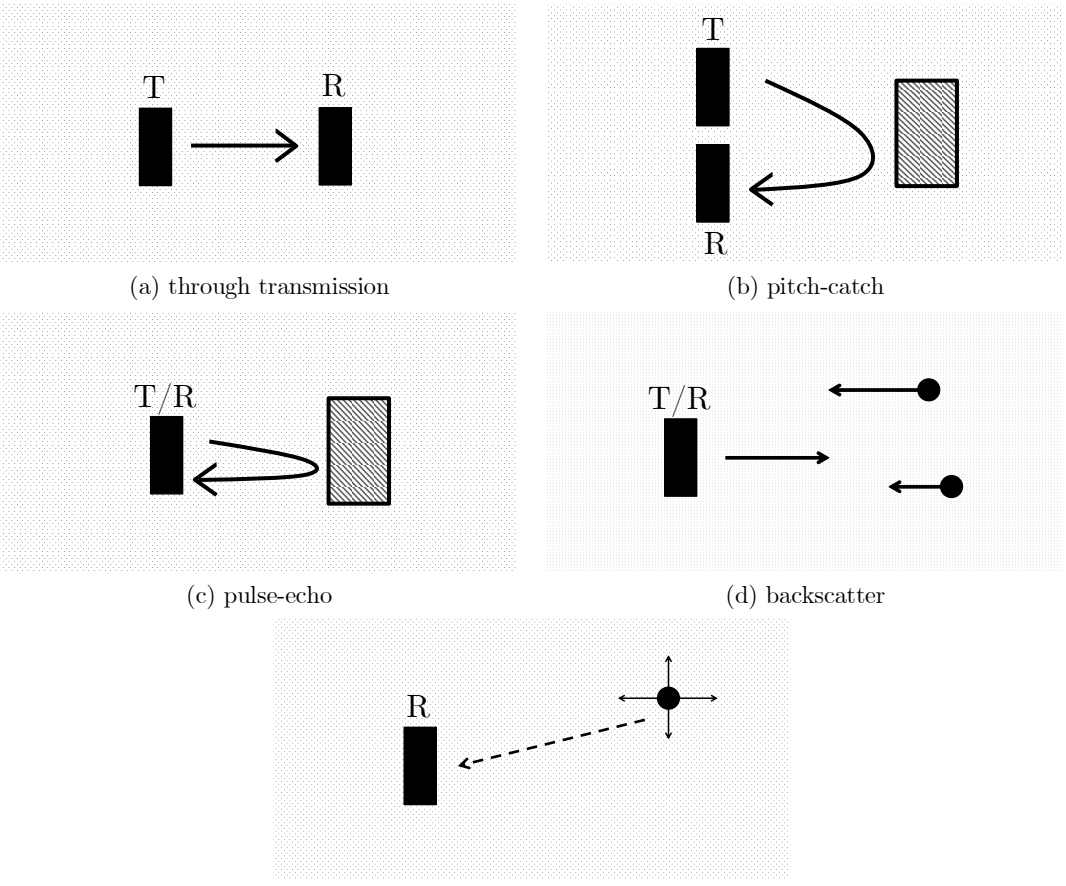
Critical Evaluation of Ultrasonic Transducers, Measurement Arrangements and Electronic Architectures for Ultrasonic Temperature Measurements

2.1 Ultrasonic measurement methods

Ultrasonic measurements frequently involve the balancing of two contradictory requirements. On one hand, increasing the operating frequency of the transducer decreases both the ultrasonic wavelength and the period, thus improving both the spatial and temporal resolution. On the other hand, increasing the operating frequency leads to a rapid increase in the ultrasonic wave attenuation, which reduces the Signal-to-Noise Ratio (SNR) at the output of the ultrasonic receiver. Insufficient SNR could lead to substantial uncertainty in the measurement results [111]. In these cases, the ultrasonic pathway may need to be reduced in order to restore the SNR to an acceptable level.

Ultrasonic evaluation can be applied to several types of objects, and it can operate within different types of mediums. Ultrasonic testing has become a popular option when the test object is opaque and difficult to access through electromagnetic radiation or conventional means.

Ultrasonic attenuation is represented by the ratio of the amplitudes of the sent and received pulses. The propagation delay evaluates the ultrasound velocity, which is mainly dependent on the object properties and on environmental conditions. For example, ultrasonic velocity is greatly dependent on temperature, but is less sensitive to other parameters such as pressure in gases or salinity in water. In most cases, ultrasonic evaluation features low-intensity non-invasive ultrasound waves. Ultrasonic evaluation can be achieved in different arrangements based on the requirements, nature or accessibility of the evaluated object, which are shown in Fig. 2.1.



(a) through transmission

(b) pitch-catch

(c) pulse-echo

(d) backscatter

(e) acoustic emission

Fig. 2.1 Experimental arrangements for ultrasonic evaluation methods [97]

2.1.1 Through transmission

In through-transmission evaluation, an ultrasonic pulse is emitted from the transmitter and received at the opposite side of an object through the receptor probe without the diffraction of the signal. This type of evaluation requires simple electronics to implement. Unlike other types of evaluation, continuous signal operation is also possible.

One advantage of this method of evaluation is that less attenuation is observed at the receiver because the pulse travels only half the distance compared to other methods such as pitch-catch [112]. However, defects cannot be properly identified if they are located in parallel to the direction of signal propagation. A typical through-transmission evaluation setup is shown in Fig. 2.1 (a).

2.1.2 Pitch-catch

Pitch-catch (or double probe) ultrasonic evaluation involves the use of two probes. The transmitter excites the energy through the object, and the receiver is aligned in a position where it receives the reflected signal from a discontinuity [113]. Because the energy can be reflected from the object in a non-uniform manner, two or more receivers are usually used. This method is widely used to evaluate cylindrical tubes and non-uniform surfaces [114].

The advantages of this method include its simple transducer setup and only the single side access of an object is required compared to the through-transmission evaluation. However, the disadvantage is that an increasing number of transducers are needed especially when a large portion of the energy is deflected. A large number of transducers can complicate the evaluation process [115]. A typical pitch-catch evaluation setup is shown in Fig. 2.1 (b).

2.1.3 Pulse-echo

The operating principle of this evaluation method is similar to pitch-catch evaluation except only a single transducer is used as both the transmitter and receiver [116]. The pulse-echo mode is highly sensitive in detecting defects or discontinuities with high accuracy. A highly automated process of pulse-echo evaluation is possible, which explains the popularity of various ultrasonic scans [117]. However, continuous operation cannot

be achieved. In addition, rough surfaces and irregularly shaped materials are difficult to inspect using this method. A typical pulse-echo evaluation setup is shown in Fig. 2.1 (c).

2.1.4 Backscatter

This method includes radiating an ultrasonic pulse into the object that needs to be evaluated. The transducer receives that first echo when it hits the object perpendicularly. It then receives the reflected pulse from the back surface of the object. Between these two instances, any pulse existence or velocity change can be used to evaluate the properties or the structure of the specimen [118]. The advantage of this method is that only a single transducer is used. However, the operation of this evaluation is limited to highly scattering objects. A typical backscatter evaluation setup is shown in Fig. 2.1 (d).

2.1.5 Acoustic emission

Acoustic emission is based on the time analysis of the elastic waves that are generated by the rapid distribution of stress across an object. When the structure of an object is subjected to an external force, energy is emitted in the form of stress, which can be detected using ultrasonic transducers [119]. Acoustic emission operates differently from other evaluation methods. Instead of transmitting energy across a medium, the ultrasound listens for the energy emitted by the object itself. Normally, this evaluation takes place when the object is under operation; therefore, it allows for the examination of active features (e.g. defect expansion).

Although this evaluation method is widely used in various applications in industry, it has some disadvantages, which include the limited number of examined parameters. For instance, it is difficult to obtain information about the size or depth of an object. Moreover, loud service equipment can result in additive noise, which complicates the measurement process. A typical acoustic emission evaluation setup is shown in Fig. 2.1 (e).

2.1.6 Summary on ultrasonic measurement methods

Ultrasonic temperature measurements can be achieved by using any of the arrangements discussed earlier. Each ultrasonic sensor arrangement was assessed by using an experimental setup in which water flowed continuously between the transducers, which

were separated by distances from 50 to 200 mm. Passive methods, such as acoustic emission, could not be used because there is no emission from the water when the temperature changes. The back scatter method is only applicable when the water contains small particles that reflect the signal. The water circulated in water-cooled electric motors is always clear to ensure heat conductivity. The pitch-catch method is also difficult to implement because the oscillating architecture usually fails to operate in a pulse mode. Hence, the through-transmission method was found to be the most suitable choice for achieving temperature measurements using oscillating ultrasonic sensors.

2.2 Ultrasonic transducers

2.2.1 Introduction

Ultrasound transducers are ultrasonic based tools that generate or receive ultrasound. They are used to detect alterations in a specific parameter that is to be measured. Transducers are designed for a wide range of applications used for the full control of a measurement system.

Most ultrasonic transducers have the ability to operate either as a transmitter or as a receiver. The sensor performance varies according to temporal and spatial factors. Ultrasonic transducers are subject to ageing, and their response may vary over time. Different types of ultrasonic transducers are available depending on their application and the accuracy required [53]. Generally, one of the main advantages of ultrasonic transducers is their robustness and ability to operate in very hostile environments, which makes them preferable to similar measurement methods. Moreover, these sensors cost much less than their competitors do. Compared with conventional temperature measurements, ultrasound is able to produce more accurate results [100]. Research has shown that ultrasonic sensors are capable of measuring various parameters, including viscosity, displacement, density and temperature [53].

2.2.2 Operating frequency and cost

Ultrasonic transducers vary in cost depending on operating frequency, bandwidth, accuracy, sensitivity, targeted application and the technology involved. For instance, because medical ultrasonic imaging systems are expensive, A £5k-ultrasonic transducer,

which is used in typical ultrasonic scanners, is a low-cost instrument [120]. High-frequency, high-accuracy ultrasonic transducers can be even more expensive. The careful selection of ultrasonic transducer specifications is not only important in terms of cost but also for the system optimisation. For example, the operation of high-frequency ultrasonic transducers exhibits high signal attenuation levels. High signal attenuation can be unsuitable in some applications: bones have a high attenuation coefficient, so low attenuation ultrasound evaluations are not recommended [100]. One of the most important factors in the pricing of ultrasonic transducers is the manufacturing process which involves very fine slicing of piezoelectric materials. For example, the thickness of a half-wavelength 20 MHz quartz transducer needs to be in the order of 0.58 mm.

In order to address cost-related issues, recent research has focussed on the development of ultrasonic transducers that are relatively inexpensive. At Newcastle University, researchers are currently working on an ultrasonic medical imaging system that costs under £40 [121]. Projects such as Philips Lumify are aimed at developing an inexpensive handheld ultrasonic imaging system that can be plugged into a smart phone or a tablet [122].

Low-frequency low-intensity inexpensive ultrasonic transducers are also available commercially. The applications of such transducers can range from security and flow sensing to temperature measurements. A pair of narrow-band ultrasonic air transducers can cost less than £6. However, some effects of these sensors, such as hysteresis specific to thermal properties of piezoelectric transducers, need to be addressed (Chapter 6).

2.2.3 Transducer types

Ultrasonic transducers are developed and fabricated depending on the requirements of the application. The selection of an appropriate transducer is essential in achieving appropriate ultrasonic measurement.

Transducers can be classified according whether they are piezoelectric transducers or magnetostrictive transducers [60]. Alternatively, they can be categorised as contact or immersion transducers.

2.2.3.1 Contact transducers

The contact transducer was developed to utilise direct measurements and inspection. Contact transducers are usually operated manually, that is, a non-automated process is involved. They feature a thick protective enclosure around their active element in order to ensure that it is insulated from the tested material. Coupling materials should be applied to the transducer's surface to eliminate the air gap, which otherwise could cause signal reflections [53]. Contact transducers are available in various configurations that enhance the inspection process. Common contact transducers include the following:

Dual element transducers

Dual element transducers usually operate in a pitch-catch mode, in which both elements are integrated in a single device. For material inspections, this type is preferable over a single element operation under the pulse-echo mode. Reflections from transducers are located at points that are relatively close to the element itself, which eliminates any signal interference that occurs in single element devices.

Delay line transducers

The basic principle of the operation of delay line transducers is the addition of a transient delay between the instances of transmitting and receiving the ultrasonic signal. These transducers have become increasingly popular for the measurement of high-precision thicknesses or of ultra-thin objects. Delay line transducers are commonly found in applications that measure high temperatures.

Angle beam transducers

Angle beam transducers are found in applications where shear wave generation is required for inspection. The angle of reflection can be fixed in the transducer while some transducers feature adjustable angles. They are commonly used in SAW generation, which detects defects.

Normal incidence shear wave transducers

Normal incidence shear wave transducers include a generation of shear wave transducers without employing angle beam transducers. Compared to shear wave transducers, these transducers are designed to maintain as low a longitudinal wave amplitude as possible, which results in less energy consumption.

Paint brush transducers

Paint brush transducers are commonly used to inspect large areas (e.g., wind turbines). A typical paint brush transducer consists of an array of elements that are matched to obtain a uniform operation and sensitivity. When a defect is detected, a smaller and more sensitive transducer can inspect the desired area.

2.2.3.2 Immersion transducers

Immersion transducers are used in the non-contact evaluation of materials. They are fabricated to operate in a submersed environment; all elements of this transducer are waterproof. Moreover, this type of transducer usually includes a thin impedance-matching layer that stimulates energy penetration in liquids and thus to the desired tested object.

2.3 Approaches to ultrasonic measurements of temperature

Hydrophones, which operate at frequencies up to hundreds of kHz, are widely used to measure temperature responses in aqueous solutions. However, hydrophones have poor off-the-shelf availability, and their cost is relatively high. Therefore, lower cost options with better reliability should be considered.

This section includes two approaches to ultrasonic temperature measurements, which were developed and tested in our group [97].

2.3.1 Ultrasonic temperature measurements using an oscillating sensor

A low-cost ultrasonic temperature measurement system was feasibly developed using inexpensive narrow-band ultrasonic sensors. The majority of low-cost ultrasonic sensors are designed to operate in air but have a protective encapsulation which potentially allows operation in aqueous solutions.

It is difficult to achieve a pulse-echo operation using narrow-band ultrasonic transducers. One method used to overcome the complications in the pulse-echo mode is to employ continuous wave operation. During the sensor operation, the phase shift of the transmitted signal is monitored instead of the TOF of a pulse.

Low-cost conventional temperature sensors usually have a resolution of ±0.25 K (e.g., DS18B20 1-Wire sensors). Therefore, in order to achieve highly accurate measurements, the fine resolution of the measured phase shift should be obtained. Let us assume that the ultrasonic pathway l was set to 1 m and the operating ultrasonic frequency f is 25 kHz (a typical oscillating resonance for narrow-band ultrasonic transducers in water), the ultrasonic velocity c is 1481 m/s (typical sound wave speed in water at 25 °C [123]). Because 1 K is required to change the ultrasonic velocity in water by approximately 2 m/s (0.1 K change for 0.2 m/s), the phase of the transmitted signal can be calculated using the following equation [61]:

$$\Delta\varphi = \frac{\Delta c}{c}\varphi_0 = \frac{\Delta c}{c}\omega\tau = \frac{\Delta c}{c} \times 360°f\frac{l}{c} = 360°f\frac{\Delta c}{c^2} \tag{2.1}$$

where ω is the angular frequency, and τ is the transmission time.

Substituting the parameters assumed in equation (2.1) would yield:

$$\Delta\varphi = 360°\frac{25 \times 10^3\ Hz \times 1\ m \times 0.2\ m/s}{(1481\ m/s)^2} \approx 0.8°$$

This high resolution of phase measurements is difficult to achieve using an inexpensive instrument. Therefore, a self-oscillatory system or oscillating ultrasonic sensor is required. A typical experimental setup for an oscillating ultrasonic sensor for measuring temperature is shown in Fig. 2.2.

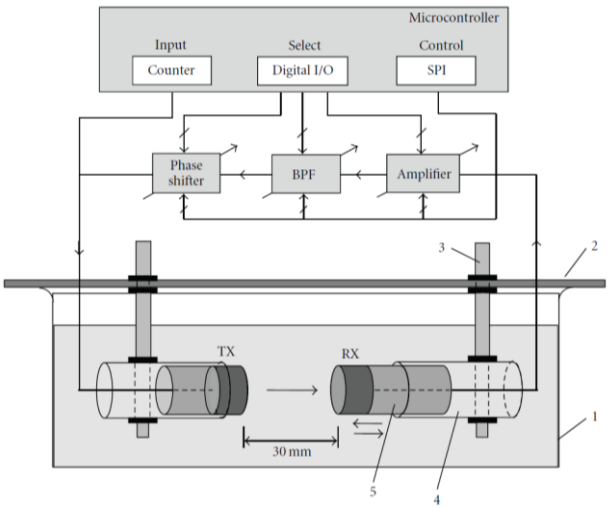
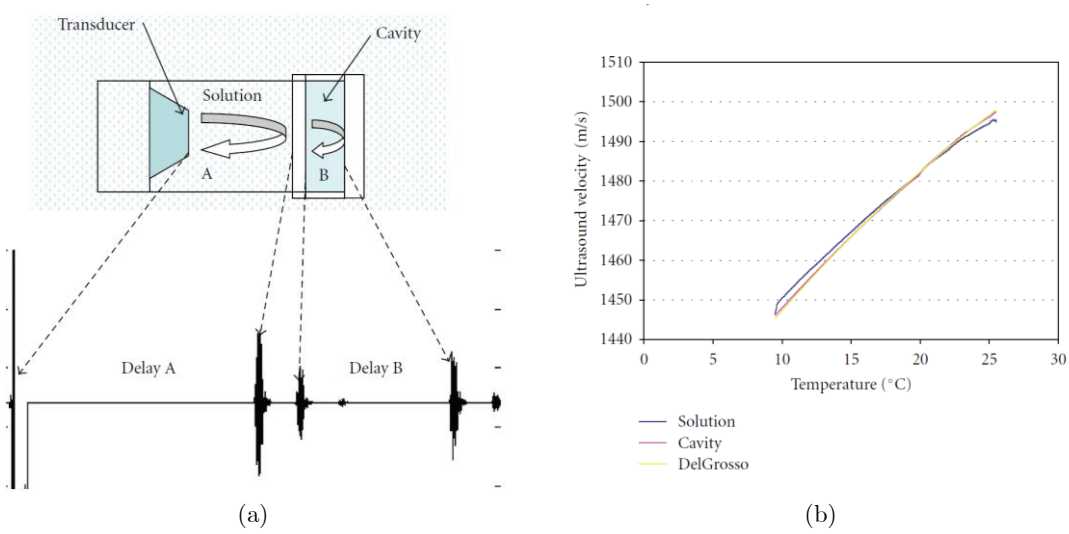


Fig. 2.2 A typical experimental setup for an oscillating ultrasonic sensor used in ultrasonic temperature sensing [61]

The circuit shown in Fig. 2.2 generates oscillations if and only if the following conditions are met: the overall gain should exceed unity, and the overall phase shift of the propagated signal is 360°. Monitoring frequency changes is a significantly simpler process than measuring changes in phase shift. A highly accurate, inexpensive frequency measurement system can be achieved by counting the output pulses during a specified interval.

2.3.2 Ultrasonic temperature measurements in pulse-echo mode

Measurements of temperature using ultrasound can be conducted in the pulse-echo mode. The received ultrasonic signal waveform consists of a transmitted pulse, the signal reflected from the front face of the reflector, and the signals reflected from the cavity boundaries. A typical experimental setup and reflected waveform for pulse-echo ultrasonic temperature sensing is shown in Fig. 2.3.



(a) (b)

Fig. 2.3 (a) A typical experimental setup and reflected waveform for pulse-echo ultrasonic temperature sensing; (b) ultrasound velocity and temperature relationship obtained from the pulse-echo experiment for different solutions [97]

In Fig. 2.3 (a), the values of delay A (which represents the ultrasonic propagation delay in the solution) and delay B (the reflection from the cavity) can be processed and calculated. The solution was placed in a temperature-controlled environment to monitor the temperature changes in response to recorded delays.

The results presented in Fig. 2.3 (b) showed good consistency between ultrasonic velocity and recorded temperature with an uncertainty figure below 0.01 m/s. This uncertainty was caused by the ultrasonic transducer itself, which represents only a small fraction of the ultrasonic velocity scale. Based on this result, it can be assumed that the single source of uncertainty in this experiment was the instrument used to measure temperature.

2.4 Comparison of electronic architectures for ultrasonic NDE sensors

2.4.1 Introduction

Ultrasonic NDE sensors can be used to measure and monitor various physical quantities using various arrangements of ultrasonic transducers [124]. Each ultrasonic sensor architecture has advantages and applications based on the uncertainty required as well as the cost of measuring ultrasonic TOF [125]. Four architectures are discussed: direct TOF measurement, sing-around, phase shift measurement and oscillating sensor.

2.4.2 Electronic architectures for ultrasonic NDE sensors

2.4.2.1 Direct TOF measurement architecture

As the name suggests, this method consists of the direct measurement of the TOF. An amplifier is used to compensate for propagation and energy conversion loss when the ultrasonic wave travels across a medium. The setup of this architecture is shown in Fig. 2.4.

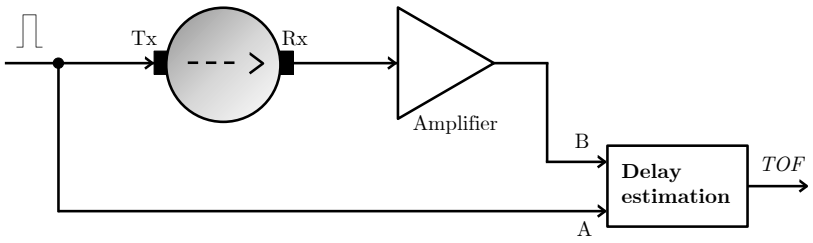


Fig. 2.4 Direct TOF measurement architecture

The ultrasonic signal attenuates as it travels along a medium. Because the signal at the receiver end is relatively weak, it requires amplification. The configurations of this

amplifier vary from one system to another based on both the distance between transducers and the medium density and the operating frequency.

The delay estimation unit calculates the time interval between the instants of the detection of the excitation pulse at input A and the detection of the propagated pulse at input B. An accurate time reference should be provided by a clock oscillator or any clocking management system. The delay estimator can be built to provide a time resolution better than the period of the clock pulses. An example of delay estimation processing is cross-correlation processing, which uses the centre of gravity instants of both pulses to estimate the TOF [126].

The accurate measurement of the delay requires high processing capabilities that are available commercially but at high cost. A cheaper option could be developed by counting the number of pulses between instances A and B, as shown in Fig. 2.4. In this case, the period of the clocking reference is smaller than the measured time interval by the inverse of the required resolution. This solution is simpler than the direct TOF measurement architecture, which requires building a delay estimator in order to provide a time resolution that is better than the period of clock pulses. In a simpler case, this requirement translates to the clock oscillator period shown below:

$$T_{req} = TOF \times r \tag{2.2}$$

where TOF is the ultrasonic time-of-flight, and r is the relative uncertainty/resolution of measured TOF.

Assuming that measurements are applied for a typical process pipe cell with a 60 mm diameter d, the expected TOF can be calculated as equation (2.3).

$$TOF = \frac{d}{c} = \frac{0.06\ m}{1500\ m/s} = 40\ \mu s \tag{2.3}$$

In order to measure temperature with the uncertainty and/or resolution of 0.1 K, the resolution of TOF is found by the following equation:

$$r = \frac{(1509\ m/s\ - 1482\ m/s)\ /(30°C - 20°C)}{(1509\ m/s\ + 1482\ m/s)/2} \times 0.1\ K \approx 1.8 \times 10^{-4} \tag{2.4}$$

where 1509 and 1482 m/s are the speeds of ultrasound waves at the water temperatures of 30 °C and 20 °C, respectively [127].

Substituting the values calculated in equations (2.3) and (2.4) in (2.2) yields:

$$T = 40\ \mu s \times 1.8 \times 10^{-4} \approx 7\ ns \tag{2.5}$$

Thus, that the reference clocking options should provide a signal that is greater than 150 MHz. However, measurements that feature such a high clock frequency are difficult to achieve using inexpensive instrumentation. Nevertheless, this process might be economically viable if the distance between transducers is increased (e.g., a 10 MHz clock reference is required for distances around 1 m). The second disadvantage of this method is the potential jitter and uncertainty related to the pulse detections due to the presence of additive noise.

2.4.2.2 Sing-around architecture

Another method used to estimate TOF involves re-circulating a pulse. This method involves sending a pulse into the medium at the instance of the detection of a pulse at the circuit receiver. A diagram of the sing-around architecture is shown in Fig. 2.5.

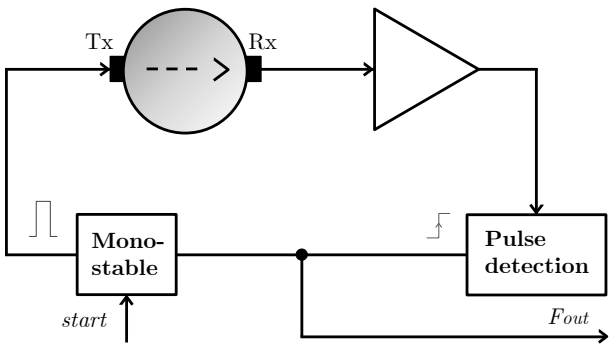


Fig. 2.5 Sing-around architecture

The setup shown in Fig. 2.5 allows for measuring the accumulated counts of pulses over a predefined period in order to estimate the TOF. To achieve an appropriate TOF resolution, the inverse resolution should be smaller than the counted number of pulses

during a time interval. Hence, the required time T_{req} for a complete period of measurement should equal the following:

$$T_{req} = \frac{40\ us}{1.8 \times 10^{-4}} \approx 0.2\ s \tag{2.6}$$

Most low-cost clocks are able to calculate the required time in equation (2.6). However, complications such as difficulty in determining zero-crossing points might develop because of the inevitable presence of additive noise at the received pulses.

2.4.2.3 Phase shift measurement architecture

A slightly different approach to measuring TOF can be implemented when the phase properties of the received signal are known. This method involves supplying two identical continuous sinusoidal signals to the transmitter and to the input of the phase shift estimator. Then the phase shift $\Delta\varphi$ should be monitored. The estimated TOF can be measured as follows:

$$\Delta\varphi = 2\pi f\tau \ => \ \tau = \frac{\Delta\varphi}{2\pi f} \tag{2.7}$$

where f is the frequency of the supplied sinusoidal wave that is kept the same as the resonant frequency of the transducers in order to increase the SNR.

A diagram of the phase shift measurement architecture is represented in Fig. 2.6.

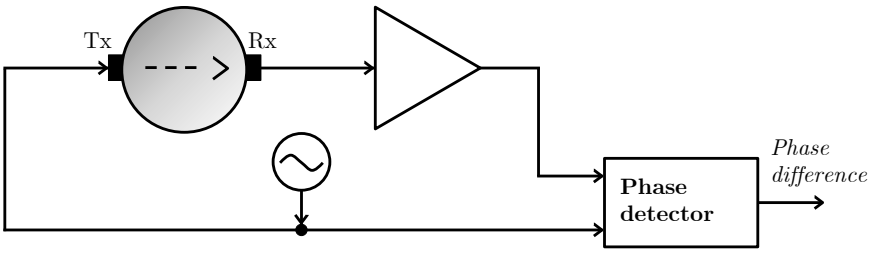


Fig. 2.6 Phase shift measurement architecture

A phase shift estimator is built to count the reference pulses gated at the instants when the sinusoidal wave of interest crosses the same amplitude level, such as at zero crossings. To achieve an appropriate resolution, the inverse resolution should be less than the number of pulses counted in the sinusoidal signal during a full period. For a 20 kHz

ultrasonic signal, the period of the sinusoidal signal is 50 μs. This period is even less than the TOF in the considered case. Therefore, the frequency of the clocking reference should be even higher than that of the direct TOF measurement architecture.

2.4.2.4 Oscillating architecture

The fourth architecture, the oscillating ultrasonic sensor, is attractive because of its potential simplicity. In this setup, a single amplifier is connected between the input and output transducers. The gain of the amplifier is set to achieve an overall gain in the signal loop that is equal to or is greater than unity (Barkhausen criteria, section 3.1.1). A diagram of an oscillating ultrasonic sensor is presented in Fig. 2.7.

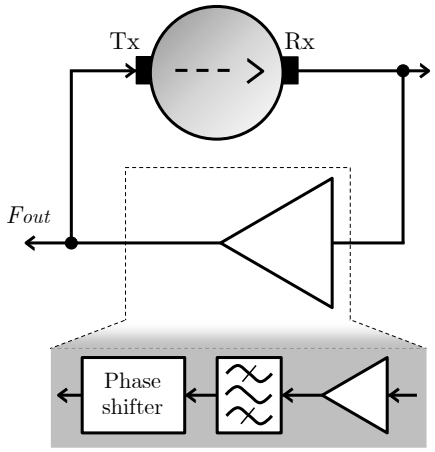


Fig. 2.7 Oscillating architecture

This configuration allows for shorter measurement time compared to previous methods. The minimum time required for measuring TOF for oscillating sensor architecture can be calculated as:

$$T_{req} = \frac{1}{20\ \text{kHz} \times 1.8 \times 10^{-4}} \approx 0.5\ \text{s} \tag{2.8}$$

This time is smaller comparing to the other methods, and it decreases further when the operating frequency is higher. Using a single amplifier sustains oscillation across the loop. However, it provides minimum control over the transducer operation. Inexpensive ultrasonic transducers feature resonances at multiple frequency bands. The system can start oscillating at any of these bands, depending on a number of factors, including gain initialisation settings, previous states and so on.

To overcome this randomness in operation, a robust design must include an electronic filter that enables a reliable operation within a particular frequency range to avoid frequency jumping. A BPF can select a particular frequency region for the operation of the oscillating sensors. Additionally, submerged operation is usually subjected to external electromagnetic sources and undesirable frequencies. For these reasons, the use of a BPF is necessary for the development of an ultrasonic oscillating sensor. The specifications of the BPF should be chosen carefully because the consistency of the results is very sensitive to bandwidth, as discussed in Chapter 5.

Theoretically, the sensor oscillates at the frequency where the peak amplitude of the frequency response occurs (the phase response goes to zero). On some occasions, this cannot be achieved unless a phase shifter is integrated into the system to ensure zero intersection.

2.4.3 Comparison of ultrasonic architectures

The comparison of various electronic architectures showed that the oscillating architecture was the most suitable because of its simplicity in relation to the complexity of the other architectures. Although different architectures can lead to similar results, the oscillating architecture has the ability of driving UOTS to achieve fast responses at low cost. Table 2.1 summarises the advantages and disadvantages of the different electronic architectures for use in ultrasonic NDE sensors.

Table 2.1 Advantages and Disadvantages of the Different Electronic Architectures for Ultrasonic NDE Sensors

Architecture	Advantages	Disadvantages
Direct TOF measurement	Inexpensive for longer ultrasonic pathway (cost)	Requires a clock reference over 150 MHz (cost)
Sing-around	Low-frequency clock reference can be used (cost)	Additive noise
Phase shift measurement	Simple circuitry	Requires very high processing capability (cost) Difficulties when operate low-frequency ultrasound
Oscillating sensor	Can be operated using a single amplifier (cost + simplicity) Shorter measurements time	BPF and phase shifter should be used for full control

Chapter 3

Development of Supporting Electronics for The Ultrasonic Driver and Frequency Meter

3.1 Electronics for the ultrasonic oscillating sensor system

3.1.1 Barkhausen stability criteria and system requirements for the supporting electronics

An oscillating ultrasonic sensor can function if and only if the energy conversion and propagation losses in the signal loop are fully compensated by an amplifier. The oscillations become sustained when the overall gain in the signal loop equals or is greater than unity. However, if the overall gain exceeds unity even slightly, the output signal of

the amplifier quickly saturates at rail voltages. The system should have an overall phase shift of zero around the loop, or an integer multiple of 360 degrees. These requirements for overall gain and phase shift are called the Barkhausen criteria [95].

The ultrasonic oscillating sensor system should include an electronic driver for the ultrasonic transducers, an accurate frequency meter that measures the sensor output frequency changes over time and a digital interface to the host.

3.1.2 Ultrasonic driver circuit

A typical ultrasonic measurement system consists of a test medium, a pair of ultrasonic transducers and a driver circuit. In order for these elements to function properly, all constituents should be properly designed to meet the requirements of the measurement system [61]. The driver circuit contains three important parts that must be integrated into the measurement system: UOTS driver, signal filtering and phase shifter.

The first stage of the UOTS driver is the signal amplification stage. The output signal with the highest amplitude possible is transmitted through a medium. Because of various factors, including energy conservation rules, the energy of the transmitted signal attenuates as it travels.

The second stage is signal filtering. When an ultrasonic wave is transmitted at a particular frequency, it picks up noisy components from external sources. The specifications of this filter should be chosen carefully to achieve best possible UOTS operation. Moreover, the transmitted ultrasonic frequency exhibits several resonances, especially in narrowband transducers. The application of a BPF results in the accurate specification of operating resonance, and it will prevent the signal from oscillating at arbitrary resonances.

A phase shifter helps to set the desired output frequency at one particular temperature. Such tuning allows achieving consistency among a set of manufactured sensors despite minor differences in the dimensions and/or properties of their inexpensive components. Therefore, the phase shifter functions to shift the phase response until the oscillation requirements are met. A typical ultrasonic sensor system consists of an ordinary acoustic cell, an electronic circuit and a controlling circuit, as shown in Fig. 3.1.

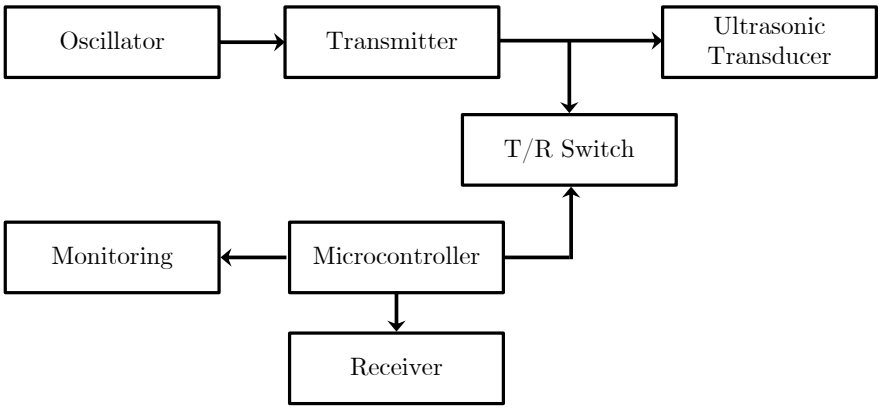


Fig. 3.1 Ultrasonic sensor system diagram

3.1.3 Electronics control of oscillating ultrasonic system

Temperature measurements using ultrasound in the oscillating architecture feature low-frequency ultrasound operation (below 50 kHz). Therefore, most inexpensive microcontrollers are capable of controlling the measurement process at such frequencies.

In previous studies [91, 99], several circuits were employed in order to drive, filter and shift the ultrasonic signal. This resulted in a less practical design with a relatively high number of physical connectors and switches, which could induce additional noise in the measured signal.

Most of the electronics required for UOTS development have analogue parts. Therefore, a controller circuitry was built in order to perform signal filtering, transducers multiplexing control and host communications. The development of a practical option was needed for the UOTS system. The Programmable System-on-Chip (PSoC) was found suitable for this development because it has the following features:

- Both digital and analogue implementations can be integrated in a single chip [128].
- There is a large selection of components with simple settings and routing.
- The devices are inexpensive (e.g., an 8-pin PSoC1 device costs less than £1.25).
- It has simple modular control and the ability to program during operation.

3.1.4 PSoC1 background, structure and capabilities

Developed by Cypress and released in 2002, PSoC is an inexpensive electronic component that consists of a chip containing complete systems that integrate a unique combination

of analogue and digital parts. The programming of these parts is a straightforward process. Moreover, controlling other parameters, such as clocking and internal connections, is possible using available PSoC software packages. A wide range of devices is available, which vary in the number of pins and the number of blocks allocated to the digital and analogue modules.

Several programmable analogue and digital parts (i.e., user modules) are available in PSoCs, including the Analogue to Digital Converter (ADC), the Digital to Analogue Converter (DAC), amplifiers, comparators, filters and counters. Some common interfaces are also available, such as LED, LCD, buttons and the Universal Asynchronous Receiver/Transmitter (UART).

PSoC Designer is a chip-level editor. This software allows setting the digital and analogue block connections. The design window allows the developer to drag and drop user modules with pin connections that have auto routing options. When a user module is placed, it is possible to alter its parameters or connect it to other modules. Global resources are available for altering any operating parameters, such as the clocking and power setting options. Finally, a code should be written in C or assembly language to operate the user modules, employing interrupts, loops and changing parameters during operation. The PSoC designer integrates special tools to allow some user modules to have better control of parameters, such as Filter Wizard, which is used to estimate the frequency response and the switched capacitor values of the desired filter. Cypress developers regularly publish new application notes that illustrate the utilisation of user modules in different applications.

Despite the large number of advantages in employing PSoCs, experiments showed some disadvantages. Relatively low-frequency configurations of analogue user modules were found appropriate for the experimental operational ultrasonic range (up to 100 kHz), which restricted the ultrasonic evaluation of higher frequency ranges. Moreover, although the full circuit was powered by a USB, PSoC1 devices have a maximum supply voltage of 5.25 V.

3.2 Development of the Automatic Gain Control system (AGC)

3.2.1 Purpose of AGC

The feedback loop in the oscillating ultrasonic system must have a gain of unity in order to oscillate. The ultrasonic driver provides the gain in its first stage, which is set to a high value to ensure that the oscillations would sustain. However, if the gain exceeds the required amount, the signal goes to saturation, thus deforming the original shape of the input signal.

The operation of the oscillating ultrasonic sensor is improved if the undistorted sinusoidal wave is maintained in the signal loop. This improvement can be realised by developing an AGC amplifier that will maintain the shape of the loop signal without distortion. This development targets the elimination or reduction of ultrasonic frequency versus the temperature hysteresis observed in previous experiments [110].

3.2.2 Design objectives

The AGC amplifier maintains the same level of the output signal in sound or radio frequency inputs. If the output signal is too low, then the AGC circuitry will increase the gain; if it is too high, then the AGC will lower the gain. The AGC principle is widely applied in AM receivers, where it is referred to as a "compressor-expander" because it acts accordingly.

The application of an AGC would preserve the sinusoidal wave shape of the circulated signal without driving it to saturation levels. This could be achieved by using several methods, such as employing comparators to control the upper and lower limits or using audio amplifiers that have integrated AGCs. Alternatively, a complex system could be designed based on the non-linear behaviour of the electronic elements, such as filament lamps or Junction Gate Field-Effect Transistors (JFET), to maintain the constant level of the output signal.

3.2.3 Development of AGC using a light bulb

3.2.3.1 Introduction

Incandescent light bulbs can be used to operate an AGC because filament lamps have non-linear I-V characteristics at low voltages. A filament lamp becomes hotter when the applied voltage is increased. As the voltage increases, the current increases but in a non-linear manner. The use of a filament lamp to maintain the undistorted output of a Wien Bridge oscillator was first reported by W. Hewlett [129].

3.2.3.2 Operation and hardware implementation

Automatic gain control can be achieved by employing a filament lamp in non-inverting amplifier configuration. To achieve this configuration, the negative feedback from a voltage divider, which consists of a resistor and a filament lamp, controls the gain of the amplifier. Because the gain is dependent on the ratio of the feedback resistors, the non-linear behaviour of the lamp automatically controls the gain. When the output voltage is increased, the resistance of the filament lamp increases, which results in reducing the gain. Fig. 3.2 presents a schematic diagram of a non-inverting amplifier.

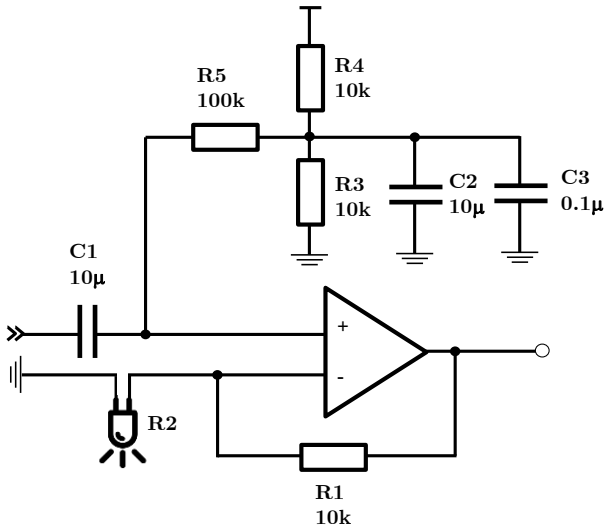


Fig. 3.2 Schematic of the AGC amplifier with a filament lamp

The overall gain of the circuit is set according to the values of resistors R1 and R2 (i.e., the filament lamp), as shown in equation (3.1):

$$Gain = 1 + \frac{R1}{R2} \tag{3.1}$$

The decoupling capacitor C1 is used to block the DC component of the input signal. The voltage divider R3R4 is used to set the voltage at half of the power supplied at the non-inverting input of the OpAmp. The inverting input is connected to the resistors, which are used to control the gain.

3.2.3.3 Results and discussion

Generally, the hot operation resistance of a filament lamp (i.e., the common light bulb) is about 10 times greater than the cold operation resistance [26]. Manufacturers usually do not provide the I-V characteristics of a filament lamp because most consumers use them at their rated voltage. The measured resistances of the filament lamp used in the design are shown in Fig. 3.3.

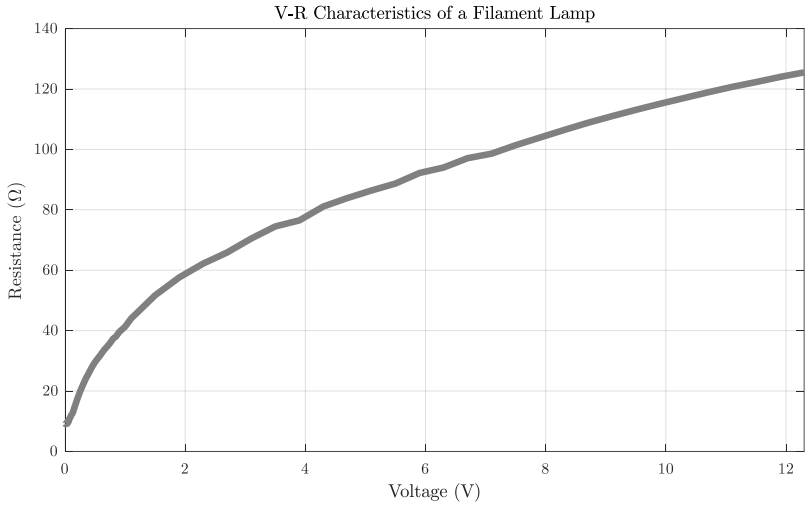


Fig. 3.3 V-R characteristics of filament lamp N9951189

The non-linear part of the R curve, which is the most useful in the AGC operation, is from about 20 up to 70 **Ω**. In the present study, this range was used to select the value for R1, which was later varied using a programmable resistor.

The filament lamp was tested, and a non-linear relationship was found at low voltages. Differently powered OpAmps from different manufacturers (e.g., Microchip and Texas Instruments) were used. In addition, various supply voltages (5, 10 and 15 V) were tested,

and the R1 values were changed accordingly based on specific voltage calculations. However, the gain was observed as almost fixed in all the input signals supplied to the system. In addition, when a 100 nF capacitor was included between the lamp and the ground terminal, the result was the same. Because the circuit did not behave as expected. The filament lamp used does not feature the required non-linearity, the AGC operation was not achieved. Therefore, the following options were explored.

3.2.4 Developments of discrete gain control

3.2.4.1 Introduction

One option in designing an AGC is to employ PSoC available modules, including the amplifier and comparators. In this section, a PSoC-based AGC design is described and evaluated.

3.2.4.2 Operation and hardware implementation

This design was developed using two comparators that monitored the upper and lower voltage levels at the amplifier output. The comparators were implemented using the relevant PSoC user modules, and the reference voltages of each comparator were fixed (Fig. 3.4). In this experiment, if the output signal were below the lower voltage level, then the gain of the amplifier would increase. If the upper level were exceeded by the output voltage, then the gain of the amplifier would decrease.

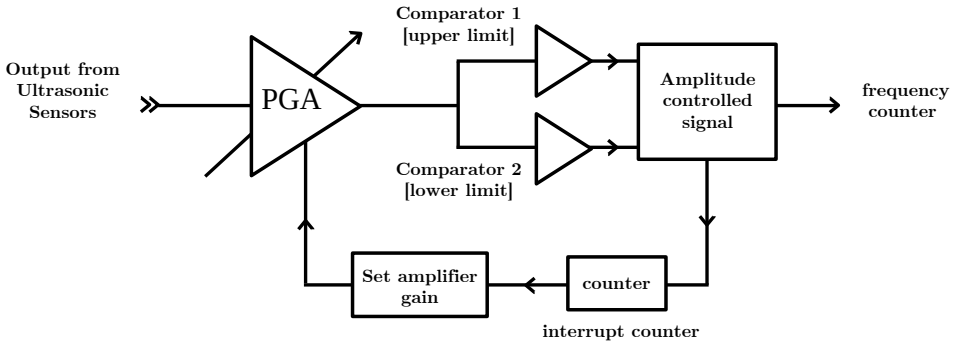


Fig. 3.4 A block diagram of the PSoC-based AGC amplifier with a digital supervisory control

The gain of the amplifier is controlled using an array of constants with the values of PSoC Programmable Gain Amplifiers (PGAs). In this array, the pointer is controlled by

the interrupts caused by the comparators, which increase or decrease the gain as appropriate. The Interrupt Service Routine (ISR) for the upper level comparator is set to have the highest priority interrupt because the output signal must not go into saturation. In the PSoCs, the controlling priorities of the ISR are based on the placements of the user modules from top to bottom and from left to right. For instance, a user module placed in row 2 of column 3 has a higher priority than another user module placed in row 2 of column 4.

It is important to monitor the number of interrupts that occur in order to avoid the continuous switching of the PGA gain, which would destabilise the system. These counters, which are incremented in the ISR, are transmitted to a PC using the UART for live monitoring of the supervisory control.

3.2.4.3 Results and discussion

The evaluation of this design showed the device did not provide a saturation-free output signal. The reason was the limited number of the available PSoC gains; if the overall gain in the signal loop was just below unity, the oscillations ceased to exist. If the signal was just above unity, the output signal was driven to saturation. Therefore, a better solution that would track even small changes in the overall loop gain was required, which called for the use of an analogue AGC.

3.2.5 Development of AGC using the AGC chip

3.2.5.1 Introduction

This method is built around an AGC system that is already integrated in a stereo audio amplifier. The mechanism connects the output from the ultrasound system to the input of this audio amplifier. The output of this amplifier is then connected back to the oscillator loop.

The class D stereo audio amplifier, TPA2016, was used for this purpose because it handles 2.8 W and is equipped with an AGC. This amplifier also was chosen because it is small and easy to program using a standard I2C interface. Class D amplifiers (or switching amplifiers) are electronic amplifiers in which the output transistors behave like switches in contrast to linear (class A, AB and even C) amplifiers, where these components operate

in a linear region. In class D amplifiers, the input signal is transformed to pulses with different Pulse Width Modulation (PWM) by using a comparator. The comparator compares the input signal with the output of a triangular wave generator. These pulses are used to connect the load either to the power supply or to a ground. The output transistors can handle substantial currents, thus enabling power amplification.

After amplification, the signal can be restored by using a Low Pass Filter (LPF), or the speaker coil itself, which filters out the high harmonics present in the PWM signal. The advantage of class D amplifiers over conventional amplifiers is their higher efficiency (up to 89%), which reduces power dissipation at the cost of increased distortion. Fig. 3.5 presents some parameters that are relevant in the AGC operation.

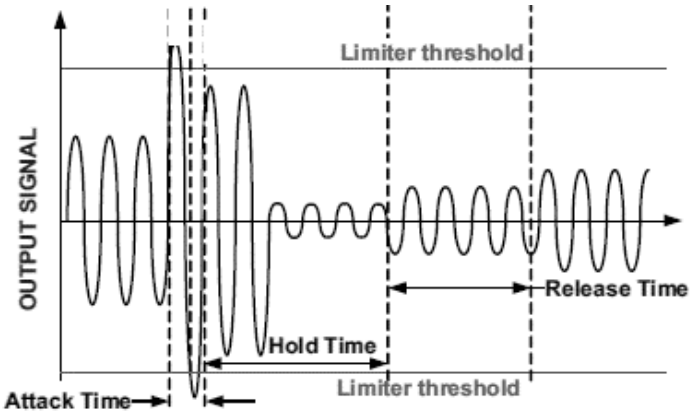


Fig. 3.5 AGC parameters of the TPA2016 2.8 W AGC stereo audio amplifier [130]

3.2.5.2 Operation and hardware implementation

After connecting the appropriate pins in the audio amplifier to a microcontroller, the following options are enabled or altered:

- AGC is enabled; otherwise, a fixed value of gain should be specified. This amplifier has a range of gains from -28 to 30 dB, which can be fixed or set as controlled output.
- The threshold of the AGC limiter is specified in the firmware; this value ranges from -6.5 to 9 dBv.
- Four compression rates can be set up to 1:8.
- Timing parameters, such as attack, hold and release time, can be specified within the code.

Initially, the AGC operation was successfully tested using an audio source. The performance was monitored using an oscilloscope when the amplitude of the input signal was altered.

This amplifier replaces the amplifier stage in the ultrasound oscillating sensors system. Fig. 3.6 represents the configuration of the system. The output signal from the ultrasound sensor is connected to a BPF to select an operational frequency of around 25 kHz. This filtered signal is passed to the AGC to amplify the signal to a certain value. The output from the AGC then is passed to a 30 kHz LPF that filters out the square wave PWM of 300 kHz that is generated to operate this class D amplifier.

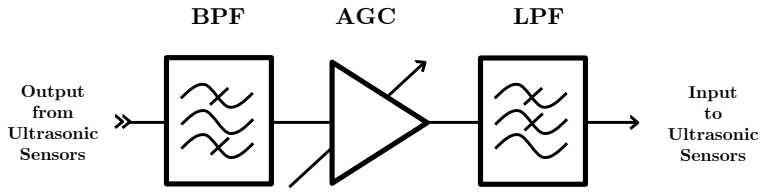


Fig. 3.6 Initial configuration of AGC using audio amplifier in ultrasonic oscillating sensors system

However, when ultrasonic frequencies were supplied at the input, the output signal was found considerably weaker than that of the audio signal because this amplifier featured a built-in LPF for audible frequencies. Therefore, some modifications (Fig. 3.7) were essential. In the first stage, the input signal was amplified using amplifier U1 at a level that the AGC could handle. The output of the AGC should output a signal with a constant amplitude. Amplifier U2 amplified the signal to cover the entire supply voltage range up to ± Vdd/2. The output of U2 was connected to the output of the ultrasound sensors, thus closing the signal loop.

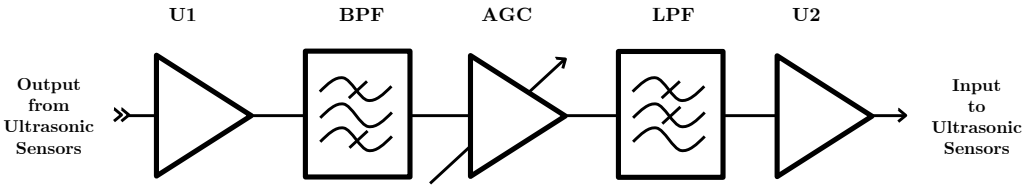


Fig. 3.7 Modifications of the configuration of AGC using audio amplifier in ultrasonic oscillating sensors

3.2.5.3 Results and discussion

This AGC was designed to operate within a range of audible signals up to 20 kHz. For testing purposes, a sinusoidal signal of frequencies from 10 to 30 kHz was supplied to the input of this amplifier. It was noted that the signal became heavily attenuated when the frequency exceeded 15 kHz. Therefore, the chosen operational frequency of the ultrasound sensor of around 25 kHz produced a heavily attenuated signal. This attenuated output resulted in distorted signal after the LPF stage. The system was able to operate only if the gain of U1 was set too high, and its output was driven to saturation levels. However, this was inappropriate for the intended AGC use. The results showed that this setup was unable to operate as an AGC in an ultrasound sensing system.

3.2.6 Development of AGC JFET

3.2.6.1 Introduction

One method used to implement the AGC is to utilise the non-linear I-V characteristics of a JFET. Three circuits for the AGC using JFET were selected for comparison: JFET1, JFET2 and JFET3.

3.2.6.2 First configuration (JFET1)

Resistors R2 and R3 are used as a potential divider to provide bias voltage for the non-inverting input of the OpAmp. Capacitor C2 is used to smooth out this bias voltage [27]. R10 is used in the negative feedback to set the DC operating point, and R3 allows for setting the DC operating point at the bias voltage. The full schematic of JFET1 is shown in Fig. 3.8.

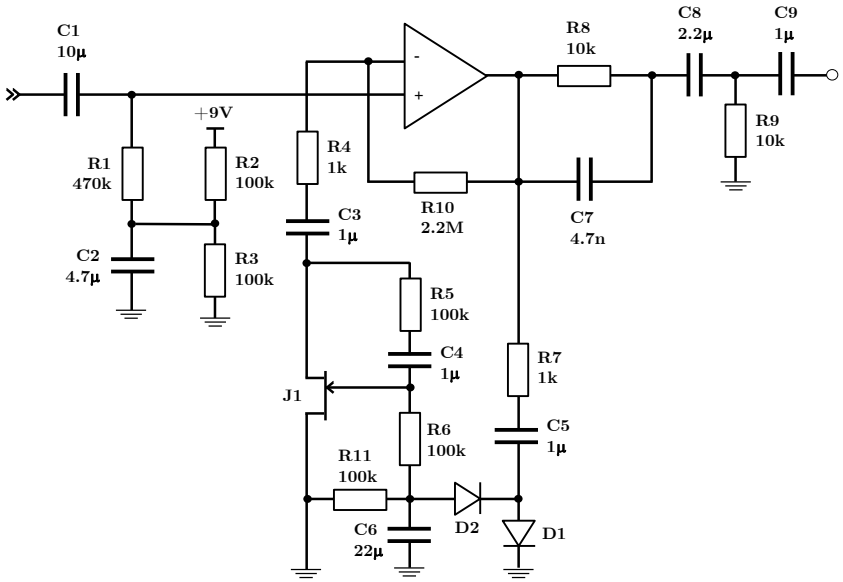
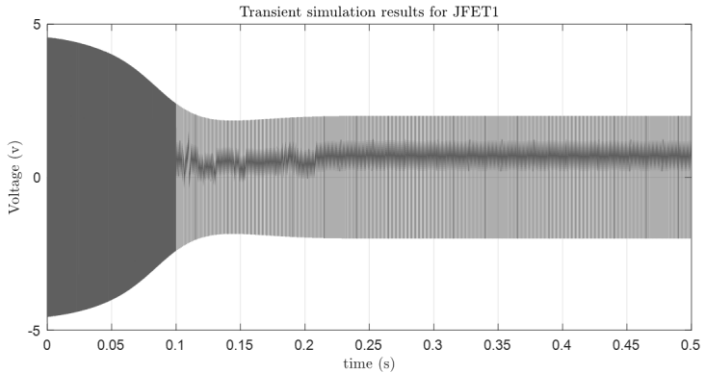


Fig. 3.8 JFET1 circuit diagram [131]

The JFET at low voltages (below 100 mV) acts as a variable non-linear resistor. When the voltage at the gate becomes negative, the JFET source-drain resistance is increased and the amplifier gain is decreased. This gain decrease is caused by the increased voltage in the output of the amplifier through the series resistor R7.

R7 and C5 supply the AC signal to the diodes that are connected as a cascade voltage doubler, which produces negative voltage that is smoothed by C6R11. This negative voltage is supplied to the JFET, increasing its resistance, which results in a smaller gain when the input voltage is increased, allowing the output voltage level to remain approximately constant. R11 is the load of the voltage doubler; when the AC output signal decreases because of regulation, the control voltage is discharged through this resistor.

The JFET acts as a non-linear resistor, especially when the operating point reaches the high end of resistance. R7 and C5 force the resistance to become linear. R8 and C7 form a pre-emphasis high-pass filter to minimise the output noise caused by the gain regulation. C8 and C9 are coupling capacitors, which are required to remove any DC components from the input and output signals. The output voltage of the JFET1 obtained via transient simulation and the specifications for a 24-kHz input signal are shown in Fig. 3.9.



Minimum input	250 mV
Maximum input	4 V
Dynamic range	×16
Response time	<5 ms

Fig. 3.9 JFET1 transient simulation results and specifications for a 24-kHz input signal

3.2.6.3 Second configuration (JFET2)

The circuit shown in Fig. 3.10 consists of four basic sections: variable attenuator (R2 & J1); fixed gain amplifier (U1); and amplitude detection (D1); bias control (Q1).

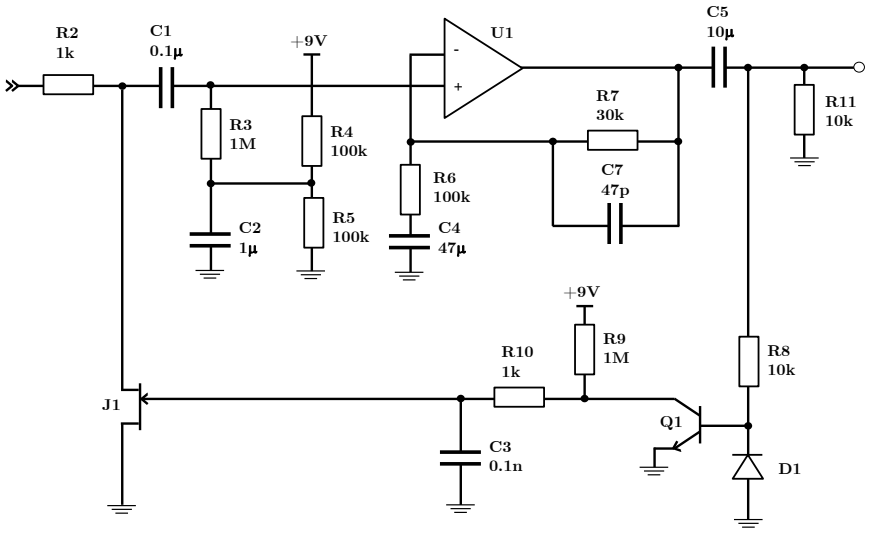


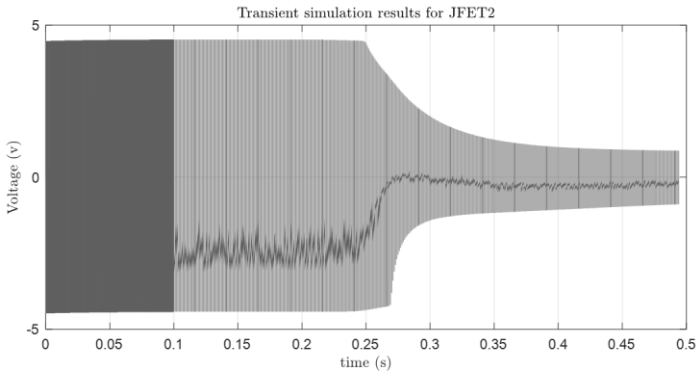
Fig. 3.10 JFET2 circuit diagram [132]

The attenuation caused by R2 and the dynamic resistance of J1 is a function of the JFET DC gate voltage: +9 V provides no attenuation at all, and 0 V provides the maximum attenuation. R4 and R5 set the bias point for U1 at 6 V where C2 acts as a bypass capacitor. R3 provides a DC path for very low OpAmp current in the order of picoamps.

Q1 is controlled by an amplitude detector that it switches on when the voltage at the base exceeds 0.65 V. When Q1 is switched on, R10 discharges C3. R10 controls the attack time (i.e., the time required to change the gain setting); a faster attack can be achieved by using a lower value of R10. The attack time should not be so fast that it cannot detect

every single peak, and it should not be so slow that it cannot react to the rapid changes in the input signal. R9 controls the recovery time; R9 and R10 discharge C3 when no peak is detected. The attack time should be about twice as fast as the recovery time.

This JFET has a "Vgs off" ranging from 3 to 6 V. This voltage affects the bias clamp voltage, the attack and the recovery time. The output voltage of the JFET2 obtained via transient simulation and the specifications for a 24-kHz signal are shown in Fig. 3.11.



Minimum input	70 mV
Maximum input	13.3 V
Dynamic range	x118
Response time	<350 ms

Fig. 3.11 JFET2 transient simulation results and specifications for a 24-kHz input signal

3.2.6.4 Third configuration (JFET3)

As shown in Fig. 3.12, with only very small modifications, the operation of this circuit is very similar to the JFET2 design.

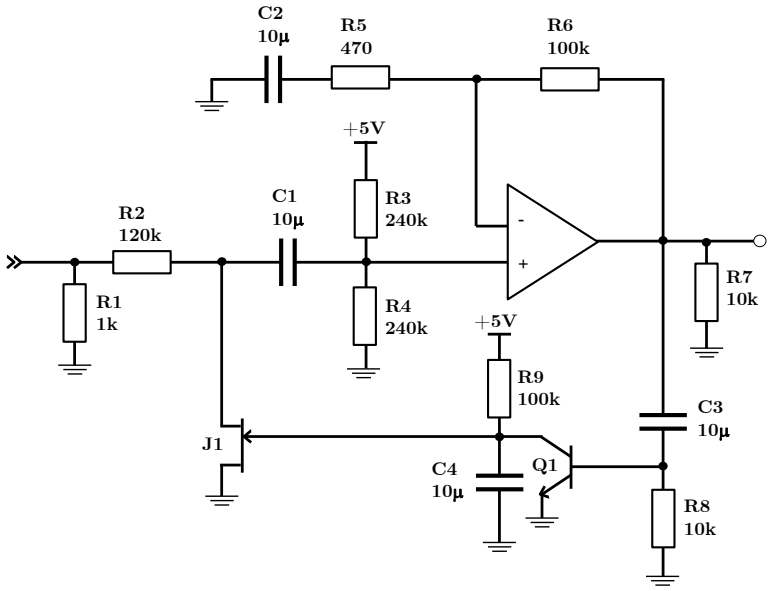
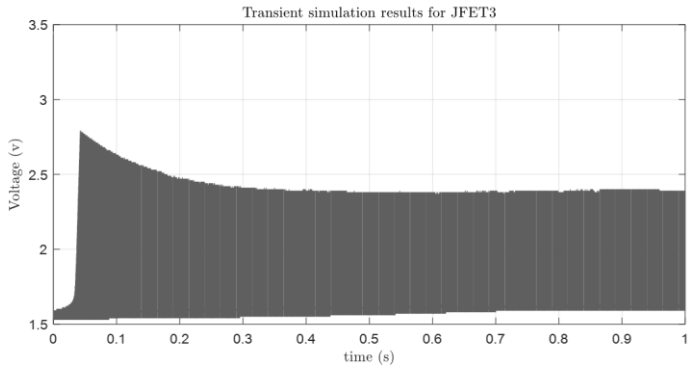


Fig. 3.12 JFET3 circuit schematic [133]

For signals below 40 mV, the input is divided between R2 and voltage divider R3R4 at the non-inverting input of OpAmp. The output signal from the OpAmp under this condition is not large enough to switch on Q1, which acts as a positive peak detector. The gate of JFET is set at the supply voltage, which produces a very high resistance between its source and drain, effectively excluding it from the circuit operation at these values of the input voltage.

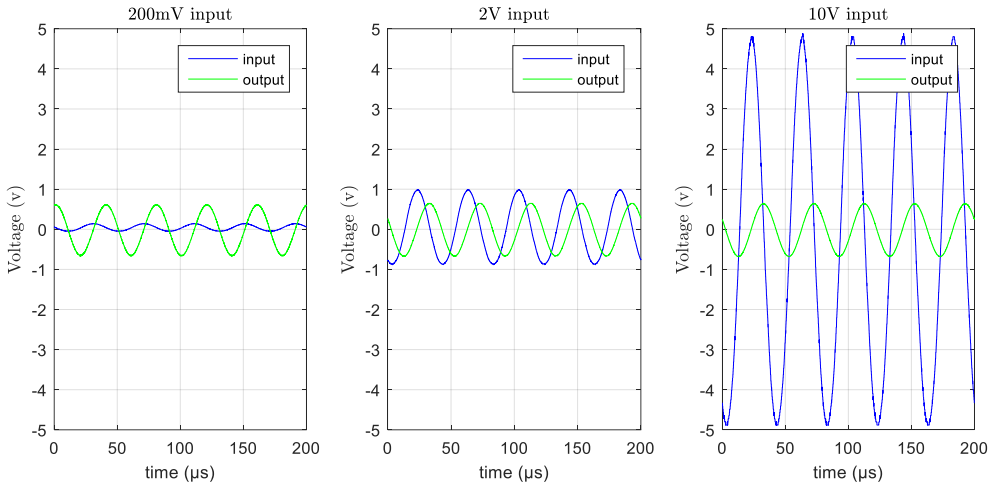
For voltages above 40 mV, high positive peaks of the OpAmp output voltage cause Q1 to switch on, which leads to the discharge of C4 via Q1, thus decreasing the +5 V steady state voltage at the gate of JFET J1. This decrease leads to the decrease in the resistance of J1 and then the output signal. The output voltage of the JFET3 obtained through the transient simulation is shown in Fig. 3.13.



Minimum input	40 mV
Maximum input	20 V
Dynamic range	x500
Response time	<300 ms

Fig. 3.13 JFET3 transient simulation results and specifications for a 24-kHz input signal

The initial construction used a breadboard design that was powered by a USB-based voltage source. To verify the operation of the AGC, three 24 kHz input signals with variable voltages (0.2, 2 and 10 V) were fed to the input of the circuit. The output signal remained about the same, as shown in Fig. 3.14.



(a) 200 mV (b) 2 V (c) 10 V

Fig. 3.14 Experimental waveforms for the input and output signals of the AGC for input signals with different amplitudes

The experimental results confirmed that this AGC design operated as expected. However, it was found that when the input signal was small, there was a large variation in the output amplitude. This variation will be discussed in detail in the next section, which describes the integration of this design into the ultrasonic driver.

3.2.6.5 Comparison of different configurations

The simulations showed that all the circuits worked perfectly with relatively small input signals and a frequency range up to 25 kHz. However, each configuration exhibited both advantages and disadvantages (Table 3.1).

Table 3.1 Comparison between Different JFET-Based AGC Designs

Circuit	Advantages	Disadvantages
JFET1	Good stability Fast response time	9 V power supply: cannot be powered from a USB unlike UOTS electronics Complexity, high number of components Limited input range
JFET2	Adjustable attack and recovery time Capable of handling small input signals	9 V power supply High number of components Slower response time
JFET3	Fast attack time Single supply voltage Wide input range with the small input voltage capability	Higher input voltages are required to stabilise output

In Table 3.1, the most important factors are the capability of controlling small input signals and the need for a single power supply. Ultrasound signals at the receiver end usually have a low amplitude (around 100 mV). Therefore, it is vital to choose a circuit that is capable of controlling low inputs. The simulation showed that applying amplification before the AGC part allowed the handling of even small input signals.

The second important factor is that a single power supply can feed different parts of the driver. The supply voltage from a USB (nominally 5 V) is used to power the ultrasonic driver and the supporting electronics, including the UOTS modular system. Therefore, operating the AGC using the same USB voltage source eliminates the need to employ an additional power source.

Response time and start-up time were not considered important in selecting the best possible circuit for the oscillating ultrasonic sensor. The measurements of its operation overnight showed that the amplitude changed within ±2.2% during 40 hours. These factors are significantly more important in some applications, such as audio applications, where input amplitude changes rapidly in short periods.

3.2.7 Integration of AGC using JFET and PSoC

Initially, the developed AGC was connected directly to the receiver transducer. However, it was found that, in small input signals, there was a large amount of instability in the output amplitude. The solution was to add two extra PSoC-based amplifiers before and after the AGC stage, as shown in Fig. 3.15.

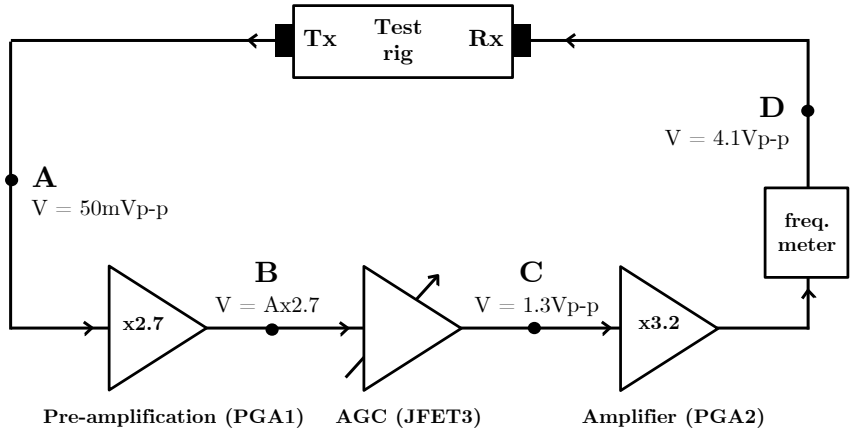


Fig. 3.15 Block diagram of the ultrasonic driver with JFET3 AGC

The gain in these two extra stages directly affected the amplitude stability of the output signal. For example, when the gains of PGA1 and PGA2 were set to 2.7 and 3.2, respectively, the variations in the output signal were about 413 mV (i.e., about 10.2% of the output amplitude). However, when the second amplifier (PGA2) was set to 48 (or saturation level), the variations were reduced by 2.2%. Therefore, it was essential to supply the AGC with an appropriate signal level in order to avoid large variations and instabilities (Table 3.2). Minimising this effect would potentially result in the greater accuracy of frequency measurements.

Table 3.2 Amplitude Stability for the Post-Amplifier PGA2 Gains of 48 and 3.2

PGA2 gain	voltage at receiver		voltage at transmitter	
	Vp-p (V)	maximum ΔV (mV)	Vp-p (V)	maximum ΔV (mV)
3.2	0.182	200	4.055	413
48	3.185	23	4.865	105

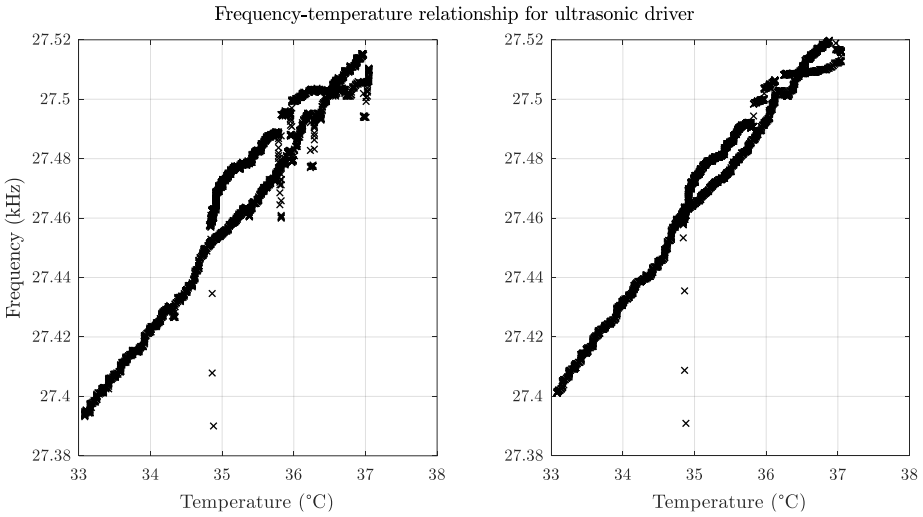
As shown in Fig. 3.15, the voltage at point A is the signal received from the ultrasonic transducer. The amplitude of this signal depends on several factors, including the level of the transmitted signal, the path length, the propagation medium and the operating frequency. In the experiment, the received signals were in the order of tens to hundreds of millivolts. The input signal was amplified by the PSoC pre-amplifier PGA1 in order to stabilise the AGC output, a gain of 2.7 was selected to ensure an input of over 200 mV is fed to JFET3. The amplitude of the amplified signal at point B was controlled by the AGC JFET3 circuit. This AGC consistently output a signal of 1.3 Vp-p at point C. The signal was further amplified to achieve the full voltage range between the ground and the power supply voltages, producing a signal of 4.12 Vp-p at point D. This signal was connected to the ultrasonic transmitter in order to complete the ultrasound oscillating sensor loop. Additionally, the output at point D was connected to a PSoC-based frequency measurements system.

3.2.8 Performance of the ultrasonic oscillating sensor with AGC

The performance of the integrated AGC system was tested by comparing it with an ultrasonic driver without an AGC. An experiment was conducted using two separate pairs of ultrasonic transducers. Both ultrasonic paths were placed in parallel to avoid

signal interference. The distance between the transducers was fixed at 0.1 m in both pairs.

The first pair was driven by ultrasonic oscillating system. The second pair was connected to a similar driver, and the pre-amplification stage was replaced by the integrated AGC. The signal at the output of the first driver was observed as a saturated square wave in which the second driver featured a sinusoidal signal with an amplitude slightly less than the supply voltage. Fig. 3.16 shows the frequency-temperature relationship in both pairs.



(a) without AGC (b) with AGC

Fig. 3.16 Frequency-temperature relationship for drivers with and without AGC

As Fig. 3.16 shows, the frequency-temperature relationships in both setups are similar. The data in (a) and (b) show a hysteresis of similar magnitude (hysteresis mitigation is fully addressed in Chapter 6). Moreover, the frequency/temperature sensitivities in both are identical. The only noticeable difference is the frequency scatter observed in the AGC, which is relatively lower than in the case without AGC. Typical scatter values observed in drivers without AGC are around 0.2 Hz. The AGC showed a slight improvement in scatter, which was measured as 0.17 Hz in a 15-second sample. Hence, the results showed an improvement of 15% in scatter performance when the AGC was employed.

This observed improvement was due to the technique used to measure frequency. In the developed frequency meter, the programmed comparator features built-in hysteresis detection capabilities for signal triggering. Generally, this technique operates more

efficiently when the zero-crossing level is set at an incline instead of vertically in the square wave case (i.e., saturated sinusoidal signal).

3.2.9 Summary

In this section, several AGC methods were evaluated to eliminate signal saturation. Typically, the oscillating ultrasonic system must have a gain of unity in order to oscillate. When a gain of more than unity is used to drive a system, the signal is saturated.

The first option was to employ non-linear filament lamps to control the gain level. A second method was to use comparators in PSoC to control amplitude. The third option was to employ an integrated audio amplifier that featured a built-in AGC system. The fourth option included developing three JFET-based configurations that benefitted from the non-linear I-V characteristics. The fifth method was to integrate one of the JFET-based designs with the PSoC-based AGC. The application of the AGC to the ultrasonic signal showed a slight improvement in frequency scatter performance without any notable changes in either temperature-frequency hysteresis or sensitivity.

3.3 1-Wire temperature sensor reader based on PSoC1

3.3.1 Introduction

In order to achieve the sensible interpretation and processing of ultrasonic frequency, a reliable temperature referencing should be provided. Moreover, ultrasonic sensors should be calibrated to produce accurate results by comparing the actual temperature value with the temperature derived from the ultrasonic sensors.

The average of the data obtained from several sensors can be employed to decrease measurement uncertainty and increase its resolution. In the proposed design, eight conventional temperature sensors were mounted on the testing chamber, which increased the precision of the results by adding three bits to the output data ($\log_2 8$). Averaging was applied to reduce any variation in the results caused by the different tolerance associated with each sensor. Using this number of sensors allows for reliable results even if a single sensor develops a fault. A very precise temperature sensor could be used, but this would increase the cost of the project, so low-cost temperature sensors were used to obtain the results.

In this section, an overview of 1-Wire temperature sensors operation is provided. In addition, digital signal processing is performed to enhance the data. Finally, software and hardware developments are discussed.

3.3.2 1-Wire temperature sensors

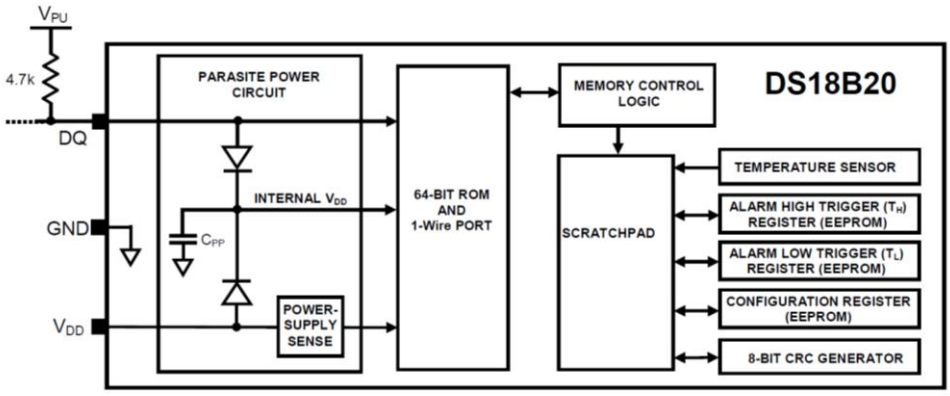
3.3.2.1 Introduction

As the name suggests, this type of sensor uses 1-Wire technology, which can be realised using most microcontrollers. The 1-Wire technique is used in these devices in order to communicate with a master PC or a microcontroller; a 1-Wire data bus is used to transmit and receive data. Theoretically, the number of 1-Wire sensors that can be connected to the same bus is unlimited. These devices were chosen because of their cost, accuracy and ability to handle digital data in transmitting and receiving information.

The basic function of these sensors (and of integrated circuit sensors in general) is to determine the current versus the voltage relation in a sensing transistor. The potential difference in the base emitter is changed when different collector currents are measured. This current has a direct relationship with the temperature of the transistor. An integrated ADC is used to convert the voltage or current readings into digital sets of data that can be accessed.

3.3.2.2 1-Wire sensor communication protocols

Designed by Dallas Semiconductor, the 1-Wire interface is a bi-directional, half-duplex, serial signalling protocol. Each sensor can be accessed in order to send or receive data and commands digitally (Fig. 3.17). Moreover, this type of sensor requires the use of only a single pin, which allows smaller circuit designs and leaves extra pins available for other purposes such as pins required for ultrasonic transducer selection. This technology does not require high-speed communication or clocking, and it operates at a data rate of 16 kbps.



(a) block diagram

SCRATCHPAD (POWER-UP STATE)

Byte 0	Temperature LSB (50h)	(85°C)	
Byte 1	Temperature MSB (05h)		
Byte 2	T_H Register or User Byte 1*	↔	T_H Register or User Byte 1
Byte 3	T_L Register or User Byte 2*	↔	T_L Register or User Byte 2
Byte 4	Configuration Register*	↔	Configuration Register
Byte 5	Reserved (FFh)		
Byte 6	Reserved		
Byte 7	Reserved (10h)		
Byte 8	CRC*		

EEPROM

*Power-up state depends on value(s) stored in EEPROM.

(b) memory map

Fig. 3.17 A typical block diagram, register structure and sensor memory map for DS18B20 1-Wire temperature sensors [134]

DS18B20S is the modified version of the eight-bit DS18S20 sensor manufactured by Maxim Integrated. These sensors can be configured to output a temperature reading with a resolution of up to 12 bits within an extended range of temperature values from -55°C to +150°C. To power up the sensors, they are connected to an external 5 V-voltage supply. Alternatively, they are operated in a parasite power mode, which involves charging the internal capacitor, C_{PP} in Fig. 3.17 (a), which supplies the power when the bus is low. The current is relatively high when the data are copied, there is a significant decrease in the voltage across the data wire and hence an increase in the current supplied to the internal capacitor.

This system operates based on slave-master technology. Data are transmitted starting with Least Significant Bytes (LSB) on the bus. Each sensor is identified by a unique 64-bit code stored in ROM. This code consists of an eight-bit family code, 48 bits (six

bytes) in a unique serial number and eight bits that contain a cyclic redundancy check (CRC) for data validation, as shown in Fig. 3.17 (b).

The core functionality of the DS18B20 is direct-to-digital temperature sensing. The memory consists of an SRAM scratchpad that includes EEPROM storage for registers. The scratchpad consists of nine bytes.

There is a trade-off between the resolution and the conversion time. The conversion time of a nine-bit resolution is eight times shorter than that for a 12-bit resolution. The maximum conversion time for a 12-bit operation is 750 ms. In this project, this conversion time is acceptable because a conversion command is broadcasted to the eight sensors, and the data are transmitted sequentially from the first to the last sensor.

3.3.2.3 Firmware development

The software is designed by creating functions and customising others that have been already designed for a 1-Wire sensor setup. The software includes a few steps that are used to obtain temperature readings and send control commands.

The function `GetSensorCount(sensor count)` is applied to find the number of sensors connected to the sensor bus. If only one sensor is connected, the measuring mode is set to single by setting the sensor count to `Single_Mode`; otherwise, `Multi_mode` will be called for multiple sensor operation.

After successfully completing the previous steps, Cyclic Redundancy Check (CRC) checks are performed on the ROM string as required. ROM strings contain the serial numbers of devices, and family codes can be obtained using `GetROMStrings()`; a separate number is dedicated to each connected sensor. All these previous steps are performed within a specially designed function. `GetTempVal(sensorId)` is called to return the MSB and the LSB temperature reading values for the required sensor.

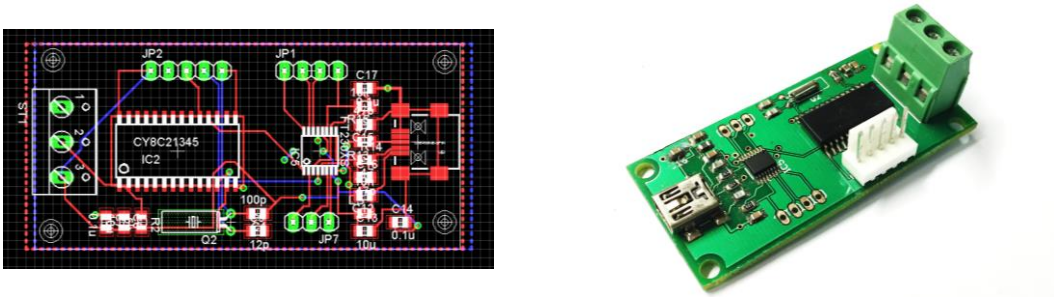
The received sensor data are transmitted in hex format with minimal mathematical and logical operations within the microcontroller in order to reduce the measurement time. The transmitted code is programmed in the following format:

ID MM LL

Number of HEX digits	2	2	2
Description	Sensors ID, starts from 01 onwards	Most significant byte of temperature reading in HEX format	Least significant byte of temperature reading in HEX format

3.3.3 Hardware implementation

A Veroboard prototype design was developed based on the previous design of an ultrasound electronics system. After successfully completing this design, a PCB design was developed to increase the robustness of measurements. This PCB design features a PSoC microcontroller, a connection to 1-Wire sensors, connections to the programmer, and a USB interface (Fig. 3.18).



(a) PCB layout (b) picture

Fig. 3.18 PCB design for the PSoC-based temperature measurement and acquisition system

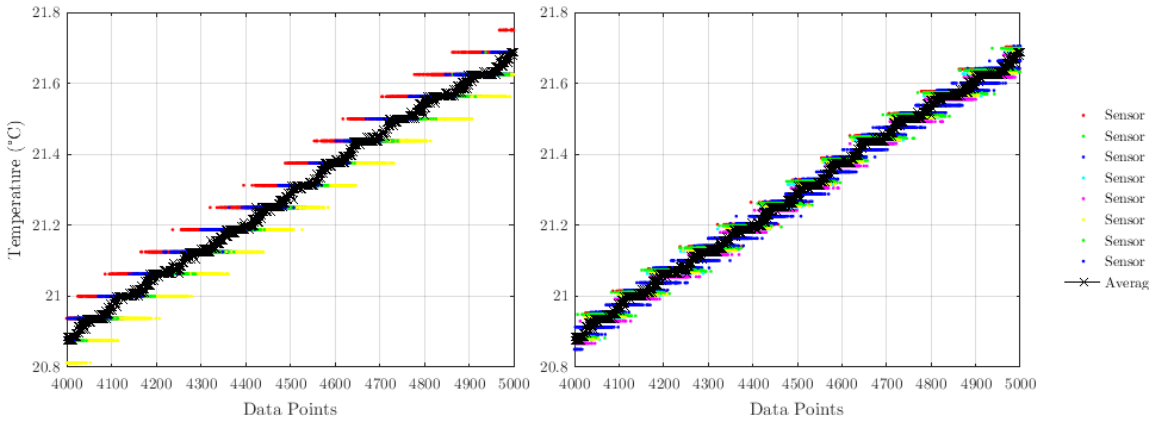
3.3.4 Calibration of sensors

Several measurements were carried out to perform calibrations of the eight sensors connected on the test rig. Shorter measurements were carried out to verify the data and the output from the sensors, and then longer recordings were obtained. Multiple measurements were taken to achieve the best possible calibration.

Longer recordings were completed to calculate the minimum achievable offsets for each sensor to be applied. The application of offsets differences allows better resolution and enhanced reliability of sensor readings even when fewer sensors are used.

To analyse the obtained data, a region was selected to apply the calibration. By calculating the average of the results, assuming that the temperature of each sensor had a constant offset during the full measurement period, it was found that the sensors offset varied from -0.08 up to 0.06 K, as shown in Fig. 3.19 (a). The sensors that featured the largest deviation from the average were automatically excluded, which resulted in a narrowed range of data around the average value.

Enhanced results were achieved by applying individual sensor offsets, which decreased the maximum variation to only ±0.05 K from the mean. Ideally, there should be no variations; however, a small variation was observed because of the assumption that the offset value of each sensor was constant throughout the duration of the measurements, which might not have been the case. Fig. 3.19 (b) shows the application of both the mean value and the standard deviation offset on the temperature data obtained in Fig. 3.19 (a).



(a) (b)

Fig. 3.19 (a) 1-Wire sensors response before processing, (b) temperature data enhanced

3.3.5 Conclusion

The overnight measurements of eight 1-Wire sensors were recorded. The output data for each sensor were analysed and documented to perform digital signal processing. Temperature readings were averaged to obtain the best achievable results. It was found that each sensor had a different offset and standard deviation from the mean value, which required some calibration. The sensors that had the largest standard deviation values were automatically excluded from the calculations. The offset values then were applied

to each sensor, which introduced a more accurate temperature graph with values closer to the average curve.

To verify the outcome of these values and implementation, the developed code was applied to additional recordings with different temperature ranges. The results showed that these offset values were applicable to this set of data. Hundreds hours of overnight measurements were successfully completed using the proposed method and processing.

3.4 Development of the frequency meter

3.4.1 Introduction

The measurement of frequency in the full range of applications is based on measuring the oscillation rate, which rate differs from an electrical or mechanical application. In electrical and electronic applications, the rate is known as Revolutions Per Minute (RPM) or cycles per second (i.e., Hz).

The main parameter of ultrasonic frequency is used to study the overall performance of ultrasonic oscillating architecture-based applications. Therefore, it is vital to choose the best possible operation to conduct the frequency measurements. This process begins with the examination of the different methods used to measure and test frequency, taking into account various factors, such as stability, scatter and the effect of crystals on the operation. The development of a novel hybrid low-cost frequency measurement system is fully described in this section.

3.4.2 Available options for frequency measurements

Inexpensive and accurate frequency measurements can be achieved by using a digital counter and a reference clock oscillator with the frequency f_r. If the frequency of the reference oscillator is much higher than the frequency that is to be measured f_x, the counter is gated by a single period of the signal of interest by counting N reference pulses. Then f_x is calculated as shown in equation (3.2).

$$f_x = \frac{f_r}{N} \tag{3.2}$$

If the frequency of the reference oscillator is much lower than the frequency to be measured, the counter is gated by a single period of the reference oscillator, and the input pulses are counted. Equation (3.3) is used for the frequency estimation.

$$f_x = f_r \times N \tag{3.3}$$

The counter output is accurate to a single pulse; thus, it can be inaccurate up to one count. Consequently, achieving the relative 10^{-4} resolution is possible if the number of pulses counted is no less than 10,000.

In some instances, the ratio between the frequencies is lower than the pulse count, which ensures the required relative resolution. In this case, the counter needs to be gated not during a single period but over several periods of either $f_x(f_x < f_r)$ or $f_r(f_x > f_r)$ as appropriate. In practice, frequency measurements with the required resolution can be achieved by employing two separate counters for the reference and input pulses. Each time the lower frequency pulse count increments, the value of the other counter is compared to the inverse of the required resolution. If the value of the counted high frequency pulses is higher, then the required resolution has already been achieved. The output frequency can be calculated and communicated, and a new frequency measurement can be started by clearing both counters.

In this section, several frequency measurements techniques are presented. These methods are applicable in operations with inexpensive microcontrollers, and they require inexpensive additional components. All methods are examined with regard to input frequency, operational range of frequency, ease of implementation and relative error.

3.4.2.1 Frequency to voltage conversion

An inexpensive Frequency to Voltage Convertor (FVC) can be used to determine the desired frequency. The resultant voltage is passed to a built-in ADC to read and calculate the voltage. A complete block diagram of the operation is shown in Fig. 3.20.

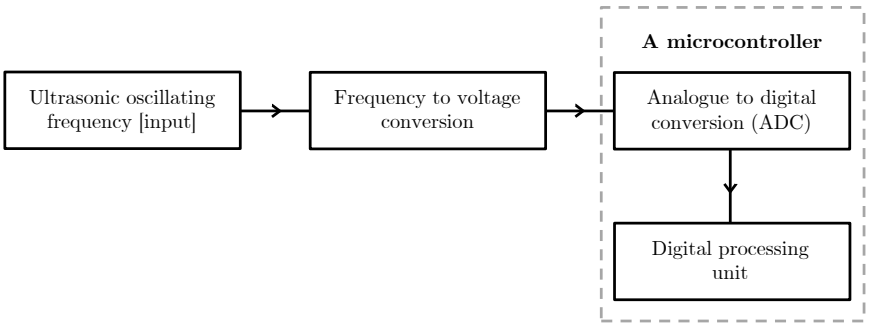


Fig. 3.20 Frequency measurements using frequency to voltage conversion

Commercially, many FVCs vary in performance, depending on linearity, operational frequency range and supply voltage. A comparison of some commercially available FVCs is shown in Table 3.3.

Table 3.3 Available FVC Devices for Frequency Meter Developments

Part number	Linearity (%)	Range (kHz)	Supply voltage (±V)	Price per unit (£)
VFC110AP	0.0002	10 to 4000	8 to 18	17.86
AD650JNZ	0.02	0 to 1000	9 to 18	14.85
AD650KNZ	0.10	0 to 1000	9 to 18	16.40
AD7740KRMZ	1.00	0 to 500	9 to 18	2.30
VFC320BP	0.10	0 to 1000	13 to 20	18.42
ADVFC32KNZ	0.50	0 to 500	9 to 18	9.94

Table 3.3 shows that the specifications of FVC devices can vary significantly depending on the cost. A linearity of 0.0002% can be achieved with a relatively expensive FVC, which results in a relative error of 1.98 ppm, whereas poor accuracy (over 10,000 ppm) is obtained with relatively cheaper 1% linearity FVC.

This method is not applied to the proposed system for two reasons. First, the design must be based on inexpensive components. However, a suitable FVC costs nearly the same as a complete UOTS electronic unit. Moreover, the processing unit features a built-in ADC with a maximum resolution of 13 bits. A 23-kHz signal results in an additional relative error of around 122 ppm, which produces a measurement resolution of about 2.8 Hz. This error is added to the existing system noise, which is included in the PSoC ADC user module datasheet, but it is not considered in the above calculations.

3.4.2.2 Counting cycles for a fixed time

These methods and the following ones utilise electronic frequency counting, in which the value of the counter is sampled at the sampling frequency rate and incremented per an input frequency cycle. Two cascaded latches allow for storing the new Accumulated Value (AV) after each cycle, as shown in Fig. 3.21. The accumulated value at the output from the latches is shown in equation (3.4).

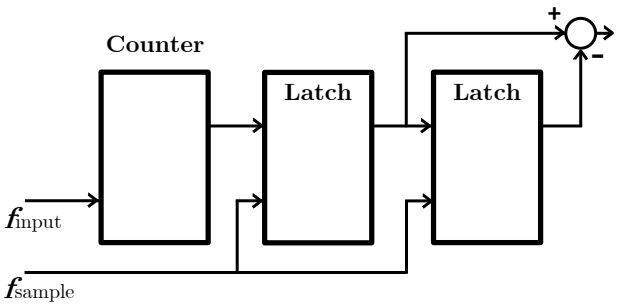


Fig. 3.21 Diagram of counting cycles for a fixed amount of time [135]

$$AV = \frac{f_{input}}{f_{sampling}} \tag{3.4}$$

The ratio in equation (3.4) is likely to be a non-integer value, whereas, by definition, a counter is only capable of producing integer values. However, the average of many AVs results in a value of frequency that is more accurate than achieved by a single measurement. For example, in measuring a frequency of 14.4 Hz, the output signal (i.e., accumulated value) is 14 Hz at 60% of the time and 40% at 15 Hz if the sample rate is set to 1 sps (sample per second).

To account for the quantisation error in equation (3.4), a fractional term e_q is added, of which its absolute magnitude is less than unity, as shown in equation (3.5).

$$AV = \frac{f_{input}}{f_{sampling}} + e_q \tag{3.5}$$

This modification is applied to equation (3.4), giving the following equation for the measured frequency:

$$f_{measured} = AV.f_{sampling} \tag{3.6}$$

Substituting AV in equation (3.5) into equation (3.6) results in equation (3.7):

$$f_{measured} = f_{input} + (f_{sampling}.e_q) \tag{3.7}$$

In calculating the worst case scenario, the maximum error in the measured frequency is approximately equivalent to the number of samples per second. For example, 1 sps results in an error of 1 Hz in the measurements. This result clearly depends on the order of frequency to be measured. In a frequency of 100 kHz, there is an error of 10 ppm. The error is considerably higher in small frequencies, which appears in the relationship between the relative error per sample e_r and the measured frequency shown in equation (3.8).

$$e_r = \frac{|f_{measured} - f_{input}|}{f_{input}} \tag{3.8}$$

Based on the input frequency of the application and the acceptable error range, a minimum input signal is defined for the requirements. Moreover, the upper limit of input frequency can be set based on the size of the counter. Generally, the input frequency is limited by the sampling frequency, and the number of bits n in the counter does not overflow as shown in equation (3.9):

$$f_{input} < f_{sampling}.2^n \tag{3.9}$$

3.4.2.3 Measuring time of a single cycle

The operation is similar to counting cycles in the fixed time method. The only difference is that the counter is incremented by clock frequency and then latched by the signal input frequency (Fig. 3.22).

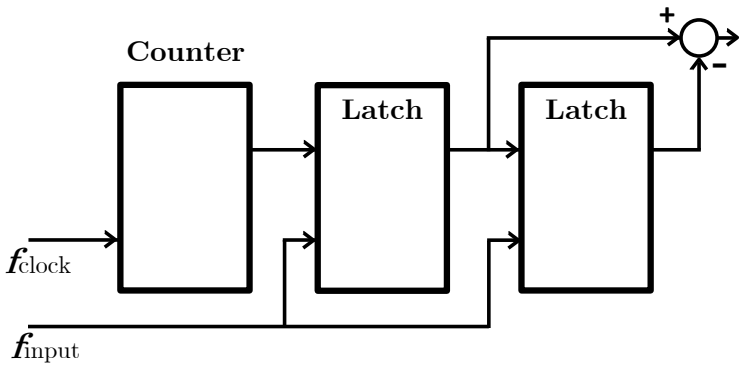


Fig. 3.22 Diagram of measuring the time of a single cycle [135]

The advantage of using this method is that the accumulated value is updated at the sampling rate of f_{input}. This will give an AV, considering the quantisation error for this approach, as shown in equation (3.10):

$$AV = \frac{f_{clock}}{f_{input}} + e_q \tag{3.10}$$

The measured frequency is in the following form:

$$f_{measured} = \frac{f_{clock}}{AV} \tag{3.11}$$

Combining equations (3.10) and (3.11) yields a measured frequency value as a function of f_{input}, f_{clock}. AV is represented by the following equation:

$$f_{measured} = \frac{f_{clock}}{\frac{f_{clock}}{f_{input}} + e_q} \tag{3.12}$$

Equation (3.12) can be approximated to give

$$f_{measured} \approx f_{input}\left(1 - e_q \frac{f_{input}}{f_{clock}}\right) \tag{3.13}$$

In addition, the relative error will be

$$e_r = \frac{|f_{measured} - f_{input}|}{f_{input}} \tag{3.14}$$

Unlike the previous method, to obtain a smaller error using this method, it is recommended that the input frequency be 1,000 times lower than the clock frequency to obtain an error in the order of 0.1%. For example, a 12 MHz clock frequency functions in the error range if it is operated with an input frequency equal to or lower than 12 kHz.

Input frequency (or measurable frequency) is limited, as shown in equation (3.15). Exceeding this limit results in counter overflow.

$$f_{input} < \frac{f_{clock}}{2^n - 1} \tag{3.15}$$

3.4.2.4 A hybrid method

This method consists of measuring the number of cycles that are fitted within one period. Fig. 3.23 shows the structure of this arrangement.

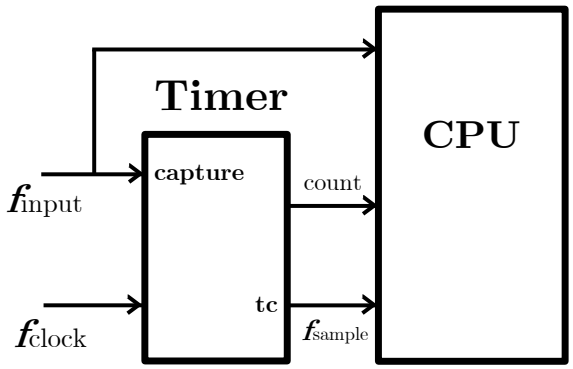


Fig. 3.23 Diagram of the hybrid method [135]

The timer decrements the counter at each clock cycle. When the counter underflows, an internal counter is enabled, which allows the sample frequency to start measuring the sample period. A microcontroller is used to synchronise the start and end of the cycle. When the capture detects a rising edge in an input signal, the microcontroller starts reading the signal.

The sample frequency, which defines the sample period, is written as a function of clock frequency and the number of bits in the counter n, as shown in equation (3.16).

$$f_{sample} = \frac{f_{clock}}{2^n} \tag{3.16}$$

Cycle count (CC) represents the number of cycles can be fitted in a sample period. This can be represented by taking into account the quantisation error, as shown in equation (3.17):

$$CC = \frac{f_{input}}{f_{sample}} + e_q \tag{3.17}$$

One sample period includes (CC-1) cycles. The accumulated value is dependent on the known clock and the input frequencies as well as CC:

$$AV = \frac{f_{clock}(CC-1)}{f_{input}} + e_q \tag{3.18}$$

The clock frequency, CC and AV are used to calculate the measured frequency:

$$f_{measured} = \frac{f_{clock}(CC-1)}{AV} \tag{3.19}$$

Although the measurement of the relative error is somewhat complicated, it is estimated as shown in equation (3.20):

$$e_r = \frac{\left|f_{measured} - f_{input}\right|}{f_{input}} \tag{3.20}$$

To determine the worst case error, a signal that is below $3 \times \mathrm{f_{sample}}$, CC is considered less than three (changes between 2 and 3). As a result, a single cycle or two cycles are counted. For a single cycle, AV will be third of a complete counter cycle. In this case, the relative error is a function of the ratio of the input frequency to the sampling rate (ra) and the counter size where ra is greater than 3 or equal to 3 in the worst case error, as shown in equation (3.21):

$$e_r = \frac{1}{2^n} \cdot \frac{ra}{ra - 2} \tag{3.21}$$

In order to estimate the worst case error in a 16-bit counter, a simulation of for equation (3.21) was conducted. The results are presented in Fig. 3.24.

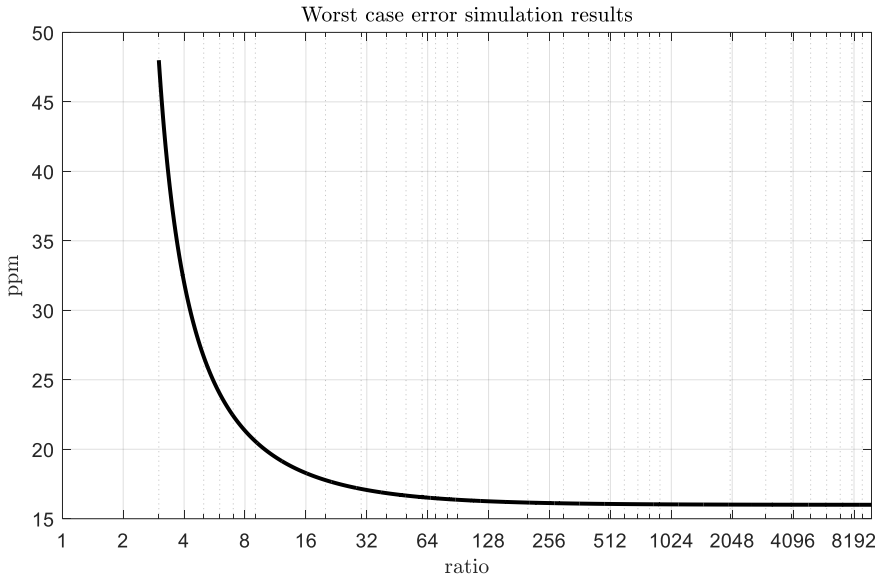


Fig. 3.24 Results of the worst case error simulation of a 16-bit counter

Fig. 3.24 shows that the worst case error was at the ratio of 3 with an error of about 48 ppm. A minimised error (about 16 ppm) is obtainable when the ratio is 16 and greater. This minimised error can be achieved by decreasing the sampling rate (a function of clock frequency and counter pulses). Higher order counters will result in even smaller minimised relative errors.

3.4.2.5 Conclusion

The results showed that the first method had advantages and disadvantages. The advantage of using frequency to voltage is that this method does not require complex software development. However, this method requires relatively expensive FVCs. Moreover, the available ADCs have a poor resolution in processing the required range of frequencies.

The second and third methods, counting cycles for a fixed time and measuring time for a single cycle, respectively, shared common features. They did not require any additional

circuitry. In addition, although they produced a reasonable relative error, they functioned only within a certain range of frequencies.

The hybrid method, which combines methods two and three, showed the optimum operation in a greater range of frequencies because of the synchronisation of the clock signal to the input signal. Table 3.4 summarises the differences between the frequency measurement techniques.

Table 3.4 Summary of the Frequency Measurement Techniques

Method	Sample rate	Minimum f_{input}	Maximum f_{input}	Relative error	Frequency range
Frequency to voltage conversion	<115 sps	0Hz	400 MHz	17.2 ppm + system noise	All
Counting cycles for a fixed time	$f_{sampling}$.	0Hz	$< f_s.2^n - 1$	$< \frac{f_{sampling}}{f_{input}}$.	High
Measuring time for a single cycle	f_{input}.	$\frac{f_{clock}}{2^n - 1}$	f_{clock}	$< \frac{f_{input}}{f_{clock}}$.	Low
Hybrid method	$\frac{f_{clock}}{2^n - 1}$	$\frac{f_{clock}}{2^n - 1}$	f_{clock}	Down to $1/2^n$	All

Based on the results shown in Table 3.4, the hybrid method is the most suitable one for the proposed system. This method guarantees a relative error less than 46 ppm in the worst case scenario, and a relative error of 16 ppm if the ratio of the input frequencies to the sampling rate is increased.

3.4.2.6 Calculations of worst case error in ppm

In this section, a worst case error is calculated considering an ultrasound oscillation of 24 kHz. The PSoC includes a 16-bit timer user module that calculates 2^{16} periods.

The CPU clock that matches the timer period counts in order to give a sampling frequency close to 1 is estimated as follows:

$$CPU\ Clock = \frac{System\ clock}{divider} = \frac{24\ MHz}{368} = 65.2\ kHz\ \approx\ 2^{16} \tag{3.22}$$

The system divider is 368. In this case, the sampling frequency is equal to the CPU clock divided by the full timer count:

$$f_{sampling} = \frac{CPU\ clock}{Period} = \frac{65{,}217.39\ Hz}{2^{16}} \approx 0.995 \tag{3.23}$$

To obtain the system's specifications, the minimum frequency should be maintained at a value lower than the doubled sampling frequency. The maximum input frequencies should not exceed the CPU clock values estimated as follows:

$$f_{input_min} = 2 \times f_{sampling} = 2 \times 0.995 \approx 1.99Hz \tag{3.24}$$

$$f_{input_max} = CPU\ clock = 65{,}217.39\ Hz \tag{3.25}$$

Therefore, the Dynamic Frequency Range (DFR) is given by

$$DFR = \frac{f_{input_max}}{f_{input_min}} = \frac{65{,}217.39\ Hz}{1.99\ Hz} = 32{,}768\ Hz \tag{3.26}$$

The predicted worst case error is calculated by the timer period counts divided by 3 as in equation (3.21). The worst case error for this example is given by

$$Worst\ case\ error = e_r(Period) \times 3 \approx 45.8\ ppm \tag{3.27}$$

With regard to Fig. 3.24 and equation (3.21), the relative error e_r rapidly decreases to a factor of 3 when the ratio between input frequency to sampling rate is increased, as shown in equation (3.28).

$$Best\ case\ error = \frac{Worst\ Case\ error}{3} = \frac{45.8}{3} = 15.3\ ppm \tag{3.28}$$

3.4.3 Firmware of the frequency measurements device

The firmware control used in the frequency measurements is based on two basic components: a comparator and a timer. The measurement process is triggered when the comparator detects the presence of a signal at half of the supply voltage range and then triggers its register. When the measurement process is triggered, the timer starts counting until the comparator detects the signal. This allows for clearing the comparator register

so the next signal can be detected. The flowchart shown in Fig. 3.25 illustrates the operation of the frequency measurement firmware.

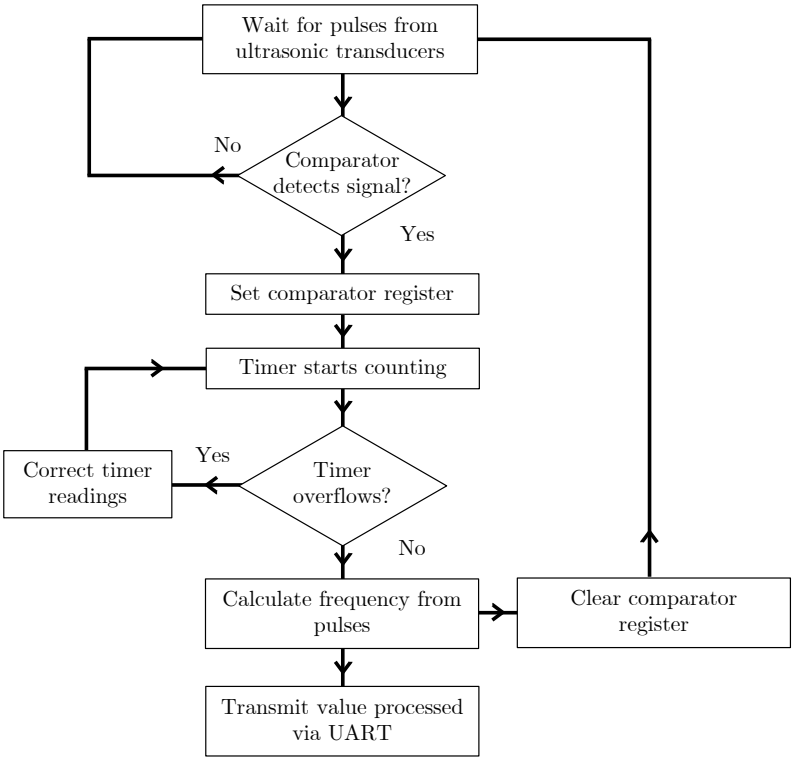


Fig. 3.25 Flowchart of the frequency measurements firmware

3.4.4 Frequency reference source

3.4.4.1 Investigation of the stability of the clocking choices available

The data collected from previous experiments featured very high scattered frequencies with several resonances [44]. Initially, these uncertain results were considered a systematic fault of electronics or due to the incorrect implementation of the ultrasonic oscillating architecture. The examination of the specifications of the reference clock revealed that an inaccurate clock reference was used independently as an oscillator, which caused the large uncertainly in the measurements. PSoC internal main oscillator (IMO) had a tolerance of ±2.5% over the full operating temperature [128]. Precise crystals were added in a PLL mode that introduced a notable difference with greater accuracy [110].

Another important factor in achieving the required resolution is the frequency stability and/or tolerance in the reference clock oscillator. Relatively inexpensive crystals ranging from 1 to 20 MHz can provide ±30-50 ppm when they are connected to the appropriate

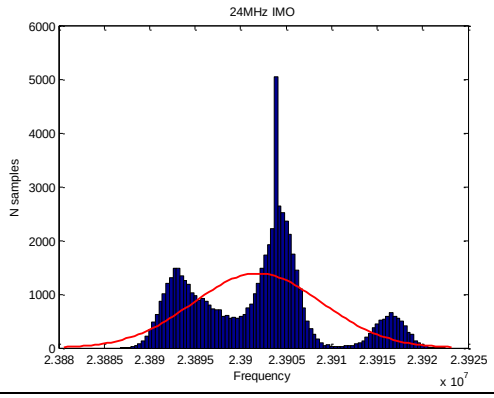
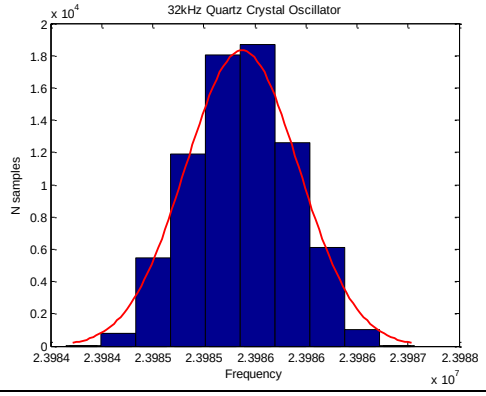
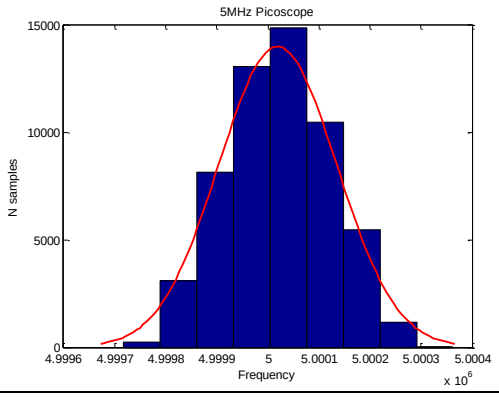
pins of a microcontroller, which could be sufficient in the present application. A crystal oscillator with similar tolerances is expensive, but its operation does not require a microcontroller, and it can generate waveforms with low jitter. Temperature Compensated Crystal Oscillators (TCXOs) are accurate reference oscillators (uncertainty of a few ppms only), but they are inexpensive.

An important factor in the selection of oscillating clocks is their cost. The objective of this project is to develop an inexpensive but accurate temperature measurements system. Therefore, the cost of these electronic components is a significant element in BOM. Very high precision reference oscillators, such as rubidium clocks, can cost hundreds of pounds, which is several times greater than the intended cost of the UOTS system as well as the supporting electronics. Highly accurate Oven Controlled Crystal Oscillators (OCXOs) are not considered inexpensive instrumentation because they typically cost several £100. Cheaper options such as TCXO can cost less than £1 with acceptable accuracy and low jitter. This section will evaluate several clock referencing options that can potentially be used in future developments.

Four different oscillators were tested in the frequency counter design. A 10-MHz OCXO reference clock was used to trigger a 16-bit timer. Typically, OCXOs are precise to a fraction of a ppm. The tested oscillators were as follows:

- IMO of a PSoC: the main internal clock that controls clock cycles for PSoC instructions. The tolerance of this oscillator is ±2.5% over the full range of operating temperature (-40°C to +85°C) [136].
- A 32 kHz low-frequency crystal watch oscillator: initially provided to the microcontroller to provide better measurement referencing. Typically, this oscillator has a maximum frequency tolerance of ±20 ppm at the operating temperature range (-20°C to +70°C) [137].
- PicoScope 5000 PC oscilloscope: generates signals up to 5 MHz with a time-based accuracy of ±50 ppm in normal operating temperatures from 0°C to +40°C [138].
- A 32 kHz TCXO: accurate to ±4 minutes/year for the full temperature range (-40 °C to + 85 °C). The frequency stability is within the range of ±7.5 ppm for the full temperature range and up to ±2.5 ppm for 0°C to + 40°C [139].

Table 3.5 Results of All Four Tested Clock References, Including Standard Deviation and a Histogram.

Oscillator	Frequency (Mhz)	Standard deviation		Histogram
		Hz	ppm	
PSoC IMO	24	1775.2	296	93 frequency levels 
32.768 kHz crystal oscillator + PLL	24	138.2	23	10 frequency levels 
PicoScope 5000 Series oscilloscope	5	115.7	23	9 frequency levels 

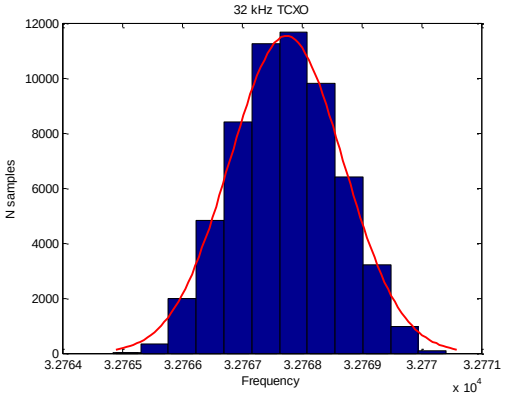
Oscillator	Frequency (Mhz)	Standard deviation		Histogram
		Hz	ppm	
32.768 kHz TCXO	0.032	0.95	29	14 frequency levels 

Table 3.5 shows that these oscillators (except PSoC IMO) had standard deviations from 23 to 29 ppm.

The reference frequency, f_x, was assumed to be 25 kHz, which is similar to the operating frequency of an UOTS. This frequency was measured using a 10-MHz OCXO reference clock, f_{ref}. Equation (3.29) was used to find the number of pulses N_{pulses} (cycle count) required to overflow a 16-bit counter:

$$N_{pulses} = \frac{f_x \times P}{f_{ref}} = \frac{25\ kHz \times 2^{16}}{10\ MHz} \approx 164 \tag{3.29}$$

If one pulse is miscounted in the timer, the period will measure $P_{new} = |2^{16} \pm 1|$, which is an error of frequency e_f as given by equation (3.30):

$$e_f = f_x - f_{x_{new}} = f_x - \frac{f_{ref} \times N_{pulses}}{P_{new}} = 25\ kHz - \frac{10\ MHz \times 164}{|2^{16} \pm 1|} \approx 0.38\ Hz \tag{3.30}$$

By increasing the number of pulses, the frequency error decreases by a factor of 15, which is shown in the graph provided in Fig. 3.26.

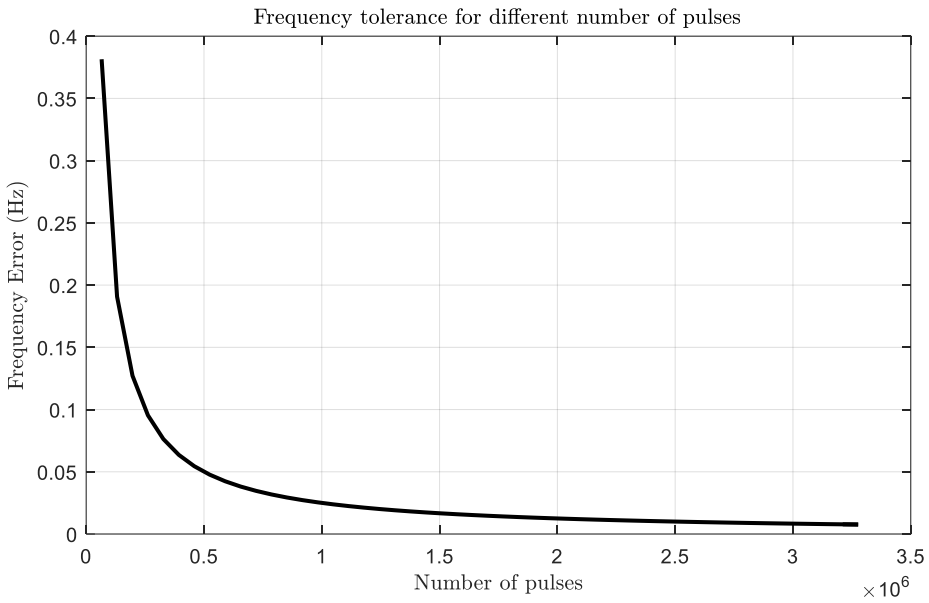


Fig. 3.26 Frequency tolerance in different numbers of pulses

Fig. 3.26 shows that the number of reference pulses counted must be increased in order to decrease tolerance. The graph shows that the error is small and stable in pulses of more than 1.5 million. Therefore, 2 million pulses were chosen as having the minimal amount of error. In order to accommodate 2 million pulses, the counter was upgraded from a 16-bit to a 24-bit timer. From equation (3.29), the number of pulses required for a 25-kHz signal with a 24-bit timer is 41943 pulses. The error, associated with measurements of 2 million pulses, is given by equation (3.31):

$$e_{f_2M} = 25\ kHz - \frac{10\ MHz \times 41943}{|2^{24} \pm 1|} \approx 0.02\ Hz \tag{3.31}$$

The numerical data indicate that the number of pulses should be increased 32 times. This increase is accommodated by a 24-bit timer, which handles more than 16 million pulses. However, using this quantity of pulses reduces the measurement time to five readings per one second as shown in equation (3.32):

$$Measurement\ time = \frac{N_{pulses}}{f_{ref}} = \frac{2\ M}{10\ MHz} = 0.2\ s/measurement \tag{3.32}$$

3.4.4.2 Achieving full scale voltage from a low voltage TCXO signal

Low-cost TCXOs have an output drive level slightly above 0.8 V in order to relegate the higher voltage circuitry, which dissipates heat and leads to frequency drift off chip. There is no clear reason for the relatively low drive level in the documentation of the manufacturers of oscillators. However, some technical notes suggest that such drive levels are a better solution to minimising internal power dissipation as well as providing better ageing and frequency stability [137].

This signal should be adjusted to operate as the external clock reference, that is, the amplitude of this signal should be the same as the microcontroller power supply voltage in a reliable operation. A one-stage OpAmp amplification circuit is not be suitable for the level conversion because most inexpensive OpAmps amplify signals with frequencies only up to 1 to 2 MHz. Hence, three low-cost options for converting the 10 MHz 0.8 V reference signal to 3.3 or 5 V levels were fully prototyped and tested:

BJT-based voltage drive level circuit

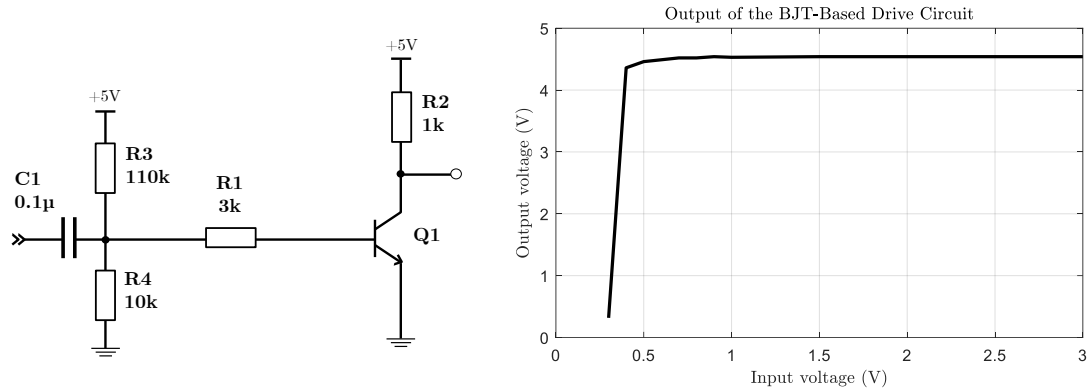
In the first option, a BJT transistor is employed to drive the signal up to the required voltage. Table 3.6 lists some BJTs with low threshold voltage that are potentially suitable for the level converter.

Table 3.6 Selected BJTs with Low-level Threshold Voltages

Part number	$V_{BE(sat)}$	
	Min	Maximum
2N3906	-0.65	-0.85
2N3904	-0.65	-0.95

The circuit shown in Fig. 3.27 (a) was constructed. The resistance of R1 was varied in order to find the best behaviour of the output waveform, a potential divider, R3R4, was added to bias the input signal. The values of R3 and R4 were chosen to shift the TCXO signals after the DC blocking capacitor C1 from -0.4–0.4 V to 0–0.8 V.

The circuit was initially tested using a 100-kHz square wave signal from a signal generator. The signal amplitude started to increase to the supply voltage level shortly after the input amplitude exceeded 0.35 Vp-p, as shown in Fig. 3.27 (b).



(a) schematic (b) experimental results

Fig. 3.27 BJT-based voltage conversion circuit

However, when this circuit was connected to a TCXO, the output signal amplitude was in the order of only a few millivolts. The circuit was re-tested using higher frequency external pulses from the signal generator. The results showed that the signal became heavily attenuated when the input frequency increased over 5 MHz due to Miller effect. Therefore, this option was considered inadequate for use in the operation of the TCXOs.

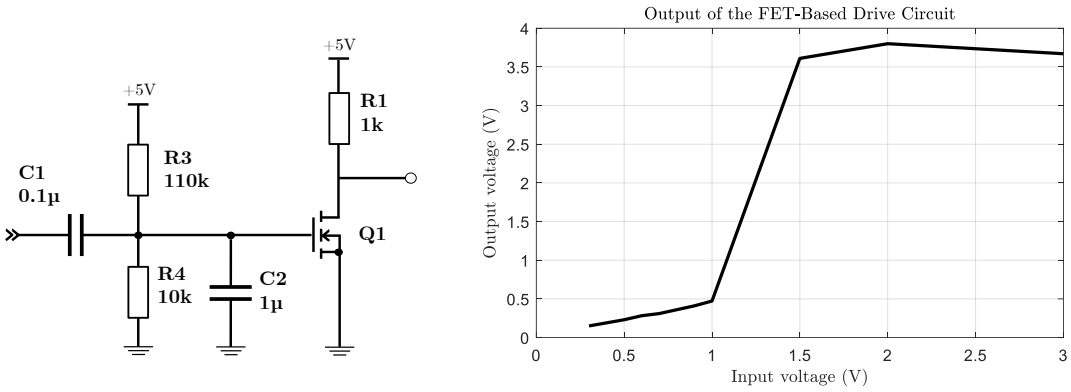
FET-based voltage drive level circuit

In the second option, an N-type MOSFET with a low threshold voltage V_{GS} (below 0.8 V) in enhancement mode configuration was utilised as an amplifier. Table 3.7 presents the specifications of some of suitable FETs.

Table 3.7 Selected FETs with Low-level Threshold Voltages

Part number	VGS (sat)		
	Min	Typical	Maximum
BF246B	-0.6		-14.5
FDN335N	0.4	0.9	1.5
FDN302P	-0.6	-1.0	-1.5

The schematic diagram and circuit response are shown in Fig. 3.28 (a) and Fig. 3.28 (b), respectively.



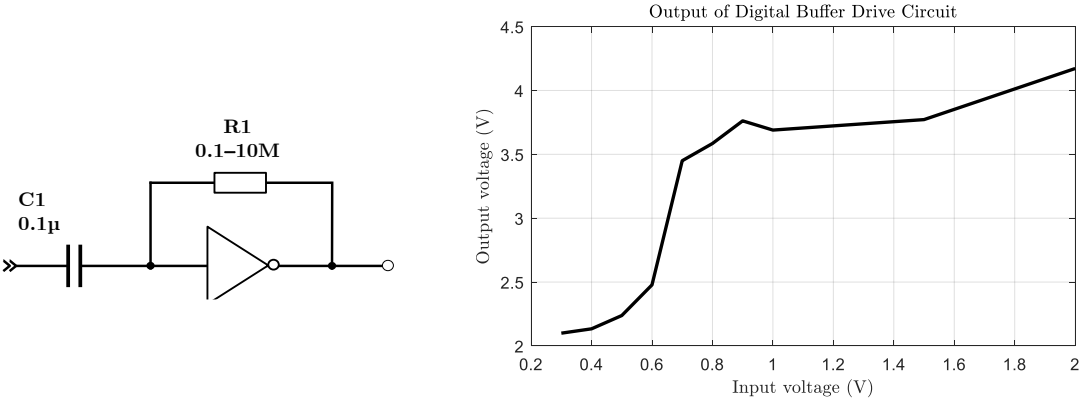
(a) schematic (b) experimental results

Fig. 3.28 FET-based voltage conversion circuit

The experimental data presented in Fig. 3.28 (b) showed that the circuit operated only when the amplitude of the input signal was above 1.5 Vp-p. Because this amplitude exceeded the TCXO output amplitude, this option was deemed unsuitable.

Digital inverter-based drive level circuit

This approach was suggested in an application note from a manufacturer of TCXO [137]. The TCXO signal is fed to a digital inverter buffer, which is biased by a feedback resistor, R1. The suggested value of the feedback resistor was within the range of 0.1–10 MΩ. No potential divider is required for this circuit because the feedback resistor provides a self-bias. The schematic diagram and circuit response are shown in Fig. 3.29 (a) and Fig. 3.29 (b), respectively.



(a) schematic (b) experimental results

Fig. 3.29 Digital inverter-based voltage conversion circuit

Fig. 3.29 (b) presents the recorded output amplitudes of a range of input voltages. The circuit functioned as expected when the input amplitude exceeded 0.6 V, which was appropriate for the TCXOs operation. The voltage converter was successfully tested with several TCXO types. This option was chosen to boost TCXO voltages in the modular system because of its simplicity (only one digital buffer and a resistor are required), low cost and capability of operation with both 3.3 and 5 V power supplies.

3.4.5 Resolution and accuracy of the developed meter

Four PSoC-based methods of measuring frequency were reviewed: frequency to voltage conversion; counting the number of cycles in a fixed period; measuring the duration of a single cycle, and a hybrid method. It was found that the hybrid method was the easiest to implement. Moreover, it featured minimal uncertainty, especially if the ratio of input frequency to sampling rate was high. The maximum error was only 15.3 ppm for a 16-bit counter and 0.18 ppm for a 24-bit counter when the ratio of the input signal and the clock reference was large.

A stable clocking reference should be chosen in order to obtain accurate measurements. The experimental results showed that TCXO provided the lowest standard deviation of uncertainty among the tested oscillators. A comparison of different clocking options was conducted using OCXO as the clock reference. Although oscillators such as OCXO or rubidium clocks have greater accuracy, they increase the BOM.

3.5 Summary

This chapter combined all supporting electronic ultrasonic temperature measurement systems. The first section discussed the electronic development of an ultrasonic driver system that is based on an ultrasonic oscillating sensor. The evaluation of system control options showed that the PSoC realisation was the most appropriate for this development. This technology was a main part of several developments in this project, including the ultrasonic driver, temperature measurements, AGC and transducer multiplexing. Moreover, these devices are available at low cost in various packages, which significantly reduced the overall BOM of the developed application.

The second section focused on developing methods for the automatic control of the amplitude of the received ultrasonic signal. Driving signal to saturation is thought to be one cause of frequency-temperature hysteresis. Several options were considered in developing an AGC system. Three JFET-based methods were introduced, which showed better control of signal levels. Each method was simulated, constructed and tested, followed by a comparison and evaluation of the methods. The JFET3 configuration showed fast response time and required a smaller number of components with wider input range. A more robust option was to integrate the JFET3 design with the PSoC-based AGC. When the ultrasonic driver was tested with the AGC, the results showed no noticeable improvement in temperature-frequency hysteresis. In addition, an improvement of 15% was found in the frequency scatter response.

The third section examined the available low-cost conventional sensors for use as a temperature reference. 1-Wire sensor technology was found to be the best candidate because of its flexible programming and low cost. The implementation of software control and the data acquisition system was fully developed and discussed.

The fourth section focused on developing an accurate frequency meter device. Several methods of implementing the device were discussed. It was found that the hybrid method resulted in low uncertainty value using a low accurate clocking reference. The firmware and software operation of the frequency meter were discussed. Several clocking reference options were evaluated, and TCXO was found to provide the least relative uncertainty at minimal cost. Finally, the three options were examined for their ability to drive the signal from TCXO to attain voltage rail levels.

Chapter 4

Development of the Modular Driver for The Ultrasonic Oscillating Sensor

4.1 Introduction

The development of a robust and flexible electronic instrument is desirable to have full control of the ultrasonic oscillating sensor system. A modular instrumentation system was developed to include reliable and convenient commands for use in controlling the driver hardware and logging the measured frequencies.

To allow a flexible approach to the experiment, a set of modules have been developed to control various functions. The modules are designed to be connected in any arrangement so the system can be reconfigured easily. Each module contains a PSoC and a control module communicated with them.

Control commands are broadcasted to all the modules simultaneously, but only the appropriate modules will perform a certain action. Most modules are designed around PSoC microcontrollers, and they have the ability to be programmed on the modules. The overall BOM of a fully functional modular system is below £15, including the cost of PCBs, relevant electronic parts and microcontrollers.

4.2 Hardware development

4.2.1 General guidelines for the developed boards

Each module is constructed using a 50×50 mm PCB in which the connecting pins are placed at fixed locations on all sides. If a modular PCB is viewed from the top, the input female pin header is on the left (connector B), and the output male pin header is on the right (connector C). The connector at the top of each board is dedicated to UART communications with the host (connector A), and the metallised PCB holes at the bottom are used to attach the PSoC programmer when necessary. Some boards feature special headers that can be configured to set signal direction as well as additional jumpers that specify the programming environment. The generic layout of the individual modules in the modular system is shown in Fig. 4.1.

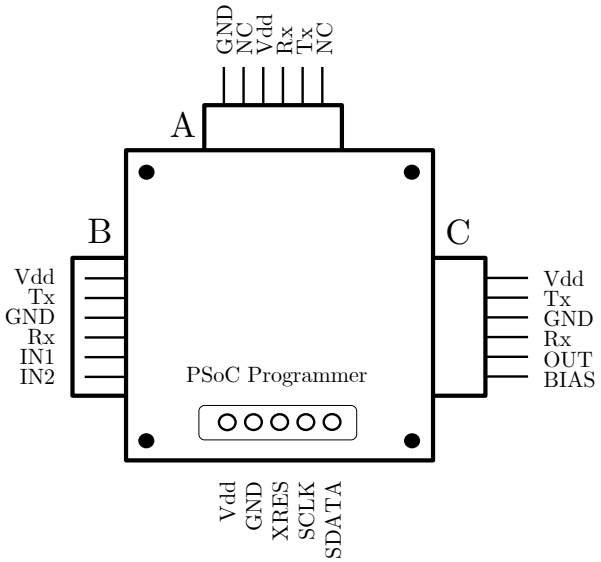


Fig. 4.1 The general layout of modular system PCBs

The positioning of connectors is accurately determined in order to match other circuits. The following three modules were successfully developed and tested:

- Electronic driver for ultrasound transducers
- Input and output sensor multiplexer
- Frequency meter

On-board PSoC programming enables convenient updates of PSoC firmware without the need to desolder it from the board. Connections to the required microcontroller pins (Vdd, Gnd, SDATA and SCLK) are routed to the PSoC MiniProg (i.e., the PSoC programmer) header.

A female pin header at connector A connects a UART to the USB serial converter TTL 6PIN module, that is, pins Tx, Rx, Vdd and Gnd. A pull-up resistor of 10 kΩ is added between the Tx pin of a PSoC and a Vdd to allow UART transmitters from different PSoCs to be connected to the same RxD input of the UART-to-USB converter without causing mutual interference. The three boards developed share the same connections and common elements discussed. PCB layouts for modular system boards are available in Appendix A.

4.2.2 Electronic driver module for ultrasound transducers

This board was developed to provide amplification and filtering stages for an ultrasonic oscillating sensor. The minimal requirement for a PSoC1 part is the availability of at least three analogue columns and one digital row. The analogue columns provide three PGAs: two for the amplification stage (gain up to 2,400) and one to buffer the bias voltage in order to set the ultrasonic signal at half of the supply voltage. In addition, two switched capacitor parts of the analogue columns are used to implement a BPF. The digital row is required for communications to a PC using a UART user module that occupies two digital blocks. Based on these specifications, various PSoC1 parts are suitable. Table 4.1 shows the PSoCs available for prices below £6.

Table 4.1 Parameters of Various PSoC1 Parts [128]

Part number	Pin count	Available packages	Analogue blocks	Digital blocks	I/O count	Price per unit (£)
CY8C27143	8	PDIP	12	8	6	4.57
CY8C20134	8	SOIC	1	0	6	1.51
CY8C21123	8	SOIC	0	4	6	1.48
CY8C24123	8	PDIP & SOIC	6	4	6	1.76
CY8C27243	20	PDIP, SSOP & SOIC	12	8	6, 16	3.36
CY8C28243	20	SSOP	12	12	16	2.23
CY8C28445	28	SSOP	12	12	24	4.08
CY8C28452	28	SSOP	12	8	24	2.26
CY8C27443	28	PDIP, SSOP & SOIC	12	8	24	3.67
CY8C29466	28	SSOP, QFN & PDIP	12	16	24	5.19

The CY8C24123 part was chosen for this module. The use of a more capable PSoC would have removed the need for a potential divider of the bias voltage but the cost would have been higher. This will save around £2.30 in the cost of the microcontroller. Four digital blocks (one digital row) are sufficient to implement the UART, which requires two digital blocks. Fig. 4.2 presents a schematic of this board, showing the PSoC-based electronic driver for an ultrasonic oscillating sensor.

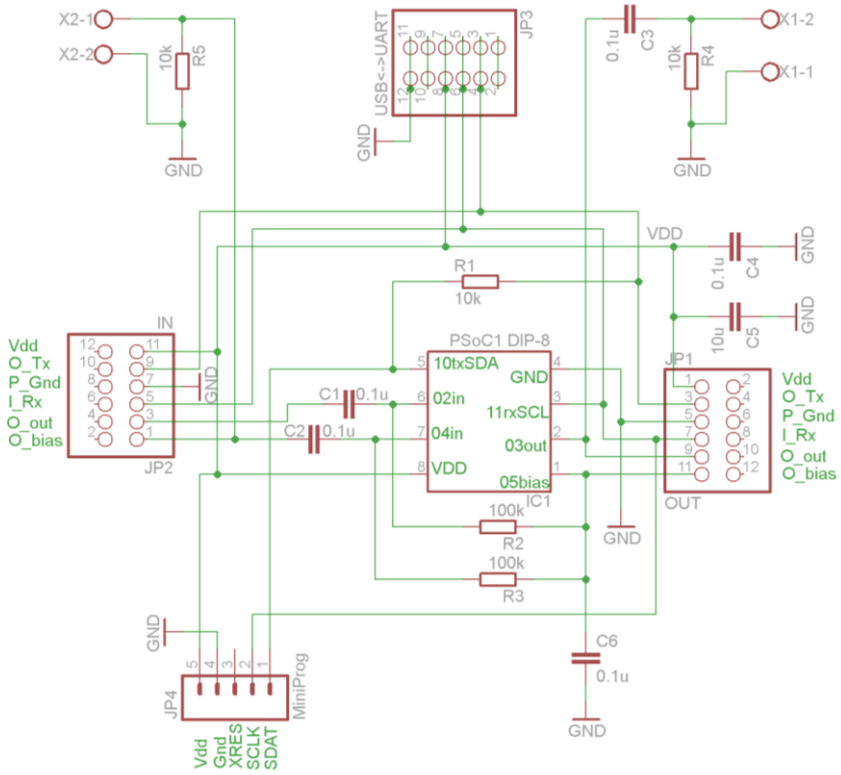


Fig. 4.2 Schematic diagram of the electronic driver for ultrasound transducers

Two port 0 pins, P0[2] and P0[4] at connector B, are configured as analogue inputs and connected to the input socket. Although only one input is required, the second input allows for future development of the phase shifter. P0[4] is connected to the input from an ultrasonic receiving transducer. The input to this pin is biased to one-half of the supply voltage supplied from the pin P0[5].

A DC blocking capacitor C2 was added in series to the input of the module in order to block any DC voltage from the receiver transducer. The input signal is then amplified using two cascaded PGAs and then filtered using the switched capacitor blocks that are built into the PSoC. The output at connector C is connected to pin P0[3] of the microcontroller, which is configured as an analogue output. The electronic driver module is shown in Fig. 4.3.

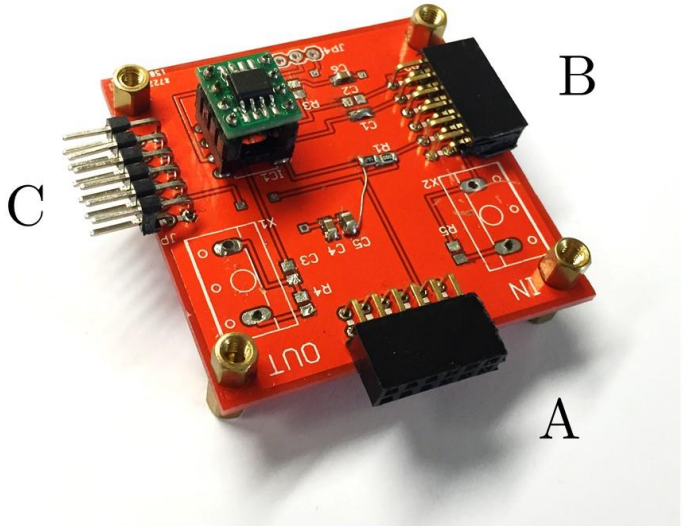


Fig. 4.3 The electronic driver module

Two screw terminals were added as the input and output connections on both sides of the board for the receiving and transmitting ultrasonic transducers.

4.2.3 Ultrasonic sensors control and signal multiplexing

The purpose of this board is to enable the controlled switching between different pairs of ultrasonic transducers. In the initial experiment with the first board, the response of a single pair of ultrasonic transducers was measured overnight. Switching between different pairs of ultrasonic transducers allows to compare the operation of multiple pairs of transducers which are operating in the same conditions at the same time of the experiment. By using the multiplexer board, it was possible to alternate different transducer pairs at the same temperatures throughout the experiment to compare the performances of different pairs in terms of frequency scatter, frequency-temperature sensitivity, accuracy, hysteresis and so forth.

The multiplexer module enables finding the best combination of the electronic driver parameters (i.e., amplifier gain and/or filter centre frequency and/or bandwidth) of each pair. In addition, numerical analysis and signal processing are applied to all the experimental curves obtained from different transducer pairs to achieve accurate readings, that is, by calculating averaged ultrasound frequency and/or applying frequency offset to the complete set (or any subset) of sensors. As a change in water temperature cannot occur quickly because of the large specific heat capacity, it is possible to log the

frequency data for four ultrasonic transducer pairs under the same temperature conditions. A schematic diagram of the complete circuit is presented in Fig. 4.4.

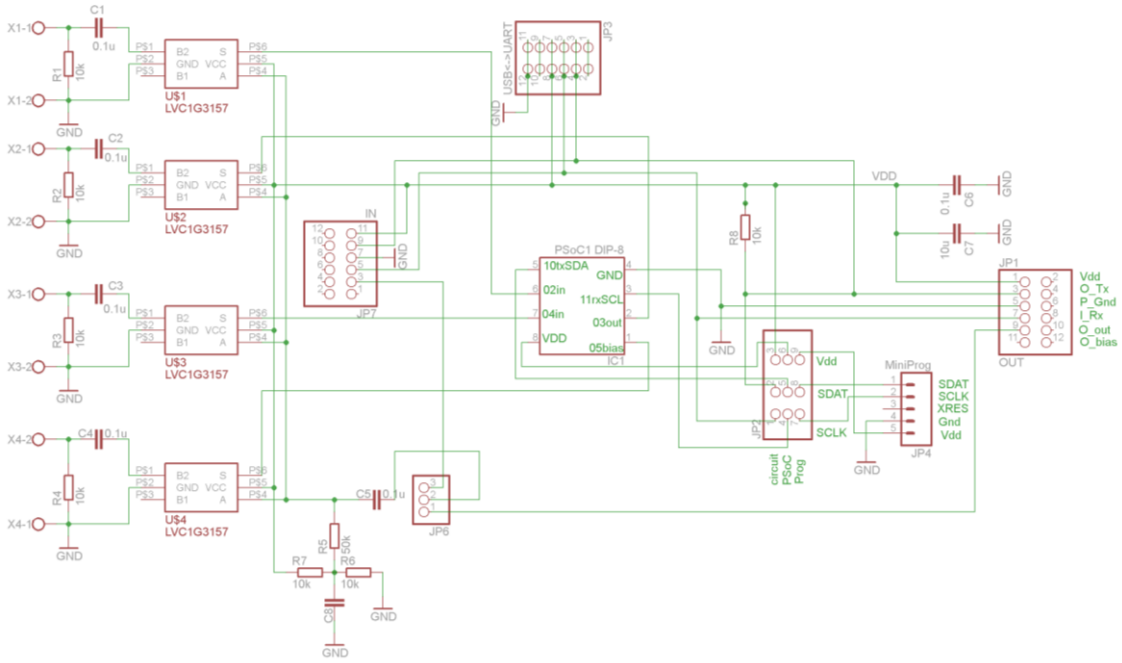


Fig. 4.4 Schematic diagram of the multiplexer moduleJP2

The general board layout and construction are very similar to the previously described board in section 4.2.2. The PCB has the same dimensions, the same PSoC part, the same screw terminals for ultrasonic transducers, input/output, UART-to-USB and PSoC MiniProg connections.

The choice of which ultrasonic transducer is connected to the electronic driver using semiconductor switches. Four two-channel analogue multiplexer/demultiplexer parts, 74LVC1G3157, were used to connect to four different pairs of ultrasonic transducers. These switches are simple to control, and they are inexpensive. These switches have two pins, B2 and B1, which can be connected to pin A. The connection is controlled by the digital control pin, S, which connects A to B1 when S is low, and A to B2 when S is high. The control pins of the four semiconductor switches are connected to pins P0[2, 3, 4 and 5] to enable the transducers 1, 2, 3 and 4, respectively as shown in Fig. 4.5. All the A pins in the four semiconductor switches are connected with biasing provided by the potential divider R7R8. The bias supplied in the module on either the left or right was not used to ensure a fully independent operation of the module.

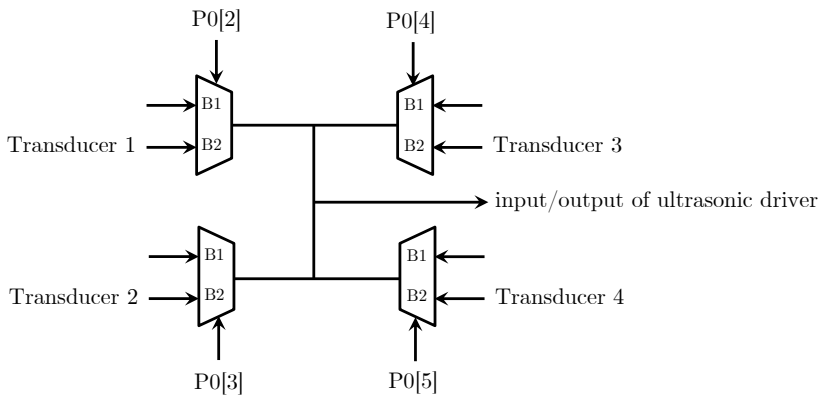


Fig. 4.5 Multiplexers connections with PSoC

Some of the PSoC pins are shared between the programming pins (SDATA and SCLK) and the digital control of the switches, therefore, the jumper set JP4 is provided to allow for in-circuit programming of the module without disconnecting it from the modular system. This jumper set consists of nine pins: pins 4, 5 and 6 are connected directly to pins P1[1], P1[0] and Vdd, respectively. The three pins on the right, pins 7, 8 and 9, are connected directly to the PSoC programmer pin header. Adding a six-pin jumper that connects pins 4 to 7, 5 to 8 and 6 to 9 allows for direct in-circuit programming.

The other three pins are connected as follows: pin 1 is connected to Rx, pin 2 is connected to the Tx bus in the circuit, and pin 3 is routed to Vdd. Adding a jumper that connects pins 4 to 1, 5 to 2, and 6 to 3 allows the UART pins, Rx and Tx, to communicate with the PSoC and the main Tx/Rx bus. This setting is used in the normal operation of the module, JP2 header configurations are shown in Fig. 4.6.

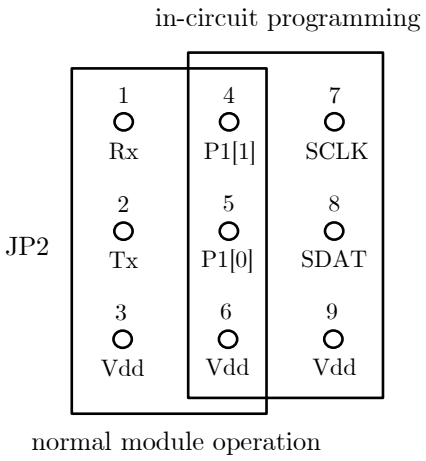


Fig. 4.6 JP2 header configurations for switching between in-circuit programming and normal module operation

This board enables switching between the input and output transducers using the jumper JP6. Pin 2 is connected to the output from switches (output from the desired transducer pair). Pin 3 is connected to the input connector on the left hand side, and pin 1 is connected to the output connector on the right side of the PCB. Explanatory labels of the connectors and possible jumper settings are printed on the PCB. The signal-multiplexing module is shown in Fig. 4.7.

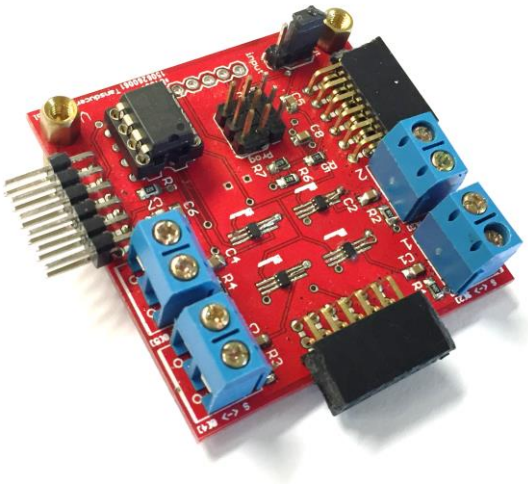


Fig. 4.7 Signal-multiplexing module

4.2.4 Frequency meter and data acquisition control

This module is designed around the Gainer PSoC development board, which was developed by Sparkfun Electronics [140]. The Gainer development board integrates the CY8C29466 part and an FTDI UART-to-USB converter for board programming and communication to a host PC. In addition, this board features one LED, a push button and an extra-regulated 3.3 V pin (Fig. 4.8).



Fig. 4.8 PSoC Gainer development board

This module measures the output frequency of an oscillating ultrasonic sensor using reliable clock references: two on-board TCXOs, operating at 10 and 20 MHz. The specifications of both TCXOs are shown in Table 4.2.

Table 4.2 Specifications and Prices of the Selected TCXOs

Part number	Frequency (MHz)	Tolerance (ppm)	Supply Voltage (V)	Price (£)
709-9240	10	±2.0	4.75 or 3.47	2.14
709-9379	20	±2.0	4.75 or 3.63	2.03

The module layout and construction are similar to those of modules one and two, particularly the board dimensions and the placement and use of the pin headers. A schematic diagram of the circuit is presented in Fig. 4.9.

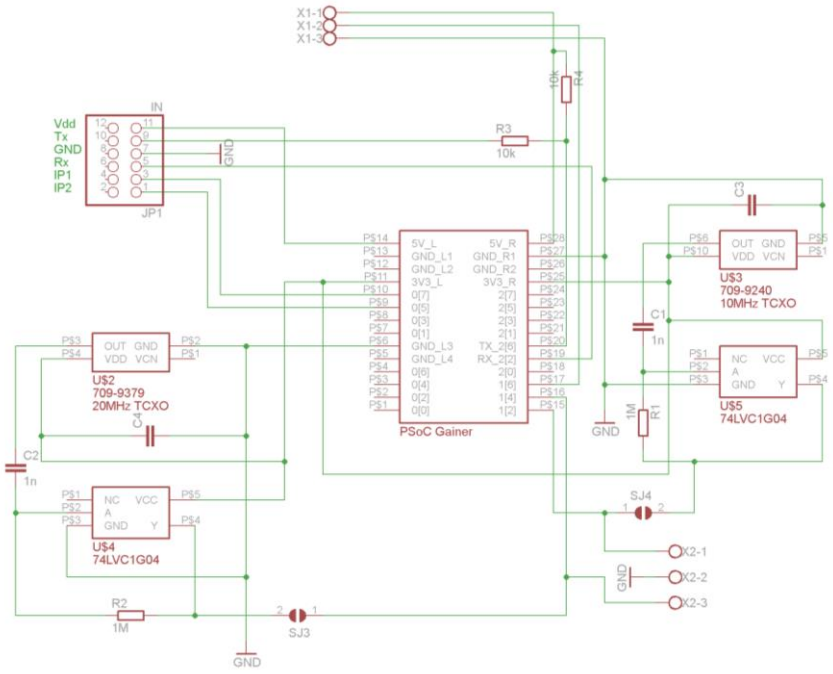


Fig. 4.9 Schematic diagram of the frequency meter module

The Gainer module has an on-board USB connector, and its Tx and Rx lines are connected to the UART bus of the modular system. Clock oscillators and digital inverters are powered by a 3.3 V source supplied by the Gainer module. In addition, a screw terminal for external clock management is added to provide an extra clock reference option for frequency measurements. On-board TCXOs are connected to pins P1[2] and P1[4]. The external clocking oscillator can be connected to the controller via pins P1[2], P1[4] and P1[6].

Pins P1[2] and P1[4] are configured to accept clock pulses from either an external clock or the on-board oscillators using two jumpers. Jumper SJ3 selects either the 20 MHz TCXO or the external clock reference; jumper SJ4 selects either the 10 MHz TCXO or the external clock reference. Pins P0[5] and P0[7] are configured as analogue inputs to accept signals from the output of the oscillating ultrasonic sensors from the pin header on the left side of the module.

Although enough unused pins can be connected directly to each of the five reference oscillators, using only three pins for clocking and one pin for analogue input will provide future cost reduction because an inexpensive single PSoC is used. Any type of oscillator from which a PSoC can be clocked could replace the existing on-board clock oscillators. The frequency meter module is shown in Fig. 4.10.

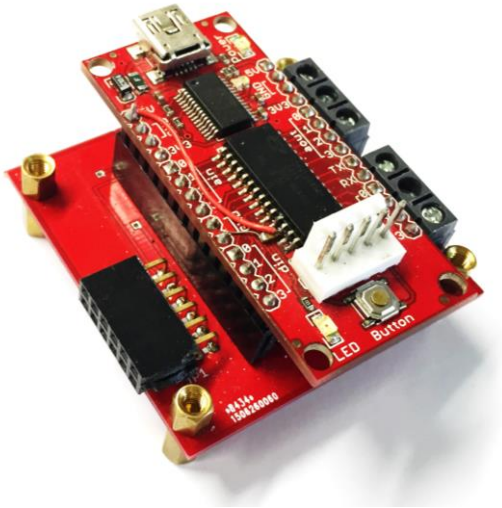


Fig. 4.10 The frequency meter module

4.2.5 Control and connection of modules

The objective of using the modular system is the simple and reliable operation of a UOTS device. The system's connections and modules are shown in Fig. 4.11.

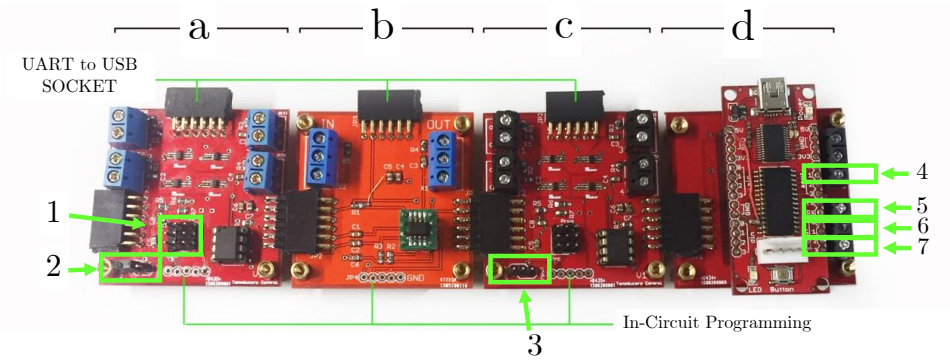


Fig. 4.11 Assembled modular system that features (a) signal input multiplexer, (b) ultrasonic driver, (c) output multiplexer and (d) frequency meter

As Fig. 4.11 shows, the boards are connected starting at (a); (c) represents the signal multiplexer; (b) is the ultrasonic driver; and (d) is the frequency meter device. The connections between the modules and the on-circuit programming control are shown in Table 4.3.

Table 4.3 Description of Connectors and Jumpers in the Modular System

Connector	Task
1	If 1,2 – 3,4 connected; programming mode. If 1,2 – 5,6 connected; circuit mode
2	If 1,2 connected; board set as input. If 2,3 connected; board set as output
3	If 1,2 connected; board set as input. If 2,3 connected; board set as output
4	If connected, on-board TCXO 10 MHz activated
5	If connected, on-board TCXO 20 MHz activated
6	If connected, external oscillator is connected
7	If connected, external oscillator is connected

4.3 Software development

4.3.1 Introduction

A broad objective of ultrasonic thermometry is the ability to select optimal operational parameters for ultrasonic oscillating sensors used in various applications. In order to study the system under different conditions, its parameters require alteration during operation. These parameters include gain, filter parameters, distance between transducers and so forth. The first two factors can be controlled programmatically during the run time. However, physical action is required to change the distance between the

transducers. In this section, firmware and software development, instruction communication, and the graphical user interface are discussed.

4.3.2 UART communications protocols

An important feature of PSoCs is their built-in analogue and digital user modules. The analogue and digital modules on the PSoC can be programmed during runtime operation. The programmability feature allows for controlling parameters by sending and receiving instructions using the UART communication protocols. The instructions sent from a PC will set the required configuration for the selected user module. A diagram of the modular design software control is shown in Fig. 4.12.

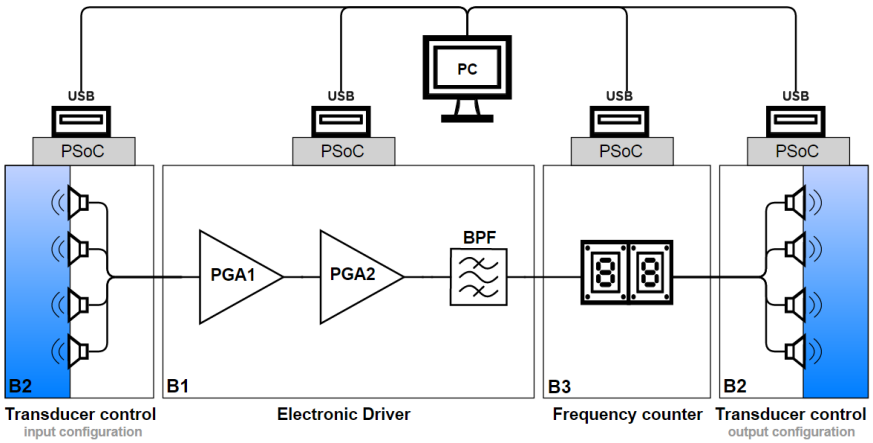


Fig. 4.12 Software control of modular system

4.3.3 Firmware for the electronic driver

The elements of this board include the first amplifier (PGA1) and the second amplifier (PGA2) and a BPF. This board accepts signals from the input transducer on board two (transducer selection) and transmits amplified and filtered output signals for the frequency measurements on board three as well as to the output transducer.

Regarding the PSoC firmware, a control code can be written in either C or assembly programming languages. However, the following discussion is based on programming in C because of its simplicity and the availability of supporting notes. The complete C codes used for controlling the boards in the modular system are presented in Appendix B.

First, the gain of each amplifier is controlled during the runtime. In order to set a new value of the PGA in a PSoC, the following function is used:

```
PGA_N_SetGain(byte);
```

where `N` is the number of the PGA, and `byte` represents the required gain setting. This setting can have 33 different values of gains ranging from 0.06 to 48. All possible settings of the gain are stored in an array, `G_gain`. The user selects the index of this array, and the gain is set when `SetGain` function is called. For example, `PGA_1_SetGain(G_gain[30])` sets the gain of PGA1 to 16. Current gain selection is stored in the variable `G1_index` for PGA1 or the `G2_index` for PGA2.

The following functions are used to control the amplifiers:

```
PGA_N_Stop();
```

```
PGA_N_Start(PGA_N_HIGHPOWER);
```

The first function is used to stop the PGA `N` from effectively opening the oscillating loop; the oscillations stop if this function is called. Stopping either the first or the second PGA leads to the same result. The second instruction is used to resume the operation of the PGA in the high power mode.

Controlling the BPF is a more complicated process. Because PSoC filters comprises switched capacitors, setting a specific filter response requires setting the appropriate values of the capacitors inside the microcontroller. Six capacitors must be controlled CA, CB, C1, C2, C3 and C4 (Fig. 4.13).

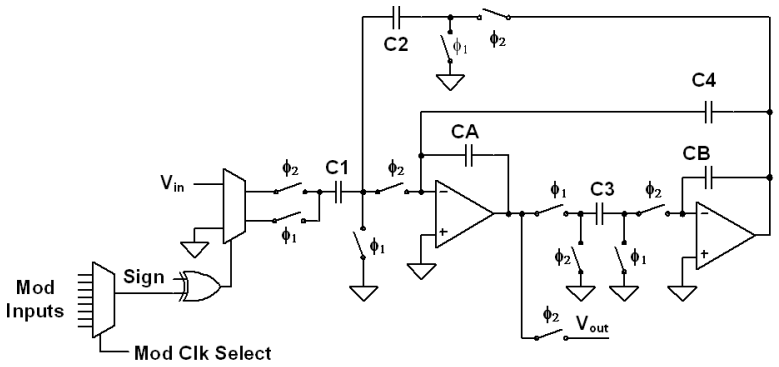


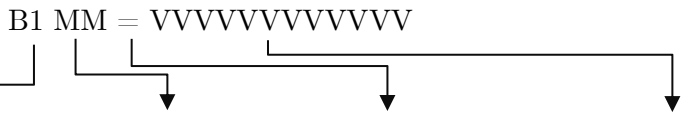
Fig. 4.13 The switched capacitor filter block [128]

Complex mathematical calculations are carried out to derive the values of the switched capacitors. After calculating these values, the following function is used to set the values of capacitors in the PSoC:

```
BPF2_1_SetCN(BPF_CN);
```

The current BPF parameters are recorded in variables `BPF_CN`, where `N` is the ID of the capacitor (A, B or 1-4) in both codes.

The commands transmitted to the PSoC using USB communication are in the form of a text string. The following instruction format is transmitted to the PSoC from a PC to set the parameters of board 1:



Field	Board ID	User module	Equal sign	Value
Number of digits	2	2	G1: 1 G2: 1 BF: 1 CO: Null ST: Null Value return: 1	G1: 2 G2: 2 BF: 12 CO: Null ST: Null Value return:1
Description	This field includes board ID number in the following format: B1: board 1 B2: board 2 etc..	This field selects the desired user module to be controlled as following: G1: PGA1 G2: PGA2 BF: BPF ST: stop both PGAs CO: start PGAs	Has no effect on sending/ receiving commands.	if MM = G1 or G2: two-digit integer values are used to choose the gain index from 0 to 33. if MM = BF: capacitor values are transmitted in the format of C1C2C3C4CACB, values of capacitors can be integers in the range of [0, 31] except for CA and CB [0, 32].

For example, `B1BF=010203040506` sets BPF parameters of the board 1 to C1 = 01, C2 = 02, C3 = 03, C4 = 04, CA = 05 and CB = 06. `B1ST` also stops the oscillations. To verify the setting of each parameter, the value field can be set to '?'. This command returns the recent parameter value of each user module as set from the PC. For example,

if the gain of the PGA2 is set to 16, `B1G2=?` returns '30', which is the index gain value of G = 16.

4.3.4 Sensor control firmware

The control of the sensor selection board is relatively simple. Two states (high and low) of specific pins can be set in order to select the required transducer. The connections between the pins and transducers as follows:

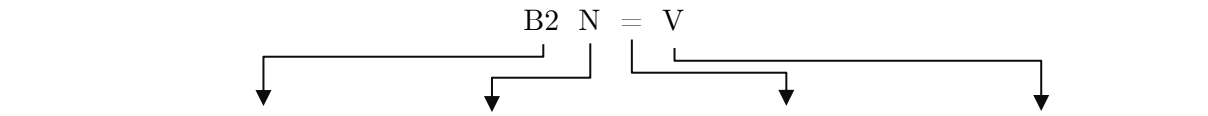
Transducer pair	PSoC Pin
1	P0[2]
2	P0[3]
3	P0[4]
4	P0[5]

In the control code, if the state of a pin is set to high, all the other pins automatically will be set to low. The following command is used to control the state of the pins:

```
PRT0DR |= 0x20; // Set P0[6], high

PRT0DR ^= 0x20; // Clear P0[6], low
```

The code transmitted to control the transducer selection is as follows:

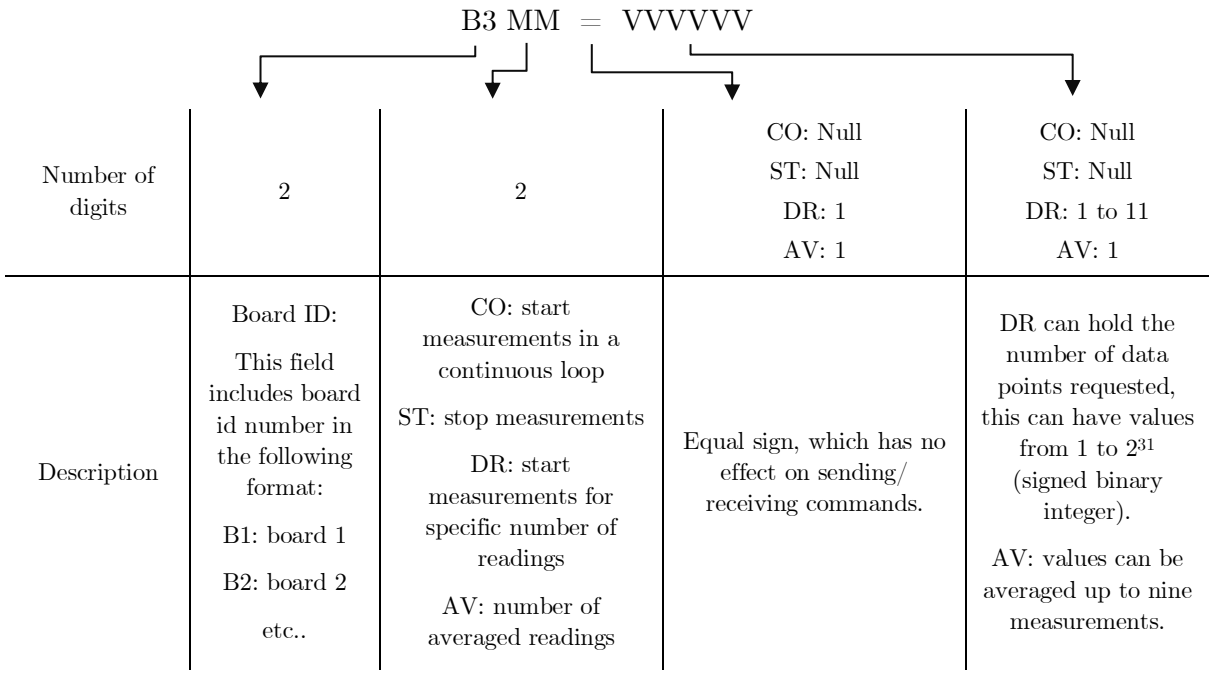


Number of digits	2	Set transducer: 1 Value return: Null	Set transducer: Null Value return: 1	Set transducer: Null Value return: 1
Description	Board ID: This field includes board id number in the following format: B1: board 1 B2: board 2 etc..	Transducer selection: N holds integer number of transducer from 1 to 4	Equal sign, which has no effect on sending/ receiving commands.	This value field is set to '?' to return the number of connected transducer.

For example, `B23` will connect ultrasonic pair '3' to the oscillating sensor system. In addition, `B2=?` will return 3, which is the ID of the connected transducer.

4.3.5 Frequency meter and data acquisition protocols

The control commands for this PSoC board include start/stop measurements, the number of readings to be averaged and the number of the recorded frequency measurements. Specifying the number of frequency measurements is useful to obtain a consistent number of measurements in several experiments for comparison. Frequency averaging is used to control the accuracy of the output frequency; however, averaging can be performed when raw data are broadcasted. The code transmitted to control this board is as follows:



Number of digits	2	2	CO: Null ST: Null DR: 1 AV: 1	CO: Null ST: Null DR: 1 to 11 AV: 1
Description	Board ID: This field includes board id number in the following format: B1: board 1 B2: board 2 etc..	CO: start measurements in a continuous loop ST: stop measurements DR: start measurements for specific number of readings AV: number of averaged readings	Equal sign, which has no effect on sending/ receiving commands.	DR can hold the number of data points requested, this can have values from 1 to 2^{31} (signed binary integer). AV: values can be averaged up to nine measurements.

For example, `B3CO` initialises the recording output frequency of the oscillating sensor system; `B3DR=1000` records 1000 frequency readings; `B3AV=5` averages five sequential readings.

4.3.6 Data verification and error management

Each module returns its board ID when a command is transmitted and successfully applied. In addition, error messages are sent when an incorrect instruction is received, such as when the required gain index exceeds 31. After the development of the graphical user interface, these error messages became obsolete because only appropriate values can be transmitted.

4.3.7 GUI of modular system

In order to simplify the process of transmitting the driver commands, a complete user interface for the modular system was developed. This interface performs mathematical calculations that otherwise require many instructions when only the PSoC processor is used. For example, the calculation of a single capacitor value for a BPF, such as C3, requires 18 mathematical operations. This number of operations will consume a significant amount of PSoC RAM, which leads to slower operation. Any PC can handle a similar amount of calculations almost instantly. In addition, one of the benefits of this interface is that it allows the user without any coding background to control several PSoC functionalities. A MATLAB graphical user interface (GUI) program was successfully developed and tested by verifying the transmitted feedback commands from individual modules after an instruction is broadcasted (Fig. 4.14).

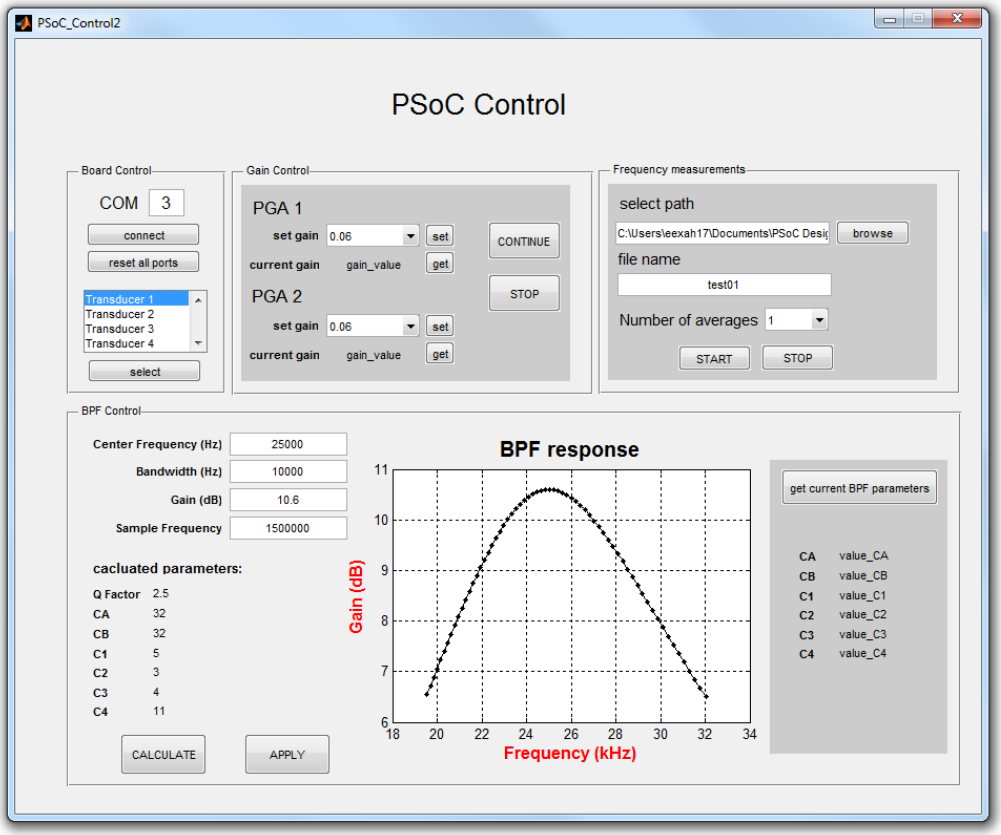


Fig. 4.14 MATLAB graphical user interface (GUI) program

This GUI consists of four main sections. The full description of each part and its controlling parameters are provided in Table 4.4.

Table 4.4 GUI Control of the Modular System

Section name	Description
Board and transducer control	This section allows selecting an appropriate port and transducer. Users can type the number of the USB port connected to the PC (this can be verified using "device manager" in the Windows operating system). The "connect" button will set the chosen pin as the main control circuit. Because all UART buses connected, any board in the modular system can be chosen. The "reset all ports" button will clear all previous port initialisations. This option is important when a serial port crashes or when the ports show as being used, which regularly occur. Below port control, the user can choose the transducer that is connected to the input and output of electronic driver via board 2.
Gain control	This section is responsible for setting the gain values of the cascaded PGA1 and PGA2. Gain can be selected using a drop-down menu that includes all possible values of gains in the PGA of a PSoC. Choosing a certain value will transmit a command that contains the index number of the gain, as discussed previously. This method prevents the PSoC code from crashing, because the user cannot transmit, for instance, an incorrect value of gain index. The "get" button returns the current value of the chosen PGA. Default amplification parameters: PGA1 = 48 PGA2 = 24
Frequency measurement and file management	This panel controls the frequency measurement and the file management. The first window allows the user to specify the folder directory. The second text box includes the file name. The next option is to choose the number of averaged ultrasound frequency readings from a drop-down menu (values from 1 to 9). The "START" button starts the frequency measurement and the button "STOP" stops it. When all boards are connected to the same bus, it is important to stop the frequency measurement data logging to avoid data interference with other instructions. MATLAB restrictions are applied in the "File name" and "File path" fields, such as spaces, symbols or etc.
Filter control	This section is responsible for BPF configurations. The user sets four values for complete BPF selection: centre frequency, bandwidth, gain and sample frequency. MATLAB calculates the Q factor and capacitor values using complex equations that are derived from PSoC BPF user module datasheet. The PSoC restrictions on these parameters, such as minimum and maximum centre frequency limits, are implemented when the user applies value outside these limits. Filter response and capacitor values are plotted when the "CALCULATE" button is selected. When the response is appropriate, the "APPLY" button transmits the capacitor values to the PSoC. On the right hand side, "get current BPF parameters" returns the current filter's switched capacitor values. This is used to verify current operational parameters. The default filter parameters applied for UOTS experiments are as follows: Centre frequency = 24.4 kHz Bandwidth = 10 kHz Gain = 10.6 dB Sample frequency = 1.5 MHz

4.4 Summary

An inexpensive and flexible modular UOTS driver system was successfully developed and tested. In UOTS experiments, its parameters were altered by using minimal physical and software modifications. In addition, the developed GUI made possible the full control of the PSoC parameters during runtime.

The hardware components of the developed boards consisted of three interconnected modules. The electronic driver operated as expected when specific gain or filter parameters were set. The signal multiplexer allowed for testing of four pairs of ultrasonic transducers.

Although the instructions were transmitted to all the modules, only the targeted module responded. The communication protocols were developed to accommodate the capabilities of all PSoC modules used. The modules were programmed on the boards by setting corresponding headers that switched between in-circuit programming and normal module operation. The PSoC was successful in responding quickly to all transmitted commands.

The frequency meter transmitted an accurate reading of the ultrasonic frequency by using appropriate frequency clock referencing discussed in Chapter 3. All four modules and their electronics were powered from a single USB port.

Although one board can be designed to accommodate the necessary footprint of all modules, the modular system allows for improved flexibility if additional modules are employed.

Chapter 5

Establishing the Operating Conditions for the Ultrasound Oscillating Sensor

5.1 Introduction

The operation of an ultrasonic oscillating system is considered as being highly nonlinear. The parameters of such a system can be extremely challenging to compute theoretically. An improved design of the UOTS system could result in a better performance and therefore a more accurate interpretation of ultrasonic frequency and temperature. To achieve high accuracy and enhance reliability, several factors should be examined carefully.

In order to study different variables within a system, the electronic elements should be simulated to resemble the actual model. The simulated model should feature every detail of the system, including the parasitic components if possible. In this chapter, the main objective of the first section is to show the simulation of an ultrasonic oscillating sensor, including the transmission line which represents the ultrasonic pathway.

The signal level is an important factor in determining the system performance. The second section of this chapter discusses the effect of the gain change on the reported ultrasonic frequency. A conclusion is drawn based on the simulated data as well as on the experimental results that supported the simulated outcomes. This analysis assesses the use of the AGC developed in Chapter 3 in controlling the signal amplitude level.

Because the system is operated via a 5V power supply, it can be fully operational using power supplied from a USB port. Ideally, the voltage from a conventional USB port should equal 5 V; however, depending on several factors, this voltage can fluctuate ±8% from its nominal value. Based on the recommendations made in this section, the required electronics, including the voltage regulator, can be integrated into the driver.

Filtering is an important tool in the design of oscillating sensor systems. It prevents the system from oscillating arbitrarily at various frequency resonances. Previous simulations showed that UOTS exhibited large frequency jumps, which led to an increased number of difficulties in data processing [110]. Hence, the effects of employing a BPF as well as a phase shifter in the system will be discussed.

A main factor in evaluating the quality performance of UOTS is the length of the ultrasonic pathway. Frequency scatter, the temperature–hysteresis relationship and the temperature/hysteresis sensitivity in various distances will be examined. Because the performances vary from one distance to another, some general observations in all evaluated distances also will be discussed.

5.2 Modelling of ultrasonic oscillating sensors

5.2.1 Introduction

The simulation of the behaviour of ultrasonic oscillating sensors is important to understand the sensor operation and the operating conditions of the design. A software

simulation was conducted in order to study UOTS under different conditions that would be inconvenient or difficult to observe experimentally (e.g., very high or very low temperatures to establish the range of operation and limitations of this device). It is challenging to simulate highly nonlinear oscillators that operate in a completely different manner than linear circuits.

5.2.2 Circuit configurations of the ultrasonic oscillating sensor

The simulated circuit of the oscillating ultrasonic sensor consists of three main parts: a model of the ultrasonic transducer element; a delay (transmission) line representing the propagation of ultrasonic waves in the medium and an amplifier that compensates for any energy losses.

5.2.3 Ultrasonic transducer model

An inexpensive narrowband air ultrasonic ceramic transducer, the 400ET180, was used in the experiments. Pairs of these ultrasonic transmitters and receivers operate at around 40 kHz, which is the resonance frequency of the piezoceramic disks that produce the waves. These devices are widely available and are used primarily for general-purpose range finding or short-range directional communications. In Fig. 5.1, the realistic transfer function of the ultrasonic transducer is represented as the elements R1, L1 and C1. The dynamic performance of a piezoelectric material relates to how it behaves under alternating stresses near the mechanical resonance. The combination of R1 with L1, C1, and RL in the equivalent circuit control the transducer's reactance which is a function of frequency. The values of these lumped components were calculated from the frequency response measured in a pair of submerged transducers.

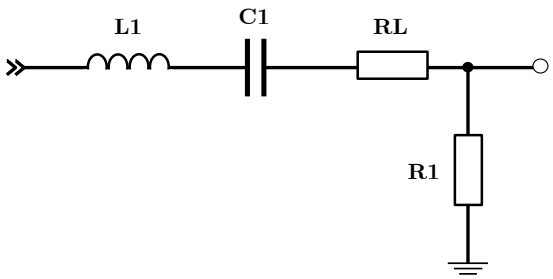


Fig. 5.1 A realistic model of ultrasonic transducer 400ET180

Fig. 5.2 (a) shows the frequency response for a 400ET180 pair operated at a temperature of around 25 °C within three temperature cycles and a distance of 100 mm between the transducers. Fig. 5.2 (b) shows the phase response of the same transducer pair.

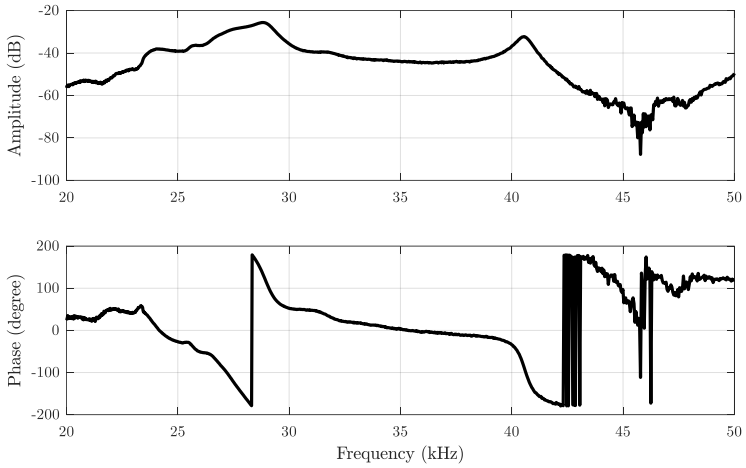


Fig. 5.2 Frequency and phase response of a pair of submerged ultrasonic transducers 400ET180

In order to calculate the equivalent parameters for this transducer model, it is necessary to obtain the resonance frequency and bandwidth values from the experimental data. These parameters were obtained by processing the experimental data presented in Fig. 5.2 (a); resonance frequency f_0 and the bandwidth can be calculated as follows:

$$BW = f_{H(3dB)} - f_{L(3dB)} = 25{,}183 - 23{,}746 = 1{,}437\ Hz$$

The reason for the relatively wide band area of about 1.44 kHz around the resonant frequency in Fig. 5.2 (a) is that a pair of ultrasonic sensors was used that do not have identical centre frequencies. To calculate the equivalent L and C values, the quality factor Q of the filter (transducer) should be calculated as shown below:

$$Q = \frac{f_0}{BW} \approx 17 \tag{5.1}$$

which also can be represented as follows:

$$Q = \frac{\omega_0 L}{R} \tag{5.2}$$

where R defines the quality factor of the considered RLC circuit shown in Fig. 5.1. Assuming that R = 5 Ω gives the following inductance value:

$$L = \frac{QR}{\omega_0} \approx 0.55\ mH \tag{5.3}$$

To calculate the capacitor value, the expression for the quality factor is given as:

$$Q = \frac{1}{R}\sqrt{\frac{L}{C}} \tag{5.4}$$

And then rearranged to find C:

$$C = \frac{L}{(QR)^2} \approx 77.6nF \tag{5.5}$$

Table 5.1 shows a list of the calculated L and C values for different R using equations (5.3) and (5.5).

Table 5.1 Different Values Calculated for L and C when R is Varied

R (Ω)	5	25	50	100	500	1k
L (mH)	0.55	2.77	5.54	11.1	55.4	111.2
C (nF)	76.5	15.3	7.65	3.82	0.77	0.39

All values presented in Table 5.1 were applied to a complete system simulation; R of 500 Ω led to the system that produced some oscillations. Therefore, RLC parameters of this ultrasonic transducer model were set as follows: R = 500 Ω, L = 55.4 mH & C = 0.77 nF.

Another model of 400ET180 was derived based on a textbook that describes piezoelectric bandwidth modifications for different types of transducers [141]. The circuit shown in Fig. 5.3 was used to obtain the equivalent circuit parameters.

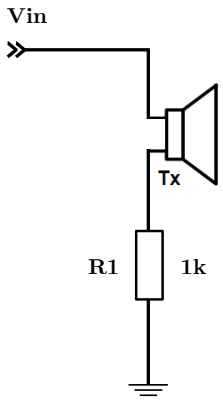


Fig. 5.3 The transmitter circuit used to derive parameters of the transducer model

This test circuit was connected to a signal generator by applying a 15 Vp-p sinusoidal signal to the transducer with a 1 kΩ resistor connected in series. Transducer SPM0204 was used as a receiver in this configuration; the results shown in Table 5.2 were corrected based on the frequency response of the receiver.

Table 5.2 Equivalent Circuit Parameters for the Transducer Model

Cp (nF)	Rs (kΩ)	Cs (nF)	Ls (mH)	Lc (mH)
3.05	1.95	0.10	160	5

The values shown in Table 5.2 refer to the parameters of the compensated piezoelectric equivalent circuit, which was derived from the Mason's equivalent circuit shown in Fig. 5.4.

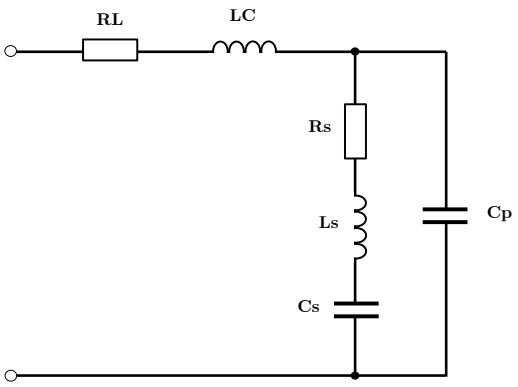


Fig. 5.4 Mason's circuit

The equivalent circuit parameters were derived when the transducers operated in air. This assumption was also valid when the transducer was submerged in water. In the

equivalent circuit, Rs represents the impedance against radiation, which had no impact on calculations. When a transducer operates, the mass of air movement in front of the transducer creates extra losses. In water, this resistor value will be slightly larger because of the greater density of the water.

5.2.4 Transmission line modelling

One of the most important parameters of an UOTS system is the distance between transducers, which can be tuned to achieve the most advantageous operating conditions. The optimal distance can be determined by comparing performances at different distances. The comparison criteria for the oscillator include the frequency scatter of the output ultrasonic frequency, the sensor sensitivity, the presence or absence of sudden frequency changes, and hysteresis. In order to simulate the performance at different distances, the time delay in the delay line component should be varied. Equation (5.6) can be used to calculate the time delays for various distances between the transducers. The delay for the distance between transducers of 0.1 m is calculated at around 60 µs:

$$Delay = \frac{distance\ between\ transducers}{speed\ of\ sound} = \frac{0.1\ \text{m}}{1500\ \text{m/s}} \approx 60\mu s \tag{5.6}$$

The speed of sound in water is dependent upon temperature. Using the speed of sound in equation (5.6), the time delay for a fixed distance between the transducers can be calculated based on the temperature of the medium (i.e., water in this case). Lubbers and Graaff's simplified equations were applied to describe the dependency of sound in pure water for a limited range of temperatures at room temperature, equation (5.7). This equation is valid for the temperature interval T = 15...35 °C at atmospheric pressure with a maximum error of 0.18 m/s [161]:

$$c = 1404.3 + 4.7T - 0.04T^2 \tag{5.7}$$

Equation (5.8) extends the range of validity to T = 10...40 °C at atmospheric pressure:

$$c = 1405.03 + 4.62T - 0.0383T^2 \tag{5.8}$$

In the simulation software, the transmission line model includes the characteristic impedance that needs to be matched at one or both ends of the line to avoid ringing. In

order to match this impedance, a resistor of same value (R3) should be added, as shown in Fig. 5.5.

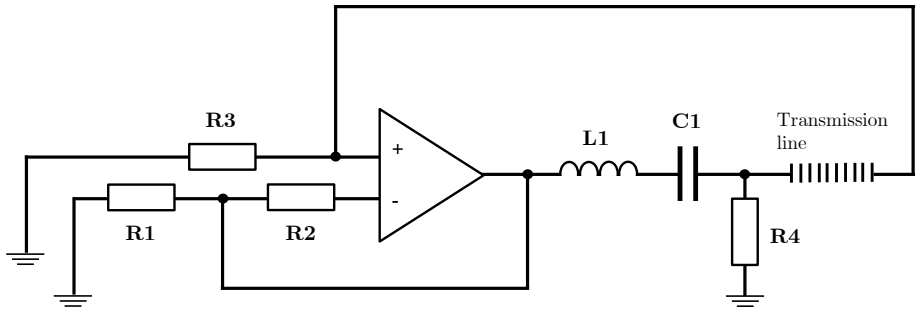


Fig. 5.5 A complete simulation model system of an ultrasonic oscillating sensor

5.2.5 An improved model for the piezoelectric transducers

Another approach to simulating ultrasonic oscillating sensors is based on the use of a piezoelectric transducer model that was developed by V. I. Kubov [142]. This model allows for the simultaneous evaluation of the electric and acoustic characteristics of a complex piezoelectric system with an acoustic load. An electromechanical model of piezoelectric transducers was built based on Mason models. These models were developed and integrated using the LTSpice simulator. The piezoelectric element in these models connects two ports: one electrical and one acoustic. The acoustic port is defined as an infinite or finite medium. The model of a piezoelectric vibrator is based on lumped elements such as capacitors, inductors and current sources. Table 5.3 shows the structure and thicknesses of the acoustic part of the simulated piezoelectric transducer.

Table 5.3 Structure and Thicknesses of the Simulated Acoustic Part of the Model

Material	Air	Piezoelectric element (400ET180)	Aluminium (400ET180)	Water	Aluminium (400ER180)	Piezoelectric element (400ER180)	Air
Thickness	Infinite	0.34 µm	0.34 µm	0.1 m	0.34 µm	0.34 µm	Infinite

Fig. 5.6 shows the complete model of an ultrasonic oscillating sensor. The system includes two piezoelectric transducers that are separated by 100 mm of water.

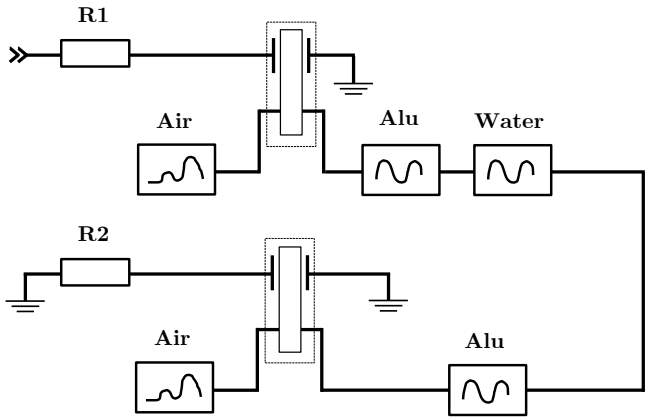


Fig. 5.6 Schematic diagram of a complete ultrasonic oscillating sensor system with simulation models of both piezoelectric transducers

This model was initially developed and verified for high-energy, high-frequency pulse-echo operation. In this research; which uses low frequency, the results in the UOTS system were inaccurate. An AC analysis was performed. The results of this simulation showed that the modelled ultrasonic sensor frequency varied in the expected range with resonances around 20...25 kHz. However, the output signal was heavily attenuated. For this reason, no conclusions could be derived from this set of simulations.

5.3 Gain change effect on ultrasonic operation

5.3.1 Introduction

As discussed in section 2.4.2, the oscillating ultrasonic sensor functions if and only if the energy conversion and propagation losses in the signal loop are fully compensated by an amplifier. In order to achieve stable operation, a suitable gain range should be selected, in which the overall gain of the signal that oscillates in the loop is greater than unity. Therefore, different amplifications must be tested to evaluate a large range of gains in order to determine the most suitable region [95].

Earlier oscillating sensor designs included a fixed gain amplifier that was built using one or two amplifiers with digital potentiometers at the input and output, which allowed for variation in the overall gain [61, 91].

5.3.2 The effects of gain change on ultrasonic oscillating sensor

The version of the PSoC device that was selected contained up to four PGAs with a wide range of available discrete gain settings. Each PGA provided up to 33 different values of gain from 0.08 to 48. By routing two PGAs internally in cascade, 33×33 different values were tested to check the stability of the output frequency. Experiments were conducted to monitor the output frequency of the UOTS with a pathway of around 50 mm and an amplifier that featured two cascaded PGAs and a BPF (Fig. 5.7). In the first stage G1, the gain was fixed to the value shown in the legend in Fig. 5.7. In the second stage G2, the gain was varied to obtain all of the curves presented.

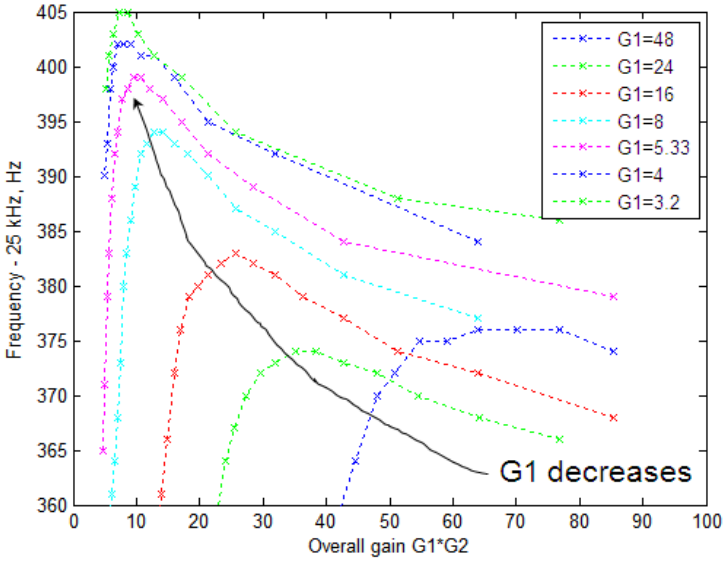


Fig. 5.7 Output frequency of an oscillating ultrasonic sensor, which was held at a constant temperature, depending on the overall gain in the signal loop and its composition [95]

The results showed that even in the same overall gain, the output frequency differed considerably depending on the gain composition by around ±10 Hz in the higher overall gains and even more in the lower gains. For each curve shown in Fig. 5.7, there was a maximum point at which the variations in the gain in the second stage affected the sensor output frequency to a small extent. For this reason, the gain composition of the amplifiers was selected at a maximum point that featured maximum flatness (G1 = 24 and the overall gain of around 55).

However, this selection could be done only once and at a single operating frequency. Temperature changes would affect both the ultrasound velocity and the gain of the

amplifiers to some extent, causing unwanted output frequency changes. Additionally, the ultrasonic transducers would age, thereby becoming less efficient in energy conversion, and in many situations the absorption of ultrasonic waves within the medium of interest could vary.

5.3.3 Simulation of the effects of the gain change on the ultrasound sensor output frequency

In the acoustic-electrical pathway, energy losses were compensated by an electronic amplifier in which the gain was varied within a substantial range. This gain could either be set permanently to achieve the least scatter of the output frequency or automatically controlled for the compensation of any signal loss changes. It was important to establish the gain range that resulted in the least scatter. This simulation demonstrated the feasibility of employing an AGC for the output signal. The gain was provided by using an OpAmp inverting amplifier configuration. In this case, the gain A_v is given by equation (5.9).

$$A_v = -\frac{R_2}{R_1} \tag{5.9}$$

Using LTSpice, the R2 in Fig. 5.5 was varied from 25 k to 2.4 MΩ; R1 was kept at 5 kΩ. This resulted in a range of gains from 5 to 480. This range was chosen to match the gain range that was obtained by cascading two PGAs. However, the system was unstable and unable to oscillate when the values of the amplification feedback resistor R2 were over 2.5 MΩ (i.e., gain around 500). Therefore, in this simulation, the gain was limited to 480. The simulation software can vary a parameter during simulation run time by setting programmed values or step parameters; this method was used to vary the value of R2 to control the overall gain. Some complications emerged when the LTSpice simulator was used to conduct an accurate FFT analysis. The graph shown in Fig. 5.8 demonstrates the frequency variations for the gains in the region from 5 to 480.

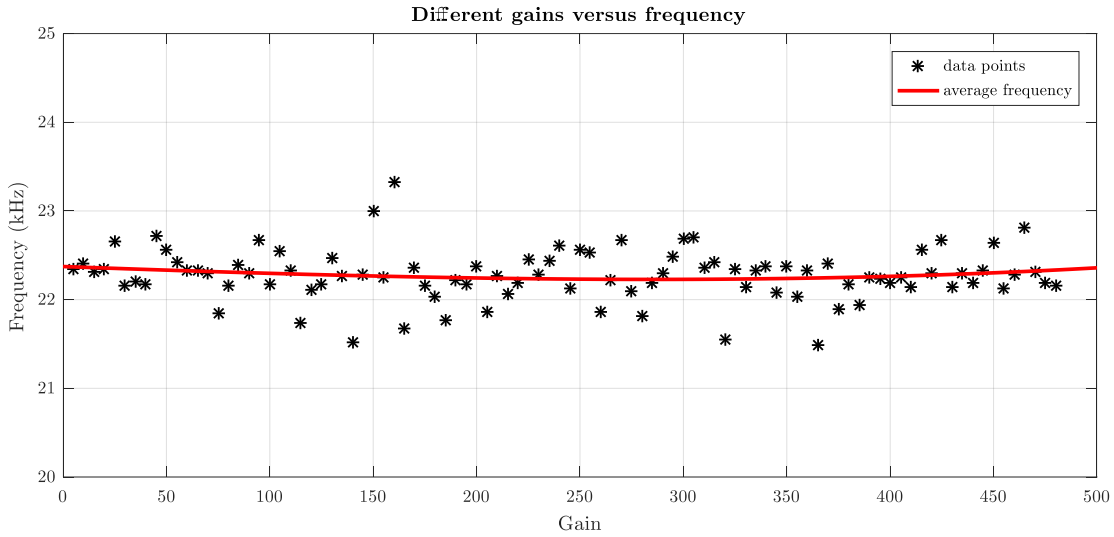


Fig. 5.8 Simulation results of output frequencies for various gains

Fig. 5.8 shows that the frequency oscillated at around the resonance frequency of 22 kHz, which verified the correct selection of the RLC model parameters. As mentioned earlier, there is a relatively large standard deviation in the simulated data points. The averaged curve was fitted to these data points for the better representation of the results. As shown in Fig. 5.8, the gains from 5 to 300 had a maximum variation of the output frequency of about 0.67% of the full frequency scale. However, the gain values over 300 exhibited larger variations of about 1.2% of the full frequency scale. Even small variations of 0.67% resulted in an output frequency change of about 150 Hz, which corresponded to a change in the measured temperature of 5–6 K, based on the frequency–temperature sensitivity obtained in several overnight measurements. This simulation indicated that gain changes could result in notable changes in the output frequency.

5.4 Supply voltage change impact

The PSoC-based ultrasonic driver is powered from a USB port, which nominally has a voltage of 5 V. When measured experimentally, this voltage may vary from 4.8 to 5 V, depending on several factors, such as the USB port circuits in different PCs. USB 2.0 specifications require that voltage stay within 4.4 to 5.25 V in low-power devices and from 4.75 to 5.25 V in high-power devices [143].

In this section, the effects of variations in the supply power voltage on the output ultrasonic frequency of UOTSs are discussed. The analysis of this effect is difficult to

conduct experimentally, as small temperature changes will result in a few ppm changes to the output frequency. In this simulation, the supply voltage was varied from 4.8 to 5 V in 2 mV steps under the same environmental conditions (Fig. 5.9).

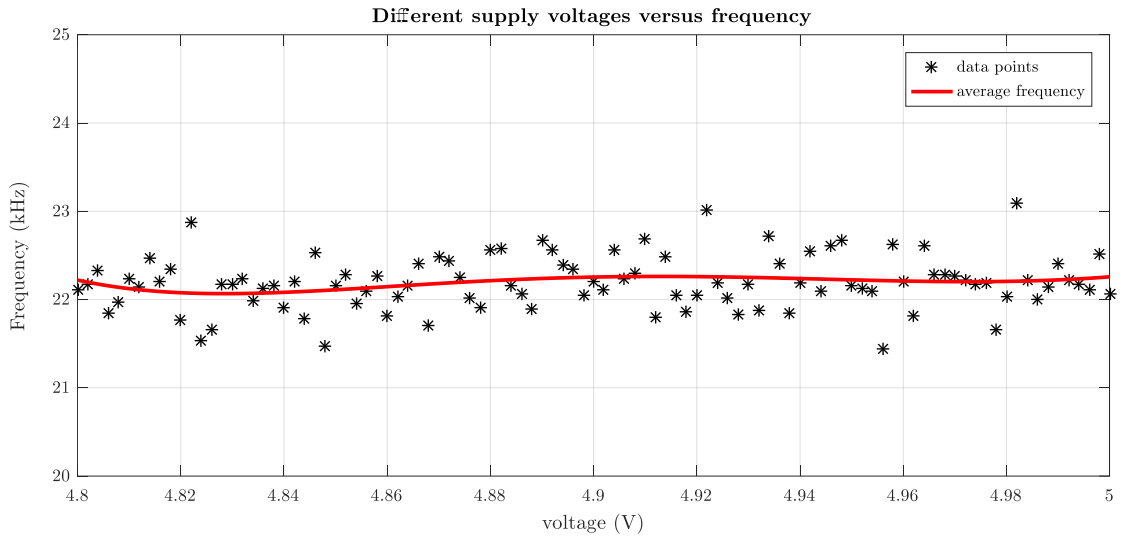


Fig. 5.9 Simulation results of frequency variations in different supply voltages

As shown in Fig. 5.9, the output ultrasonic frequency varied with the supply voltage by only 0.41% for the complete range of supply voltages. However, this variation seems to have fewer effects than the gain change did, as the supply voltage from USB was expected to remain constant during the complete set of measurements. Therefore, the inclusion of an in-circuit voltage regulator was unnecessary.

5.5 BPFs for oscillating ultrasonic sensors

5.5.1 Introduction

The inclusion of a BPF in the signal loop of an oscillating ultrasonic sensor is essential because ultrasonic transducers feature a multiple-resonance performance. This is frequently the case in low-cost, mass-produced transducers when they are securely attached to a supporting frame and/or are submersed.

Although the total cost of the BOM in this development is not overly high, the adoption of specialised mixed-signal integrated circuits provides an opportunity to reduce costs further. PSoC devices include switched capacitor blocks that can be configured as various types of filters. They also allow for adjustments of the filter properties during the run

time. Due to the continuity nature of the UOTS signal, there was a concern that using the switched capacitor principle would break the signal loop continuity, thereby disabling the sustained oscillations. However, these BPFs have proven to be a viable low-cost option for implementing oscillating ultrasonic sensors, which on numerous occasions reliably operated for long periods [110].

5.5.2 Results and discussion

Several sets of BPF parameters were tested in overnight ultrasonic measurements. The first set of experiments focused on establishing the best operational filter bandwidth, where the centre frequency was fixed at 22.7 kHz for all experiments. This centre frequency was observed as the main resonance of the UOTS when the filter was absent from the signal loop. A summary of the results obtained from overnight measurements is shown in Table 5.4. To verify and ensure the repeatability of the results, each experiment was performed twice and was conducted during a period of 48 hours.

Table 5.4 Summary of Results of UOTS Measurements with a Fixed BPF Centre Frequency of 22.7 kHz

Bandwidth (kHz)	Sensitivity (Hz/K)	Temperature–frequency consistency	Number of frequency jumps in a 30-min window	Maximum hysteresis (K)
2.5	50	No consistency	N/A	N/A
5	74	Moderate	7	1.2
7.5	61	Good	5	1.5
10	55	Good	6	1.2

Table 5.4 shows that at low bandwidths, the temperature–frequency consistency was poor. The reason is that the signal started oscillating at frequencies greater or less than 22.7 kHz; a limited bandwidth reduces the likelihood of the signal being passed through the filter. This then attenuated the signal and amplified noise or oscillations at other unwanted resonances.

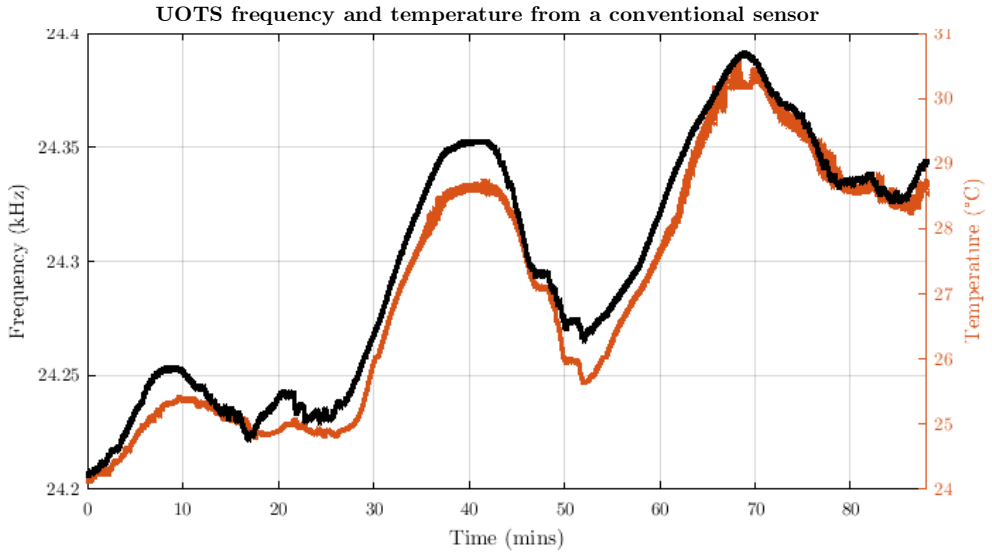
It was observed that the frequency–temperature sensitivity increased when the filter's bandwidth was decreased. However, this observation might not hold in a bandwidth of

2.5 kHz because it featured poor temperature–frequency consistency; hence, its sensitivity could not be determined with certainty. This occurred because narrower bandwidths feature a sharper phase response. It is also important to note that the sensitivity changed in bandwidths 5 and 7.5 kHz when different experiments were conducted. Further investigations were conducted by altering the filter centre frequency and fixing the bandwidth and even completely removing the filter.

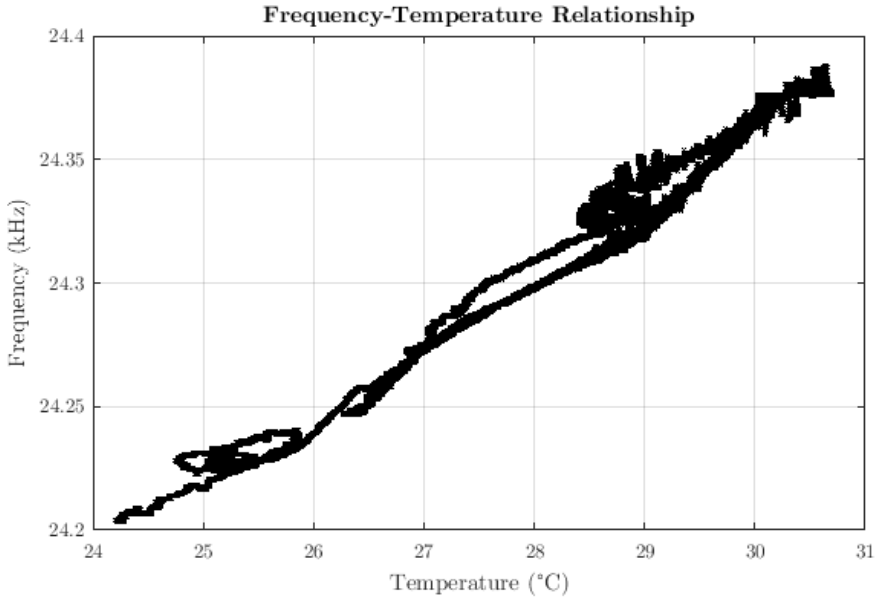
Table 5.5 Summary of Results of the UOTS Measurements with a Fixed BPF Bandwidth of 10 kHz

Filter centre frequency (kHz)	Sensitivity (Hz/K)	Temperature–frequency consistency	Number of frequency jumps in a 30-min window	Maximum hysteresis (K)
22.7	55	Good	6	1.4
24.4	54	Good	5	1.2
No filter	56	Good	11	1.5

Table 5.5 shows that the performance was almost the same when the filter centre frequency was varied. However, the sensitivity was improved in lower bandwidths, and higher bandwidths showed greater stability. Removing the filter was also an option to provide additional room to employ other user modules. Fig. 5.10 shows a typical operation of the UOTS system using a BPF with a centre frequency of 24.4 kHz.



(a) UOTS frequency and temperature from a conventional temperature sensor



(b) Temperature vs. frequency

Fig. 5.10 Temperature from conventional sensors and frequency measurements for ultrasonic oscillating sensor with a BPF (centre frequency 24.4 kHz, bandwidth of 10 kHz)

Removing the filter eliminates the selectivity of the operational resonance and the system oscillates at an arbitrary resonance usually within the first ultrasonic resonance available. When the filter was removed, the gain was set as high as possible to achieve stable operation.

Because the first resonance was used, employing an LPF was also possible; however, a BPF features the additional control of the resonance selection, which simplifies the process of selecting higher resonances if necessary.

5.6 Phase shift inclusion

The UOTS oscillates at the frequency where the maximum amplitude of the frequency response is found (i.e., when the phase response goes to zero). In some cases, this frequency cannot be achieved unless a phase shift is inserted into the system to ensure the overall zero phase shift that is required to sustain the oscillations.

In a previous research, a fully programmable PSoC-based phase-shifting circuit was successfully constructed [144]. The phase shift circuitry operated in conjunction with a BPF in order to obtain the accurate selection of the desired frequency. The phase-shifting system was developed using an amplifier, LPF, ADC and a switched capacitor block, all of which were integrated in a single device. In the worst case, the error in the set phase was measured at around $\pm 1^{\circ}$ for all the phases programmed.

The results of many experiments showed temperature–frequency consistency without the use of phase shift circuitry [110]. Instead of tuning the phase to obtain repeatable ultrasonic frequency readings, conventional temperature sensors, which are used as a temperature reference, can be calibrated to interpret the ultrasonic frequency readings.

5.7 Distance between transducers

5.7.1 Experimental setup

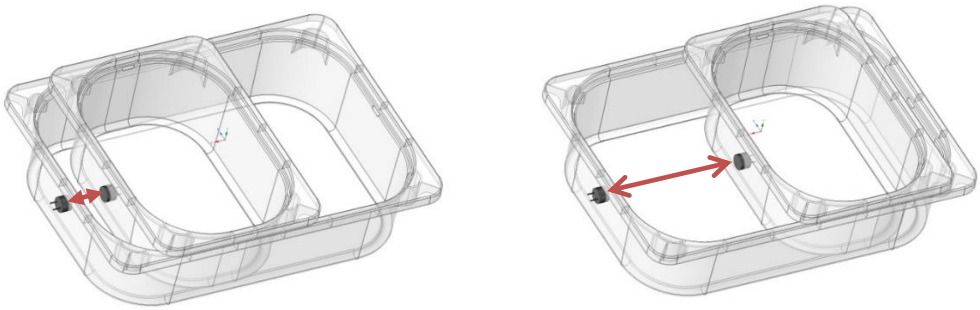
The experimental setup of distance measurements includes a pair of ultrasonic transducers with a physical arrangement that features an adjustable distance between them in addition to conventional temperature sensors for reference.

The proposed design consists of two boxes that act as a drawer in which the sensors are installed face to face. Some modifications to these boxes were made, including making two holes to accommodate the transducers. The distance was chosen based on the constraints shown in Table 5.6.

Table 5.6 Distance Limits Considerations for Test Rig Design Specifications

Item	Distance (mm)	
	Minimum	Maximum
Distance that ultrasonic sensors can operate in water without any disconnections	35	200
3D printing size limitation for available printers within the department	-	200

Based on the recommendations shown in Table 5.6, distances from 30 to 170 mm were chosen for the measurements. The experimental setup was designed accordingly. Fig. 5.11 shows the experimental setup.



(a) minimum distance (b) maximum distance

Fig. 5.11 SketchUp model of the experimental setup for UOTS distance measurements

The boxes were completely filled with water, leaving the back of the transducers to face air. Four conventional temperature sensors were submerged in water. This ultrasonic sensor pair was connected to the modular system that was previously developed and described in Chapter 4.

5.7.2 Results and discussion

In previous experiments where the distance between transducers was fixed at 100 mm, a BPF was used with specific parameters that were chosen to obtain the best operation at this distance. However, changing the distance caused the ultrasonic frequency to oscillate at different frequency ranges. A preliminary investigation was made by monitoring the ultrasonic frequency online, in which a BPF was employed and the distance was increased. The signal exhibited some discontinuities, especially in distances above 120 mm and below 70 mm.

In addition, experiments were conducted overnight in which the distance was set at 150 mm. The ultrasound started to oscillate at around 31 kHz for 14 hours. A sudden decrease in frequency to 26 kHz was observed and remained oscillating until the experiment was completed after 10 hours, the reason of this sudden drop in frequency is that the system being shifted from one mode of oscillation to another. Based on this result, the BPF was removed to allow ultrasonic sensors to oscillate freely without any attenuations or signal loss at any given distance.

To ensure repeatability, two overnight measurements using three different pairs of ultrasonic transducers were conducted for each distance. Changing sensors allowed the further study of the differences in the results, and it enhanced repeatability. A single experimental duration was set at 22 hours, which included two temperature cycles that were programmed in a thermostat oven, as shown in Fig. 5.12. A Carbolite PIF120 oven, which has an operating temperature ranging from 10 to 80 °C, was used to ensure that the testing environment was at a controlled temperature. The temperature cycles were in the range of 15 K, which proved adequate to study the ultrasound frequency response under different temperature environments. Because of the large specific heat capacity of water, each temperature cycle lasted four hours to ensure that the water reached a temperature close to 35 °C and cooled naturally to about 20 °C.

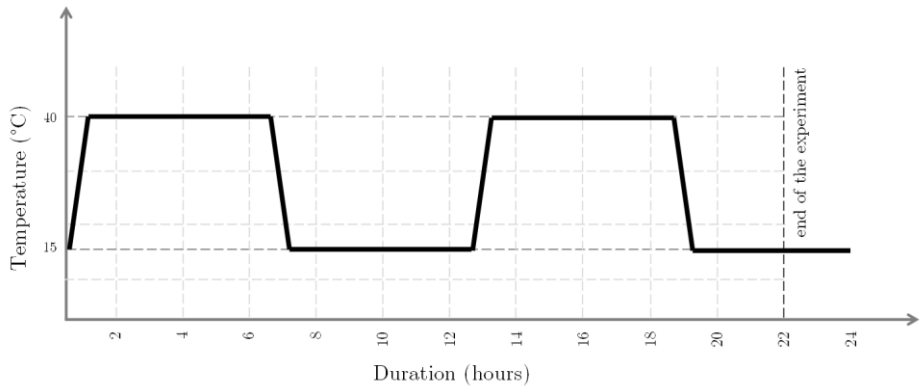


Fig. 5.12 The programmed temperature profile of thermostat for ultrasonic distance measurements

The following sections discuss the results of the analysis of the overnight UOTS measurements when the distance was changed. Each experiment lasted 22 hours and was performed in a temperature-controlled environment.

Generally, good consistency was established across the full operational range of ultrasonic oscillating sensors. In all the experiments conducted here, four important factors were examined:

- Frequency–temperature consistency: the visually observed measure of the overall frequency response compared to the temperature.
- Frequency scatter: the amount of ultrasonic frequency that deviates from the mean value, which is represented by the standard deviation in a 300-second interval.
- Average sensitivity: the frequency change in Hz per 1 K of the temperature change
- Temperature–frequency hysteresis: the maximum difference between the minimum and maximum frequencies recorded at the same temperature reading.

5.7.3 Ultrasonic frequency scatter analysis

The analysis of frequency scatter analysis is important for not only the system performance but also the assessment of the accuracy of the developed instrument. The values were calculated for a duration of 300 seconds with the temperature at constant levels (usually at the peak or trough of a temperature cycle). Fig. 5.13 shows the scatter behaviour in each distance tested. The numbers shown beside each measurement represent the relative scatter uncertainty to resonance frequency of 25 kHz in ppms.

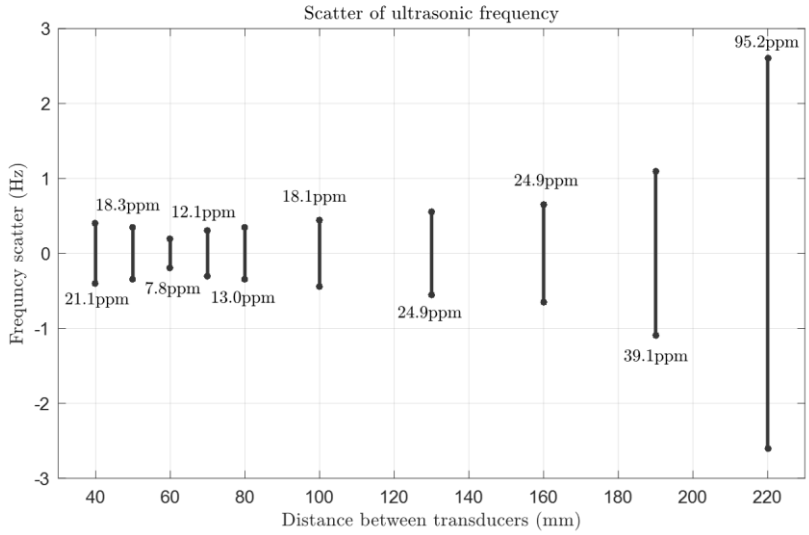


Fig. 5.13 Ultrasonic frequency scatter behaviour for various tested distances

Initial experiments were conducted with distances from 40 to 220 mm at a 30 mm step. A further analysis was conducted on additional three distances at 50, 60 and 80 mm, where the temperature–frequency responses appeared more consistent with less jumps in frequency.

Fig. 5.13 shows that the frequency scatter had values within the range ±0.1 to ±2.5 Hz. The best performance was obtained at the distance of 60 mm. In addition, Fig. 5.13 clearly shows seen that the frequency deviation gradually increased when the distance was increased, which was due to the attenuation of the signal when it was received because it travelled longer paths. Although this attenuation was compensated by the amplifier in the driver, it also had worse SNR, which was also amplified. Moreover, the signal picked greater numbers of reflections and EM waves that interfered with the signal.

The first oscillation mode was located at different frequency levels within the same band, which will be discussed in section 5.7.7. Therefore, the relative frequency error (i.e. frequency scatter) was calculated in order to determine the optimum frequency performance. For example, any given scatter value has a greater impact on the signal performance if the first mode frequency is changed from 19.9 to 28 kHz. Table 5.7 shows the relative frequency error in ppms for each distance measured.

Table 5.7 Frequency Deviations in Different Distances between Transducers

Distance (mm)	40	50	60	70	80	100	130	160	190	220
Frequency deviation (ppm)	21.1	18.3	7.8	12.1	13.0	18.1	24.9	24.9	39.1	95.2

Table 5.7 shows that the signal at the distance of around 60 mm had the least scatter and lowest frequency deviation (around 7.8 ppm). This deviation included the worst-case instrument error in frequency measurement of about 16 ppm for a 16-bit counter, which was established in Chapter 3.

5.7.4 Temperature–frequency sensitivity analysis

A previous experiment [61] showed that the frequency changed by 250 Hz per 1 K when the frequency oscillated at higher band of about 250 kHz. The amount of sensitivity (in addition to scatter and hysteresis) is dependent on the current mode at which the signal operates. In this experiment, the frequency oscillated at frequencies near 25 kHz, which

resulted in sensitivity values from 40 to 57 Hz/K. Sensitivity is an important factor to study the specifications of the UOTS system. The frequency differs in the single mode because of variations in the transducer phase response, which will be fully explained in section 5.7.7. The average values of sensitivity within the same oscillating mode are shown in Fig. 5.14.

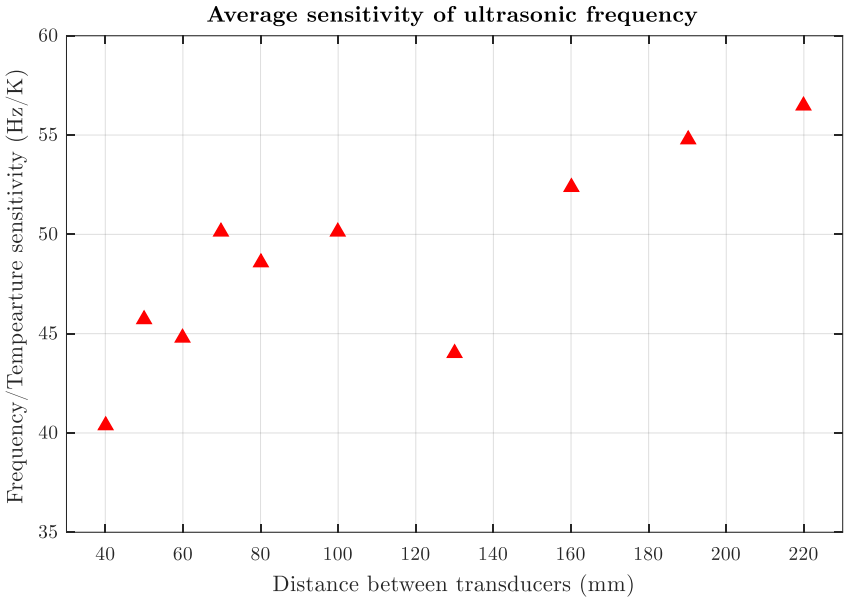


Fig. 5.14 Frequency/temperature sensitivity response for various tested distances

Fig. 5.14 shows that the best performance was achieved when the distance was increased above 160 mm because the system oscillated at a greater frequency. However, the sensitivity performance was limited by the scatter values.

5.7.5 Hysteresis analysis

Hysteresis needs to be considered in ultrasonic oscillating systems in which inexpensive narrowband ultrasonic transducers are used. The main reason for this effect is the deformation of piezoelectric material with temperature variations. These variations are very small, but they are not negligible because a very small change in piezoelectric thickness results in large differences in frequency response. Additional hysteresis analyses and methods proposed to compensate for hysteresis are introduced in Chapter 6.

Because the amount of hysteresis differs at the beginning and mid-way through a temperature cycle, average hysteresis values do not reflect the performance at a specific

distance. Typical minimum and maximum hysteresis values in different distances were recorded and presented in Fig. 5.15.

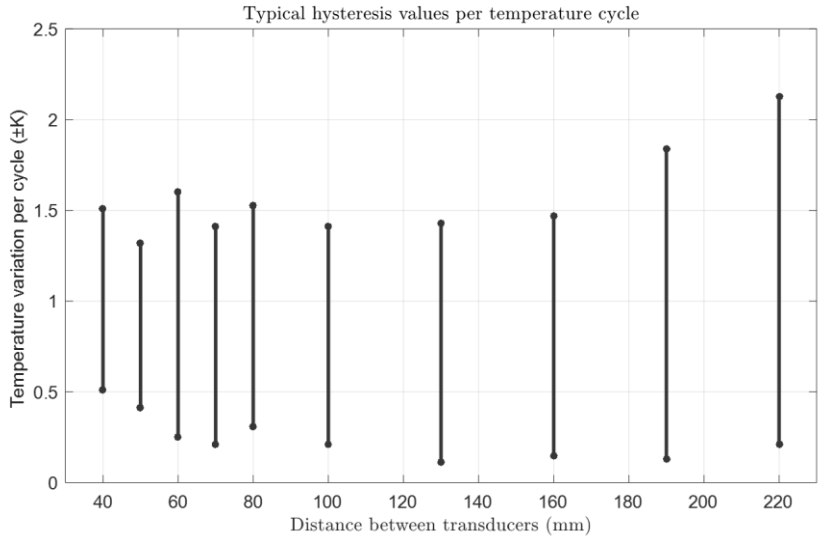


Fig. 5.15 Hysteresis values of various distances observed in UOTS

Fig. 5.15 shows that the hysteresis values were about the same in distances up to 160 mm. Distances above 160 mm showed larger hysteresis because the frequency oscillation bands were relatively wider. The results showed that frequencies from 40 to 50 mm had slightly better performance in their resonance frequencies, especially at 50 mm.

5.7.6 Overall comparison of different distances between transducers

Table 5.8 shows the comparison of the overall performance at different distances between transducers in terms of frequency–temperature consistency, frequency scatter, sensitivity and hysteresis per cycle.

Table 5.8 Hysteresis Scatter and Sensitivity of UOTS for Different Distances between Transducers

Distance between transducers (mm)	Frequency/temperature consistency	Frequency scatter (±Hz)	Sensitivity (Hz/K)	Hysteresis per cycle (±K)
40	good consistency, some discontinuities	0.40	40.4	0.51 – 1.51
50	good consistency	0.35	45.7	0.41 – 1.32
60	good consistency	0.20	44.8	0.25 – 1.60
70	good consistency	0.30	50.1	0.21 – 1.41
80	good consistency	0.35	48.6	0.31 – 1.53
100	good consistency	0.45	44.0	0.11 – 1.43
130	good consistency	0.55	52.4	0.15 – 1.47
160	moderate consistency	0.65	54.8	0.13 – 1.84
190	moderate consistency, few jumps observed	1.10	56.5	0.21 – 2.13
220	Poor consistency	-	-	-

To illustrate the data presented in Table 5.8, a graph showing the parameter evaluation is provided in Fig. 5.16.

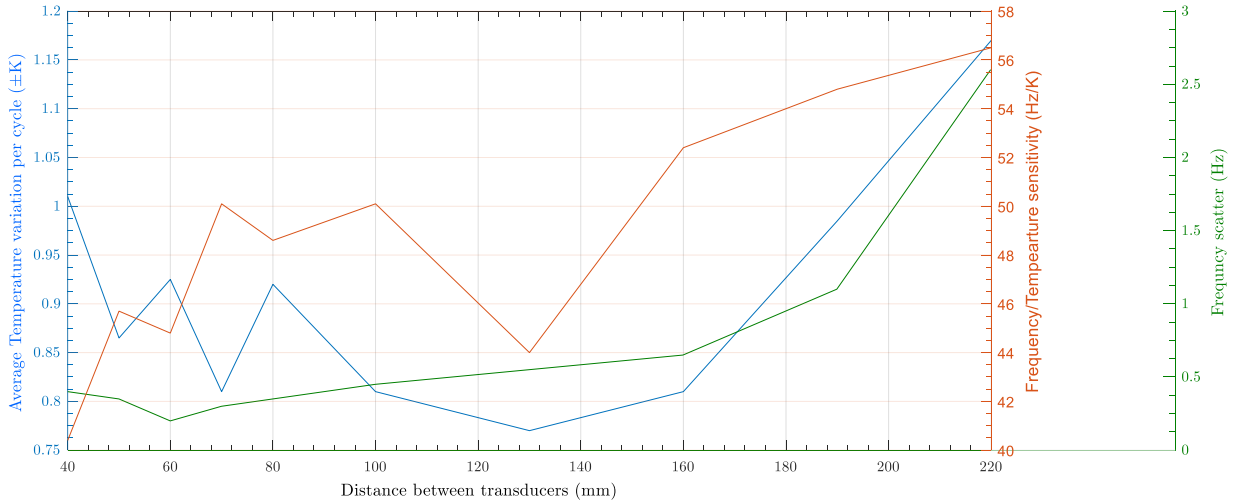


Fig. 5.16 Overall analysis of frequency scatter, hysteresis and sensitivity of distance measurements

A good ultrasonic oscillating sensor should feature high sensitivity, low hysteresis and low scatter. Fig. 5.16 shows that the scatter value was the lowest at distances of around 60 mm. The scatter value rapidly increased at distances above 160 mm. Sensitivity showed low performance in distances from 40 to 60 mm and at 130 mm. Distances above

160 mm had an excellent level of sensitivity but larger frequency scatter. Hysteresis performance was the lowest at 130 mm because of the very low sensitivity observed.

The results showed that the distance of 60 mm represented the best performance compared to other distances, followed by distances 70, 100 and 160 mm. Setting the distance at 60 mm allowed for the lower scatter of frequency and minimal hysteresis. However, sensitivity was not optimal compared to distances above 160 mm. Therefore, a distance of 60 mm between transducers will be set for the future development of an UOTS system.

5.7.7 General observations and discussion

The results showed some observations were common to all the distance experiments. These effects are discussed in this section.

Dependency on the transducer

Several pairs of ultrasonic transducers were used in overnight measurements. It was found that the results were heavily dependent on the sensors themselves. Different pairs of sensors produced different figures of hysteresis, scatter and operation with or without BPF. Moreover, different pair arrangements resulted in variations in the observed oscillating frequencies.

Expensive transducers (e.g., Panametrics NDT transducers) produce repeatable results in all transducer arrangements. However, the use of inexpensive transducers leads to the lack of repeatability of the measurements.

The variations in performance observed were due to imperfections in the manufacturing of this type of inexpensive narrowband transducer. Even a slight change in the piezoelectric plate resulted in a completely different performance. However, in some common operational parameters, the majority of sensors used showed similar performances under the same conditions. These performances included the gain value at which the sensors started to operate as well as some BPF configurations wherein all sensors were set for operation.

Previous state dependency

The operation of the transducers was also dependent on the previous arrangements by which the sensor operated. For example, in distance measurements, the system oscillated at 19.1, 25.5 and 24.8 kHz in distances of 50, 60 and 70 mm, respectively. If the distance was set at 60 mm and approached at 70 mm, the signal oscillated at frequencies around 25 kHz. In contrast, when the distance was set to 60 mm and approached at 50 mm, the system oscillated at frequencies within 20 kHz. This result occurred because there was an integer number of wave periods between the transducers for each distance set. However, when the distance was changed, the ultrasonic frequency oscillated at the previous number of periods.

Frequency–temperature cycles mismatching (hysteresis)

In all experiments, frequency–temperature hysteresis was found at different magnitudes. As a general observation, the rate of increase in frequency was higher by a factor of 1.3 compared to the rate of decrease. The effect of hysteresis and some solutions to overcome it are discussed in Chapter 6.

Frequency jumps

Relatively large frequency jumps occurred. The rate at which these jumps reoccurred was dependent on the distance between the transducers. The larger the distance, the greater the number of jumps that occurred. When the distance was increased, there were additional optional modes in which the system could operate (Fig. 5.17). Consequently the system could have several modes of frequency generation, which is shown in equation (5.10):

$$\lambda = \frac{c}{f}$$

$$d = n\lambda = n\frac{c}{f} \tag{5.10}$$

$$f_{generation} = \frac{nc}{d}$$

where d is the distance between transducers, c is the speed of sound waves in water, n is the integer mode number and λ is the wavelength.

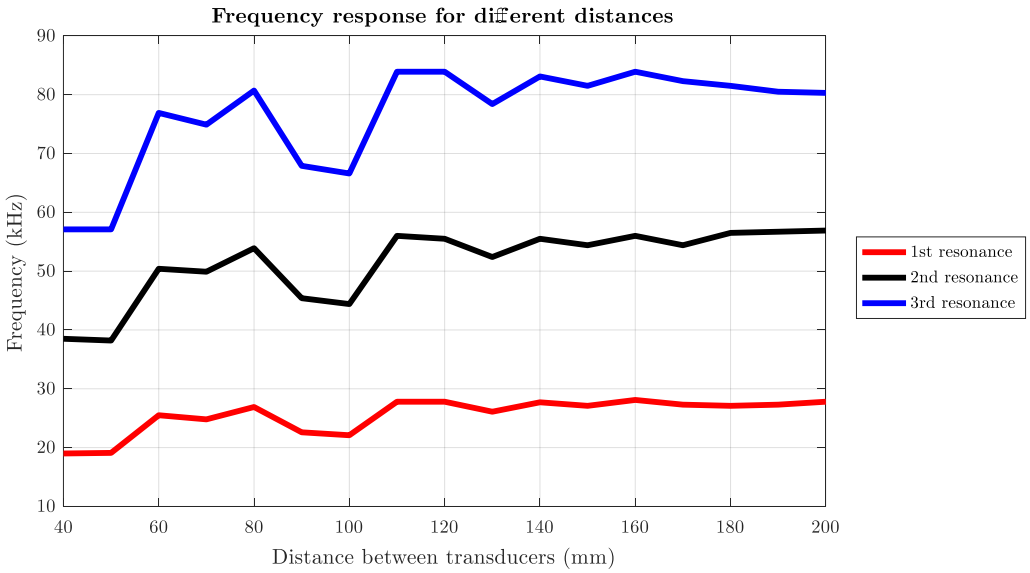
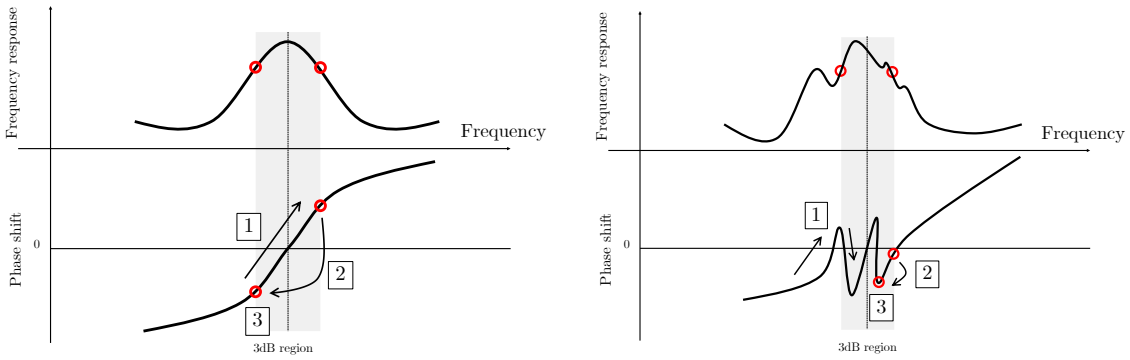


Fig. 5.17 Frequency resonances of various distances between transducers

Small jumps occurred within one mode for two reasons. Theoretically, in order to sustain oscillations, the ultrasonic wave should start propagating from a transducer and arrive at the receiver at the same level without any phase shift. This operation is described as standing waves. However, this situation is ideal when the phase shift associated with the electronic circuit is negligible. Therefore, n was slightly above or below an integer number. The inclusion of a BPF prevented the frequency from jumping from one mode to another. The frequency was shifted to the start of the mode of the frequency region.

The transducers had frequency responses at several resonances within the same mode (Fig. 5.2). In addition, several resonances affected sensitivity. Inner resonances had different phase shifts that allowed the frequency to oscillate at different sensitivities within a frequency band. These jumps occurred when the frequency reached the end or the start of a frequency oscillation band. In smaller scale jumps within the same mode, the signal shifted to the next oscillating inner band and continued oscillations at a sensitivity that corresponded to this band. Fig. 5.18 shows the comparison between the ideal and non-ideal frequencies and phase responses in the ultrasound oscillating sensor.



(a) ideal response

(b) non-ideal response

Fig. 5.18 The ideal and non-ideal frequencies and phase responses of the ultrasonic oscillating sensor

Fig. 5.18 demonstrates the process of the inner band frequency switching where in [1] the speed, hence frequency (i.e., temperature reading), increased until it reached point [2] where the frequency shifted back to the start of the inner frequency band [3]. This effect will be eliminated using data sensor fusion introduced in Chapter 6.

Initial calibration time

It was found that the sensors required some time to calibrate and start producing consistent results. This setting time was dependent on the previous distance setting (frequency band). If the frequency band was close to the next level, the time it took to stabilise was minimised. In general, it takes a transducer 20 to 60 seconds to calibrate fully. This issue was overcome by rapidly increasing the temperature at the beginning of a measurement. However, the final setup of the UOTS will feature a fixed distance; therefore, the setting time will be negligible.

5.8 Summary

This chapter examined the optimal operational parameters of a UOTS system, including gain level, supply voltage, filtering, phase shifting and distance between transducers.

Simulations were conducted in order to understand the sensor operation and optimise its design. The analysis of ultrasonic oscillator circuit was structured in three main parts: the transducer model, the delay line and the amplification stage. The delay line was important in simulating the transmission path of the ultrasound. The delay value was

dependent on the velocity of the ultrasound, which was heavily dependent on the temperature. An improved model of the piezoelectric transducer was used to improve the evaluation.

The initial experimental results showed that the ultrasonic frequency was dependent on the gain. Two cascaded amplifiers were used for this purpose. It was found that different gain compositions resulted in variations of ±10 Hz; the simulation results supported this observation. The gain chosen ensured maximum flatness and therefore stable frequency readings within that gain range. Although some difficulties were encountered in processing the data in the simulation software, the results showed that the frequencies varied according to different gain values.

Variations in the supply voltage resulted from the unstable power output of the USB port. These variations resulted in a negligible change in the ultrasonic frequencies observed in the simulations. Therefore, the addition of an in-circuit voltage regulator was found unnecessary.

The inclusion of a BPF in the signal loop of an oscillating ultrasonic sensor is essential when the ultrasonic transducers feature multiple resonances. This was verified experimentally by conducting several tests with and without a filter. The results without the filter showed oscillations at several resonances. This effect was partially eliminated by employing a BPF. Moreover, the inclusion of a phase shift was found to be inessential because a temperature reference was used and the required calibration was conducted.

The results showed that changing the distance between the transducers resulted in the oscillations at different frequency ranges. Each range showed a specific performance in terms of frequency–temperature consistency, frequency deviation, average sensitivity and amount of hysteresis across the full test sample. Overall, the results showed that the lowest hysteresis, the lowest scatter frequency and an acceptable frequency–temperature sensitivity were at the distance of 60 mm. The experiments with each distance were conducted twice in a temperature-controlled environment.

Some observations of the frequency responses were common to all experiments. The results were heavily dependent on the sensors themselves; different pairs of sensors produced different amounts of hysteresis. The operation of the transducers was also

dependent on the previous arrangements according to which the sensor had operated. Frequency–temperature hysteresis in different amounts was found in all the experiments. Large frequency jumps occurred; the rate of the reoccurrence of these jumps was dependent on the distance between the transducers. In addition, it was found that the sensors required time to stabilise and start producing consistent results. Table 5.9 summarises the outcomes of the UOTS system studied in this chapter.

Table 5.9 Outcomes of UOTS Parameters

Factor	Value
BPF operational range	20 to 32 kHz
BPF optimum centre frequency	26 kHz (optional)
BPF operational bandwidth	5 kHz or more
BPF optimum bandwidth	10 kHz
Phase shift	Not required
Gain range	10 upwards
Optimum gain value	55 - 70
Supply voltage	5 ± 0.25 V
Range of distance between transducers	20 to 250 mm
Optimum distance between transducers	60 mm

It is important to note that the experiments with the distance measurements took longer than expected because different pairs of sensors showed slightly different performances. Therefore, additional measurements were completed in order to ensure the repeatability and the reproducibility of the results.

Chapter 6

Thermal Hysteresis in Piezoelectric Transducers and Data Sensor Fusion Processing

6.1 Introduction

A limitation associated with the performance of UOTS systems is frequency–temperature hysteresis. Therefore, the elimination or reduction of hysteresis would result in ultrasonic frequency readings that are accurate and easy to calibrate.

In this chapter, the background information regarding hysteresis in piezoelectric materials will be introduced, and the presence of such phenomena will be explained. The data-

sensor fusion technique will be fully developed and discussed to examine hysteresis under different processing capabilities. UOTS data will be processed to prove that it features the faster determination of the inflection point, which is important in detecting thermal runaway in machinery.

The application of the data sensor fusion processing method on UOTSes is considered one of the main contributions of this project to the field of NDE in ultrasonic oscillating sensors.

6.2 Overview of hysteresis in piezoelectric devices

6.2.1 Introduction to the piezoelectric hysteresis literature

The literature refers to various hysteresis mechanisms for piezo materials, both proposed and discovered, including contamination redistribution, strain change, change in quartz, twinning and oscillator circuit hysteresis [145]. Some of these effects are well understood, and their impact has been reduced or eliminated by manufacturers of piezoelectric materials. However, some previous studies claimed that the causes of hysteresis in piezoelectric materials were not well understood [146].

Several previous studies focused on this area, such as designing the material at precise scale or employing feedback to compensate hysteresis changes. This previous research provided the basis for improving and developing improved oscillators that are capable of minimising, compensating and eliminating the effects of hysteresis.

Unfortunately, the research on hysteresis in piezoelectric materials is limited, and there is a notable lack of related research publications. Moreover, the majority of the research related to frequency–temperature hysteresis in piezoelectric devices was conducted prior to 1992 [145].

6.2.2 Piezoelectric materials

Piezoelectric materials are used in many different engineering applications. The main principle of operation is the transformation of energy from the mechanical form to the electrical form. These devices are used to measure a wide range of parameters, such as

displacement, when they are configured to operate as actuators or to measure temperature [145].

The definition of piezoelectric materials can be understood by considering an insulating material to which an electric field $E(V/m)$ is applied. This application results in the separation of charges with different polarities, which are represented as surface charges or electric polarisation $P(C/m^2)$. The electric field is related to the electric polarisation vector in the format shown in equation (6.1):

$$P = xE \tag{6.1}$$

where x is the array of dielectric susceptibility, $D\ (C/m^2)$, which represents the density of the total charge in the material surface when an electric field is applied.

In addition to the electric polarisation P of the material, vector x includes a term that represents the resultant charge by free space polarisation. This quantity is a product of the electric field and a scalar $\varepsilon_0 = 8.854 \times 10^{-12}\ (F/M)$, which is known as the dielectric permittivity of a vacuum, as shown in equation (6.2).

$$D = P + E.\varepsilon_0 \tag{6.2}$$

By substituting equation (6.1) into (6.2), a general form of dielectric displacement vector is derived, as shown in equation (6.3):

$$D = xE + E\varepsilon_0 = E(x + \varepsilon_0) \tag{6.3}$$

The term $(x + \varepsilon_0)$ is represented by the dielectric permittivity of a material, ε_i. The relative dielectric permittivity k can be given by $(\varepsilon_i/\varepsilon_0)$. In piezoelectric materials, this ratio is in a range between 10 and 10,000 [145].

6.2.3 Hysteresis in piezoelectric materials

The relationship between stress σ and strain ϵ in an elastic material is given by Hooke's law, which states that the stress and strain of a material have a linear relationship:

$$\sigma = -c\epsilon \tag{6.4}$$

where c is a multi-order tensor known as the elasticity tensor [46].

In a piezoelectric material, this elasticity tensor is replaced by the piezoelectric coefficient, d, which is given by a third rank tensor that can take positive or negative quantities. In most cases, the charge-versus-density relationship in a piezoelectric material exhibits hysteresis [145].

The fundamental principles of hysteresis in piezoelectric materials are complex because it occurs in various forms. Nonlinearity, the independency of quantity and the unrepeatability of results present theoretical and practical challenges to the analysis of hysteresis. Several physical principles govern hysteresis, including changes in mechanical strain. The developments in electric field applications have led to the increased interest in studying the effects of hysteresis [146].

6.2.4 Hysteresis mechanisms

6.2.4.1 Introduction

In this section, the possible causes of hysteresis in piezoelectric materials are discussed based on previous research that focused on piezoelectric materials and their properties.

6.2.4.2 Contamination redistribution

Some previous studies showed that contamination in the crystal formed when the oscillator operated for a few days was a cause of frequency hysteresis [45, 147]. The improper cleaning of the crystal or its connections can worsen the performance of hysteresis in a system [148]. This effect can be eliminated by setting the electrodes at active or at static levels [149].

6.2.4.3 Strain changes

Stress can cause frequency to shift in a resonator during operation. This stress consists of several sub-stresses, such as mounting stresses [150], bending effects, bonding stresses and electrode stresses [151, 152].

6.2.4.4 Changes in quartz

Change in quartz occur as stress is applied in each temperature cycle. This effect is considered the greatest cause of hysteresis [153]. It was found that perfect crystals are not affected by temperature cycling and hysteresis. These changes in quartz are caused

by surface defects, dislocations, impurities, inclusions and twins. Previous research focused on reducing or eliminating these effects [148].

6.2.4.5 Change of twins in a quartz plate

This phenomenon is similar to changes in the quartz effect; however, twinning is produced when high stresses are applied [154]. Change in twinning in a quartz plate are not considered major contributors to hysteresis because the structure of the majority of resonators allows for reducing these phenomena [155].

6.2.4.6 Oscillator circuit hysteresis

The electronic components in a system that contains crystal-based elements can be a potential cause of hysteresis. For example, it has been experimentally proven that a 14 pF resonator could produce 0.1 ppm thermal hysteresis if it were connected to a 20 pF load capacitor [156]. Inductors can exhibit the same effect as stress is applied to the winding of inductors [154]. The contributions of electronic parts to hysteresis can be significantly reduced or eliminated by the careful selection of components and proper circuit design [154].

6.2.5 Examples of hysteresis in piezoelectric materials

Two of the most common applications that affect piezoelectric hysteresis are piezoelectric actuators (PEA) and thermal retrace, which are discussed in this section.

6.2.5.1 Hysteresis in piezoelectric actuators

PEAs are fast-response devices that measure displacement using the piezoelectric elements controlled by electrical signals. The displacements can be measured to fine accuracies of a few nanometres. Fig. 6.1 shows a typical PEA operation. These devices are very popular in high-precision instruments, such as atomic microscopes because of their fast response, compact size, high operating bandwidth and frictionless contact [157, 158]. These devices were developed to replace the traditional tripod positioners in order to increase precision and to facilitate integration with existing microscopes [159].

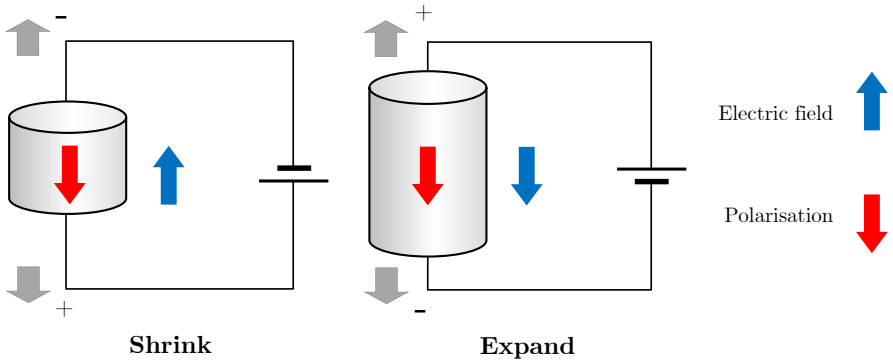


Fig. 6.1 A typical piezoelectric actuator and its principle of operation

A significant drawback of this type of actuator is that it exhibits a nonlinear response, which leads to inaccurate reproducibility [158]. Hysteresis is clearly observed when displacement (or stress) is measured when voltage is applied [159], as shown in Fig. 6.2.

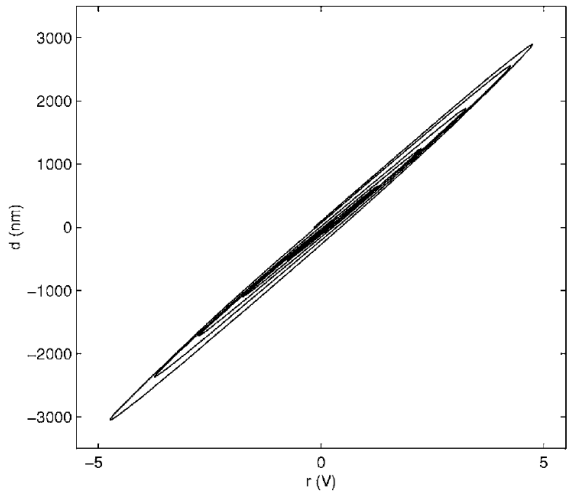


Fig. 6.2 Hysteresis effect observed in the relationship between an applied voltage and the resulting displacement of a piezoelectric tube scanner [159]

Several efforts have been made to reduce this effect, one of which was the development of a feed-forward control to compensate hysteresis. Some research suggested using complex and expensive methods, such as the integration of a displacement feedback control [158]. A recent study employed a charge amplifier method that significantly reduced hysteresis; however, it introduced additional complexity in the circuit design [157].

6.2.5.2 Thermal hysteresis in temperature–frequency relationship

Oscillators powered by crystal elements exhibit this phenomenon without exception [148]. The thermal hysteresis effect occurs when the temperature–frequency characteristics of a piezoelectric crystal oscillator fail to repeat in exactly the same value in each cycle, an example of which is shown in Fig. 6.3. Hysteresis is quantified by calculating the difference between the upper and lower frequency–temperature cycles.

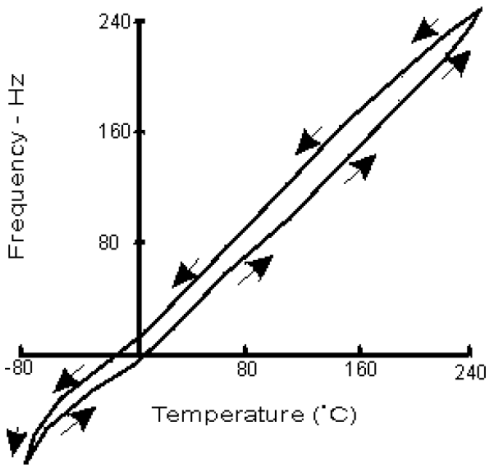


Fig. 6.3 A typical frequency–temperature hysteresis curve in oscillators that mainly operate using crystal elements [148]

This effect was first discovered in the late 1960s when a quartz thermometer was developed. Hysteresis was first reported in temperature cycles at ±220 °C. It was concluded that this effect could be considered one of the properties of quartz or the result of a defect in the structure of the crystal [160]. Subsequently, the same research group found this effect was the result of micro-contamination in the crystal [161].

Since the 1970s, several studies have proposed thermal compensated TCXOs. These oscillators were built based on the following research outcomes:

i. Hysteresis was dependent on the highest temperature a crystal can reach in each cycle [162].
ii. Maximum hysteresis was observed at the lowest crystal temperature of a cycle [163].
iii. It was reported that the highest hysteresis occurrence was observed within the first cycle of operation before the crystal reached a relatively repeatable hysteresis pattern [164].

iv. Some reports showed that frequency–temperature hysteresis was also dependent on the pressure of the crystal [165].

v. Subsequent research found that hysteresis at the lower limit of the hysteresis curve was slightly wider than at the upper one in oscillators with gold electrodes [166], which confirmed the outcomes in (ii).

vi. A crystal fault was considered the main cause of thermal hysteresis. In addition, this research found that the appropriate sectioning of the crystal significantly lowered hysteresis [167].

vii. Subsequent research found that lower temperatures did not always imply worse hysteresis [168], which contradicted the previous findings in (ii) and (v).

The majority of research related to thermal hysteresis in piezoelectric oscillators was published in or before the early 1990s. The research conducted during this period was based on the lack of information regarding temperature–frequency hysteresis in piezoelectric elements [148]. In addition, some textbooks related to oscillators either briefly mentioned this effect or ignored it completely. After this period, only a few studies focused on the phenomenon. The majority of the related research focused on the improvement of oscillators.

6.2.6 Ageing and hysteresis

Crystal ageing is the physical property in which the resultant frequency changes in quartz are function of operational time [148]. The several reasons for ageing include the thermal gradient effect, the pressure release effect, the change in the crystal polar plates mass and the change in the crystal structure [163]. A typical ageing profile of crystal resonators is shown in Fig. 6.4. Self-temperature compensated crystal oscillators (S-TCXOs) were developed to compensate or reduce this effect.

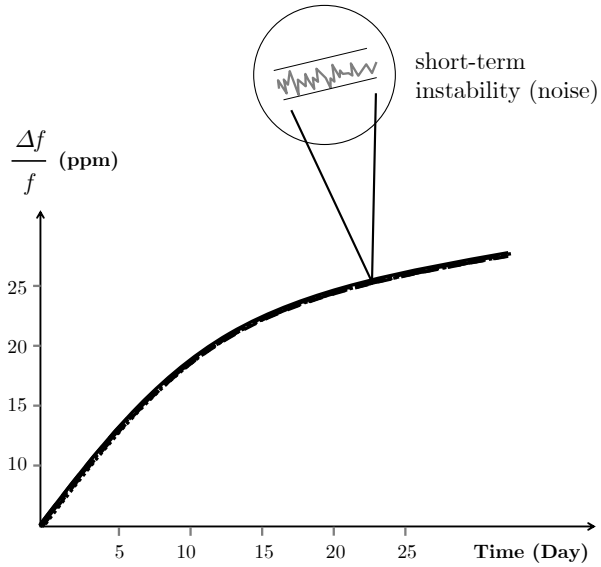


Fig. 6.4 Typical ageing profile of crystal resonators [156]

6.3 Overview of data sensor fusion

6.3.1 Introduction to sensor fusion

Sensor fusion is a data processing technique that combines data from several types of sensors in order to enhance the overall results. It aims at ensuring that the processed information is better than the information obtained from processing the data of each sensor individually. The advantages of applying sensor fusion to a set of heterogeneous or homogeneous sensors include increased robustness, reliability, extended spatial and temporal coverage, increased confidence, reduced ambiguity and uncertainty, robustness against interference and improved resolution [168].

6.3.2 Sensor fusion architectures

Because sensor fusion is heavily dependent on the application, it is highly unlikely that an architectural model could be derived to produce a solution that fit all applications. A fusion model that is frequently referred to in the literature is the fusion model developed by the US Joint Directors of Laboratories (JDL), which is the JDL fusion architecture. This model, which is widely used in military and commercial applications, is based on five interconnected data processing levels (Fig. 6.5).

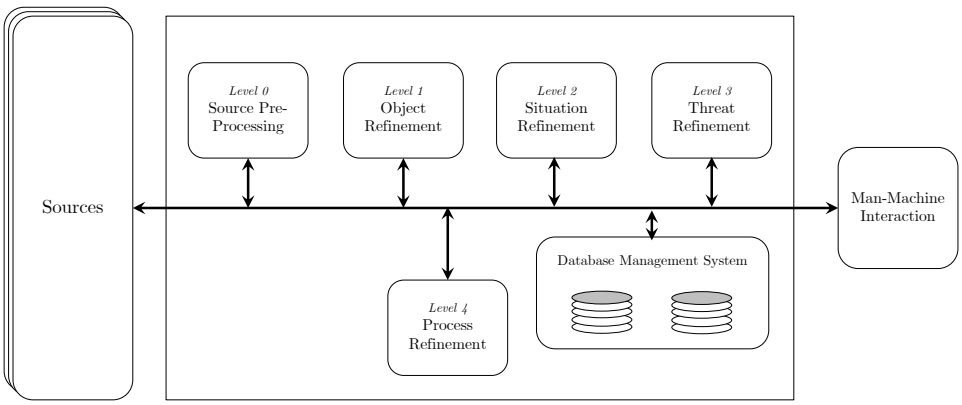


Fig. 6.5 The JDL sensor fusion architecture

The levels shown in Fig. 6.5 are not processed in a strict order, and they can be slightly rearranged based on the application requirements. The (sources) provide data and information about sensors, human interactions and data imported from databases. In Level 0 (source pre-processing), the processing load is reduced and data are allocated to a corresponding process. In Level 1 (object refinement), the data are aligned to current and predicted locations. In Level 2 (situation refinement), the relationship between objects and observed events is established. In Level 3 (threat refinement), further opportunities for the process are constructed. In Level 4 (process refinement), the real-time performance with the sensor is monitored, and additional sources are reallocated if needed. The database management system updates and adds additional processes to the fusion during the operation [169, 170].

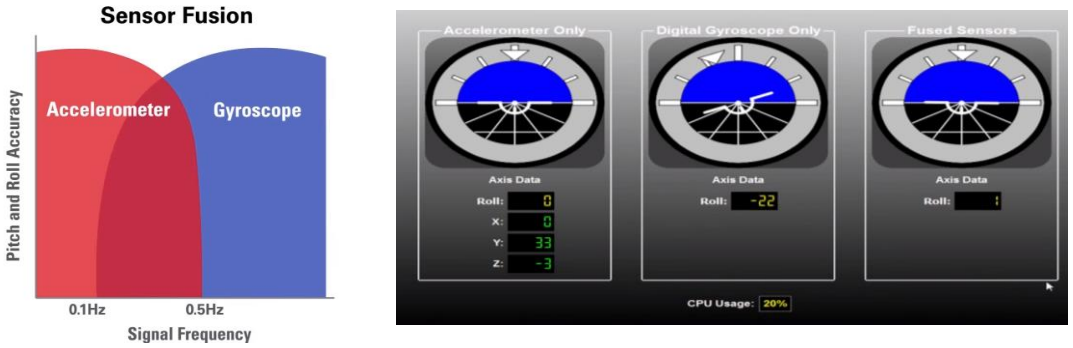
In addition to the JDL model, other architectures and models have been used in various fields, including the waterfall fusion process model, the Boyd model, the LAAS architecture and the omnibus model [171].

6.3.3 Examples of existing applications of sensor fusion

One application of data fusion is called dead reckoning. This technology is used in smartphones to enhance GPS positioning when the GPS signal is lost (e.g., position tracking inside tunnels). Dead reckoning tracks position changes in real time using the data from the smartphone's acceleration and magnetic field sensors.

Accelerometers can produce reliable absolute readings at low frequencies. In contrast, gyroscopes showed poor performances at lower frequencies because of accumulated drift,

but they showed more stable results at high frequencies [171]. Fig. 6.6 represents the process of dead reckoning; Fig. 6.6 (a) shows the roll accuracy response for an accelerometer and a gyroscope with their frequencies. Fig. 6.6 (b) represents the real time results extracted from the accelerometer and gyroscope sensors in a smartphone, as well as the fused sensor results.



(a) (b)

Fig. 6.6 Dead reckoning process: (a) Sensor fusion processing using accelerometer and gyroscope (b) Real time results extracted from a smartphone for accelerometer and gyroscope sensors as well as fused sensor results

Sensor fusion processing is used in various types of applications, such as robotics, industrial control (e.g., platform stabilisation) and human body position monitoring. The latter is widely used in gaming, the military, movement science and medical applications.

6.4 Sensor fusion in ultrasonic oscillating sensors

6.4.1 Why use sensor fusion?

In the previous experiments described in Chapter 5, a large amount of hysteresis was observed in the output frequencies of ultrasonic oscillating sensors and the temperatures measured using conventional temperature sensors. Several sets of results were obtained for the different parameters of UOTS in electronics, particularly the parameters of the BPF. Both UOTS and temperature data were recorded for hundreds of hours in order to find the best possible arrangements for reducing hysteresis. Hysteresis was also observed during the operation of a high-frequency ultrasonic TOF instrumentation [97] and during low-frequency ultrasonic tilt measurements [91].

In Chapter 3, a method was introduced to reduce the effects of hysteresis by employing a supervisory gain control. In an ultrasonic oscillating sensor system, the minimal overall gain of unity should be maintained for the system to oscillate. The initial investigation of hysteresis found that driving the signal to saturation across the supply voltage rails (i.e., gain above unity) would result in hysteresis. However, it also was found that this system resulted in a partially reduced frequency scatter response. In terms of hysteresis, no notable improvement or reduction in temperature–frequency hysteresis response was observed. Based on these results, further methods were investigated for the potential reduction and elimination of hysteresis.

In the experiments conducted in the present research, conventional temperature sensors were employed as temperature references. As discussed previously, because a nonlinear response was observed in the transducer response, the recorded ultrasonic frequencies varied from one experiment to another. The results showed that variations included initial oscillating points as well as slight differences in frequency–temperature sensitivity even in identical experiments. In addition, changes occurred during the experimental runtime. Because piezoelectric materials are subject to ageing, any temperature–frequency table is potentially invalid in the long run. The presence of hysteresis led to ambiguities and additional complications in converting UOTS readings to the temperature curve. In all experiments conducted, hysteresis existed in similar patterns, but it was very unpredictable. Therefore, based on these results, a process involving a single temperature calibration point is not possible because the UOTS frequency is dependent on the previous temperature reading.

Data sensor fusion processing was found to be a suitable solution because tackling various variables in this highly nonlinear operation is difficult. Because calibrated conventional temperature sensors were used as temperature references, no additional hardware amendments were required.

If sensor fusion is to be employed, it will compromise some potential advantages of UOTS measurements; the remaining and compromised advantages are shown in Table 6.1.

Table 6.1 List of the Remaining and Compromised Advantages of Sensor Fusion

Compromised Advantages	Remaining Advantages
The accuracy of fused temperature is equal or slightly better comparing to the accuracy of temperature sensor Dynamic differences between the two readings due to large thermal inertia of conventional sensors Reference readings are recorded from a single location, which does not represent a complete average of the ultrasonic pathway	Fast detection in temperature change or detection of the inflection point The resolution of fused readings is increased compared to the digitised output from conventional sensors

6.4.2 Acquisition and preliminary processing of the sensor data

The experiment was performed using the chamber developed in Chapter 5. The design consisted of an enclosed box in which were placed four conventional temperature sensors and a pair of ultrasonic transducers 60 mm apart. The water in the chamber was heated to around 3.5 K then cooled by 3 K in the duration of around 60 minutes. Each full set of temperature readings was communicated in around 6 s, whereas a single UOTS reading takes approximately 0.3 s to be processed and communicated. In the calibration of the raw temperature data discussed in Chapter 3, it was found that sensor 2 resulted in the minimal STD difference with the one computed for mean temperature. Because a single sensor was used in the fusion process, it was assumed that the temperature reading for the full interval of four sensors was represented by a single constant reading of sensor 2. Fig. 6.7 shows sensor 2 data in addition to different readings from other temperature sensors.

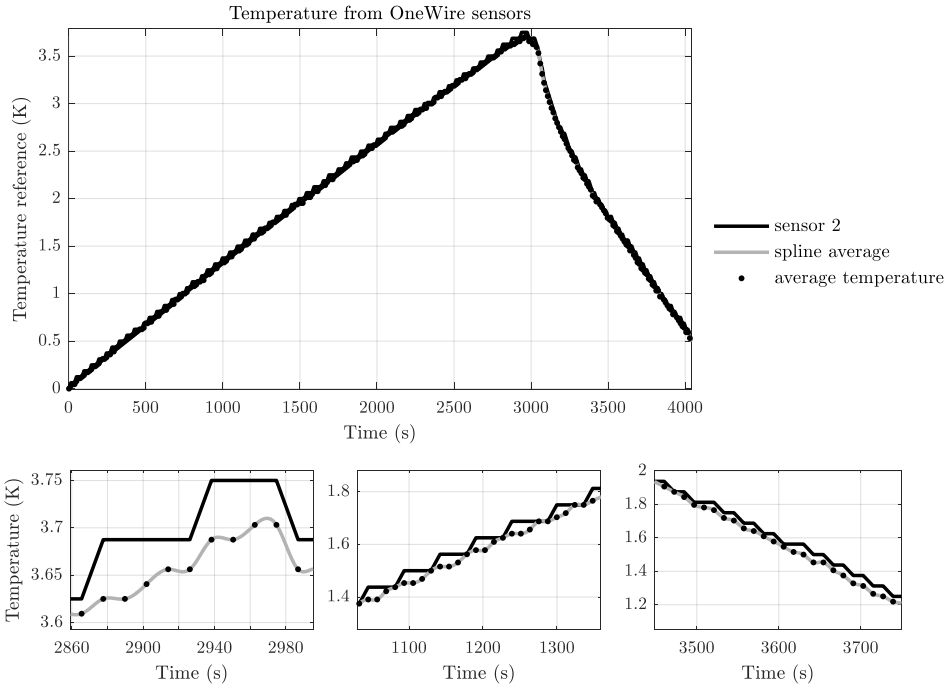


Fig. 6.7 Typical temperature profile from temperature sensors with calibration processing

The analysis of the UOTS frequency profiles showed that they featured large intermittent jumps from the smooth trend line and then returned to the trend over time. In addition, high scatter in some instances and a few single incorrect frequency readings across a full set of results were observed. Examples of these effects are shown in Fig. 6.8.

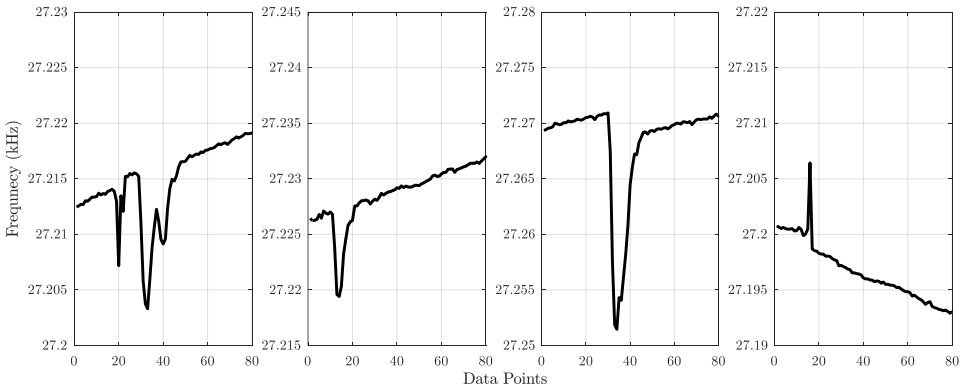


Fig. 6.8 Examples of frequency noise, scatter and jumps in UOTS operations

The magnitudes of the jumps were on the order of fractions of Hz to several Hz, which represents 4–30 ppm of the full frequency scale. These variations originated in measurements errors of 15.3 ppm, which were calculated in Chapter 3, in addition to the uncertainty associated with the clock reference used. Although this percentage was small,

it resulted in an error of 0.01-0.2 K considering that the UOTS sensitivity was approximately 27 Hz/K.

The application of a moving average filter to alter the frequency value yielded unreliable results especially in ultra-high resolution measurement applications. Therefore, it was essential to set a criterion that returns only the actual readings of ultrasonic frequency and discards incorrect readings. This was achieved by developing a custom algorithm that evaluates k number of frequency samples before and after a specific frequency reading. If a neighbouring point separated from f_0 by k samples is within the threshold, frequency value is passed; otherwise, frequency readings exceeding the threshold are discarded. Each neighbouring point has a different threshold based on its distance from the examined point. Values for thresholds were adjusted and evaluated visually accordingly. The threshold given for each frequency value were calculated using equation (6.5):

$$Threshold_k = f_0 \pm 0.33k \qquad k \in [-2,2] \tag{6.5}$$

where k is the number of samples apart from f_0, which is the frequency at point $k = 0$.

Because UOTS readings do not change rapidly from one reading to another, any occurrence of frequency jumps can be addressed and eliminated by using any appropriate signal processing technique. These boundaries were selected by trial and error to achieve balance between removing the outliers while retaining the valid data although some noise remained [172]. Based on equation (6.5), the accepted frequency readings that formed the filter are shown in Fig. 6.9.

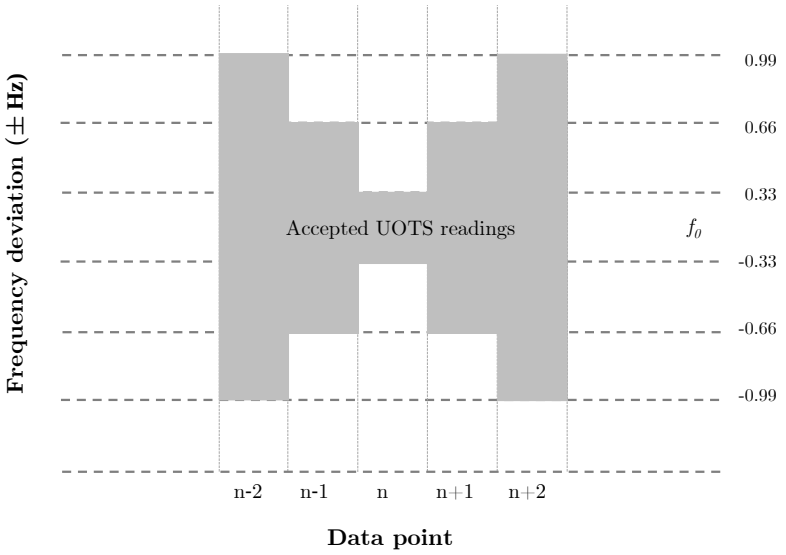


Fig. 6.9 Design of a customised filter for evaluating frequency data

The criteria for acceptable UOTS readings acceptance were applied to the experimental results, as shown in Fig. 6.10. By applying these criteria, around 78% of UOTS readings were retained, which limited the frequency scatter to around 0.2 Hz in six consecutive readings.

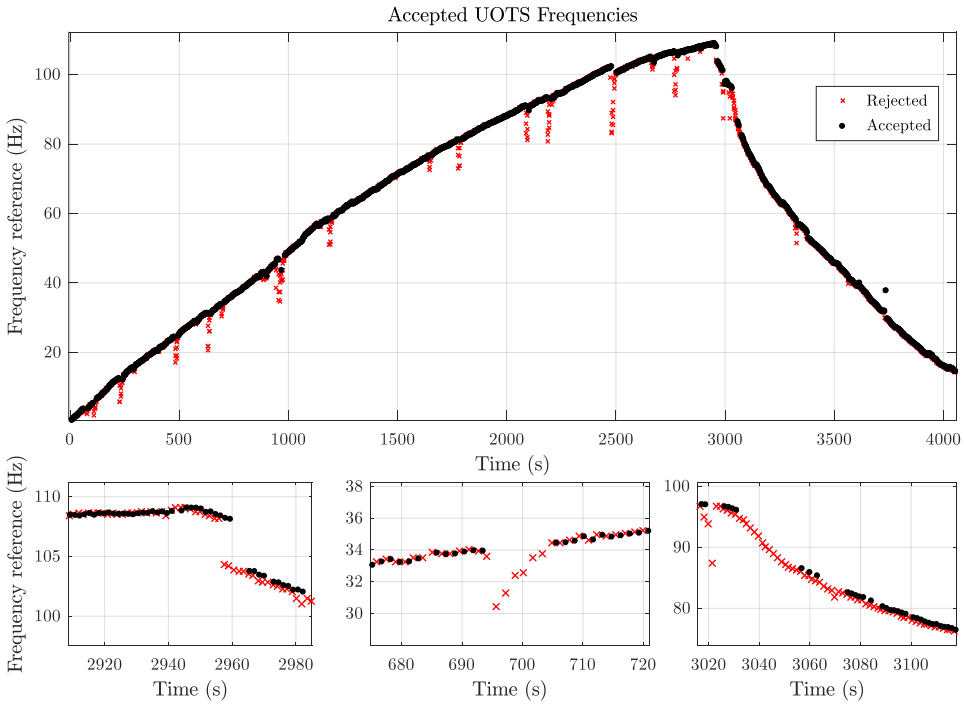


Fig. 6.10 Accepted and rejected UOTS readings based on the derived criteria

Fig. 6.10 shows a region around 3,000 s where the most of the frequency data were rejected although the frequency at this interval seemed adequate. Based on these results, a dynamic acceptance criterion was established by measuring the gradient, that is, the frequency change within small time intervals and then setting the acceptance criteria based on the value of a given interval. The dynamic threshold for a time interval τ is calculated as follows:

$$Threshold_{\tau} = f_0 \pm \sigma k \qquad k \in [-2,2] \tag{6.6}$$

where σ represents a constant that is directly proportional to the frequency change.

The constant σ was set by the calculating gradients of small time intervals, that is, 10 s intervals with a 5 s overlap. Fig. 6.11 shows the raw frequency data and both acceptance criteria—static and dynamic.

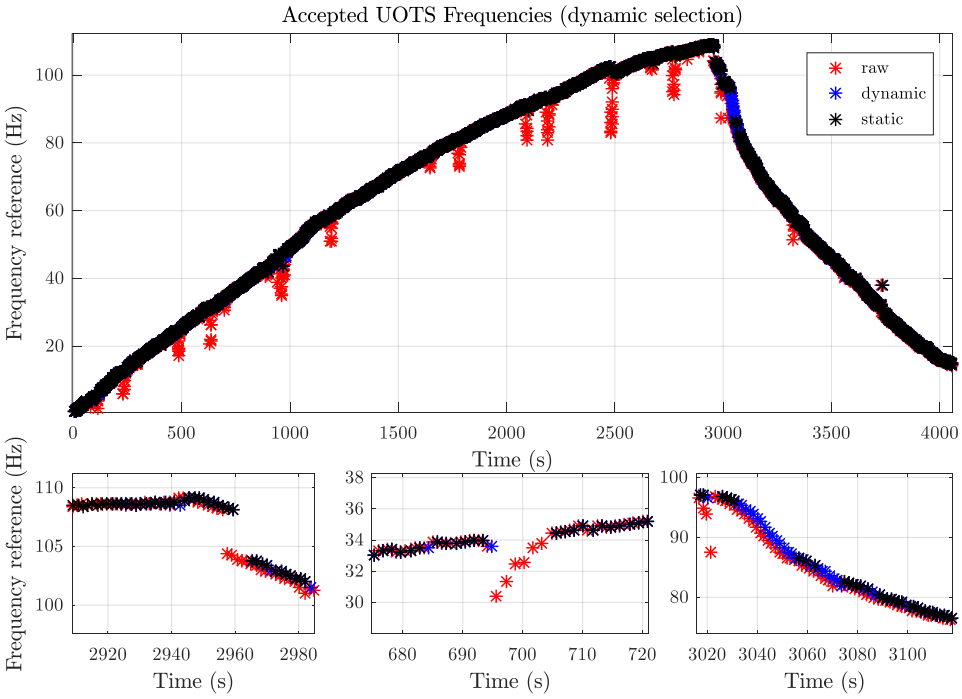


Fig. 6.11 Accepted and rejected UOTS readings based on the static and dynamic acceptance criteria

As Fig. 6.11 shows, additional accurate frequency readings were acceptable, particularly around the inflection point at 3,000 s. The application of the dynamic selection of frequency data allowed for accepting around 86% of the UOTS readings, which was an

improvement of 8% compared to the static frequency selection in which 78% of the readings were accepted.

6.4.3 Estimation of the inflection point

The fast detection of the inflection point is useful in the early detection of thermal runaway in machinery, as well as equipment failures and misuses. In this section, UOTS will be evaluated with regard to its ability to detect inflection points compared to conventional temperature sensors.

In the experiment, the external heater continued to heat the water until it was switched off. The thermal equilibrium level was reached quickly, and the response of the temperature sensors in this region was noisy. The inflection point was estimated by finding the intersection point of the long-term trends in the heating and cooling profiles.

During the heating period, the water gained a constant quantity of heat over the heating region. In cooling, the profile decreased exponentially following Newton's law of cooling [173]. The trend lines of the cooling and heating stages were computed as shown in Fig. 6.12.

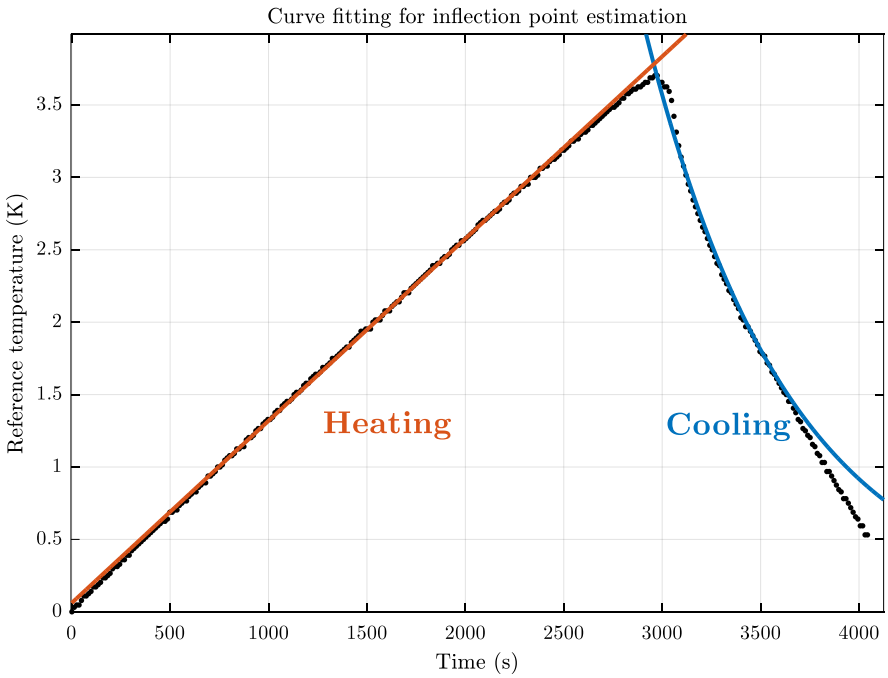


Fig. 6.12 Curves fittings of inflection point for heating and cooling regions of calibrated temperature data from conventional temperature sensors

Fig. 6.12 shows that the curves intersected at t = 2955 s, which represent fit calibrated readings from the both temperature sensors and UOTS. The parameters of both curves, which were derived from the MATLAB function fit, are shown in Table 6.2.

Table 6.2 Approximation of the Experimental Curves for the Temperature Data

	Heating	Cooling
Fitting interval (s)	496 to 2492	3097 to 3690
MATLAB Model	Linear Poly1	General Exp1
Model equation	$AT(t) = p1 * t + p2$	$AT(t) = a * e^{b*t}$
Coefficients [95% confidence bounds]	p1 = 0.001262 [0.001258, 0.001265] p2 = 0.06632 [0.06097, 0.07166]	a = 210.5 [201.5, 219.4] b = -0.001359 [-0.001372, -0.001347]

The computation of the response curves of the UOTS readings required additional considerations compared to processing the temperature curves. According to the Barkhausen criterion referred to in Chapter 3, the UOTS can function if and only if the energy conversion and propagation losses in the signal loop are fully compensated. Moreover, the system must have an overall phase shift of 360° in order to sustain oscillation, which is dependent on the ultrasound TOF (hence, ultrasonic velocity and temperature). The second condition is described as in (6.7).

$$\frac{l}{\lambda} + \phi = 2\pi n, \quad n \in N \tag{6.7}$$

where λ is the ultrasonic wavelength $= cf^{-1}$, c is the ultrasonic velocity and f is the UOTS frequency.

Assuming that the amplification gain, the distance between transducers and the phase shift are independent of the temperature and therefore UOTS frequency, λ, will remain constant regardless of any velocity changes. Therefore, if the temperature changes, ultrasonic velocity changes by Δc, resulting in a frequency change in Δf, which leads to the UOTS frequency reading derived by in (6.8):

$$\frac{c + \Delta c}{f + \Delta f} = \frac{c}{f}$$

$$\frac{\Delta c}{c} = \frac{\Delta f}{f} \Rightarrow \Delta f = \frac{f \Delta c}{c}$$

$$\Delta f = \frac{f}{c} \frac{dc}{dT} \Delta T \tag{6.8}$$

This derivation can be estimated by equations that determine sound velocity in water, including Grosso and Mader's fifth order polynomial approximation or Lubbers and Graaff's second order approximation shown in equation (6.9), which covers a narrower range of validity [102].

$$c(T) = 1404.3 + 4.7\,T - 0.04\,T^2$$

$$\frac{dc}{dT} = 4.7 - 0.08\,T \tag{6.9}$$

where T is the temperature in degrees Celsius.

The second order approximation is valid in this approximation because it features an uncertainty as low as 0.18 m/s in the temperature range between 15 and 35 °C at atmospheric pressure. Substituting equation (6.9) in (6.8) yields the temperature change with frequency in equation (6.10).

$$\Delta f = f \frac{4.7 - 0.08\,T}{1404.3 + 4.7\,T - 0.04\,T^2} \Delta T$$

$$\frac{\Delta T}{\Delta f} = \frac{1}{f} \frac{1404.3 + 4.7\,T - 0.04\,T^2}{4.7 - 0.08\,T} \tag{6.10}$$

Equation (6.10) represents the nonlinear relationship between temperature and frequency in UOTS, demonstrating that its sensitivity is heavily dependent on the ambient temperature as well as the ultrasonic operating frequency, which was observed in the experimental results.

In the ultrasonic frequency data shown in Fig. 6.10, unlike the temperature profile where heating stage was represented by a straight line, the UOTS reading in the heating stage was represented by a second order polynomial. In the cooling stage, the curve was still represented by an exponential curve. The parameters of both curves that were computed are shown in Table 6.3.

Table 6.3 Approximation of the Experimental Curves of the UOTS Data

	Heating	Cooling
Fitting interval (s)	500 to 2505	3100 to 3701
MATLAB Model	Linear Poly2	General Exp1
Model equation	$OF(t) = p1 * t^2 + p2 * t + p3$	$OF(t) = a * e^{b*t}$
Coefficients [95% confidence bounds]	p1 = -7.94e-06 [-8.058e-06, -7.823e-06] p2 = 0.06265 [0.06229, 0.06301] P3 = -4.568 [-4.816, -4.32]	a = 5129 [5019, 5239] b = -0.001348 [-0.001355, -0.001342]

The approximation curves are shown in Fig. 6.13.

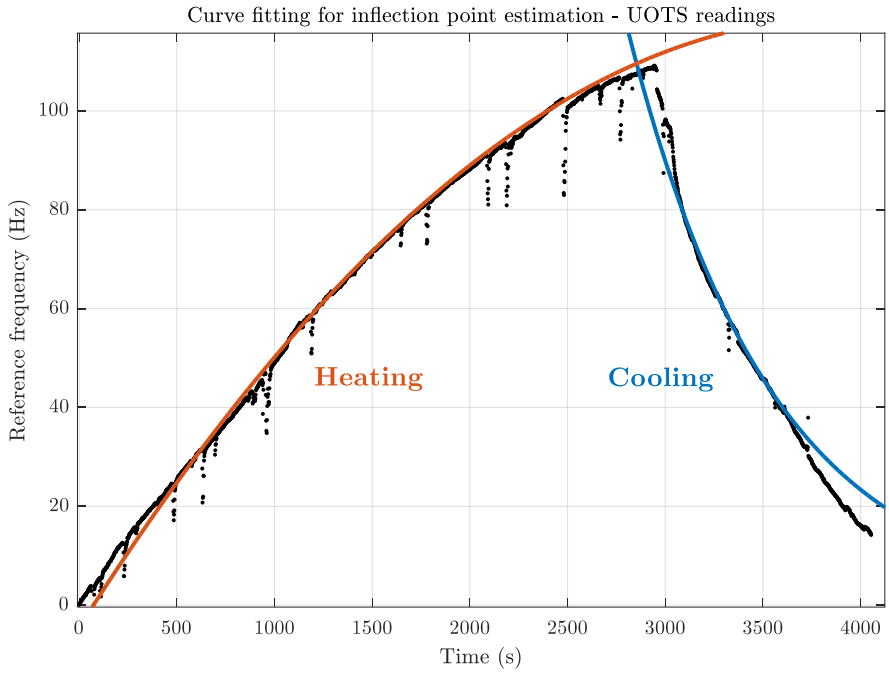


Fig. 6.13 Line fittings for inflection points in the heating and cooling regions of the UOTS readings

Following a procedure similar to that used in the previous intersection point estimation, it was shown that the intersection point of the UOTS readings occurred at t = 2,852 s, which was faster by 100 s compared to the data on the temperature sensors. The actual UOTS readings showed that it started decreasing at t = 2941 s and decreased rapidly around t = 2,957 s, whereas the temperature readings for sensor 2 started decreasing at t = 2975 s. This result showed that the UOTS was capable of detecting the inflection point more quickly than temperature sensors can by around 18.28 s. A similar procedure was applied to the other experimental results, which showed that the UOTS responded faster than the temperature sensors did by approximately 15 to 25 s.

6.4.4 Quantification of the observed hysteresis

Hysteresis can clearly be seen in the UOTS response by overlapping temperature and frequency results. In general, the hysteresis profiles of the heating and cooling stages differ; UOTS frequency is usually above the temperature for heating and below the temperature in cooling intervals, as shown in Fig. 6.14.

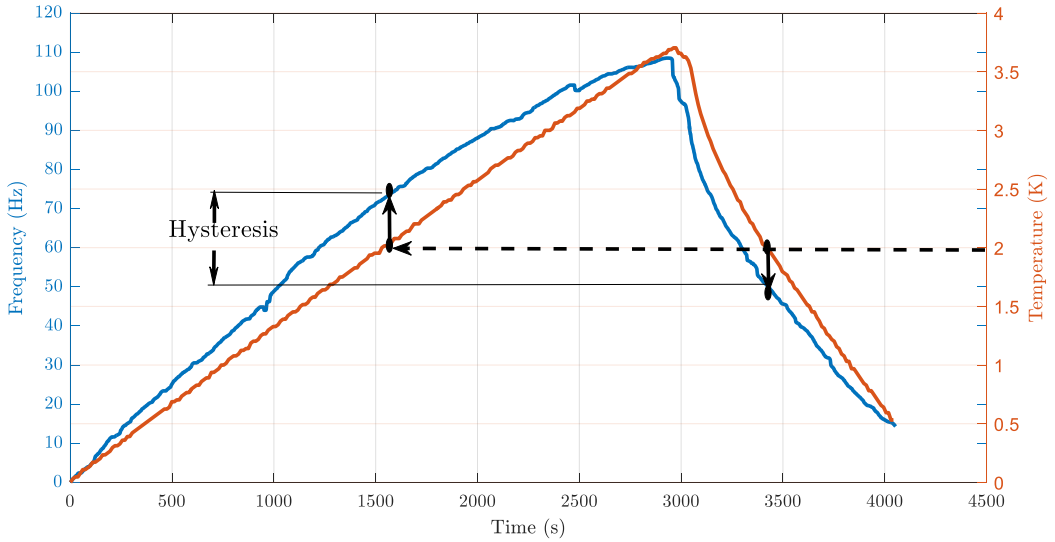


Fig. 6.14 Experimental data for the UOTS output frequency and average temperature vs. time [172]

Average temperature and UOTS frequency are plotted against each other as shown in Fig. 6.15. The results showed variations in frequency–temperature sensitivity in the heating and cooling stages. In addition, the nonlinear approximation of change in

temperature and frequency derived in equation (6.10) is plotted in the same figure. The observed sensitivity in the experimental results was notably smaller.

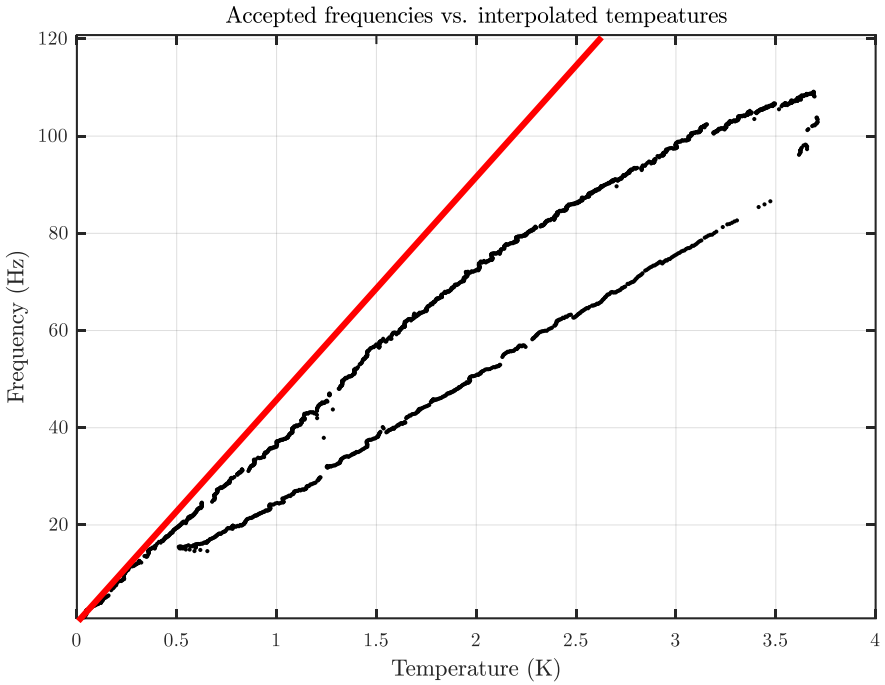


Fig. 6.15 Accepted UOTS output frequencies vs. temperature difference are shown in black dots, and the curve expected from equation (6.10) is represented by a red line

Fig. 6.15 shows that the UOTS performance around the inflection point exhibited a change that was related to the step change in the physical properties observed in the crystal oscillators [148]. The sensitivity calculated for previous experiments varied nonlinearly in both heating and cooling stages, depending on the temperature history before the inflection point. Consequently, the direct calibration of UOTS readings and the derivation of a look up frequency-temperature table was increasingly complicated. Therefore, these results showed that employing a conventional temperature measurement sensor for referencing is essential to interpret UOTS frequencies.

6.4.5 Sensor fusion extrapolation analysis for the correction of temperature–frequency hysteresis

The previous experimental results showed that ultrasonic frequency in the UOTS followed the temperature pattern. In Fig. 6.16, a typical set of results is considered where T_1, T_2 and T_3 are temperature readings for uniform or non-uniform time intervals where

the temperature reading is changed. In Fig. 6.16, f_1, f_2 and f_3 represent ultrasonic frequency readings at corresponding time instances of temperature reading points.

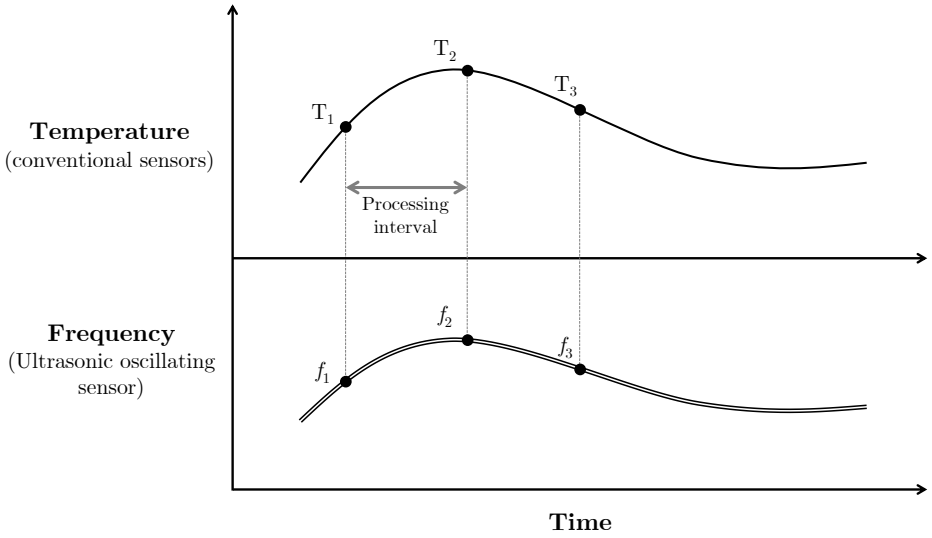


Fig. 6.16 Typical results obtained for ultrasonic oscillating temperature sensors where the processing interval is the duration

To start the fusion process, the graphs were superimposed to determine their differences. Fig. 6.17 shows a graph combining temperature and ultrasonic frequency.

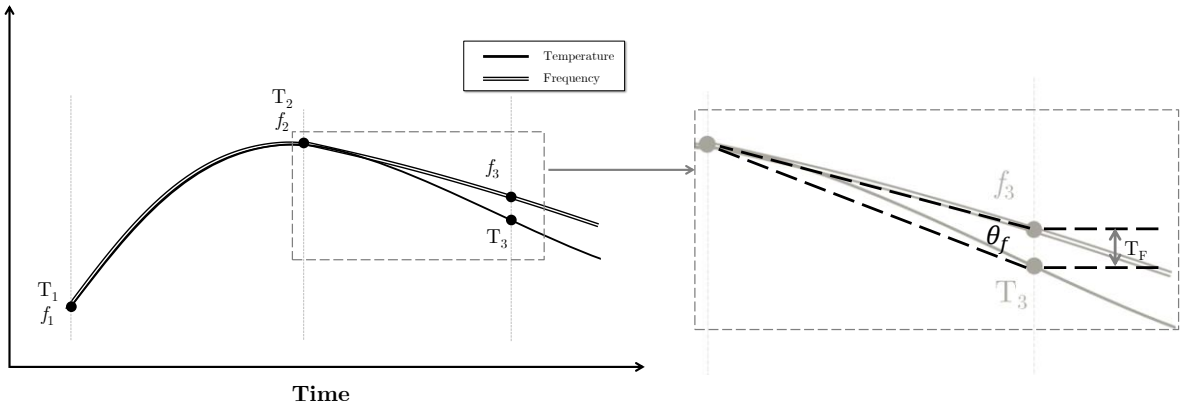


Fig. 6.17 Superimposed temperature and ultrasonic frequency with magnified 2nd and 3rd intervals

As shown in Fig. 6.17, a difference was expected in the readings of the curves because of hysteresis. Based on the frequency readings, the reading corrected for temperature at T_3 was derived from the linear extrapolation estimation given in equation (6.11).

$$T_F = T_1 + \left[\frac{\Delta T}{\Delta f}\right]_1 (f_2 - f_1) \tag{6.11}$$

In the approximation shown in equation (6.11), the recorded temperature and the UOTS output frequency were saved as the present values every time the digital reading of the reference sensor changed. After the processing of a given sample was completed, it moved to the next one. The gradient was numerically estimated as shown in equation (6.12).

$$\left[\frac{\Delta T}{\Delta f}\right]_1 = \frac{T_2 - T_1}{f_2 - f_1} \tag{6.12}$$

This expression was applied as the primary equation for data fusion because equation (6.10) does not reflect the frequency–temperature observed in the experimental results. The fused temperature, which was derived from processing the UOTS readings and the temperature readings in sensor 2, is presented in Fig. 6.18.

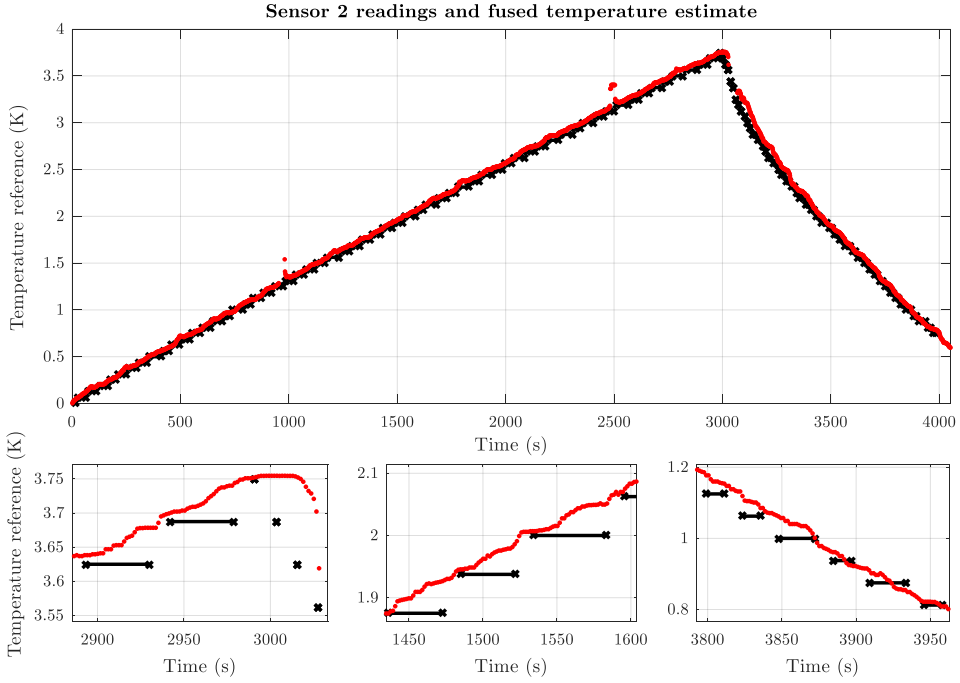


Fig. 6.18 Fused temperature estimates (red dots) and stepwise readings of the reference sensor 2

As shown in Fig. 6.18, as the ultrasonic transducers featured faster responses to temperature sensors and faster inflection point detection, some errors were observed near the inflection point, which was expected. Overall, as expected, the fused temperature

data were consistent with the temperature readings and the increased measurement resolution.

6.4.6 Resolution and precision of fused temperature

The resolution of fused temperature results is determined by the smallest measureable change which occurs when the counter is incremented by just a single pulse. Given that the number of pulses required for a 25 kHz signal with a 24 bit timer is 41943 (section 3.4.4.1), the difference in frequency f_d can be measured as:

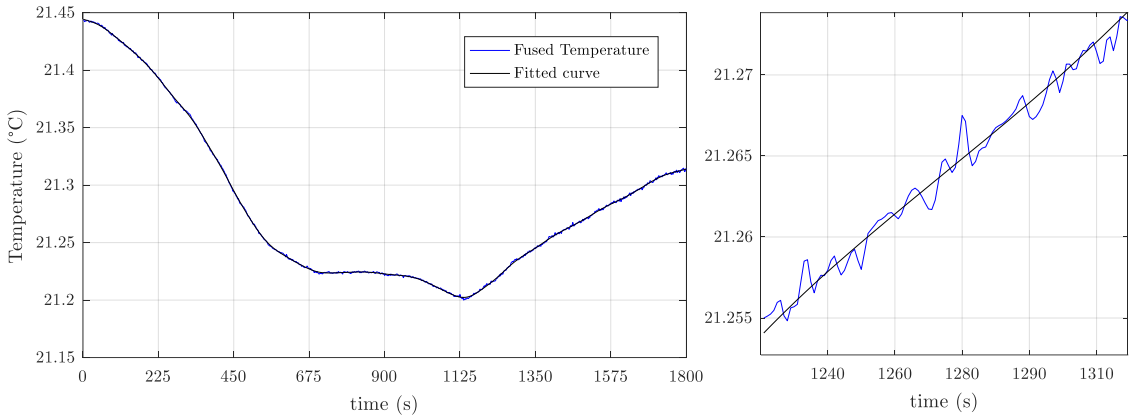
$$f_d = \frac{f_{ref} \times N_{pulses}}{P} - \frac{f_{ref} \times N_{pulses}}{P+1}$$

$$= \frac{10MHz \times 41943}{2^{24}} - \frac{10MHz \times 41943}{2^{24}+1} = 1.5\,mHz \qquad (6.13)$$

Using the average frequency-temperature sensitivity of 27 Hz/K as shown in Table 7.9, the resolution of the UOTS is calculated as approximately 0.1 mK.

In order to measure the precision of the fused temperature measurements, a large number of measurements must be taken when the temperature being measured remains constant. The variation in the sensor output for this experiment allows the precision of the sensor to be calculated. In practice it is not possible to achieve a constant temperature, so steps must be taken to minimise the temperature change.

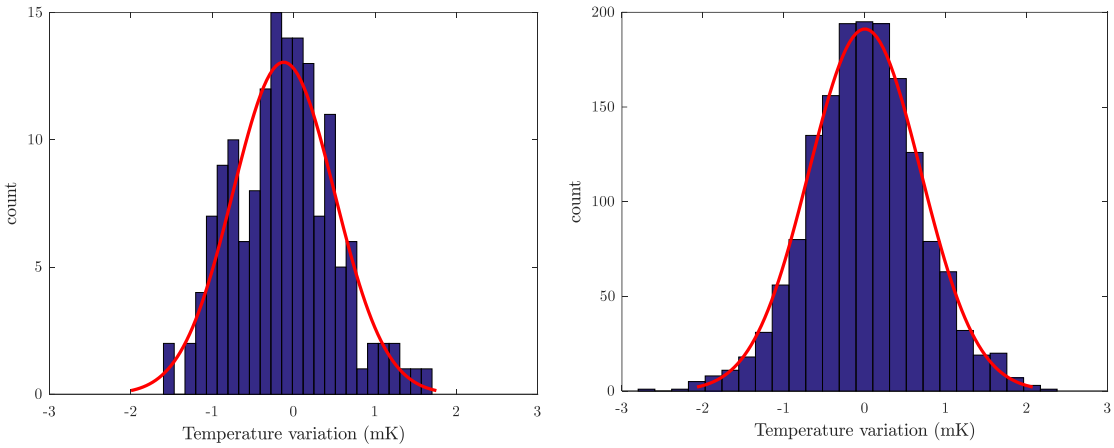
An experiment was conducted to carry out these measurements. The chamber with ultrasonic sensors and conventional temperature sensor was submerged in approximately 120 L of water. The inlet and outlet pipes were left open and unconnected the water pump pipes so there was no flow present through the chamber. The aim of submerging the chamber in the large volume of water was to take advantage of the high specific heat capacity of water to minimise the temperature variations present inside the chamber, even as the surrounding environment underwent changes. Measurements were taken in an overnight experiment of around 40 hours. From this data, a 30 minute window was selected that featured the lowest change in temperature. The resulting experimental data is shown in Fig. 6.19 and has an overall temperature variation of approximately 0.25 K.



(a) (b)

Fig. 6.19 Experimental results after the application of data sensor fusion, (a) full experimental and (b) a zoomed region

The region of data between approximately 698 to 868 s (170 samples in total) has a temperature variation below 5 mK, which is the region with the least temperature change. The distribution of values in this region is shown in Fig. 6.20 (a). Although the distribution of results appears to follow a normal distribution, greater confidence in the results would be obtained if a greater number of samples were used, particularly if these results were from a wider range of input temperatures. By fitting a curve (derived from the MATLAB function fit) to the full experimental data, the low frequency background variation can be removed by subtracting the fitted curve, which can be seen in Fig. 6.19 (b), from the fused data results. The distribution of the data after carrying out this subtraction is shown in Fig. 6.20 (b). Comparing the two distributions, the full experiment matches the normal distribution very well. The standard deviation for the 170 sample distribution is 0.267 mK and the standard deviation for the full experiment is 0.269 mK. This gives confidence that the curve fitting technique for removal of the low frequency background temperature is valid, and allows the processing of data sets where there is a bigger temperature variation.



(a) (b)

Fig. 6.20 Histograms for (a) fused temperature variations in t = 698 to 868 s and (b) the difference between the fitted curve and the fused temperature for the full experimental duration

The same technique for removing the low frequency temperature variation was applied to 13 data sets acquired during the course of this work. This represents a total experimental duration of approximately 170 hours. The temperatures measured vary from a minimum of 19.6 °C to a maximum of 42.7 °C. The data sets represent a range of different experimental conditions, for example with or without temperature control, or with periods of fast or slow temperature change.

The results of these analyses are shown in Table 6.4, which includes the results already presented above as data set A110. The standard uncertainty (i.e., uncertainty of the result of a measurement expressed as a standard deviation and one method of defining precision) was calculated as 1.34 ± 0.2 mK.

Table 6.4 Different Data Sets and Standard Deviation Values for Precision Measurements

Data set	Duration (hrs)	Maximum temperature (°C)	Minimum temperature (°C)	Standard deviation (mK)	Notes
C24	10	26.2	24.2	0.676	-
C25	35	27.5	19.6	0.661	Overnight experiment
C28	35	36.6	25.6	0.679	Overnight experiment
C41	15	39.5	29.6	0.681	-
C42	10	42.7	28.1	0.660	Fast temperature change of 0.5 K/min
C44	10	25.1	19.6	0.671	-
C48	10	32.2	20.6	0.678	-
B29	15	27.1	24.0	0.658	No water flow
C57	35	28.9	25.5	0.674	Overnight experiment
C74	5	35.5	28.4	0.670	-
C75	5	35.9	27.4	0.659	-
A109	2	27.7	27.1	0.683	Slow temperature change, submerged in water
A110	40	24.1	20.4	0.678	Slow temperature change, submerged in water

6.5 Summary

Hysteresis is a property of piezoelectric elements. It is related to strain-stress changes in quartz. Because this effect has a nonlinear response in the temperature-frequency relationship at different magnitudes in heating and cooling stages, it is difficult to calibrate UOTS readings without a temperature reference. Therefore, data sensor fusion, which uses data from a temperature sensor as a reference, is used to calibrate ultrasonic frequency to measure temperature.

By employing a conventional temperature sensor, some advantages of the UOTS were sacrificed, such as the limited accuracy of temperature sensors, slower response and single location measurements. However, the UOTS still detected the inflection point faster than the temperature sensors could. The inflection point was estimated by computing the response curves for both the temperature and frequency data in the cooling and heating stages. By numerical processing, the UOTS estimated the inflection point 100 s before

the temperature sensors did and by around 18 s in the real data. In order to obtain an accurate fused temperature, a criterion that validated each frequency reading was applied, which resulted in discarding around 22% of the measurements. A better selection criterion was followed by dynamically selecting UOTS readings based on the frequency change, which resulted in an improvement of 8% in the acceptance rate, especially around the inflection points.

Sensor fusion was successfully applied to the experimental results. By employing sensor fusion, the resolution of the conventional sensors readings was increased. 1-Wire temperature sensors produced a maximum resolution of 62.5 mK. In sensor fusion, the resolution is significantly higher at around 0.1 mK. As expected, the estimate included some outliers around the inflection point because of the faster UOTS response. In the remaining temperature profile, the estimate was valid, allowing for the successful calibration of ultrasonic frequency with the temperature. The specifications of the fused temperature are shown in Table 6.5.

Table 6.5 Specifications of the UOTS Fused Temperature

Factor	Value
Sensitivity	26.5 – 27.5 Hz/K
Accuracy	± 0.25 K (1-Wire sensors)
Precision (standard uncertainty)	1.34 ± 0.2 mK
Resolution	0.1 mK
Operating range (400ET18S)	0–80 °C

Overall, the results showed that the UOTS is a potentially valuable addition to process control instrumentation. Hysteresis was eliminated by employing data fusion. The process of analysing ultrasonic frequency was more complicated than expected. The temperature-frequency relationship showed different patterns in each experiment conducted, which prompted an additional study. In contrast, the UOTS measurements featured large intermittent jumps, which might have led to incorrect estimates. The acceptance criterion was applied to the raw data but at the cost of the measurement rate.

Chapter 7

Differential Measurements of Heat Loss in Water-Cooled Electric Motors

7.1 Introduction

In this chapter, an experimental analysis of the differential heat loss measurements in water-cooled electric motors will be described. The chapter begins with an analytical analysis of heat loss measurements. First, the simulation of different electric motors to illustrate the importance of high accurate measurements in motor losses evaluation will be discussed. Three designs for the chambers will be proposed. A CFD analysis will be conducted to study the different effects on the system, including pressure, velocity and turbulence. Based on these outcomes, a final design will be 3D-printed and assembled.

Finally, differential measurements will be completed using different flowrates derived from various observations, such as frequency scatter, sensitivity and hysteresis.

7.2 Investigation of power loss in water-cooled electric motors

7.2.1 Power loss measurements

In electric motors, power loss is related to the conversion from the electrical supply to the dissipated thermal energy. The power loss within a water-cooled electric motor can be estimated by measuring the temperature at the coolant inlet and outlet of the motor. The power loss is calculated by measuring the difference in temperature between the inlet and outlet, the coolant flowrate and its specific heat capacity. In the manufacturing process, the accurate measurement of these variables results in better motor grading and facilitates the optimisation of the motor in the design stage. Fig. 7.1 shows the experimental setup used for motor efficiency calculations.

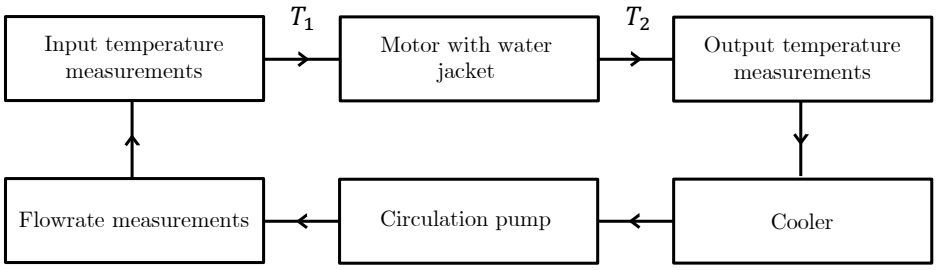


Fig. 7.1 Experimental setup diagram of power loss for water-cooled electric motors

A circulation pump can be used to simulate the water circulation inside the electric motor, as shown in Fig. 7.1. In this experimental setup, the pump circulates the water in a closed-loop system. Heat difference can be measured at the inlet and outlet of the electric motor, where T_1 represents the temperature at the motor inlet and T_2 represents the temperature at the motor outlet. The subtraction of temperatures results in the temperature difference, which occurs because of the power loss and subsequent heat dissipation in the motor. When the temperature measurement process is completed, a cooler is placed at the outlet to allow the recirculation of cool water in the loop. Power loss P_{loss} can be calculated using the measured temperature difference at the inlet and outlet of water jacket ΔT as shown in equation (7.1).

$$P_{loss} = CQ\Delta T \tag{7.1}$$

where P_{loss} is the heat flow rate or heat dissipated into the cooling water (J/s), C is the specific heat at the constant pressure of pure water (J/kg.K), Q is the mass flow rate of the cooling water circulating through the system (kg/s) and ΔT is the difference in the temperature of the cooling water (K) at the outlet and the inlet [174].

The maximum temperature difference ΔT_{max} should be maintained within the range specified by the motor manufacturer (e.g. 7–10 K [175]) for a constant flowrate.

The motor efficiency η is given by the difference between the consumed power P and the dissipated power P_{loss} divided by the consumed power as in equation (7.2).

$$\eta = \frac{P - P_{loss}}{P} \tag{7.2}$$

7.2.2 Deriving an analytical expression for variations in estimated efficiency

Deriving an analytical expression of the variations in estimated efficiency allows for a better illustration of the accurate temperature measurements in evaluating motor losses. To derive an accurate expression of efficiency, the accuracy of the temperature sensors (or resolution if they are digital) should be considerably smaller than the temperature difference when the coolant flowrate is kept constant. This criterion is easily achievable when oscillating ultrasonic temperature sensors are used. By rearranging equation (7.1), the flowrate required to achieve the recommended heat difference in the liquid between the inlet and outlet of the water jacket equals the power loss of the motor divided by the product of temperature difference and specific heat capacity of the coolant as in equation (7.3):

$$Q = \frac{P_{loss}}{\Delta TC} \tag{7.3}$$

In order to derive an expression of the flowrate in terms of the power efficiency factor $\eta_0 = 1 - \frac{P_{loss}}{P}$, the power loss can be substituted by consumed motor power P, which leads to the flowrate as in equation (7.4):

$$Q = \frac{P(1 - \eta_0)}{\Delta TC} \tag{7.4}$$

By combining equations (7.1) and (7.4), the experimental P_{loss} of an electric motor is derived as in equation (7.5).

$$P_{loss} = \frac{P(1-\eta_0)\Delta T_x}{\Delta T_0} \tag{7.5}$$

where ΔT_0 is the temperature difference between the outlet and inlet of the actual temperature reading, and ΔT_x is the measured temperature difference between the outlet and inlet.

The efficiency factor of the measured power loss in an electric motor η_x can be rearranged by substituting equation (7.2) by a motor power loss in the expression derived from the experimental calculations of the power loss in the motor as in equation (7.5), which leads to equation (7.6).

$$\eta_x = \frac{P - \frac{P(1-\eta_0)\Delta T_x}{\Delta T_0}}{P}$$

$$\eta_x = 1 - (1-\eta_0)\frac{\Delta T_x}{\Delta T_0} \tag{7.6}$$

Equation (7.6) can be rearranged to give equation (7.7):

$$\eta_x = 1 - \frac{\Delta T_x}{\Delta T_0} + \eta_0 \frac{\Delta T_x}{\Delta T_0} \tag{7.7}$$

To ensure that the derivation is correct, let us assume that $\Delta T_x = \Delta T_0$ in equation (7.6), which indicates that the operation features error-free temperature measurements. The efficiency factor of the measured power loss will equal the power loss in the actual power loss $\eta_x = \eta_0$, which is a true statement.

In order to calculate the effects of temperature reading accuracy on the power loss measurements, the measured temperature difference, ΔT_x, can be considered in terms of the actual temperature difference value as represented in equation (7.8).

$$\Delta T_x = \Delta T_0 + \varepsilon \tag{7.8}$$

where ε is the error in measuring the temperature difference.

This error is compounded by inaccurate readings of two independent temperature sensors: one measures the temperature at the inlet and the other measures the temperature at the outlet. This error value could be positive or negative. Rearranging equation (7.8) gives the ratio of the measured to the actual temperature in equation (7.9).

$$\frac{\Delta T_x}{\Delta T_0} = 1 + \frac{\varepsilon}{\Delta T_0} \tag{7.9}$$

In order to derive the final expression of the measured power efficiency accounting for the errors in measured temperature, equation (7.9) is substituted into equation (7.7), which gives equation (7.10):

.

$$\eta_x = 1 - \left(1 + \frac{\varepsilon}{\Delta T_0}\right) + \eta_0 \left(1 + \frac{\varepsilon}{\Delta T_0}\right)$$

$$= -\frac{\varepsilon}{\Delta T_0} + \eta_0 + \frac{\varepsilon\, \eta_0}{\Delta T_0} \tag{7.10}$$

Equation (7.10) leads to the simplified expression of the measured power efficiency in equation (7.11):

$$\eta_x = \eta_0 + \frac{\varepsilon}{\Delta T_0}(\eta_0 - 1) \tag{7.11}$$

This equation is consistent with the expectation of obtaining the correct efficiency value from the calculations if the temperature difference measurement is error free ($\varepsilon = 0$).

7.2.3 Simulation of the effect of temperature measurement resolution on power loss measurements

A numerical simulation was conducted to evaluate motor efficiency using differential temperature measurements. The data on 26 industrial electrical water-cooled motors were extracted from their datasheets. These data included rated power, efficiency and suggested temperature differences of the cooling water at the inlet and outlet. The required coolant flowrate is calculated from equation (7.12).

$$Q = \frac{P_{loss}}{\Delta TC} = \frac{\eta P}{\Delta TC} \tag{7.12}$$

The range of ΔT is measured by defining two finite accuracy sensors with the error of ε, which can be calculated as $\Delta T = \Delta T_0 \pm 2\varepsilon$, where ΔT_0 is the resultant temperature difference determined if the rounding of 0.1 L/min is applied. P_{loss} is determined as the maximum and minimum values of the new measured ΔT in equation (7.8). Finally, the estimated motor efficiency is calculated. Fig. 7.2 illustrates the simulation results for 2-, 4- and 6-pole electric motors with rated power of 0.75 kW for different efficiencies, assuming that the temperature difference between the outlet and inlet of the motor is 10 K.

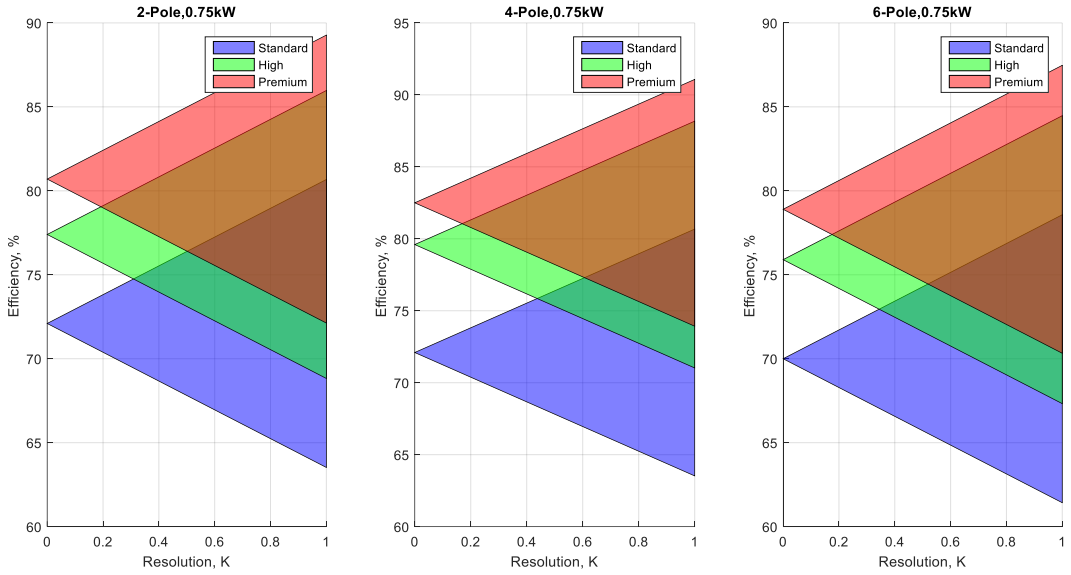


Fig. 7.2 Simulation results for 2-, 4- and 6-pole electric motors with rated power of 0.75 kW for various motor efficiencies against the resolution of the temperature measurement device

Manufacturers need to correctly classify motor efficiency to be able to set their efficiency class. Fig. 7.2 shows that the efficiency class (i.e., the selling price) of the motor can be incorrectly classified in cases where the accuracy of the temperature measurements system used is greater than 0.5 K with an associated measurement resolution greater than 0.1 K. In Fig. 7.2, this case is clearly shown in the overlapping regions of lower accuracies in all graphs. In a sensor with 1 K resolution, it is not possible to distinguish between different efficiency classes in measurements in the range of 72–80% of 2-pole

motors. Based on the data collected from the simulations of the full range of motors tested, it can be concluded that the efficiency of 2- and 4-pole motors was as accurate as 99% when sensors with a resolution better than 0.05 K were employed. For 6-pole motors, the resolution should be below 0.5 K to achieve the same degree of accuracy. Such sensor specifications can be very challenging to achieve using a low-cost conventional temperature measurement instrument usually deliver a resolution of about 0.1 K which means they do not meet the required specifications for 2- and 4-pole motors.

Most liquid-cooled electric motors utilise low-cost conventional temperature sensors to measure temperatures in power loss estimation; a list of some commercial motors is provided in Table 7.1.

Table 7.1 Temperature Sensor Technologies Used in Commercial Liquid-cooled Electric Motors

Motor	Manufacturer	Temperature sensors Technology	Liquid temperature range
Three-phase induction motors cooled by water jacket [176]	Weg	RTDs	An alarm is set if temperature exceeds 90 °C
low voltage standard motors [177]	ABB	Thermistors	Below 95 °C
Water-cooled three-phase asynchronous motors [178]	VEM	Thermistors	10 K difference
Liquid-cooled asynchronous motors ADF ADF1x4 [179]	Rexroth	NTC Thermistors	Up to 10-40 °C with maximum 10 K difference
GVM global vehicle motor [180]	Parker	PTC Thermistor	Up to 65 °C

7.2.4 Using ultrasonic temperature sensors to evaluate motor loss

When the temperature difference and flowrate have been measured, the conservation of energy principle can be applied to calculate the power loss.

Many benefits will be derived when improvements are made to the temperature measurements by using ultrasonic sensors, including the quicker and more accurate evaluation of the power loss in an electrical machine, which is essential for its design optimisation. The time required to measure the temperature is linked to the speed of sound propagation between the transmitter and receiver which means the ability to

measure dynamic changes in efficiency is significantly improved. Ultrasound also has the potential for high-resolution measurements which enables the detection of the effects of small improvements made to the design or the operating conditions of the electrical machine.

7.3 Motor power rating capabilities

As will discussed later in this chapter, the maximum flowrate at which the system can operate in low scatter was found to be around 10 L/min. Moreover, water-cooled electric motor manufacturers recommend that the temperature difference between the inlet and outlet of a motor should not exceed 10 K. By knowing these quantities, the capabilities of the developed UOTS can be used to determine the specifications of the electric motors to be evaluated.

Power loss can be calculated for maximum temperature difference and flowrate as in equation (7.13).

$$P_{loss} = CQ\Delta T = 10\ L/min \times 4181\ J/kg \times 10\ K = 6.9\ kW \tag{7.13}$$

Based on these results, the maximum power ratings for standard, high and premium efficiency water-cooled electric motors that can be evaluated using the development are shown in Table 7.2. Power losses in motors below the maximum ratings shown in Table 7.2 can be determined easily.

Table 7.2 Maximum Power Ratings (in kW) of Water-cooled Electric Motors can be Evaluated Using Current Developments

Motor classification	2-pole	4-pole	6-pole
Standard	45	45	43
High	55	57	52
Premium	75	77	73

The values shown in Table 7.2 encompass various applications from low-power products to medium-power applications, such as electric car motors (typically rated between 20 and 30 kW [181]).

7.4 Test rig modelling and CFD simulation analysis

7.4.1 Introduction

In order to evaluate the performance of the ultrasonic oscillating sensor developed in this study, a physical test rig will be constructed. This model will be used to measure the power loss in a water-cooled electric system. Two identical copies of the same design will be developed to act as calorimeters for the differential processing of temperature. The models will be designed using a Computer-Aided Design (CAD) tool, simulated using a Computational Fluid Dynamics (CFD) package and printed using a 3D printer before they are tested with water circulating in them.

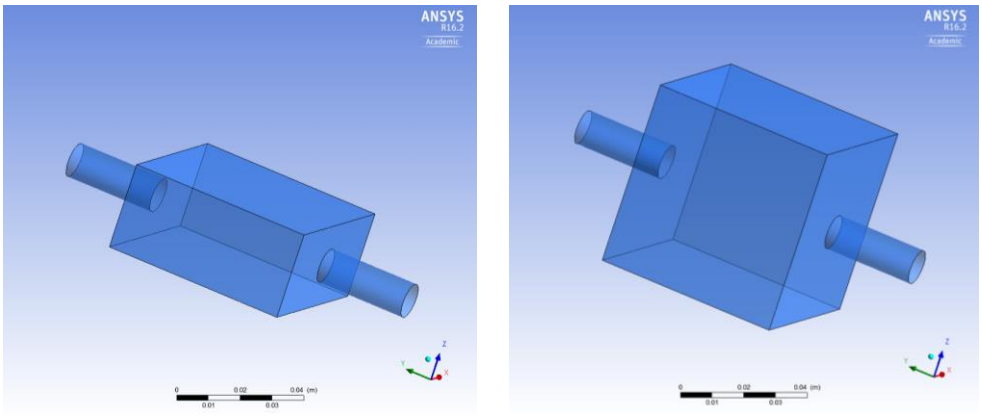
7.4.2 CFD simulations

7.4.2.1 Model criteria and specifications

Three models were developed based on the criteria established in Chapter 5; these parameters are shown in Table 7.3. In addition, in the design, an inlet and outlet are connected to the water-cooled electrical motor. Fig. 7.3 shows the various chamber models developed for UOTS.

Table 7.3 Design Specifications and Criteria for UOTS Hardware Configurations

Item	Length (mm)
Optimum distance between ultrasonic sensors	60
3D printing size limitation	200×200



(a) RCSC (b) SCSC

(c) CCSC

Fig. 7.3 Various chamber models developed for UOTS measurements

7.4.2.2 Proposed models

Rectangular cross-sectional chamber

The first proposed model, the rectangular cross-section chamber (RCSC), consists of a simple box with a water inlet and outlet as shown in Fig. 7.3 (a). A box-shaped design was chosen because it is simple to produce. Moreover, it is easier to install sensors on a flat surface than on a curved surface. Ultrasonic sensors were set 60 mm apart on the sidewalls of the chamber. The disadvantage of this arrangement is its small size, which results in a turbulent flow especially at higher water flowrates.

Square cross-sectional chamber

The square cross-section chamber (SCSC) is similar to the RCSC, but its height is greater as shown in Fig. 7.3 (b). This additional height allows additional room for water to circulate, which results in a less turbulent flow and reduced pressure in the wall facing the inlet.

Circular cross-sectional chamber

The circular cross-sectional chamber (CCSC) consists of a tube of varying diameters, from the diameter of the inlet hose to 60 mm between the transducers. This design promotes the smoother movement of water, specifically near the outlet as shown in Fig. 7.3 (c). This causes less pressure on chamber walls and a more laminar flow.

7.4.2.3 Turbulence CFD simulations

A fluid within a cross-sectional area can be characterised as two flow types: laminar flow and turbulent flow. The flow type depends on the ratio of the inertial force to the viscous forces. It is identified by calculating the Reynolds number as in equation (7.14).

$$R_e = \frac{\rho v D_H}{\mu} = \frac{v D_H}{v} = \frac{Q D_H}{vA} \tag{7.14}$$

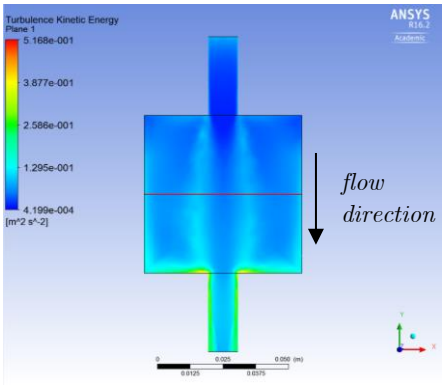
where D_H is the hydraulic diameter (m), Q represents the volumetric flowrate (kg/s), A is the cross-sectional area (m^2), ρ is the density (kg/m^3), v is the mean velocity (m/s), and μ and v are the dynamic (Pa.s) and kinematic (m^2/s) viscosities, respectively.

If the Reynolds number is less than 2300, then the flow is laminar. However, the flow is considered turbulent if the Reynolds number is greater than 4000. Numbers between 2300 and 4000 indicate that the flow is within a transition region where both types of flow can occur.

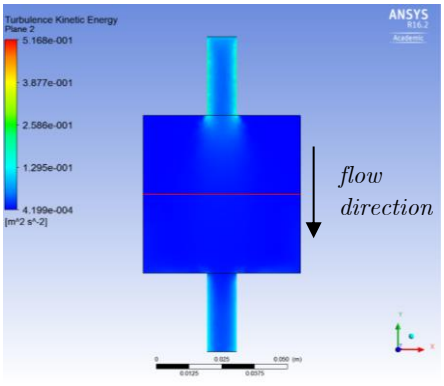
In the three proposed models, water flows from a hose with a relatively small diameter to a larger area. This transition results in turbulent flow and vortices inside the model. Ideally, the flow through the entire of the chamber is laminar. However, because of the limits on the allowable size, a length suitable for the settling of all turbulent flow is not viable. Hence, the non-laminar flow velocity and direction affect the measurements made by the range of temperature sensors contained within the chamber.

A CFD analysis was completed using the software package Fluent, using a Kappa Epsilon turbulence model, which is a two-equation model based on Kappa turbulence kinetic energy and Epsilon turbulence dissipation rate. This model was used because it is robust, quick-to-converge and scientifically reinforced [44]. All three models were analysed at

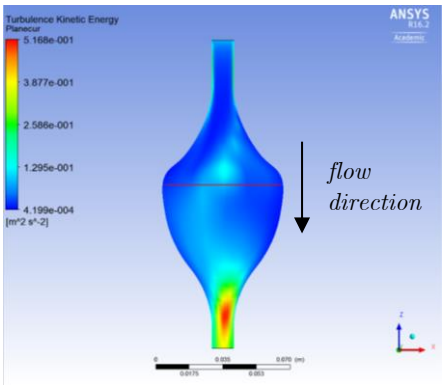
flowrate values of 0.06, 4, 8, 16 and 25 L/min. Fig. 7.4 shows the performances of the three proposed designs at a flowrate of 8 L/min in a horizontal cross-sectional plane.



(a) RCSC



(b) SCSC



(c) CCSC

Fig. 7.4 Turbulence of water flowing at 8 L/min inside the chamber

The SCSC had more laminar flow compared to the RCSC because of its larger water capacity as shown in Fig. 7.4. In Fig. 7.4 (a), turbulence is clearly present at the wall facing the water inlet due to pressure on the facing wall. Moreover, some turbulent areas are present in the sidewalls. As shown in Fig. 7.4 (c), in the CCSC, some turbulence is present in the middle of the chamber due to the circular motion of water when it hits the sidewalls. Fig. 7.5 shows the amounts of turbulence in all models at different flowrates in the ultrasonic transducer path, which is shown as the red line in Fig. 7.4.

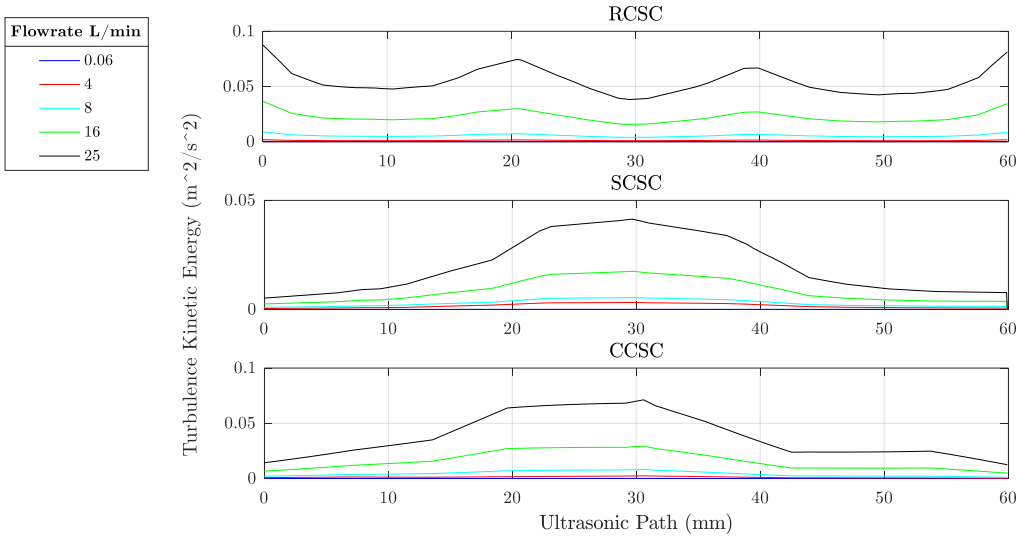


Fig. 7.5 Turbulence performance for all models at different flowrates

The graphs in Fig. 7.5 show that the turbulence performance differed among the three models. In the RCSC, two turbulence peaks occurred at 20 and 40 mm of the ultrasonic path, which were due to the small volume of water. The turbulence analysis showed that laminar flow was established at flowrates below 8 L/min and produced turbulence values as low as 0.01 m^2s^{-2}. Turbulence significantly increased above flowrates of 10 L/min. In the SCSC, the turbulence values were similar to those in the RCSC. However, no peaks occurred at 20 and 40 mm because of the larger chamber capacity. Although the values were slightly higher, especially mid-way along the ultrasonic path, the mean values were smaller than in the first case.

The performance of the CCSC was similar to that of the SCSC with the exception of slightly higher turbulence values at 30 mm in the middle of the path. Moreover, turbulence was slightly higher in the first half of the path compared with the SCSC because of the gravity encountered during the simulation process.

Flowrates greater than 10 L/min contained reciprocating eddies in most of the chambers, similar to a Karman vortex street. At these flowrates, many eddies were formed. Because the simulation was not a transient analysis, the formation of eddies was shown at one point in time. During the transient analysis, the smaller and larger eddies at the outer circumference nearest the smaller diameter inlet switched per cycle. Recirculation points were also identified at locations other than at the circumference of the chamber entrance

at flows greater than 10 L/min. A clear comparison of the turbulence at a fixed flowrate within the ultrasonic pathways in all models is shown in Fig. 7.6.

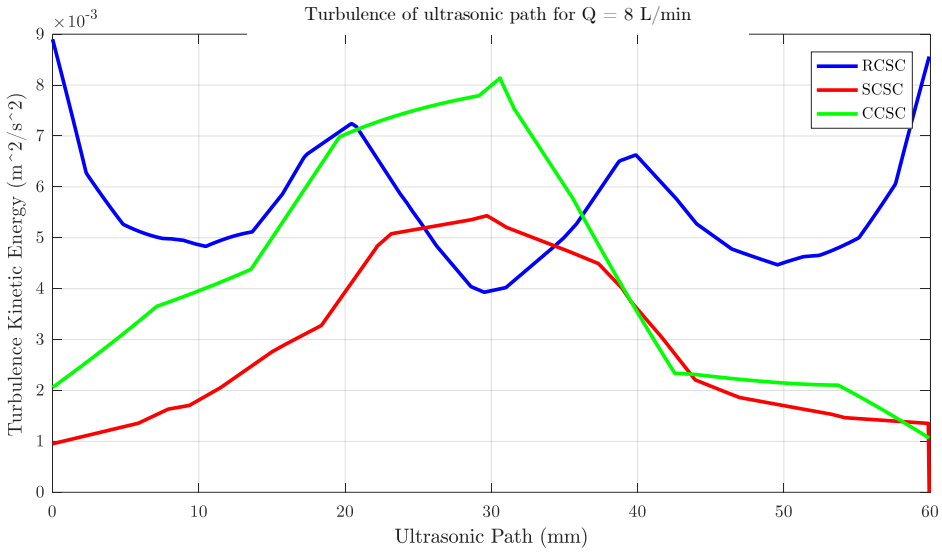
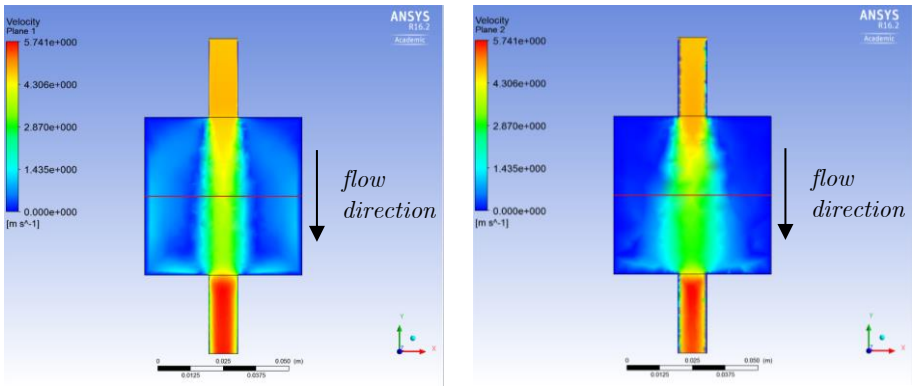


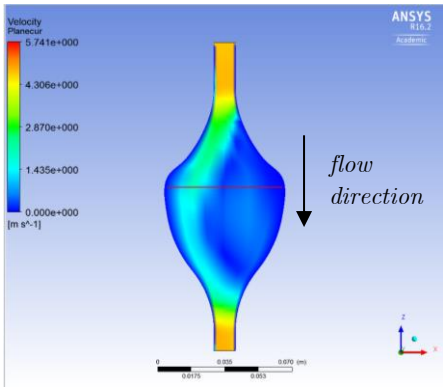
Fig. 7.6 Comparison of turbulence of all models at the flowrate of 8 L/min

7.4.2.4 Velocity CFD simulations

The velocity of water is an important factor in determining the performance of ultrasonic sensors at a certain flowrate. A low and constant velocity is desirable to obtain accurate ultrasonic frequency readings. Previous experiments showed that flowrate affected frequency readings. Based on this finding, an ultrasonic-based flowmeter was developed [61]. Fig. 7.7 shows the velocity of water at a flowrate of 8 L/min in the three models in a cross-sectional plane.



(a) RCSC (b) SCSC



(c) CCSC

Fig. 7.7 Velocity of water flowing at 8 L/min inside the chambers of the three models

As shown in Fig. 7.7 (a) and (b), the velocity of the water stream is more widely spread over the chamber area in the SCSC than in the RCSC. In the RCSC (Fig. 7.7 [a]), water is shown flowing in the right and left directions from the inlet, which is due to the turbulence. The high velocity at the outlet is a result of water flowing from larger to smaller (hose outlet) areas. Fig. 7.7 (c) shows the more stable transition of water from the inlet to the outlet at approximately similar velocities on each side. Some water is shown flowing on one side, which is due to gravity. Fig. 7.8 shows the quantities of the velocity in all three models at different flowrates in the ultrasonic transducer paths, which are shown as red lines in Fig. 7.7.

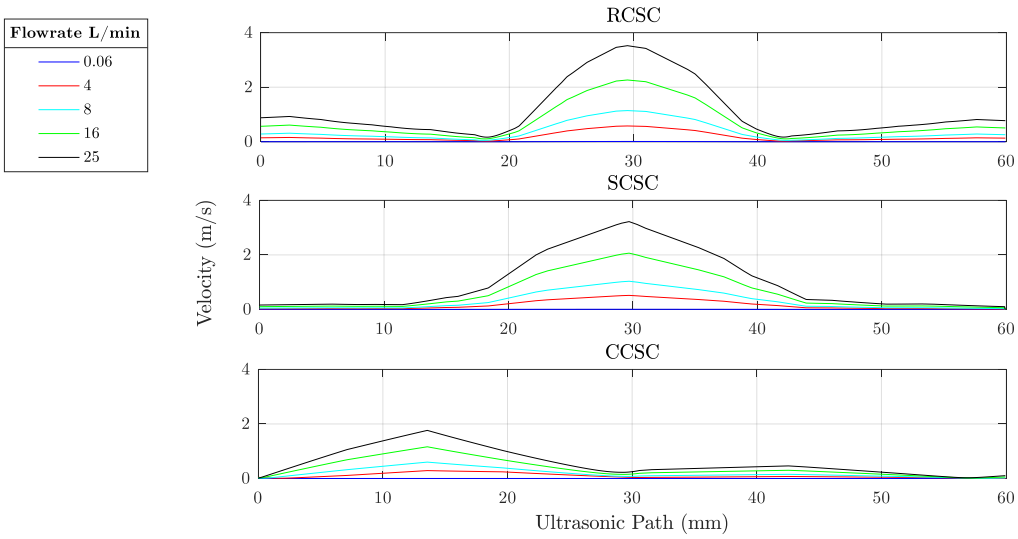


Fig. 7.8 Velocity in all models at different flowrates

The graphs in Fig. 7.8 show that the velocities in the RCSC and SCSC had similar values. However, in the RCSC, the velocity was slightly larger at the beginning and at the end compared to the SCSC, which was due to turbulence. Compared to the RCSC, the SCSC had a relatively lower velocity of water because of its size. The CCSC showed less velocity and less turbulence compared to the first two models because of its larger capacity. The flowrate on the left side of the ultrasonic path was faster than on the right side, which was due to gravity when the model was set horizontally. The velocity of the water in the CCSC was about half the velocity in the RCSC and SCSC models.

Unlike turbulence, velocity spread evenly as the flowrate increases. It was observed that the turbulence increases significantly when it exceeds 10 L/min. The comparison of the velocities at a flowrate of 8 L/min in all models is shown in Fig. 7.9.

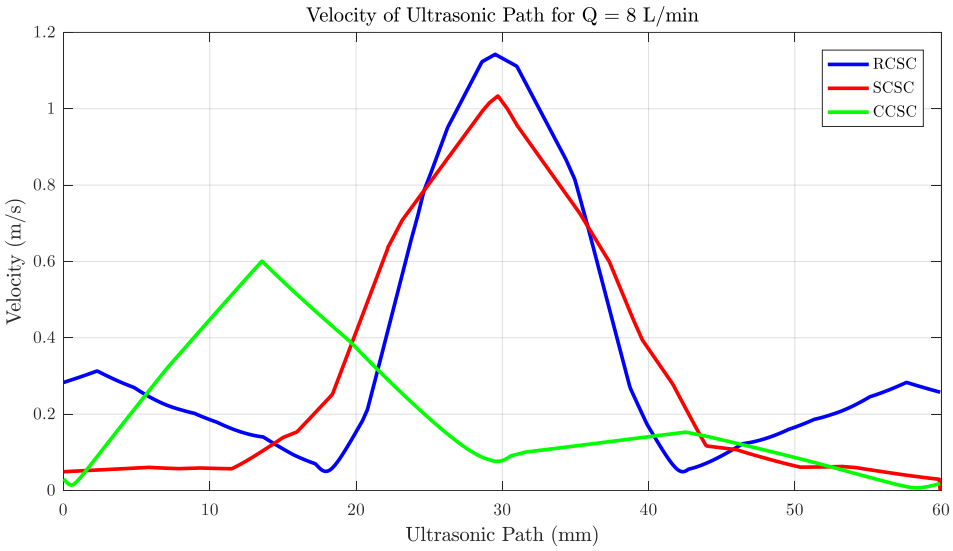


Fig. 7.9 Comparison of turbulence in all models at the flowrate of 8 L/min

Fig. 7.9 shows similar velocities in the RCSC and SCSC models although the velocity was relatively slower in the SCSC. It is important to note that there was a relatively faster flow of water at the beginning and at the end of the ultrasonic path in the RCSC compared to the SCSC, which was due to turbulence. The flow velocity in the CCSC was slower and significantly slower.

7.4.3 Summary

A CFD simulation was conducted to establish the best method for the evaluation of motor power loss. Differential heat was measured in the three models. Table 7.4 shows a summary of the tested models.

Table 7.4 Comparison of Turbulence, Velocity and Thermal Response in the Proposed Chambers

Design	RCSC	SCSC	CCSC
Turbulence	Poor	Good	Excellent
Velocity	Good	Good	Good
Thermal contact	Good	Good	Good

The outcomes shown in Table 7.4 indicate that the CCSC and SCSC models featured good responses for turbulence, velocity and thermal contact. In the CCSC model, turbulence had a better response because of the smoother water transition of the curved

walls as well as the larger chamber volume compared to the chambers in the other three models.

With regard to the construction of both chambers using 3D printing facilities, the CCSC model was the most complex. Depending on whether the model was printed as a single object or in several parts, an additional excessive volume of supporting rafts was required. Moreover, because the external structure of the chamber was not a flat surface, further complications arose when the sensors were mounted.

The results showed that the SCSC model produced a good performance in terms of turbulence, velocity and thermal response. In addition, the 3D printing of this model was less complex than the CCSC model because it could be printed and joined without a supporting structure. As shown in Fig. 7.29, the SCSC design provided low frequency scatter performance in flowrates up to 10 L/min with values close those when there was no flow. Therefore, further research will be carried out on the use of this chamber.

7.5 Design and assembly of the test rig

7.5.1 3D printing overview

7.5.1.1 3D printing technology

In the last five years, 3D printing technology has become an important factor in various areas of engineering industries, including automotive, medical and others [182]. Statistics have shown that the 3D printing market and its associated services will amount to around $16.2 billion in 2018 with a 76% increase over the same market share in 2014 on a worldwide scale [182]. In 2014, a survey showed that over 60% of enterprises and research institutions were using or considering 3D printing [183].

The option of 3D printing is effective in highly customable designs using a minimal amount of resources. This method allows for developing a system that is easy to modify and reproduce. Using modelling software, 3D printing converts a virtual design to a physical object that was made in a CAD file. Alternatively, the design could be imported directly from a model that was constructed by a 3D scanner. Several leading IT companies enabled their hardware to digitise real objects into 3D models using novel, inexpensive tools, such as Kinect by Microsoft [184]. In printing a 3D model, the

modelling software slices the final model into several horizontal layers (a few hundred layers to thousands of layers) based on design size, resolution and complexity. When a design is loaded to the printer, it starts to melt or soften the material to build the object layer by layer. The printer constructs the final design from layers of 2D images that represent horizontal slices.

The American Society for Testing and Materials (ASTM) developed a set of standards that classify the additive manufacturing processes into seven categories according to the standard terminology for additive manufacturing technologies. These seven processes are as follows: Vat photo-polymerisation, material jetting, binder jetting, material extrusion, powder bed fusion, sheet lamination and directed energy deposition [185].

The 3D printing technology has several advantages and disadvantages, which are shown in Table 7.5.

Table 7.5 Advantages and Disadvantages of 3D Printing

Advantages	Disadvantages
Highly customisable design	Relatively high cost of 3D printers
Ease of reproducibility and mass production	Requires good knowledge of 3D modelling
Cheap printing materials	Printing can take a long time
Produces complex shapes that are difficult to be made physically	Size, accuracy and model shape limitations
Environmentally friendly and efficient [186]	Limited types of materials can be used [188]
Increased employment opportunities, as the market will have an increased demand for designers and printer operators [187]	

7.5.1.2 3D printers

Several printers are available commercially. The website 3ders.org, which focuses on the 3D printer market, had a database of over 250 printers in early 2016. Prices range between $140 and $846k based on the technology, the build envelope, the printing materials used and other factors. For example, the Mcor IRIS printer features ultra-precise resolution, coloured printing models, and it costs about $32k [189]. Inexpensive 3D printers are also commercially available.

At the University of Nottingham, two printers are available in the Department of Electrical and Electronic Engineering. The printers are the Velleman K8200 by Conard and the Ultimaker2 by Ultimaker. A brief comparison of these printers is shown in Table 7.6.

Table 7.6 Comparison of the Ultimaker2 and the Velleman K8200

	Ultimaker2	Velleman K8200
Assembly	Assembled	DIY kit
Build envelope (W x D x H mm)	230×225×205	200×200×200
Nozzle diameter (mm)	0.4	0.50
Layer thickness (mm)	0.02	0.20-0.25
Speed (mm/s)	300	120
Printing material	PLA, ABS or CPE	PLA or ABS
Price ($)	2,500	549
		

As shown in Table 7.6, the Ultimaker2 is faster and more precise compared to the Velleman K8200. In addition, it features a larger build plate and hence a larger print size. Moreover, the Ultimaker2 is more than twice as fast as the Velleman K8200. In the Ultimaker2, the LCD display indicates the status of the printing and allows for setting other parameters, such as print material, speed and so on. The software Cura for Ultimaker allows easier control than other software do, and it has several more printing options than Repetier has. Therefore, the Ultimaker2 was chosen for use in the present study.

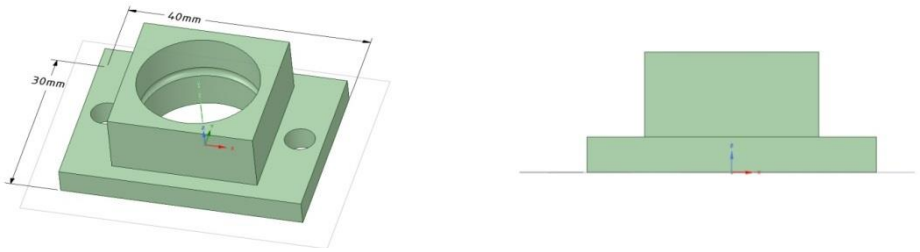
7.5.1.3 Printing materials

Both printers support polylactic acid (PLA) and acrylonitrile butadiene styrene (ABS). Each material has advantages, disadvantages and specific uses. In addition, each material requires different printing settings. Table 7.7 shows some key differences between PLA and ABS [187].

Table 7.7 Comparison of Polylactic Acid (PLA) and Acrylonitrile Butadiene Styrene (ABS)

PLA		ABS	
Advantages	Disadvantages	Advantages	Disadvantages
High water resistance Less part warping Environmentally friendly Strong and Rigid High printing speeds Low layer heights	Low accuracy Low melting temperature	Good accuracy Strong plastic High temperature resistance Mild flexibility	Slight rounding of the corner for sharp edges Cracks as the height of the object increases

As shown in Table 7.7, PLA has a greater resistance to water, which is important in the test rig operation. Both materials were experimentally printed and tested. In order to test the two materials, a design that featured an ultrasonic transducer holder (Fig. 7.10) was printed using different types of materials. This experiment was completed in order to evaluate the two materials and to demonstrate the optimal diameter in which the transducer could be fitted.

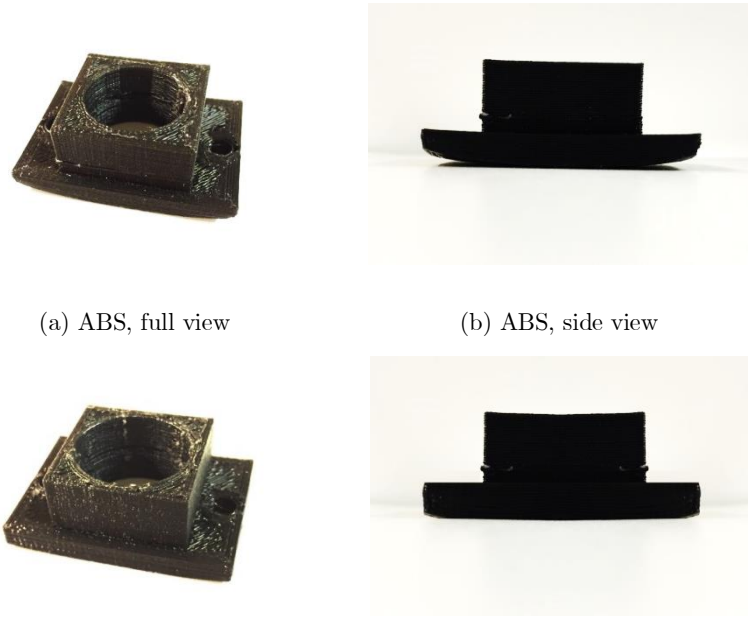


(a) full view (b) side view

Fig. 7.10 The transducer holder model

The transducer holder model features one circular hole (diameter = 190 mm) for the transducer and two smaller holes (diameter = 5 mm) for screws.

The proposed models of the transducer holder were printed using ABS and PLA and are shown in Fig. 7.11. The total printing time using ABS was about 3 hours, consuming around 30 grams of plastic compared to 2.75 hours using PLA and 28 grams of plastic.



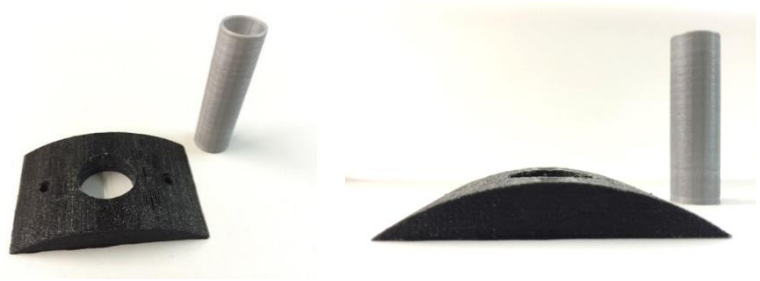
(a) ABS, full view (b) ABS, side view

(c) PLA, full view (d) PLA, side view

Fig. 7.11 Images of printed models of the transducer holder using ABS and PLA

The results of the two printing runs are shown in Fig. 7.11. Printing with ABS resulted in the base surface being slightly curved at the edges. This distortion was due to the fast cooling temperature of this type of material. A few solutions were found to overcome this effect, including the application of a thin layer of glue to the build plate or the use of a specially made sheet that was applied to the build plate to ensure better contact with the base during printing. Fig. 7.11 (d) shows that printing with PLA, which slightly reduced the initialisation printing time, resulted in better base contact (with a lower temperature of the build plate around 60 °C). The use of glue with PLA had disadvantages, including difficulty in removing the object from the glass build plate. Both designs showed similar performance regarding resolution and printing precision.

Additional prints were made using PLA to ensure that the printing was completed at high standards for future models. The additional prints included a transducer holder model that could be fitted to the inner wall of the curved tubes and a cylindrical inlet tube for hose connections. The printed models are shown in Fig. 7.12.



(a) full view (b) side view

Fig. 7.12 Models of the printed curved transducer holder and inlet tube using PLA

The printed models were acceptable. By applying a thin layer of glue to the glass build plate before starting the print, the base was completely flat without any curved edges.

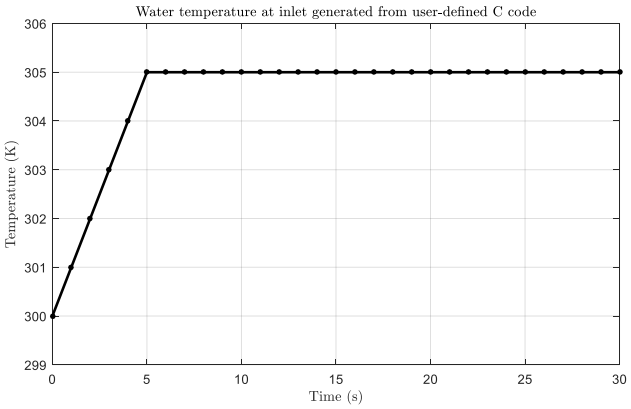
7.5.2 Transient thermal flow analysis

Thermal analysis was used to investigate the optimal position of the ultrasonic transducers. Water has a higher heat capacity than air, ice and other materials, such as gold and glass (4.18 J/°Cg compared to 1.01 J/°Cg for air and 0.13 J/°Cg for gold). Because of this high heat capacity, more time is required to reach thermal equilibrium levels when the water at inlet changes. The aim of the UOTS is to measure the change in temperature more quickly than conventional temperature sensors. Therefore, it is important to place the ultrasonic transducers where the temperature changes at its fastest rate.

The positioning of ultrasonic transducers adjacent to the water inlet results in fast changes in temperature. However, this position is valid only when the diameter of the water inlet is similar to the developed models, which is not true in this case. In this design, water flows through a hose that has a diameter of only 12 mm into a large chamber that has a cubical configuration with a volume of 0.2 L.

CFD simulations were conducted to determine the best ultrasonic sensor placement in the SCSC model, which was chosen based on its thermal transient analysis. The software package Ansys was used, which allows the option of feeding a user-defined variable that controls the temperature in each iteration. The temperature profile at the inlet was set to change from 300 to 305 K in 5 seconds and then remains at 305 K for 25 seconds. In order to control the temperature of the inlet water, some code was written and then was

loaded to the simulations as an external user-defined variable. The resulting profile of the water inlet temperature in C code is shown in Fig. 7.13.

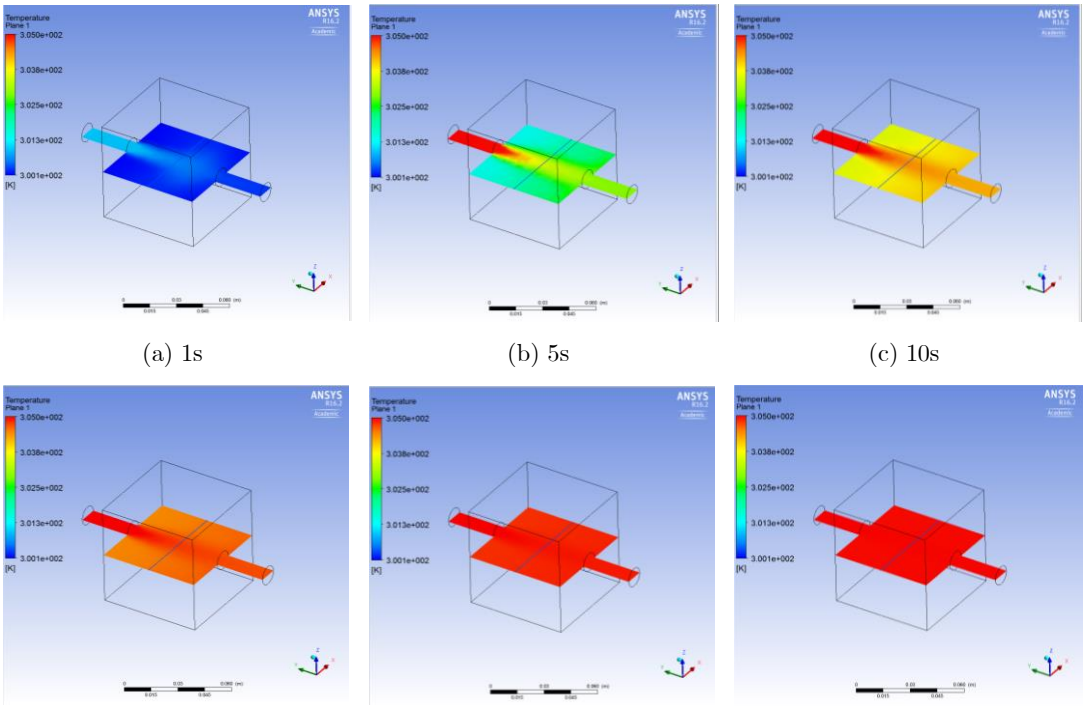



```
#include "udf.h"
DEFINE_PROFILE(unsteady_temperature,
thread, position){

face_t f;
real t = CURRENT_TIME;
begin_f_loop(f, thread) {
if (t<6){
 F_PROFILE(f,thread,position)=300+t;}
else if (t>5){
 F_PROFILE(f,thread,position)= 305;}
}
end_f_loop(f, thread)
}
```

Fig. 7.13 Water temperature profile at the inlet generated with user-defined C code

Fig. 7.14 shows the temperature change in a horizontal cross-sectional area at 1, 5, 10, 15, 20 and 30 seconds.



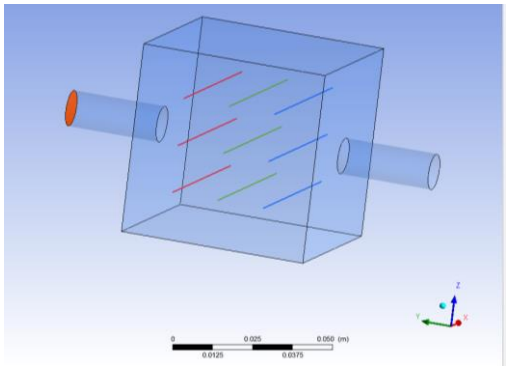
(a) 1s (b) 5s (c) 10s

(d) 15s (e) 20s (f) 30s

Fig. 7.14 Temperature changes in a horizontal cross-sectional area

Nine different locations were chosen to study the effects of the change in water temperature at a flowrate of 8 L/min. These locations were chosen as horizontal straight lines that represented ultrasonic signal pathways. As the ultrasonic sensors averages

temperature across the complete pathway, the recorded temperatures were averaged across these lines. Fig. 7.15 shows the SCSC model with the assigned calculations lines for each location and the corresponding line names of each location.



	Left top	Middle top	Right top	
inlet	Left centre	Middle centre	Right centre	outlet
	Left bottom	Middle bottom	Right bottom	

Fig. 7.15 Temperature calculation lines for each location in the SCSC model. The water flow starts at the inlet that is marked as an orange circle; the figure includes the corresponding line names chosen for each location.

The average temperature of each location was recorded; these are plotted in Fig. 7.16. The graph shows a slight difference in temperature profiles, which peaks around 5 seconds from the start of the simulation.

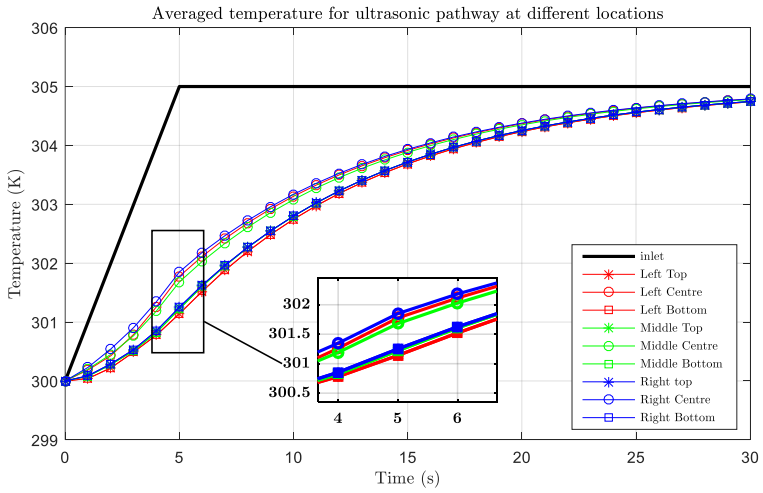


Fig. 7.16 Averaged temperature results for each location in the SCSC model with a zoomed region at 5 seconds

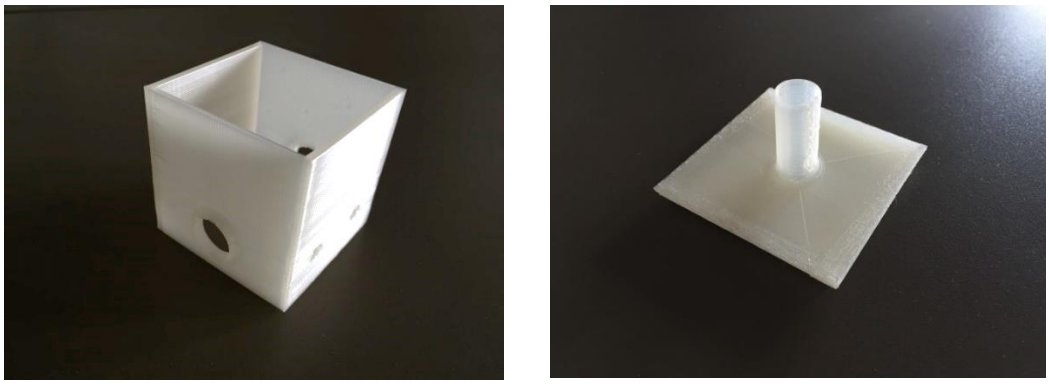
All temperature profiles reached 304.8 K (about 96% of the full temperature) at the end point of the simulation after 30 seconds. Generally, measurement locations were categorised by performance into two sections. The first category included regions on the

centre horizontal line parallel to the water inlet, which are shown in Fig. 7.16 as curves with circles. The second category includes upper and lower horizontal vertical planes. The first category showed a faster thermal response compared to the second category. In the first category, the performance was recorded faster in the right, left and then middle sides consequently on the horizontal centre. In the second category, slower thermal performance was shown with similar values of upper (shown as curves with stars) and lower (shown as curves with squares) sides. However, because of gravity, the lower side showed a slightly faster temperature response compared to the upper side.

Generally, the temperature response was relatively slow because of the high heat capacity of water. About 25 seconds was required for the water to heat from 302 to 305 K when the inlet temperature was set to 304.8 K at a flowrate of 8 L/min.

7.5.3 Parts and test rig structure

The SCSC model was chosen for development. There are several approaches to printing the design. As previously mentioned, 3D printing technology is complicated when a horizontal structure is printed without any supporting rafts. Therefore, the design has to be printed in separate parts, which allows for both a shorter printing time and enhanced accessibility in mounting the sensors. The design was divided into two parts: sidewalls that hold transducers and the top and bottom inlet and outlet of electric motors coolant, as shown in Fig. 7.17.



(a) side view (b) top cover

Fig. 7.17 Printed model parts of the SCSC model

The ultrasonic and temperature sensors were mounted on the sidewalls using a special plastic glue. After the sensors were fixed in the model, a silicon water-proof sealant was

applied to the edges to block any water leakage, especially at high flowrates, which increased the pressure on the sensors.

The 3D printing G-code generator has a default fill density of 30%, which is the ratio normally used in general-purpose printing. The fill density is automatically lowered to consume the least amount of plastic resources and shorten the printing time. The first printed model, which used the default density, leaked from the walls even with zero flowrate. The second model was printed with a fill density of 60%, and it showed no leakage without a flow. However, when the flowrate increased above 6 L/min, water leakage was observed. The final model was printed with a full fill density, which showed no leakage when all flowrates achieved by the water pump were tested. This fill density increased plastic consumption by 32% and the printing time by 20%.

The printed designs were glued together and sealed by the silicon. Fig. 7.18 shows the design after the construction and mounting of the ultrasonic and temperature sensors.

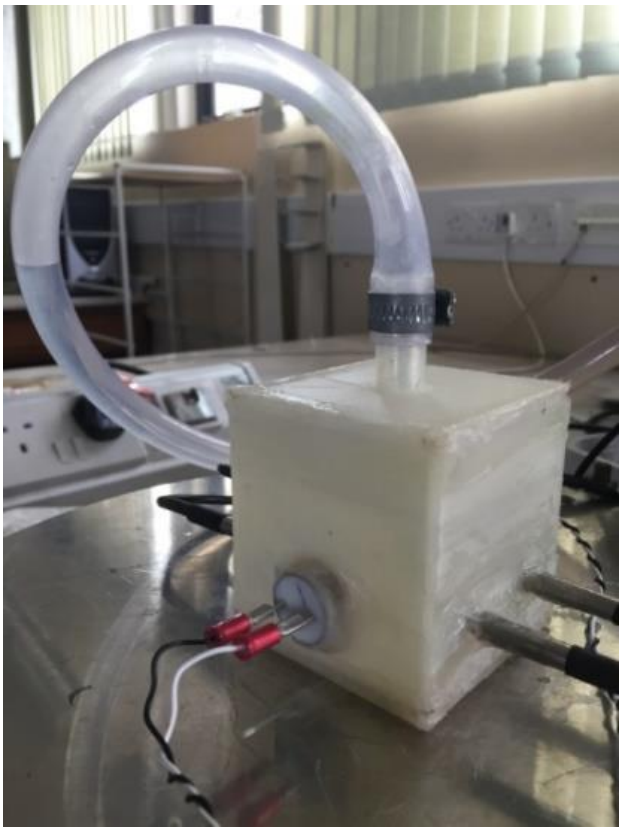


Fig. 7.18 Image of the design after the construction and mounting of the ultrasonic and temperature sensors

7.6 Experimental setup and results

7.6.1 Experiments in UOTS with flow in a single chamber

7.6.1.1 Equipment and experimental setup

The experiments conducted focused on measuring the ultrasonic frequency when water flowed between transducers. The water was circulated in a closed-loop system using a submersible electric pump. Fig. 7.19 shows the fully generated experimental setup.

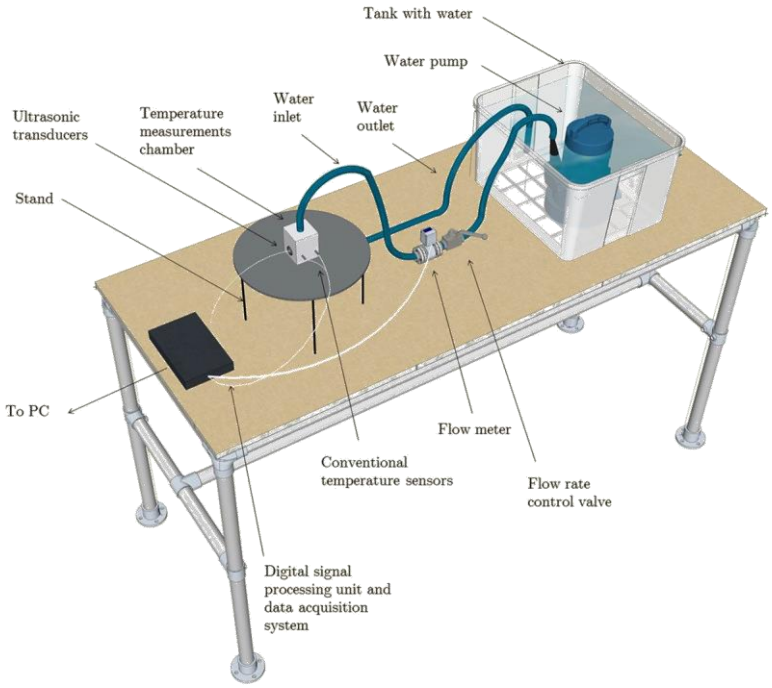
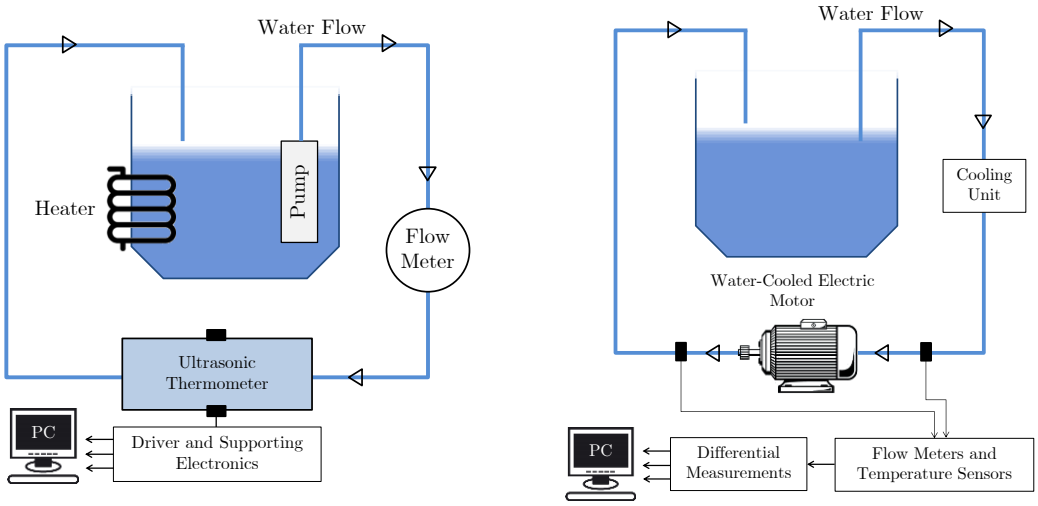


Fig. 7.19 Experimental setup for measuring water temperature with flow in a single chamber

This type of pump was chosen in order to eliminate the effect of the jerk observed in low-power aquarium water pumps. The submersible water pump has a fixed flowrate of 100 L/min. This flowrate was found to be dependent on the pressure at the pump outlet; therefore, it was important to control the water flow to an appropriate level. A float switch was used to have full control of the flowrate. The pump was placed in a 120 L tank to ensure the constant flow operation. An aquarium heater was placed inside the tank to simulate the heat generated by the electric motor. The experimental setup for evaluating the power loss of the water-cooled electric motor is shown in Fig. 7.20 (a); the classic method setup for motor evaluation is shown in Fig. 7.20 (b).



(a) UOTS system (b) classic method

Fig. 7.20 Experimental setup for measuring temperature using ultrasonic oscillating sensors for water-cooled electric motors

The water flow was measured using an inexpensive Hall Effect flowmeter, as shown in Fig. 7.21 (a). These types of flowmeters are capable of measuring flowrates up to 30 L/min, and they can be powered by a low voltage source. The flowmeter transmits the flowrate readings to a PC using a simple microcontroller setup. Because this flowmeter was found to have an orientation dependence, it was important to calibrate the readings using a more accurate flowmeter. Therefore, the MBLD flowmeter, which is shown in Fig. 7.21 (b), was used for the calibration. This flowmeter must be installed vertically; the position of the metal ring indicates the flowrate on a graduated scale.

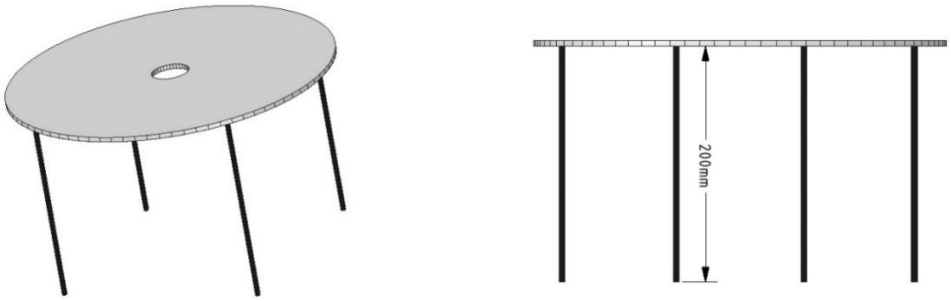


(a) Hall Effect (b) MBLD

Fig. 7.21 Flowmeters used to measure the flowrate of water

A stand was constructed in order to minimise the vibration of the test rig and the ultrasonic transducers at the maximum flowrate. This stand consisted of four legs and a

circular plate at a height of 200 mm. A hole was inserted in the middle of plate to allow the solid connection with the water outlet. Top and side views of the stand are shown in Fig. 7.22.



(a) top view (b) side view

Fig. 7.22 Test rig stand and holder

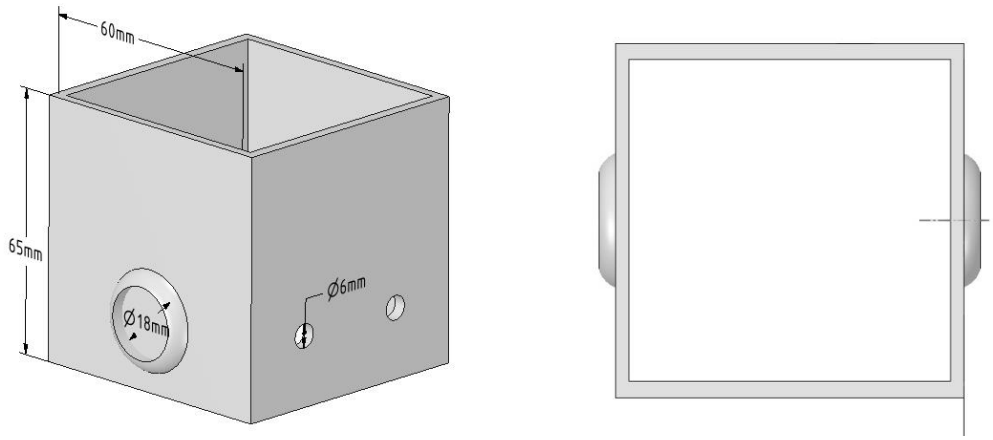
The supporting electronics were connected to the appropriate parts from the chamber and then to the PC. These electronics included the PSoC-based modular system that was developed in Chapter 4, which contains an ultrasonic driver, a signal multiplexer and a frequency meter. In addition, supporting electronics, including the temperature data logger and flowmeter system developed to log flowrate data, were also connected to the corresponding hardware.

7.6.1.2 Chamber construction

The comparison of the models showed that the SCSC model provided the best response in terms of turbulence and pressure. The construction of this model is relatively simple. The design includes one pair of ultrasonic transducers, a transmitter and receiver as well as four conventional 1-Wire temperature sensors.

On the sides of the chamber are circular holes 2×18 mm in diameter in two facing walls, which hold the ultrasonic transducers. The sensors are placed 45 mm apart from the inlet, which is on the top side. This placement achieved the fastest thermal response. Each of the remaining two sides contain holes 2×6 mm in diameter, which fit the 1-Wire temperature sensors placed on the same horizontal axis as the ultrasonic sensors in order to estimate the average temperature of the ultrasonic pathway.

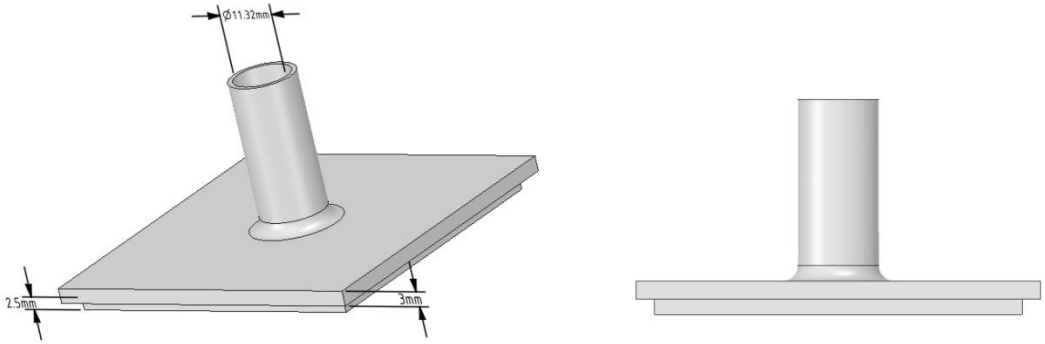
The wall thickness was set at 2.5 mm to avoid water leakage. The width of the chamber was set at 60 mm and the height was set at 65 mm, which allowed the inlet and outlet to be inserted at 2.5 mm from each end. The top and side views of the SCSC parts are shown in Fig. 7.23.



(a) side view (b) top view

Fig. 7.23 The walls of the SCSC design

The inlet and outlet connector sides consist of two square plates. The upper plate has an area of 65×65 mm and a thickness of 3 mm; the lower plate has an area of 60×60 mm and a height of 2.5 mm, which allows this model to be securely placed inside the sidewall section. An inlet with a diameter of 11.3 mm is placed at the centre of the plates to ensure the appropriate fitting of the water tube leading from the pump. A screw clamp is fitted on the tube to prevent water leakage. The top and side views of the inlet and outlet of the SCSC design are shown in Fig. 7.24.



(a) top view (b) side view

Fig. 7.24 The inlet and outlet connector parts of the SCSC design

All three parts were carefully glued together, and then a waterproof silicon sealant was applied to avoid any leakage. Because the joint area showed good stability with no leakage at the maximum set flowrate, screws were not required.

7.6.1.3 Temperature control analysis

In order to study different qualities of the parameters of ultrasonic frequency, such as temperature-frequency sensitivity and hysteresis, it was necessary to perform temperature cycles. In the previous experiments, when no flow was present, a controlled oven was programmed to heat and cool the water in a given number of temperature cycles. However, for several reasons, it is difficult to apply the exact temperature control methodology when water is circulating. The water flows continuously within the chamber placed outside the oven, forcing the temperature of the water to be balanced with the ambient temperature. Moreover, the tank holds about 120 L of water, and this amount requires a considerable amount of time to heat. Therefore, instead of heating the surrounding environment, a heating element was placed inside the tank (i.e., an aquarium heater). Hence, the temperature was controlled by turning on the aquarium heater until the desired temperature was achieved and then allowing the water to cool naturally.

The graph in Fig. 7.25 shows the temperature profiles of the water before and after removing the heating source (natural cooling) while the water pump was under operation.

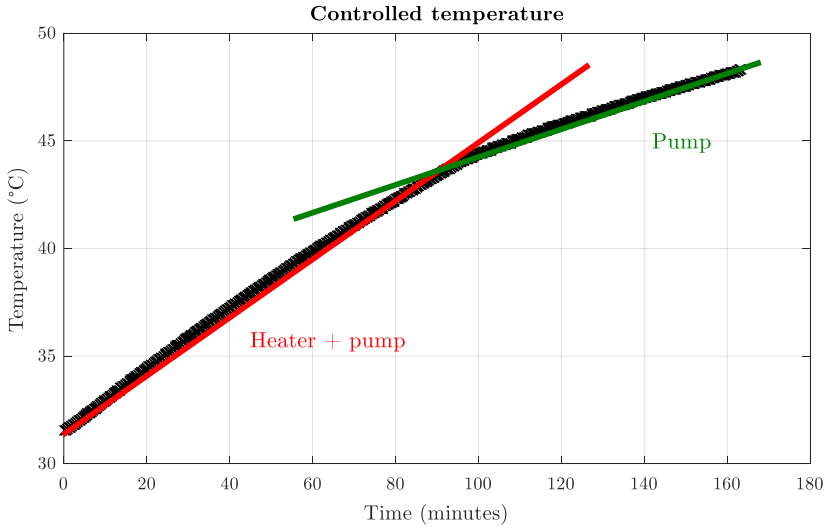
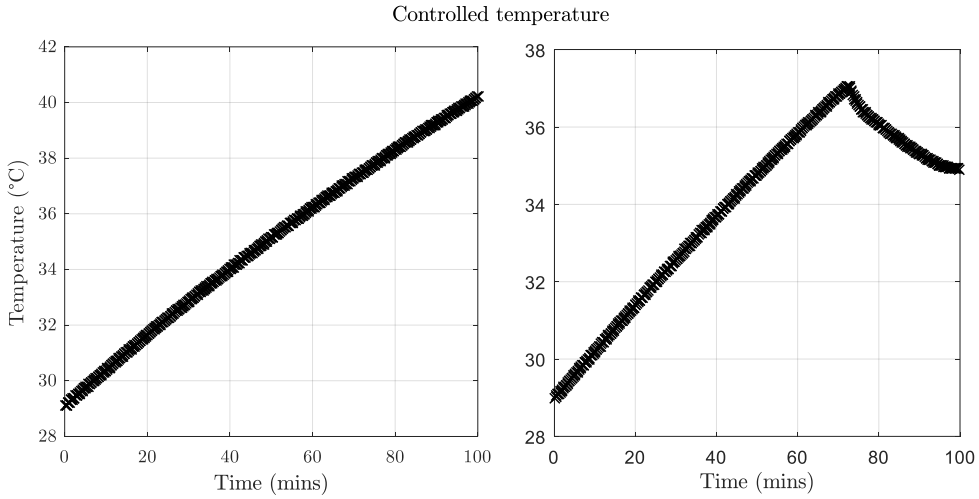


Fig. 7.25 Rate of increase in water temperature when the aquarium heater was turned on (red line) and turned off (green line)

In Fig. 7.25, the red gradient line represents the rate of change in the water temperature when the aquarium heater was operating. After 90 minutes, the heater was turned off, and the water was cooled naturally to room temperature. However, as shown in Fig. 7.25, the temperature continued to increase, which indicates that the electric pump continued to generate some heat. This heat was produced by the high water friction inside the motor.

In order to study the behaviour of ultrasonic frequency, the temperature needs to be controlled in cycles. One solution was to employ a water cooler to compensate the heat generated by the electric pump. Because cooling equipment was not available, and simple temporary cooling options could be used, ice was added to the tank. Three litres of ice were found sufficient to decrease the water temperature by 3 K as shown Fig. 7.26 (b). The graph in Fig. 7.26 (a) shows the temperature response when two litres of cold water were added with no significant decrease in the water temperature.



(a) cold water (b) ice addition

Fig. 7.26 Water temperature response when ice and cold water were added

7.6.1.4 Results and discussion

The first experiment was conducted by varying the flowrate while keeping the temperature at a constant level. The purpose of this experiment was to study the behaviour of the ultrasonic frequency when the flowrate of the water changed.

In this experiment, the flowrate was increased by a step of 2 L/min from 0 to 14 L/min. In each flowrate tested, the ultrasonic frequency was recorded for five minutes. The graph in Fig. 7.27 shows the results.

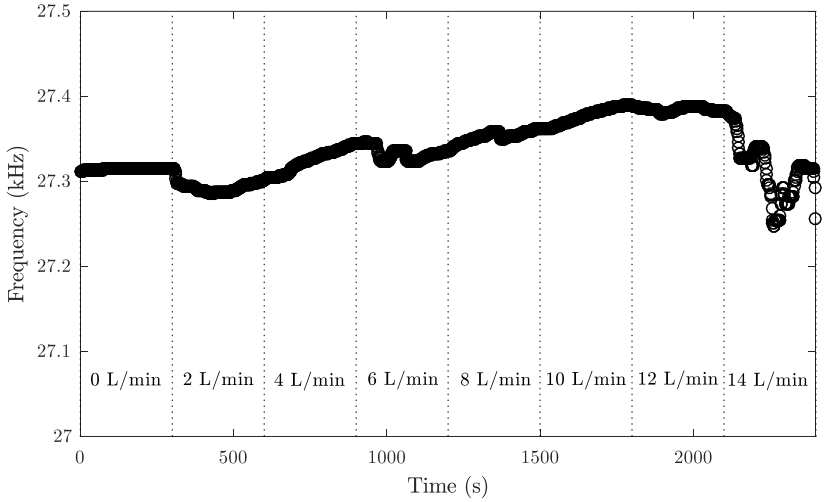


Fig. 7.27 Ultrasonic frequency response to flowrate changes

As shown in Fig. 7.27, when the flowrate was zero, the frequency was stable and no jumps were observed. However, the frequency exhibited a few jumps and some notable scatter when the water started to flow. At some flowrates, the ultrasonic frequency required a few minutes to stabilise, and the amount of the stabilisation time varied from one flowrate to another. Moreover, at some flowrates, the ultrasonic frequency exhibited high scatter and several jumps. Overall, the frequency oscillated at the same resonance frequency in all flowrates tested. The frequency continued to increase for the full duration of the experiment because of the heat produced by the electric pump. The observed increase of scatter was due to the higher turbulence inside the chamber which affects the ultrasonic signal transmitted between transducers.

At some flowrates, such as $Q = 2$ L/min, the frequency had not stabilised by five minutes, which increased the complexity of the evaluation. Hence, in the experiments, longer durations were required to determine the parameters of the ultrasonic frequency. Each flowrate was tested for 30 minutes with the temperature kept at a constant level. The graph in Fig. 7.28 shows the results at the flowrates of 0, 6 and 14 L/min.

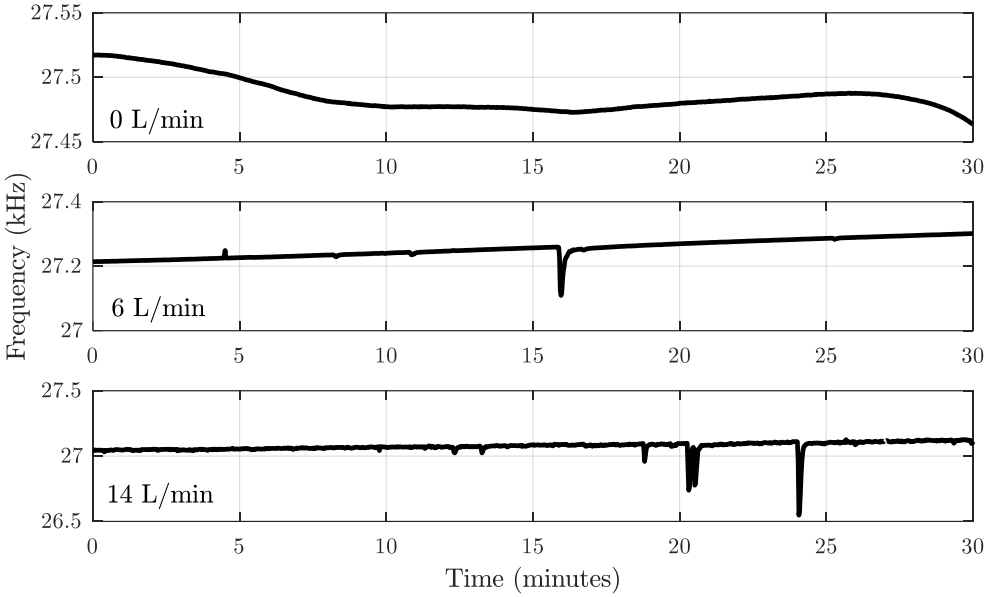


Fig. 7.28 Output frequincies responses at different flowrates

Some important parameters were found in the results of the flow experiments. The first parameter was frequency scatter, which is the frequency variation in flat regions. The scatter information was important in evaluating the overall performance and in deriving the filtering requirements when data sensor fusion was applied. In Fig. 7.29, the graph shows the frequency variations (scatter) at different flowrates.

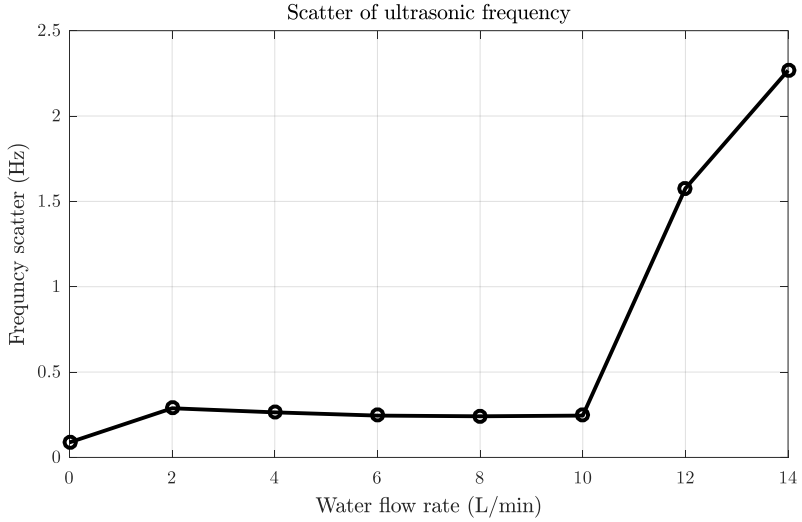


Fig. 7.29 Frequency variations (scatter) at different flowrates

The second parameter that was analysed was the occurrence of jumps. By observing different sets of data, a jump was defined as a sudden change in frequency greater than

5 Hz across a 30-minute sample. Table 7.8 shows the number of jumps found at each flowrate.

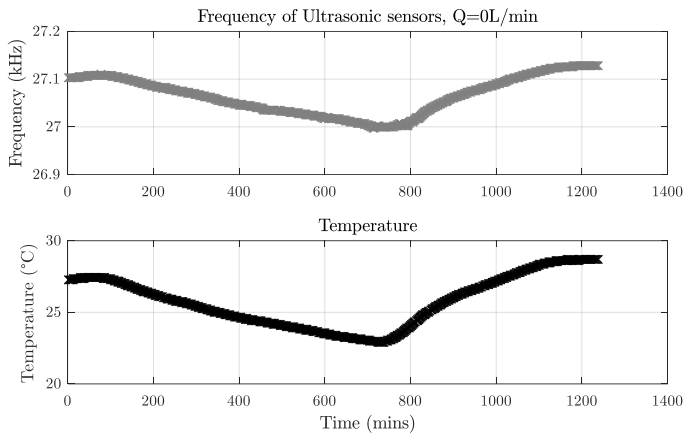
Table 7.8 Number of Jumps Found at Each Flowrate

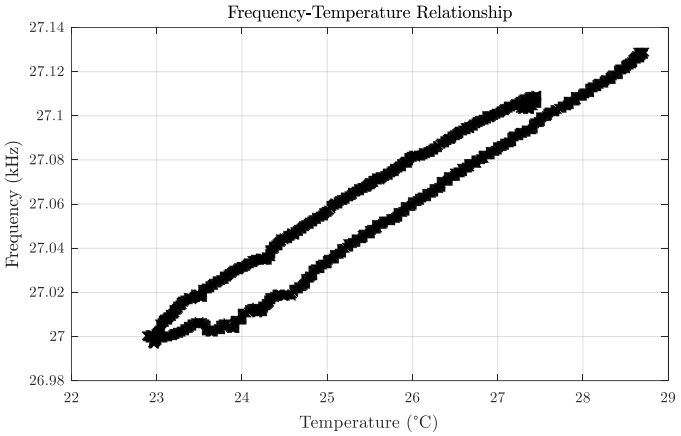
Flowrate (L/min)	0	2	4	6	8	10	12	14
Number of Jumps occurrence	0	0	1	3	4	6	8	13

Fig. 7.29 shows that the scatter remained under 0.3 Hz in flowrates up to 10 L/min. The scatter significantly increased after 10 L/min, reaching 2.3 Hz at 14 L/min. The jumps occurred for the several reasons described in Chapter 5, which include different centre frequencies in both transducers, noisy phase response and the non-integer wavelength number. The number of jumps was important in evaluating the performance of each flowrate operation. Moreover, this information was used in the application of sensor fusion processing.

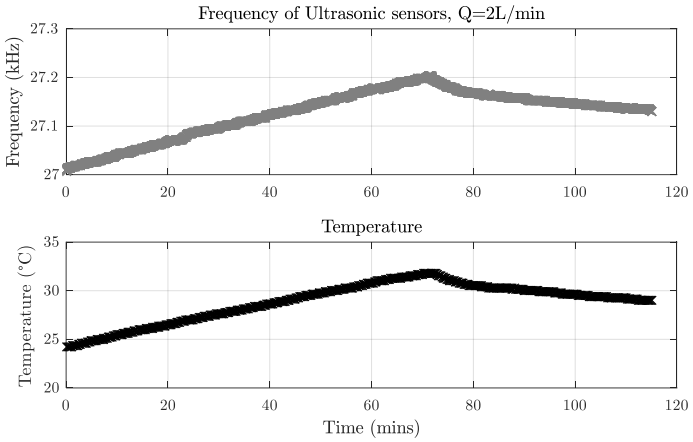
The rapid increase in frequency scatter occurred for two reasons. First, the maximum flowrate of the electric water pump was dependent on the water level above and below the pump itself. The quantity of bubbles formed at the motor outlet was also dependent on the water level. For flowrates over 10 L/min, it was observed that bubbles formed at the pump outlet. These bubbles affected the readings of ultrasonic frequency as they passed across the ultrasonic pathway, resulting in some reflections and hence unstable frequency readings. The second reason was that the water turbulence significantly increased when it reached 16 L/min compared to the turbulence value below 10 L/min. The increase in turbulence was nearly four times greater than in the flowrate of 8 L/min. This result was consistent with the CFD simulation shown in Fig. 7.5.

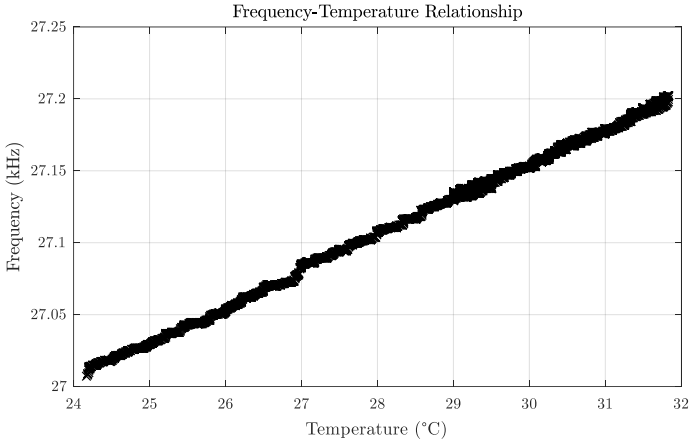
To study parameters such as hysteresis, temperature cycles were performed at the flowrates of 0, 2, 6 and 12 L/min. The recorded ultrasonic output frequencies and temperature changes from conventional temperature sensors, in addition to temperature versus frequency graphs, are shown in Fig. 7.30.



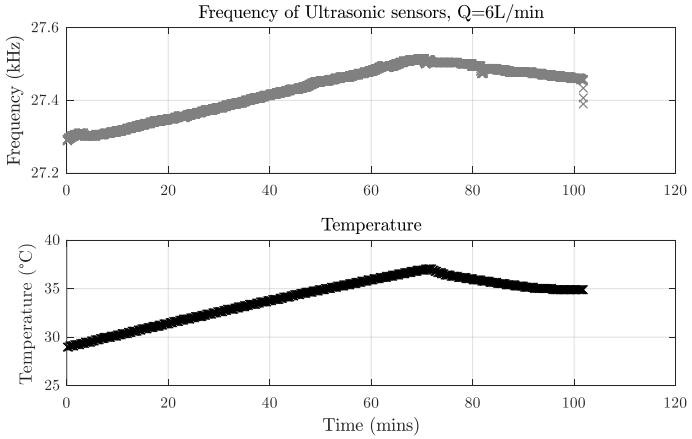


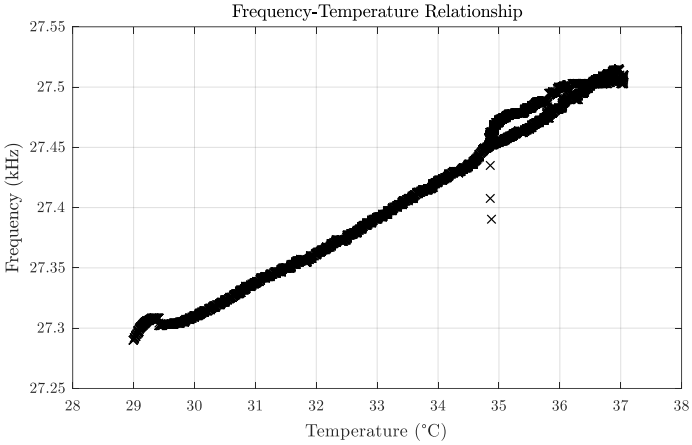
(a) 0 L/min



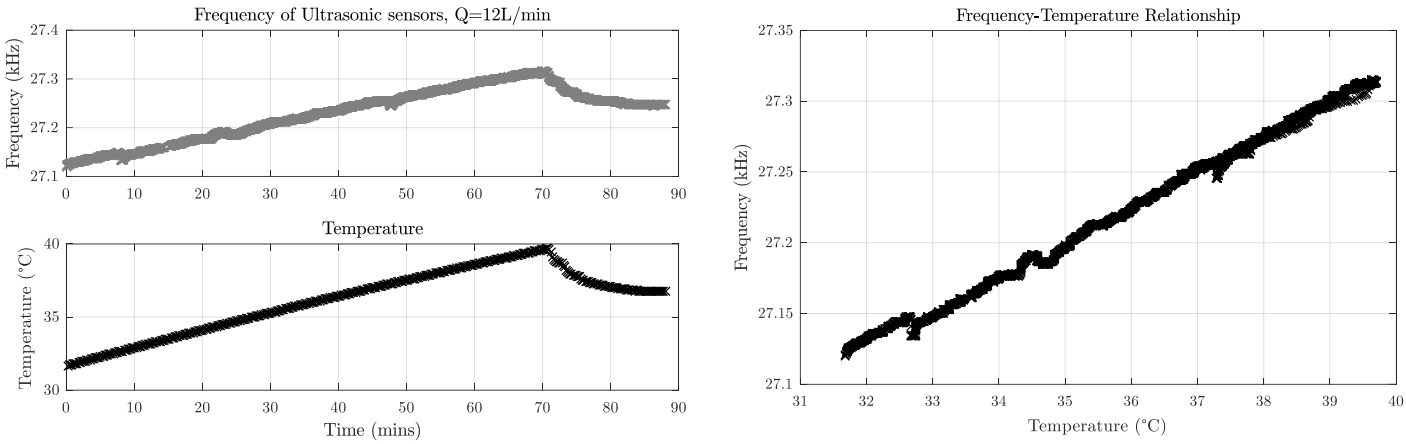


(b) 2 L/min





(c) 6 L/min



(d) 12 L/min

Fig. 7.30 Temperature and frequency responses versus time (left) and temperature-frequency relationships (right) in different flowrates

The results showed similar responses for ultrasonic frequency and temperature profiles. With regard to frequency–temperature hysteresis, when some flow was present, the results showed reduced hysteresis. However, as shown in Fig. 7.30 (a), when the water was in a still state, the hysteresis was notably large. The reason was that the duration of the measurement of the flow Q = 0 L/min was significantly longer than in the other experiments because it was subjected to natural heating and cooling. As discussed earlier, when the flowrate was at the maximum of 12 L/min, the ultrasonic frequency exhibited relatively greater scatter and more jumps, as shown in Fig. 7.30 (d).

With regard to the frequency–temperature sensitivity, Table 7.9 provides the sensitivity values at different flowrates shown in Fig. 7.30.

Table 7.9 Frequency and Temperature Sensitivity at Various Flowrates

Flowrate (L/min)	0	2	6	12
Sensitivity (Hz/K)	26.5	27	27	27.5

Fig. 7.29 shows that the scatter slightly increased when the flow was increased. The reason for this result might be that the higher scatter values increased the uncertainty in measuring the sensitivity values. Convergent sensitivity values would have facilitated the data-sensor fusion process.

7.6.2 Experiments using UOTS heat loss differential measurements

7.6.2.1 Equipment and experimental setup

In order to evaluate the power loss in real water-cooled electric motors, differential temperature measurements were taken at the inlet and the outlet of the cooled motor, equation (7.1).

To simulate a real motor, two identical chambers were used to take differential measurements. Chamber 2 contained the outlet-heated water, and chamber 1 contained the inlet-cooled water. The experimental setup diagram is shown in Fig. 7.31.

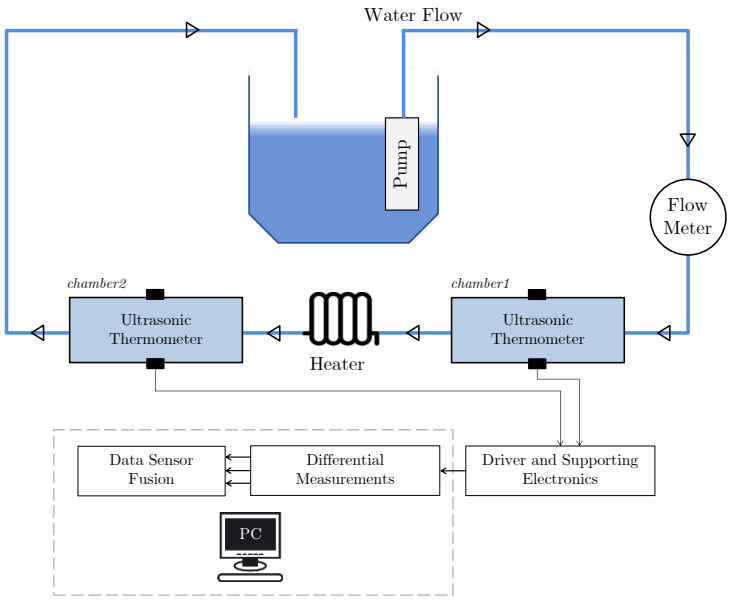


Fig. 7.31 Experimental setup for taking temperature differential measurements using ultrasonic oscillating sensors for water-cooled electric motors

An experimental procedure similar to that used in the previous experiment with a single chamber was followed. Water was pumped to the system using an electric pump; a flowmeter was then added to monitor the volume flow. After the water passed the first chamber, it was heated to achieve the difference in temperature between the two chambers.

Several methods could be implemented to heat and to cool the water. In one method, a Peltier device can be used to increase the temperature of the water. The Peltier device allows the accurate determination of the amount of heat generated by measuring the voltage across the device. This device is also capable of cooling the water. Peltier devices

are usually safer than aquarium heaters are because they operate from a lower voltage source and generate a relatively low heating power of around 10 W. In the second method, an aquarium heater was placed inside the enclosed heating tank. A mesh was created inside the tank in order to force the water flowing inside the tank to heat. A third method of heating was achieved by using an external aquarium heater. Inexpensive heaters can easily generate 300 W of heat, and the outlet water temperature can be fixed at any value within the range of 20 to 35 °C. However, the third method was the least complex, and can result in the least amount of water leakage.

Because the heater and the pump continued to heat the water, ice and cold water were added to the water tank to lower the temperature. The amount of coolant was quantified by monitoring the temperature in both chambers. The experimental setup for taking differential measurements of the temperature of the water-cooled electric motor is shown in Fig. 7.32.

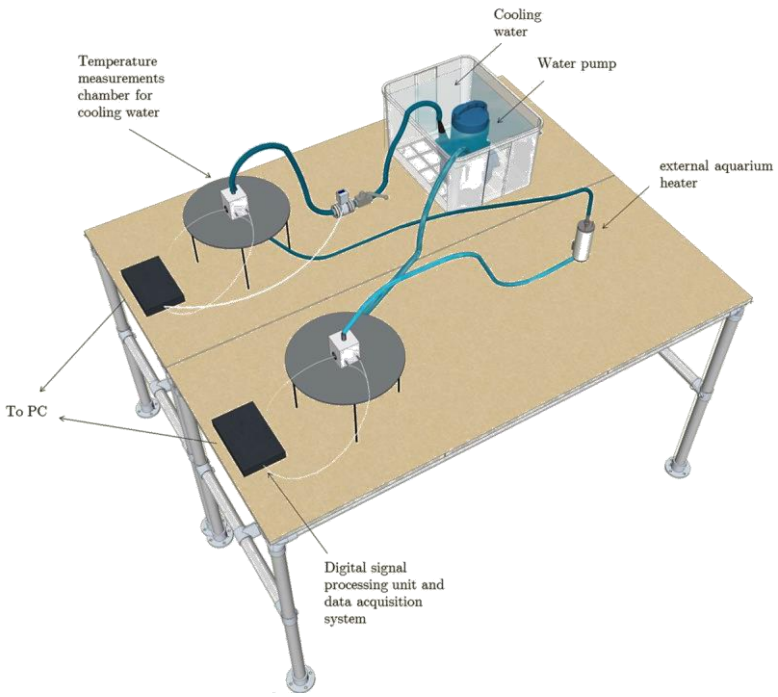
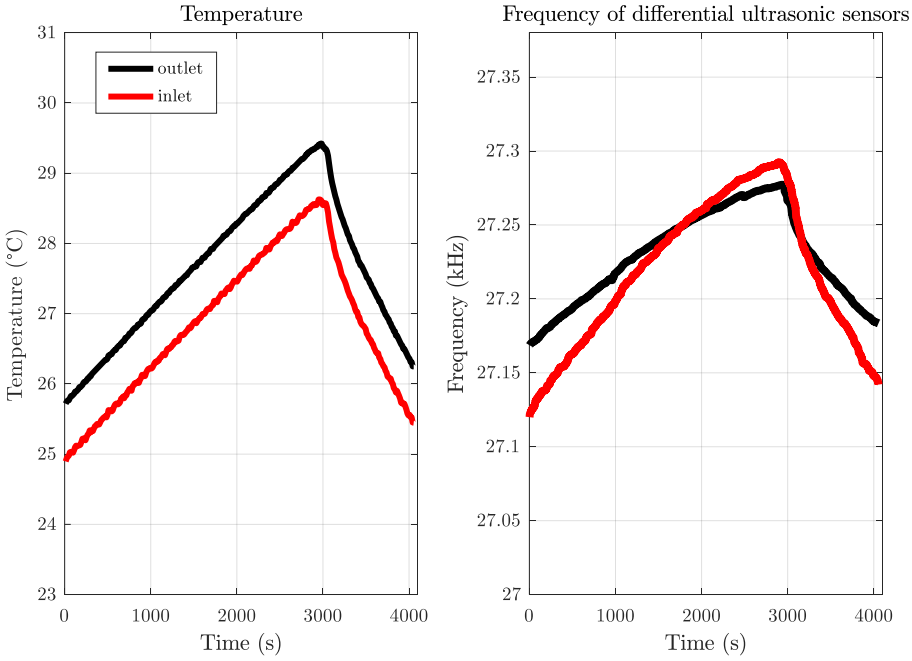


Fig. 7.32 Experimental setup for temperature differential measurements

7.6.2.2 Results and discussion

The results obtained from this experiment with two chambers were similar to those of the previous experiment with one chamber. The same equipment and parameters were used in both experiments.

The results of the experiment that was conducted using a temperature control are shown in Fig. 7.33. The amount of heat generated by the aquarium heater was 75% of its full heating power. Extra cold water and ice were added to the tank to study the behaviour near the inflection point. This experiment was conducted to investigate the cooling process in a real motor and to estimate the heat dissipated in the system.



(a) Temperature (b) Ultrasonic Frequency

Fig. 7.33 Temperature recorded using conventional sensors and ultrasonic output frequencies versus the time

As Fig. 7.33 shows, the ultrasonic frequency followed the temperature in the full cycle without any noticeable jumps in either chamber. The water was heated by 4 K during the testing period, and the frequency changed by about 110 Hz at the inlet, resulting in the sensitivity of 27.5 Hz/K. The outlet chamber showed a similar increase in temperature; however, the UOTS sensitivity was greater because different pairs of transducers were used, which was explained in Chapter 5.

The data fusion developed in Chapter 6 was applied to the results shown in Fig. 7.33 in order to process the output frequency of UOTSes. The results of the application of the data fusion are shown in Fig. 7.34.

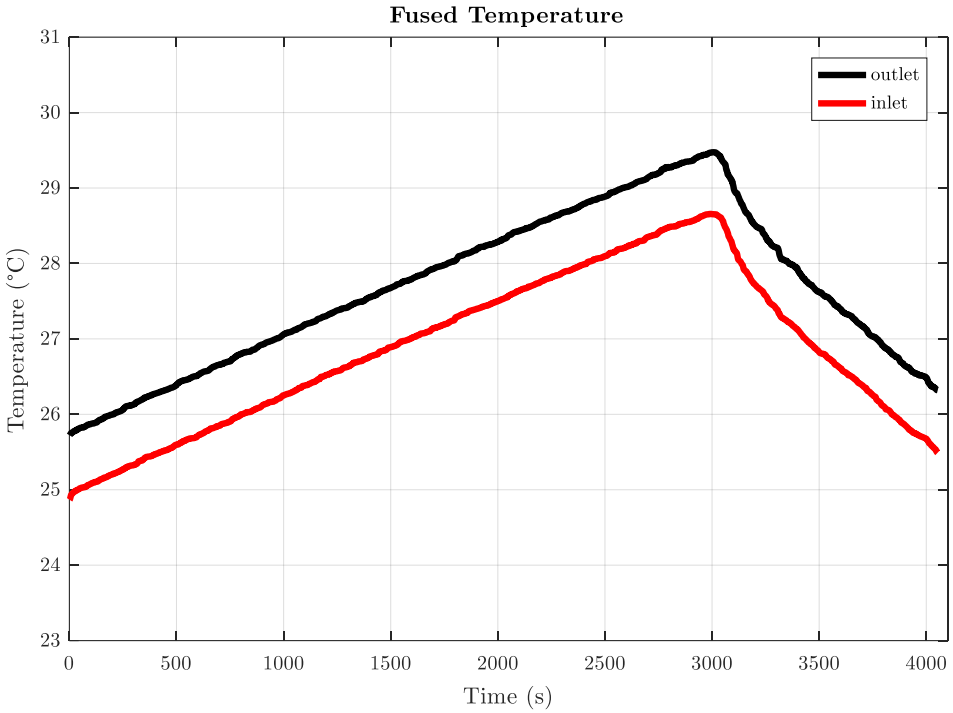


Fig. 7.34 Results of applying data fusion processing to the inlet and the outlet of the electric motor

The differential measurements were determined by subtracting the water temperature at the outlet from the water temperature at the inlet. The results of the differential measurements are shown in Fig. 7.35.

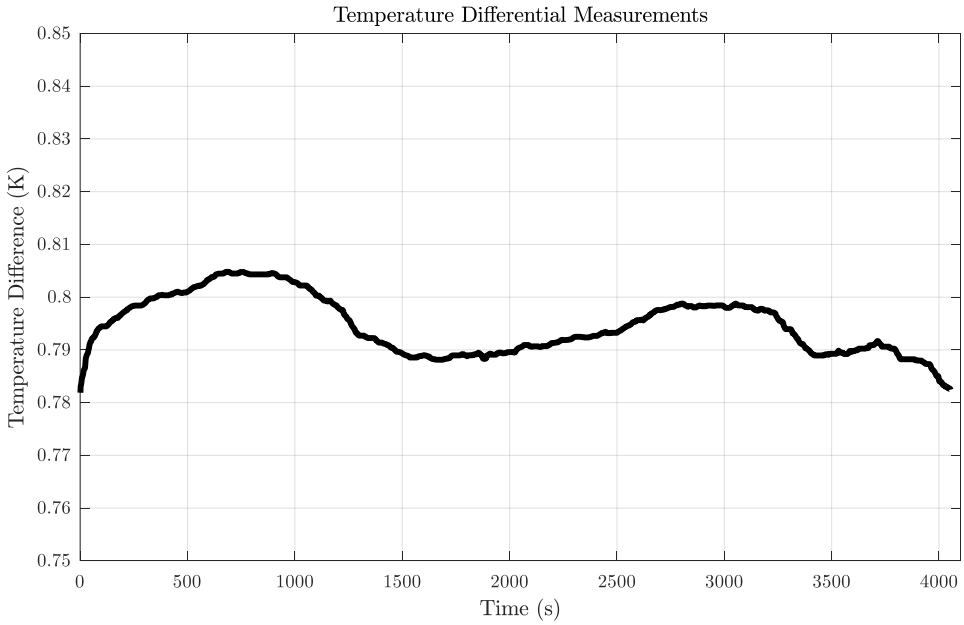


Fig. 7.35 Differential fused temperature measurements

Equation (7.1) was used to measure the power loss in a water-cooled electric motor.

$$P_{loss} = CQ\Delta T \tag{7.15}$$

where

P_{loss}		heat dissipated to cooling water in watts
C	4180 J/kg.K	specific heat capacity of pure water at 25°C
Q	0.068 kg/s	water flow rate at 4 litres per min
ΔT	From Fig. 7.35	temperature difference between outlet and inlet in kelvins

Fig. 7.36 shows the profile of the overall power loss in the system when the flowrate of the water pumped through the system was equal to 4 L/min.

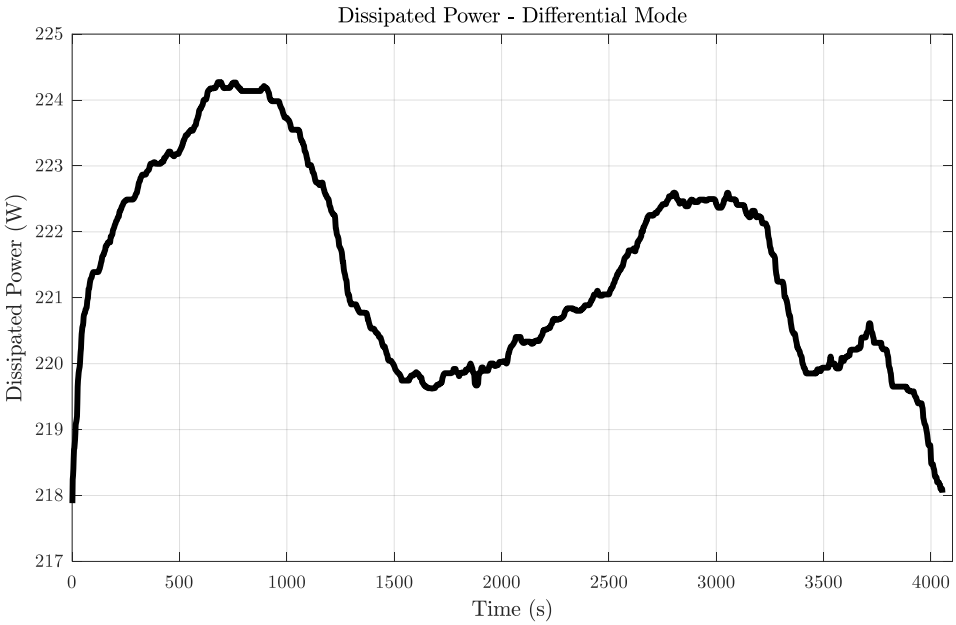


Fig. 7.36 Power loss in the simulated motor during the experimental period

As shown in Fig. 7.36, the power loss estimation matches the specifications of the aquarium heater, the heating power of which was rated at 300 W. The dissipated power fluctuated around 220 W when the aquarium heater was operated at 75% of its rated power.

Regarding the analysis of the data fusion performance, the graph shown in Fig. 7.37 was plotted using raw data collected by four calibrated conventional temperature sensors.

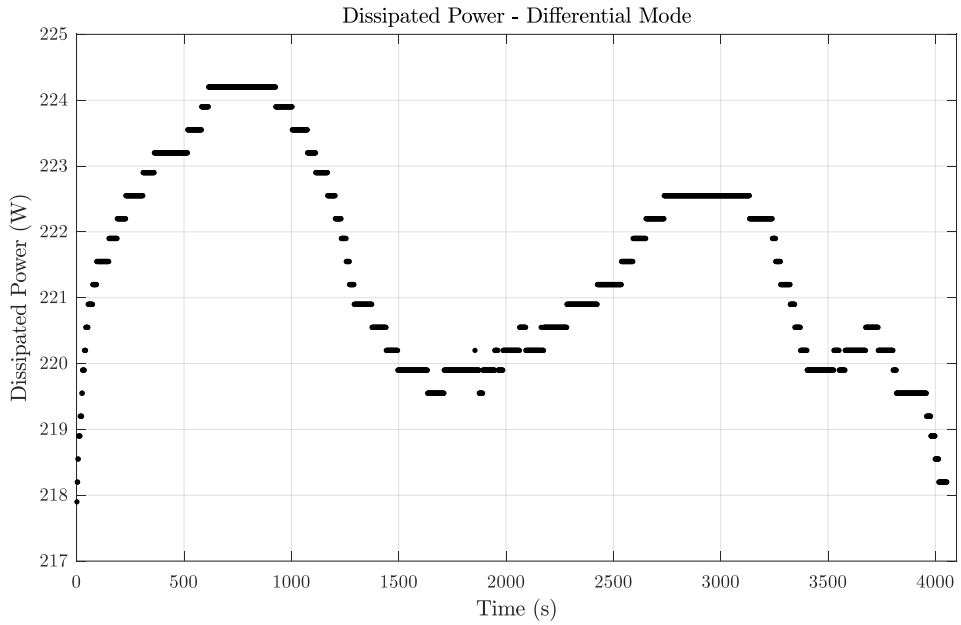
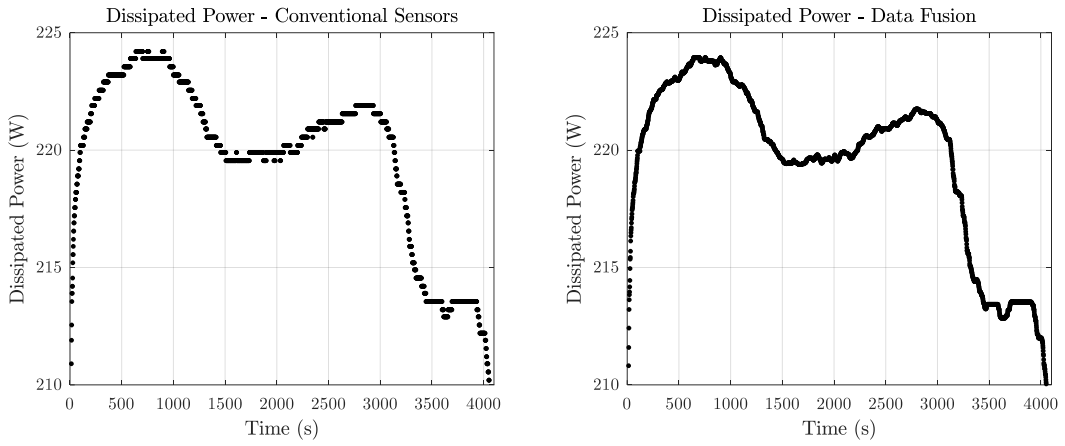


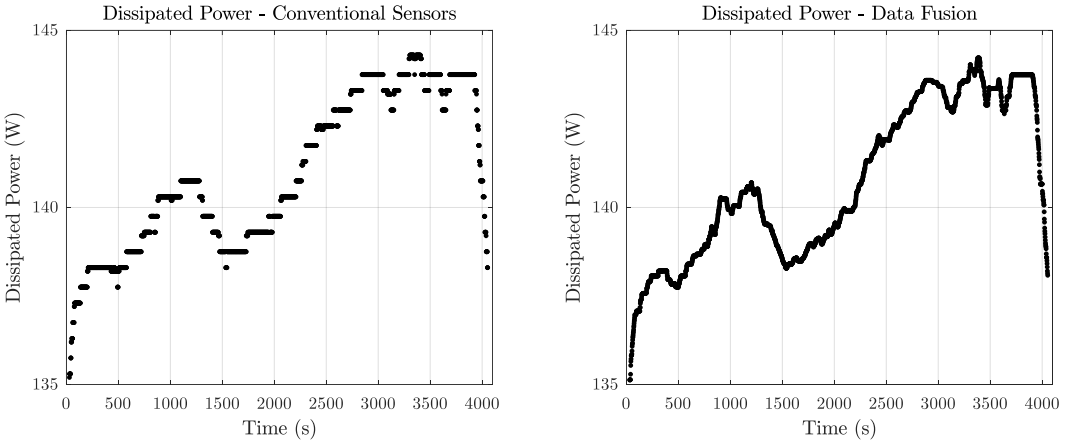
Fig. 7.37 Power loss estimation using raw data from conventional temperature sensors

Fig. 7.37 shows that the application of data fusion increased the resolution of power loss measurements compared to power calculations based on the use of conventional temperature sensors.

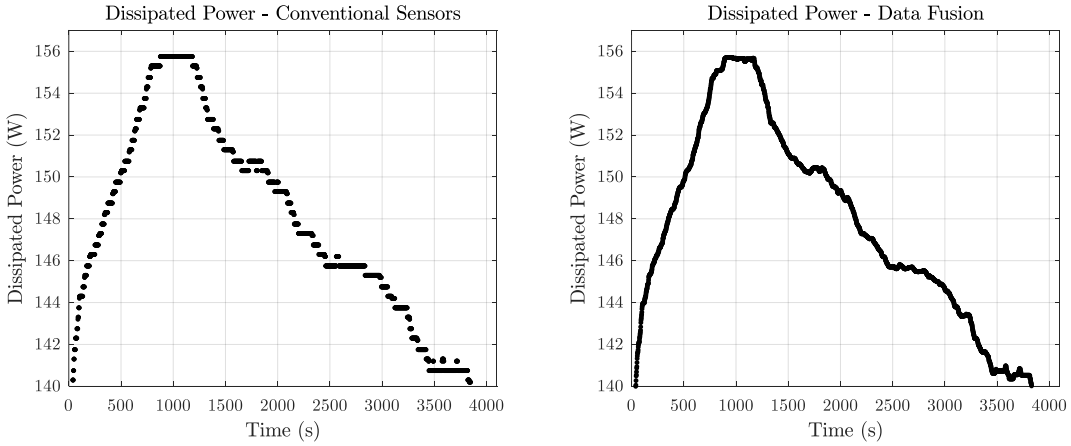
In order to ensure the repeatability of the results, four sets of results were collected; two showing that the heater operated at 75% of its full load [Fig. 7.36 and Fig. 7.38 (a)] and two showing that the heater operated at 50% of its full load [Fig. 7.38 (b, c)].



(a)



(b)



(c)

Fig. 7.38 Power loss calculated from the fused temperature (left) and power loss estimation using raw data from conventional temperature sensors (right) in heaters set at (a) 75%, and (b, c) 50% of the rated power

7.7 Summary

In this chapter, a UOTS-based system for measuring differential heat in a water-cooled electric motor was developed. The development was initiated by simulating heat loss measurements in two chambers that represented the inlet and outlet of an electric motor.

The results showed that employing a temperature measurements device with an accuracy less than 0.5 K in electric motors would complicate the motor classification process. Hence, a UOTS that featured precise accuracies could be employed to achieve a more reliable classification at a lower cost.

Three chamber designs were fully developed, analysed and compared based on the following factors: pressure, velocity, turbulence and manufacturing simplicity. The SCSC model was chosen because it showed good turbulence in flowrates up to 10 L/min. Thus, it was suitable for conducting differential measurements in temperatures of 10 K between chambers.

The 3D printing technology was chosen to construct the chamber. Several samples were printed in order to verify the best printing parameters, including printing infill, supporting rafts and printing resolution.

Using CFD, various parameters were varied to evaluate the performance and establish the limitations of the developed model. These parameters included the placement of ultrasonic transducers in a location with the fastest thermal response detection. In addition, the results of the flow analysis showed that the low turbulence inside the chamber was achieved when the flowrate was equal to or below 10 L/min.

The experimental results showed that the values of the ultrasonic frequency scatter were 0.3 Hz in flowrates below 12 L/min, which verifies the outcomes of the CFD simulations. Experiments with longer durations of UOTS at different flowrates were also conducted. The results showed that the hysteresis effect was minimised (compared to cases in which the water was still) because of reduced history effect.

Experimental results were determined for a single chamber, and differential measurements were conducted using two chambers. After applying the data fusion of UOTS and the temperature measured by the conventional sensors, the dissipated power

was estimated for a 300 W aquarium heater that was operated at 50% and 75% of its rated power.

Chapter 8

Summary and Conclusion

8.1 Summary of individual chapters

8.1.1 Chapter 1

In Chapter 1, the need for the development of an inexpensive but accurate instrument for measuring temperature based on an oscillating sensor was identified. The broad field of heat measurements was discussed, and the relevant phenomena and technologies were considered within the three main groups: heat loss in motors, calorimeters and conventional temperature measurement devices. Different approaches to ultrasonic thermometry were discussed. The majority of the developments in this field were conducted using expensive, narrowband ultrasonic transducers. In this study, the aim of producing a low-cost UOTS instrument for differential measurements was to be achieved through the following steps:

- Development and verification of sensor electronics using inexpensive components.
- Development of an AGC system for ultrasonic signals in order to avoid saturation and preserve ultrasonic transmitted signals.
- Elaboration and verification of the data fusion procedure used by the sensor to compensate for different piezoelectric effects, such as temperature–frequency hysteresis.
- The design of a 3D-printed experimental test rig for differential power loss measurements and the classification of water-cooled electric motors.

8.1.2 Chapter 2

In this chapter, ultrasonic sensors and their applications, including temperature measurements, were discussed. Ultrasonic measurement methods were considered through four approaches: through transmission, pitch-catch, pulse-echo, backscatter and acoustic emission.

In the experimental setup where water flows continuously between transducers separated by distances from 50 to 200 mm, passive methods (e.g., acoustic emission and back scatter) cannot be employed because there is no emission from the water when the temperature changes. The pitch-catch method is also difficult to implement. The through transmission method was found to be the most suitable ultrasonic arrangement for conducting temperature measurements. Different measurement architectures were also discussed, among which the oscillating sensor was the simplest to implement by using a single amplifier and enabled the shortest measurement time. However, additional electronics for filtering or phase shifting should be included to achieve comprehensive system control.

8.1.3 Chapter 3

In this chapter, the supporting electronic devices required for the development of a UOTS system were discussed. The general evaluation of system control options determined that the PSoC realisation was the most appropriate for the development of the UOTS system in this study. PSoC technology was chosen among the other options for several reasons, the most important of which was availability of integrated programmable digital and analogue parts.

The second section of this chapter focused on developing methods for the automatic amplitude level control of the received ultrasonic signal. Driving the signal to saturation is a potential reason for frequency–temperature hysteresis. Several options were considered in developing an AGC system. Each method was simulated, constructed and tested. The most efficient option was to integrate a JFET-based AGC circuit with a PSoC-based supervisory gain control system. The results of this method showed good signal control and provided the required amplification with minimal frequency scatter. However, no notable improvement in hysteresis performance was observed.

The available options for a low-cost conventional sensor that could be used as a temperature reference were examined. 1-Wire sensor technology was found to be the best candidate because of its flexible resolution, reasonable accuracy and low cost. Software control and the implementation of a data acquisition system, including the calibration of the sensors, were described and discussed.

Several methods for the implementation of an inexpensive but accurate frequency meter were described: frequency to voltage conversion; counting the number of cycles in a fixed amount of time; measuring the amount of time for a single cycle to complete; and a hybrid method. It was found that a system could achieve the worst-case error of 16 ppm using an inexpensive TCXO in a hybrid configuration.

8.1.4 Chapter 4

An inexpensive and flexible modular system was successfully developed and tested. The modules included signal multiplexers, an ultrasonic driver and a frequency meter. The full control of UOTS parameters during the run time was possible by using a GUI with minimal physical and software modifications. The user commands broadcasted to initiate the corresponding board actions.

8.1.5 Chapter 5

In this chapter, the optimal operational parameters of a UOTS system were examined: gain level, supply voltage, filtering, phase shifting and distance between transducers. Simulations were conducted to achieve the better understanding of sensor operation and the optimisation of its design. The simulation of an ultrasonic oscillator circuit was

concerned with the three main parts: transducer model, delay line and amplification stage.

The initial experimental results showed that the ultrasonic frequency was dependent on the amplifier gain applied. It was found that the same gain with different compositions resulted in around ±10 Hz variations in the measured ultrasonic frequency. The gain region chosen (G = 55-70) ensured the maximum flatness and hence a more stable frequency reading within that gain range.

Although the supply voltage from USB power sources could vary, these variations showed small changes in the ultrasonic frequency observed in the simulations. Therefore, the addition of an in-circuit voltage regulator was not required. Previous research found that the inclusion of a BPF in the signal loop of an oscillating ultrasonic sensor is essential if the ultrasonic transducers feature multiple resonances. This was verified experimentally by conducting several tests with and without a filter. The results without filtering showed oscillations at several resonances.

It was found that changing the distance between the transducers resulted in ultrasound oscillations at different frequency ranges. Each range showed advantages and disadvantages in terms of frequency–temperature consistency, ultrasonic frequency deviation, average frequency–temperature sensitivity and temperature–frequency hysteresis across the entire test sample. Overall, it was found that the distance of 60 mm showed low hysteresis, the lowest scatter and acceptable frequency–temperature sensitivity.

All the experiments conducted showed similar patterns for the UOTSes output frequencies. The results were heavily dependent on the sensors used; different pairs of sensors produced different amounts of hysteresis. The operation of the transducers was also dependent on the past history of the sensor operation. Moreover, frequency–temperature hysteresis of different magnitudes was found in all experiments. Large frequency jumps were observed at some times; the rate of the reoccurrence of these jumps was dependent on the distance between the transducers. In addition, it was found that the transducers required some time to stabilise and start produced consistent results.

Most of these results because of the highly nonlinear frequency and phase responses of the UOTSes components.

8.1.6 Chapter 6

In order to eliminate or reduce the effects of temperature–frequency hysteresis, the data fusion method was applied. This method is based on the extrapolated estimation of temperature response.

By employing a conventional temperature sensor, some UOTS advantages were sacrificed. Nevertheless, the UOTS was able to detect the inflection point faster than the temperature sensors did. The inflection point was estimated by computing the response curves for both temperature and frequency data in the cooling and heating stages. In the experiments conducted, the UOTS estimated the inflection point 18 s faster than temperature sensors when the water was heated and then naturally cooled. In order to obtain an accurate fused temperature, a frequency validity criterion was applied to validate each frequency reading. The fused temperature results showed a resolution of 0.1 mK and a standard uncertainty of around 1.34 mK.

Overall, the UOTS was proven a potentially valuable addition to the process control instrumentation. By employing data fusion, ambiguities related to the existence of hysteresis were completely eliminated.

8.1.7 Chapter 7

In this chapter, an UOTS-based system for differential heat measurements of a water-cooled electric motor was developed. It was found that employing a temperature measurement device with an accuracy less than 0.5 K in electric motors would complicate the motor classification process. Hence, a UOTS with a much higher resolution could be employed to achieve reliable classifications at a low cost.

Three chamber designs were developed and compared based on several factors: velocity, turbulence and manufacturing simplicity. The SCSC model was chosen because it produced low turbulence at the flowrates up to 10 L/min. The 3D printing technology was chosen to construct the chamber.

Using CFD simulations, various parameters were varied to establish the performance and limitations of the developed model. The parameters included the placement of the ultrasonic transducers and a flow analysis, which showed that low turbulence inside the chamber was achieved when the flowrate was below 12 L/min. The experimental results showed that the ultrasonic frequency scatter had values below 0.3 Hz in flowrates up to 10 L/min, which verified the outcomes of the CFD simulations.

Experimental results were obtained for a single chamber and for differential measurements using two chambers.

8.2 Cost considerations

This project was aimed to develop an accurate but inexpensive temperature measurement device using ultrasound. A modular system was developed to drive and control the ultrasonic system. The cost of the full modular system was less than £15 as shown in Table 8.1. The total price of the hardware used in this development was less than £35 as shown in Table 8.2. The total BOM was reduced by employing inexpensive, narrowband ultrasonic transducers.

Table 8.1 Total Cost of the Modular System

Item	Part number	Cost per unit (£)	Quantity	Total cost (£)
PSoC controller	CYPRESS CY8C24123	1.76	4	7.04
PCB 50×50 mm	N/A	1.07	4	4.28
Resistors	YAGEO RC0805FR-071KL	0.01	17	0.17
Capacitors	MULTICOMP MC0603F104	0.01	8	0.08
Digital switches	NXP 74LVC1G3157GW	0.08	8	0.64
TCXO	TAITIEN 709-9240	1.83	1	1.83
Mini USB to DIP adapter	Unbranded	0.33	1	0.33
Connectors, headers, jumpers and screw terminals	Estimated price =>	0.50	1	0.50
Total price =>				14.87

Table 8.2 Total Cost of the Developments, Including the Construction of the Modular System and the Test Rig

Item	Part number	Cost per unit (£)	Quantity	Total cost (£)
Ultrasonic transducer Rx	Prowave 400ER18S	6.08	1	6.08
Ultrasonic transducer Tx	Prowave 400ET18S	5.23	1	5.23
1-Wire temperature sensor	DS18B20, shielded	1.14	4	4.55
3D printed model	280 gm of PLA filament	2.80	2	5.60
Modular system		14.85	1	14.87
Total price =>				36.33

The BOM shown in Table 8.2 reflects the actual cost of the system, including the modular system. However, the overall system would have cost less than £19 if the design parameters were optimised because only a single PCB board and a single PSoC can perform all the necessary actions. The electronics involved in the developed modular system cost less than £15. The cost could be significantly reduced if the components were ordered in mass quantities.

8.3 Recommendations for future research

The following list summarises recommendations and suggestions for the development of a UOTS in particular and ultrasonic oscillating sensors in general:

1. The development of a UOTS that features an automatic BPF setting during run time could be achieved by communicating the output from the frequency meter and the ultrasonic driver. The operation would start without a BPF, and based on the resonance frequency found, the ultrasonic driver would calculate the BPF parameters. During the data acquisition, the system would be able to detect any fault that required the repetition of the process used to adjust the BPF operation.
2. Additional models of the test rig could be developed. The constructed design is capable of handling flowrates up to 10 L/min with reliable results. Another chamber could be developed to extend this range in order to cover a greater number of application requirements. This could be achieved by reconstructing the developed test

rig in CFD software. This would allow for changing the dimensions of the design and monitoring the performance parameters according to the size and dimensions of the model.

3. The online estimation of the temperature inflection points that indicates the detection of thermal runaway in machinery as well as the online processing of data fusion.
4. Re-design differential heat measurements for water-cooled electric motors for use in various calorimeter-based applications, including food calorimeters.

8.4 Overall summary

A low-cost UOTS system was successfully developed to measure the temperature with a high resolution and accuracy. Data sensor fusion was employed to correct ultrasonic frequency and to estimate the temperature inflection point. In addition, data fusion effectively eliminated the temperature–frequency hysteresis found in the experiments. Experimental data collected over several hundred hours were analysed in order to enhance the operation and select appropriate operation parameters. The modular system developed was shown to be a powerful tool for investigating the operation of the UOTS in various arrangements.

References

[1] W. Zielenkiewicz and E. Margas, *Theory of calorimetry*. Dordrecht: Kluwer, 2002.

[2] P. F. Sullivan and G. Seidel, "Steady-state, ac-temperature calorimetry," *Physical Review,* vol. 173, p. 679, 1968.

[3] S. M. Sarge, G. W. H. Höhne, and W. Hemminger, *Calorimetry : Fundamentals, Instrumentation and Applications*. Somerset, DE: Wiley-VCH, 2014.

[4] A. Baggini and A. Sumper, *Electrical Energy Efficiency: Technologies and Applications*: Wiley, 2012.

[5] J. E. Traister and F. Press, *Handbook of Electric Motors: Use and Repair*: Fairmont Press, Incorporated, 1992.

[6] A. Hughes, *Electric Motors and Drives: Fundamentals, Types and Applications*: Elsevier Science, 2005.

[7] M. K. Yoon, C. S. Jeon, and S. K. Kauh, "Efficiency increase of an induction motor by improving cooling performance," *IEEE Transactions on Energy Conversion,* vol. 17, pp. 1-6, 2002.

[8] W. W. Beaumont, *Motor Vehicles and Motors*: Cambridge University Press, 2014.

[9] A. Schletz, B. Eckardt, S. Egelkraut, and H. Rauh, "Power electronics system integration for electric and hybrid vehicles," in *Integrated Power Electronics Systems (CIPS), 2010 6th International Conference on*, 2010, pp. 1-10.

[10] C. W. Ayers, J. S. Hsu, and K. T. Lowe, "Fundamentals of a floating loop concept based on R134a refrigerant cooling of high heat flux electronics," in *Twenty-Second Annual IEEE Semiconductor Thermal Measurement And Management Symposium*, 2006, pp. 59-64.

[11] E. Kee. (2012, 8/10/2014). General Motors reinforces hybrid car battery. Available: http://www.ubergizmo.com/2012/01/general-motors-reinforces-hybrid-car-battery/.

[12] B. G. Liptak, *Temperature Measurement*: Taylor & Francis, 1993.

[13] T. D. McGee, *Principles and Methods of Temperature Measurement*: Wiley, 1988.

[14] R. E. Bentley, *Handbook of Temperature Measurement* vol. 1: Springer, 1998.

[15] J. Fraden, *Handbook of Modern Sensors: Physics, Designs, and Applications*: Springer International Publishing, 2015.

[16] L. Michalski, *Temperature Measurement*: Wiley, 2001.

[17] J. G. Webster, *The Measurement, Instrumentation and Sensors Handbook*: Taylor & Francis, 1998.

[18] H. M. Hashemian. (2003, 17/11/2015). Comparing RTDs and Thermocouples in Industrial Applications. Available: http://archive.sensorsmag.com/articles/0203/temp/main.shtml

[19] W. Boyes, *Instrumentation Reference Book*: Elsevier Science, 2009.

[20] M. Elwenspoek, *Sensor Technology 2001: Proceedings of the Sensor Technology Conference 2001, held in Enschede, The Netherlands 14–15 May, 2001*: Springer Netherlands, 2011.

[21] W. Y. Du, *Resistive, Capacitive, Inductive, and Magnetic Sensor Technologies*: CRC Press, 2014.

[22] D. P. Jones, *Biomedical Sensors*: Momentum Press, 2010.

[23] S. Yurish, *Sensors and Biosensors, MEMS Technologies and its Applications*: Concha Books, 2014.

[24] H. Budzier and G. Gerlach, *Thermal Infrared Sensors: Theory, Optimisation and Practice*: Wiley, 2011.

[25] W. E. K. Middleton, *A history of the thermometer and its use in meteorology*: Johns Hopkins Press, 1966.

[26] J. Mitchelmore, *Exploring Science*: Nelson Thornes Limited, 1990.

[27] S. K. Singh, *Industrial Instrumentation & Control,2e*: McGraw-Hill Education (India) Pvt Limited, 2003.

[28] A.V.Bakshi and U.A.Bakshi, *Instrumentation*: Technical Publications, 2009.

[29] P. Goodwin, *How Everyday Things Work: 60 Descriptions and Activities*: J Weston Walch Pub, 1992.

[30] G. Wang, W. Wang, K. Li, and H. Liu, "A digital thermometer with fast response and high precision," in *2014 7th International Conference on Biomedical Engineering and Informatics*, 2014, pp. 504-510.

[31] W. Nawrocki, *Measurement Systems and Sensors*. Norwood, US: Artech House Books, 2005.

[32] H. Chang, *Inventing Temperature: Measurement and Scientific Progress*: Oxford University Press, 2004.

[33] T. W. Kerlin, *Practical Thermocouple Thermometry*: Instrument Society of America, 1999.

[34] K. Johnson, *New Physics for You*: Nelson Thornes Limited, 2001.

[35] R. M. Stitt and D. Kunst. (2000, 16/8/2015). Diode-Based Temperature Measurement. Available: http://www.ti.com/lit/an/sboa019/sboa019.pdf

[36] Y. M. Shwarts, M. M. Shwarts, and S. V. Sapon, "A new generation of cryogenic silicon diode temperature sensors," in *Advanced Semiconductor Devices and Microsystems, 2008. ASDAM 2008. International Conference on*, 2008, pp. 239-242.

[37] S. Gupta and U. Kamath. (2012, 12/1/2015). Make accurate temperature measurements using semiconductor junctions.

[38] M. Mansoor, I. Haneef, S. Akhtar, A. De Luca, and F. Udrea, "Silicon diode temperature sensors - A review of applications," *Sensors and Actuators A Physical,* 2015.

[39] TN1115. (2010, 10/5/2015). Temperature Sensing Diode in LatticeSC Devices. Available: http://www.latticesemi.com/~/media/LatticeSemi/Documents/ApplicationNotes/PT/TemperatureSensingDiodeinLatticeSCDevices.PDF?document_id=21985

[40] J. Smolen and A. Van Der Spek. (2003, 10/4/2015). *Distributed Temperature Sensing, A DTS Primer for Oil & Gas Production.* Available: http://drilling.posccaesar.org/export/385/projects/DailyProductionReport_1.0/XML/Version1.0/WITSML131/doc/Shell_DTS_Primer.pdf

[41] V. F. Bense, T. Read, and A. Verhoef, "Using distributed temperature sensing to monitor field scale dynamics of ground surface temperature and related substrate heat flux," *Agricultural and Forest Meteorology,* vol. 220, pp. 207-215, 4/15/ 2016.

[42] A. Minardo, R. Bernini, and L. Zeni, "Distributed Temperature Sensing in Polymer Optical Fiber by BOFDA," *IEEE Photonics Technology Letters,* vol. 26, pp. 387-390, 2014.

[43] S. C. Steele-Dunne, J. Dong, O. A. C. Hoes, N. C. van de Giesen, C. Sayde, T. E. Ochsner*, et al.*, "Recent Developments in Active and Passive Distributed Temperature Sensing for Soil Moisture Monitoring," presented at the AGU fall meeting 2015, San Francisco, USA, 2015.

[44] M. Harriott, "Experimental Assessment of Power Losses in Water Cooled Electrical Machines," MEng, Department of Electrical and Electronic Engineering, The University of Nottingham, 2012.

[45] R. A. Sykes, W. L. Smith, and W. J. Spencer, "Performance of Precision Quartz-Crystal Controlled Frequency Generators," *IRE Transactions on Instrumentation,* vol. I-11, pp. 243-247, 1962.

[46] G. Mavko, T. Mukerji, and J. Dvorkin, *The Rock Physics Handbook: Tools for Seismic Analysis of Porous Media*, 2 ed. Cambridge: Cambridge University Press, 2009.

[47] R. Vallery-Radot and R. L. Devonshire, *The Life of Pasteur*: Literary Licensing, LLC, 2013.

[48] Dorling Kindersley Limited, *The Science Book*: Dorling Kindersley Limited, 2014.

[49] M. Lucibella. (2014, 16/9/2015). *The Curie Brothers Discover Piezoelectricity.* Available: https://www.aps.org/publications/apsnews/201403/physicshistory.cfm

[50] D. Damjanovic, "Hysteresis in Piezoelectric and Ferroelectric Materials A2 - Bertotti, Giorgio," in *The Science of Hysteresis*, I. D. Mayergoyz, Ed., ed Oxford: Academic Press, 2006, pp. 337-465.

[51] R. Arshadi and R. S. C. Cobbold, "A pioneer in the development of modern ultrasound: Robert William Boyle," *Ultrasound in Medicine and Biology,* vol. 33, pp. 3-14, 2007.

[52] A. M. K. Thomas, W. A. Kalender, A. K. Banerjee, and U. Busch, *Classic Papers in Modern Diagnostic Radiology*: Springer Berlin Heidelberg, 2005.

[53] D. Ensminger and L. J. Bond, *Ultrasonics: Fundamentals, Technologies, and Applications, Third Edition*: Taylor & Francis, 2011.

[54] G. Andria, F. Attivissimo, and N. Giaquinto, "Digital signal processing techniques for accurate ultrasonic sensor measurement," *Measurement,* vol. 30, pp. 105-114, 9// 2001.

[55] J. A. Gallego-Juárez and K. F. Graff, "Introduction to power ultrasonics," in *Power Ultrasonics*, ed Oxford: Woodhead Publishing, 2015, pp. 1-6.

[56] J. A. Gallego-Juárez and K. F. Graff, *Power Ultrasonics: Applications of High-Intensity Ultrasound*: Elsevier Science, 2014.

[57] S. Satomura, "Ultrasonic Doppler Method for the Inspection of Cardiac Functions," *Acoustical Society of America Journal,* vol. 29, p. 1181, 1957.

[58] R. Sepúlveda, O. Castillo, P. Melin, and O. Montiel, "An Efficient Computational Method to Implement Type-2 Fuzzy Logic in Control Applications," in *Analysis and Design of Intelligent Systems using Soft Computing Techniques*, P. Melin, O. Castillo, E. G. Ramírez, J. Kacprzyk, and W. Pedrycz, Eds., ed Berlin, Heidelberg: Springer Berlin Heidelberg, 2007, pp. 45-52.

[59] Y. Yasuda and S. Satoh, "Ultrasonic flow meter," ed: Google Patents, 1985.

[60] R. E. Berg. (2015, 9/7/2015). *Ultrasonics.* Available: https://www.britannica.com/science/ultrasonics

[61] S. Alzebda, "Low-cost Oscillating Sensor for Ultrasonic Testing and Monitoring of Liquids," PhD, The Department of Electrical and Electronic Engineering, The University of Nottingham, 2011.

[62] A. M. K. Thomas, A. K. Banerjee, and U. Busch, "Ultrasound," in *Classic Papers in Modern Diagnostic Radiology*, ed Berlin, Heidelberg: Springer Berlin Heidelberg, 2005, pp. 137-251.

[63] D. Ensminger and F. B. Stulen, *Ultrasonics: Data, Equations and Their Practical Uses*: CRC Press, 2008.

[64] H. J. Walter, "Ultrasonic cleaner," ed: Google Patents, 1978.

[65] L. Azar, "Cavitation in ultrasonic cleaning and cell disruption. Controlled Environments," ed, 2010.

[66] S. R. Soudagar and S. D. Samant, "Semiquantitative characterization of ultrasonic cleaner using a novel piezoelectric pressure intensity measurement probe," *Ultrasonics Sonochemistry,* vol. 2, pp. S49-S53, 1995/01/01 1995.

[67] A. Siddiq and E. Ghassemieh, "Thermomechanical analyses of ultrasonic welding process using thermal and acoustic softening effects," *Mechanics of Materials,* vol. 40, pp. 982-1000, 2008.

[68] J. Tsujino, "Recent developments of ultrasonic welding," in *Ultrasonics Symposium, 1995. Proceedings., 1995 IEEE*, 1995, pp. 1051-1060 vol.2.

[69] S. Z. Dushkes, "A Design Study of Ultrasonic Bonding Tips," *IBM Journal of Research and Development,* vol. 15, pp. 230-235, 1971.

[70] G. Harman and J. Albers, "The Ultrasonic Welding Mechanism as Applied to Aluminum-and Gold-Wire Bonding in Microelectronics," *IEEE Transactions on Parts, Hybrids, and Packaging,* vol. 13, pp. 406-412, 1977.

[71] P. Li, Y. Cai, X. Shen, S. Nabuzaale, J. Yin, and J. Li, "An Accurate Detection for Dynamic Liquid Level Based on MIMO Ultrasonic Transducer Array," *IEEE Transactions on Instrumentation and Measurement,* vol. 64, pp. 582-595, 2015.

[72] T. J. Kim, Z. Kojro, M. Pluta, M. Schmachtl, M. Schubert, T. Gudra*, et al.*, "Confocal scanning acoustic microscopy in air at normal conditions at frequencies close to the phonon cut-off regime," *Physica B: Condensed Matter,* vol. 263–264, pp. 588-594, 1999.

[73] H. Peter, H. Niels, and P. Alf, "Application of ultrasonic sensors in the process industry," *Measurement Science and Technology,* vol. 13, p. R73, 2002.

[74] E. Aguirre and A. González, "A Fuzzy Perceptual Model for Ultrasound Sensors Applied to Intelligent Navigation of Mobile Robots," *Applied Intelligence,* vol. 19, pp. 171-187, 2003.

[75] E. I. Bluth, *Ultrasound: A Practical Approach to Clinical Problems*: Si P, 2000.

[76] W. N. McDicken and T. Anderson, "Basic physics of medical ultrasound A2 - Allan, Paul L," in *Clinical Ultrasound (Third Edition)*, G. M. Baxter and M. J. Weston, Eds., ed Edinburgh: Churchill Livingstone, 2011, pp. 3-15.

[77] T. Fritzsch, W. Krause, and H. J. Weinmann, "Status of contrast media research in MRI, ultrasound and X-ray," *European Radiology,* vol. 2, pp. 2-13, 1992.

[78] Y. Lu, "Piezoelectric micromachined ultrasonic transducers for fingerprint sensing," University of California, Davis, 2015.

[79] A. M. Zungeru, "Design and Development of an Ultrasonic Motion Detector," *arXiv preprint arXiv:1303.1732,* 2013.

[80] B. H. Sunil, "Household Security System Based on Ultrasonic Sensor Technology with SMS Notification," *European Journal of Academic Essays,* vol. 1, pp. 6-9, 2014.

[81] S. Yi and H. Cha, "An Active Tracking System Using IEEE 802.15.4-Based Ultrasonic Sensor Devices," in *Emerging Directions in Embedded and Ubiquitous Computing: EUC 2006 Workshops: NCUS, SecUbiq, USN, TRUST, ESO, and MSA, Seoul, Korea, August 1-4, 2006. Proceedings*, X. Zhou, O. Sokolsky, L. Yan, E.-S. Jung, Z. Shao, Y. Mu*, et al.*, Eds., ed Berlin, Heidelberg: Springer Berlin Heidelberg, 2006, pp. 485-494.

[82] A. C. Aylsworth, "Ultrasonic gas measuring device," ed: Google Patents, 1991.

[83] X. Liu, S. Cheng, H. Liu, S. Hu, D. Zhang, and H. Ning, "A survey on gas sensing technology," *Sensors,* vol. 12, pp. 9635-9665, 2012.

[84] H. Kumazawa, T. Aoki, and I. Susuki, "Analysis and experiment of gas leakage through composite laminates for propellant tanks," *AIAA journal,* vol. 41, pp. 2037-2044, 2003.

[85] O. Behrend and H. Schubert, "Influence of hydrostatic pressure and gas content on continuous ultrasound emulsification," *Ultrasonics Sonochemistry,* vol. 8, pp. 271-276, 2001.

[86] D. Knorr, M. Zenker, V. Heinz, and D.-U. Lee, "Applications and potential of ultrasonics in food processing," *Trends in Food Science & Technology,* vol. 15, pp. 261-266, 2004.

[87] R. van Eldik and C. D. Hubbard, *Chemistry Under Extreme and Non-Classical Conditions*: John Wiley & Sons, 1996.

[88] M. Villamiel and P. de Jong, "Inactivation of Pseudomonas fluorescens and Streptococcus thermophilus in Trypticase® Soy Broth and total bacteria in milk by continuous-flow ultrasonic treatment and conventional heating," *Journal of food engineering,* vol. 45, pp. 171-179, 2000.

[89] B. Thakur and P. Nelson, "Inactivation of lipoxygenase in whole soy flour suspension by ultrasonic cavitation," *Food/Nahrung,* vol. 41, pp. 299-301, 1997.

[90] A. Patist and D. Bates, "Ultrasonic innovations in the food industry: From the laboratory to commercial production," *Innovative Food Science & Emerging Technologies,* vol. 9, pp. 147-154, 4// 2008.

[91] P. Popejoy, "Development of a Ultrasonic Tilt-Sensor," PhD, The Department of Electrical and Electronic Engineering, The University of Nottingham, 2013.

[92] T. Suda, A. Sato, M. Ida, H. Gemma, H. Hayakawa, and K. Chida, "Hypersensitivity pneumonitis associated with home ultrasonic humidifiers," *CHEST Journal,* vol. 107, pp. 711-717, 1995.

[93] A. Pantano and D. Cerniglia, "Simulation of laser generated ultrasound with application to defect detection," *Applied Physics A,* vol. 91, pp. 521-528, 2008.

[94] A. M. Mayer, "II. On an acoustic pyrometer," *The London, Edinburgh, and Dublin Philosophical Magazine and Journal of Science,* vol. 45, pp. 18-22, 1873.

[95] A. Hashmi, M. Malakoutikhah, R. A. Light, and A. N. Kalashnikov, "Embedded Supervisory Control and Output Reporting for the Oscillating Ultrasonic Temperature Sensors," in *Intelligent Systems in Cybernetics and Automation Theory: Proceedings of the 4th Computer Science On-line Conference 2015 (CSOC2015), Vol 2: Intelligent Systems in Cybernetics and Automation Theory*, R. Silhavy, R. Senkerik, K. Z. Oplatkova, Z. Prokopova, and P. Silhavy, Eds., ed Cham: Springer International Publishing, 2015, pp. 139-150.

[96] A. Hashmi, A. N. Kalashnikov, and R. A. Light, "Experimental evaluation of ultrasonic oscillating temperature sensors (UOTS) under cyclically changing temperatures," in *Ultrasonics Symposium (IUS), 2015 IEEE International*, 2015, pp. 1-4.

[97] A. Afaneh, S. Alzebda, V. Ivchenko, and A. N. Kalashnikov, "Ultrasonic Measurements of Temperature in Aqueous Solutions: Why and How," *Physics Research International,* vol. 2011, 2011.

[98] A. Hashmi, M. Malakoutikhah, and A. N. Kalashnikov, "Measuring thermal losses of water cooled motors using oscillating ultrasonic temperature sensors," *ББК 32.81 C91,* p. 130, 2014.

[99] A. Hashmi, A. N. Kalashnikov, and R. A. Light, *Inexpensive Differential Ultrasonic Calorimeter for Accurate Measurement of Heat Loss*: Imperial College Press, 2015.

[100] C. R. Hill, J. C. Bamber, and G. R. Haar, *Physical Principles of Medical Ultrasonics*: John Wiley & Sons, 2004.

[101] N. Bilaniuk and G. S. Wong, "Speed of sound in pure water as a function of temperature," *The Journal of the Acoustical Society of America,* vol. 93, pp. 1609-1612, 1993.

[102] J. Ablitt. (2000, 12/12/2015). *Technical Guides - Speed of Sound in Pure Water.* Available: http://resource.npl.co.uk/acoustics/techguides/soundpurewater/speedpw.pdf

[103] J. Williams and O. Sanchez-Felipe. (2011, 11/1/2015). *An Introduction to Acoustic Thermometry.* Available: http://cds.linear.com/docs/en/application-note/an131f.pdf

[104] J. D. Sternhagen, C. E. Wold, W. A. Kempf, M. Karlgaard, K. D. Mitzner, R. D. Mileham*, et al.*, "A novel integrated acoustic gas and temperature sensor," *IEEE Sensors Journal,* vol. 2, pp. 301-306, 2002.

[105] B. Drafts. (2000, 23/11/2015). *Acoustic Wave Technology Sensors.*

[106] W. K. Spratt and J. F. Vetelino, "Torsional acoustic waveguide sensor for temperature and liquid level," in *2009 IEEE International Frequency Control Symposium Joint with the 22nd European Frequency and Time forum*, 2009, pp. 850-854.

[107] C. E. Weld, J. D. Sternhagen, R. D. Mileham, K. D. Mitzner, and D. W. Galipeau, "Temperature measurement using surface skimming bulk waves," in *Ultrasonics Symposium, 1999. Proceedings. 1999 IEEE*, 1999, pp. 441-444 vol.1.

[108] I. Ihara and M. Takahashi, "Laser-Ultrasonic Monitoring of Temperature Distribution of Material Surface during Heating," in *Mat. of 1st International Symposium on Laser Ultrasonics: Science, Technology and Applications, Montreal, Canada*, 2008, pp. 188-192.

[109] J. Bardong, M. Schulz, M. Schmitt, I. Shrena, D. Eisele, E. Mayer*, et al.*, "Precise measurements of BAW and SAW properties of Langasite in the temperature range from 25 degrees C to 1000 degrees C," in *2008 IEEE International Frequency Control Symposium*, 2008, pp. 326-331.

[110] A. Hashmi, "PSoC1-Based Data Logging Instrumentation for Overnight Measurement of the Output Frequency of Ultrasonic Oscillating Sensors versus the Ambient Temperature," MSc, Department of Electrical and Electronic Engineering, The University of Nottingham, 2013.

[111] A. N. Kalashnikov and R. E. Challis, "Errors and uncertainties in the measurement of ultrasonic wave attenuation and phase velocity," *IEEE Transactions on Ultrasonics, Ferroelectrics, and Frequency Control,* vol. 52, pp. 1754-1768, 2005.

[112] R. Truell, C. Elbaum, and B. B. Chick, *Ultrasonic Methods in Solid State Physics*: Elsevier Science, 2013.

[113] S. Delrue, K. Van Den Abeele, E. Blomme, J. Deveugele, P. Lust, and O. B. Matar, "Two-dimensional simulation of the single-sided air-coupled ultrasonic pitch-catch technique for non-destructive testing," *Ultrasonics,* vol. 50, pp. 188-196, 2010.

[114] NASA. (1999, 13/2/2015). *Ultrasonic Testing of Aerospace Materials*. Available: http://llis.nasa.gov/lesson/765

[115] H. R. Hartzog, "Multiple-Transducer Ultrasonic Techniques," *The NDT Technician,* vol. 6, p. 12, 2007.

[116] J. Blitz and G. Simpson, *Ultrasonic Methods of Non-destructive Testing*: Springer Netherlands, 1995.

[117] L. Cartz, "Nondestructive testing," 1995.

[118] B. Fay, "Ultrasonic Backscattering: Fundamentals and Applications," in *Physical Acoustics: Fundamentals and Applications*, O. Leroy and M. A. Breazeale, Eds., ed Boston, MA: Springer US, 1991, pp. 41-53.

[119] C. U. Grosse and M. Ohtsu, *Acoustic emission testing*: Springer Science & Business Media, 2008.

[120] M. Garcia-Rodriguez, J. Garcia-Alvarez, Y. Yañez, M. J. Garcia-Hernandez, J. Salazar, A. Turo*, et al.*, "Low cost matching network for ultrasonic transducers," *Physics Procedia,* vol. 3, pp. 1025-1031, 2010/01/01 2010.

[121] ScienceDaily, "Low cost design makes ultrasound imaging affordable to the world," ed. Newcastle University, 2012.

[122] T. Cook, "After the Match: What's in Your Pocket?," *Emergency Medicine News,* vol. 38, p. 12, 2016.

[123] The Engineering Toolbox. (2015, 21/11/2015). *Water and Speed of Sound*. Available: http://www.engineeringtoolbox.com/sound-speed-water-d_598.html

[124] R. C. Asher, *Ultrasonic sensors for chemical and process plant*: Institute of Physics Pub., 1997.

[125] P. Popejoy, S. Alzebda, O. Sonbul, and A. N. Kalashnikov, "Linear angle measurement using continuous wave ultrasonic oscillator," in *Instrumentation and Measurement Technology Conference (I2MTC), 2012 IEEE International*, 2012, pp. 733-736.

[126] A. Afaneh and A. N. Kalashnikov, "Embedded processing of acquired ultrasonic waveforms for online monitoring of fast chemical reactions in aqueous solutions," in *Intelligent Data Acquisition and Advanced Computing Systems (IDAACS), 2011 IEEE 6th International Conference on*, 2011, pp. 253-257.

[127] G. W. C. Kaye and T. H. Laby. (2013, 12/3/2016). The speed and attenuation of sound. *Kaye & Laby Tables of Physical & Chemical Constants*. Available: http://www.kayelaby.npl.co.uk/general_physics/2_4/2_4_1.html

[128] Cypress Semiconductor, "Technical Reference Manual," *Document No. PSoC TRM,* vol. 1, 2006.

[129] D. L. Schilling, *Electronic circuits, discrete and integrated*: McGraw-Hill, 1989.

[130] Adafruit. (2014, 10/4/2014). *Adafruit TPA2016 2.8W AGC Stereo Audio Amplifier*. Available: https://learn.adafruit.com/adafruit-tpa2016-2-8w-agc-stereo-audio-amplifier?view=all

[131] J. Keith. (2013, 10/05/2015). *Automatic Gain Control – AGC Circuit*. Available: http://www.electroschematics.com/248/automatic-gain-control-agc/

[132] J. Keith. (2014, 27/05/2015). *Audio Compression Amplifier /AGC*. Available: http://www.electroschematics.com/9400/audio-compressor-agc/

[133] W. Wong. (1998, 12/06/2016). *Effective AGC Amplifier Can Be Built At A Nominal Cost*. Available: http://www.electronicdesign.com/analog/effective-agc-amplifier-can-be-built-nominal-cost

[134] J. ZHANG, "Smart Temperature Sensor DS18B20 and Its Application [J]," *Instrumentation Technology,* vol. 4, pp. p68-70, 2010.

[135] D. V. Ess, "PSoC® 1 Measuring Frequency," Cypress Application Note2007.

[136] G. Raaja, "UART Clock Accuracy Requirement in PSoC 1," *Cypress Semiconductor,* 2009.

[137] ABRACON. (2002). *Datasheet - AB15T, Low Frequency Cylindrical Watch Crystal*.

[138] PicoScope. (2009, 12/5/2015). *Datasheet - PicoScope® 5000 Series, Flexible Resolution USB Oscilloscope*. Available: https://www.picotech.com/oscilloscope/5000/flexible-resolution-oscilloscope

[139] Maxim Integrated. (2007, 23/7/2014). *Datasheet - DS32kHz, 32.768kHz Temperature-Compensated Crystal Oscillator*. Available: http://datasheets.maximintegrated.com/en/ds/DS32kHz.pdf

[140] Sparkfun. (2010, 6/7/2015). *Gainer PSoC Development Board*. Available: https://www.sparkfun.com/products/retired/8480

[141] T. Kenjō, *Electric motors and their controls: an introduction*: Oxford University Press, Incorporated, 1991.

[142] V. I. Kubov, Y. Y. Dymytrov, and R. M. Kubova, "LTspice-model of thermoelectric Peltier-Seebeck element," in *2016 IEEE 36th International Conference on Electronics and Nanotechnology (ELNANO)*, 2016, pp. 47-51.

[143] R. Kollman and J. Betten. (2005, 10/2/2016). Powering electronics from the USB port. *Power Management*. Available: http://www.ti.com/lit/an/slyt118/slyt118.pdf

[144] M. Malakoutikhah, "Optimisation of the Oscillating Ultrasonic Temperature Sensor Cell for Differential Calorimeter Use," MSc, Department of Electrical and Electronic Engineering, The University of Nottingham, 2014.

[145] G. Bertotti and I. D. Mayergoyz, *The Science of Hysteresis*: Academic, 2006.

[146] H. Zhou, C. Nicholls, T. Kunz, and H. Schwartz, "Frequency accuracy & stability dependencies of crystal oscillators," *Carleton University, Systems and Computer Engineering, Technical Report SCE-08-12,* 2008.

[147] J. Armstrong, P. Blomster, and J. Hokanson, "Aging Characteristics Of Quartz Crystal Resonators," in *20th Annual Symposium on Frequency Control. 1966*, 1966, pp. 192-207.

[148] J. A. Kusters and J. R. Vig, "Hysteresis in quartz resonators-a review," *IEEE transactions on ultrasonics, ferroelectrics, and frequency control,* vol. 38, pp. 281-290, 1991.

[149] J. Thomas III and S. Sharma, "Adsorption and desorption of water on Au by the quartz-crystal-oscillator method," *Journal of Vacuum Science & Technology,* vol. 13, pp. 549-551, 1976.

[150] E. P. Eernisse, "Temperature dependence of the force frequency effect for the AT-, FC-, SC-, and rotated X-cuts," in *34th Annual Symposium on Frequency Control. 1980*, 1980, pp. 426-430.

[151] E. Fletcher and A. Douglas, "A Comparison of the Effects of Bending Moments on the Vibrations of AT and SC (or TTC) Cuts," in *33rd Annual Symposium on Frequency Control. 1979*, 1979, pp. 346-350.

[152] R. L. Filler and J. R. Vig, "The Effect of Bonding on the Frequency versus. Temperature Characteristics of AT-Cut Resonators," DTIC Document1976.

[153] E. EerNisse, "Quartz resonator frequency shifts arising from electrode stress," in *29th Annual Symposium on Frequency Control. 1975*, 1975, pp. 1-4.

[154] M. Bloch, M. Meirs, and J. Ho, "The microcomputer compensated crystal oscillator (MCXO)," in *Frequency Control, 1989., Proceedings of the 43rd Annual Symposium on*, 1989, pp. 16-19.

[155] J. Markgraaff, "Elastic behavior of quartz during stress induced dauphiné twinning," *Physics and Chemistry of Minerals,* vol. 13, pp. 102-112, 1986.

[156] J. R. Vig, "Quartz crystal resonators and oscillators," *US Army Communications-Electronics Command, January,* 2001.

[157] H. Kawashima and K. Sunaga, "Frequency temperature behavior and its hysteresis of S-TCXOs using new shape GT cut quartz crystal resonators," in *Frequency Control Symposium, 1992. 46th., Proceedings of the 1992 IEEE*, 1992, pp. 434-441.

[158] M. Bazghaleh, S. Grainger, M. Mohammadzaheri, B. Cazzolato, and T. Lu, "A digital charge amplifier for hysteresis elimination in piezoelectric actuators," *Smart Materials and Structures,* vol. 22, p. 075016, 2013.

[159] J. E. Segel, *Piezoelectric Actuators*: Nova Science Publishers, 2011.

[160] D. L. Hammond and A. Benjaminson, "The crystal resonator-A digital transducer," *IEEE spectrum,* vol. 6, pp. 53-58, 1969.

[161] A. B. Mroch and G. R. Hykes, "A Minature High Stability TCXO Using Digital Compensation," in *30th Annual Symposium on Frequency Control. 1976*, 1976, pp. 292-300.

[162] A. B. Mroch and G. R. Hykes, "High stability temperature compensated crystal oscillator study," *Interim Progress Report, 28 Feb. 1974-28 Feb. 1975 Rockwell International Corp., Cedar Rapids, IA. Collins Radio Group.,* vol. 1, 1976.

[163] H.-J. Foerster, "Thermal Hysteresis of AT+ SC-Cut Quartz Crystal Resonators. Automated Measurement Method and Results," DTIC Document1982.

[164] J. A. Kusters and G. S. Kaitz, "Characteristics of natural, swept natural, and cultured X-and Z-growth quartz material in high temperature, high stress applications," in *39th Annual Symposium on Frequency Control. 1985*, 1985, pp. 223-229.

[165] K. Tuladhar, B. Adams, and E. Fletcher, "Hysteresis Effects in Quartz Crystal Resonators," in *International Conference on Frequency Control and Synthesis: the University of Surrey, Guildford, Surrey, 8-10 April 1987*, 1987, p. 19.

[166] J. BEAUSSIER, "Thermal hysteresis in quartz resonators and oscillators(Hysteresis thermique dans les resonateurs et les oscillateurs a quartz)," *ONERA, TP,* p. 14, 1988.

[167] S. S. Schodowski, "Resonator self-temperature-sensing using a dual-harmonic-mode crystal oscillator," in *Frequency Control, 1989., Proceedings of the 43rd Annual Symposium on*, 1989, pp. 2-7.

[168] W. Elmenreich, "Sensor fusion in time-triggered systems," 2002.

[169] J. L. Crowley, "Principles and techniques for sensor data fusion," in *Multisensor Fusion for Computer Vision*, ed: Springer, 1993, pp. 15-36.

[170] A. N. Steinberg and C. L. Bowman, "Rethinking the JDL data fusion levels," *NSSDF JHAPL,* vol. 38, p. 39, 2004.

[171] F. Abyarjoo, A. Barreto, J. Cofino, and F. R. Ortega, "Implementing a sensor fusion algorithm for 3D orientation detection with inertial/magnetic sensors," in *Innovations and Advances in Computing, Informatics, Systems Sciences, Networking and Engineering*, ed: Springer, 2015, pp. 305-310.

[172] A. Hashmi and A. N. Kalashnikov, "Sensor Data Fusion for Responsive High Resolution Ultrasonic Temperature Measurement Using Piezoelectric Transducers," *IEEE TUFFC JOURNAL*.

[173] R. Winterton, "Newton's law of cooling," *Contemporary Physics,* vol. 40, pp. 205-212, 1999.

[174] T. K. Jack and M. M. Ojapah, "WATER-COOLED PETROL ENGINES: AReview OF CONSIDERATIONS IN COOLING SYSTEMS CALCULATIONS WITH VARIABLE COOLANT DENSITY AND SPECIFIC HEAT," 1963.

[175] ABB, "Low Voltage Water cooled motors," 2011.

[176] WEG, "Three phase induction motors cooled by water jacket," ed, 2016.

[177] ABB, "The Motor Guide- basic technical information about low voltage standard motors," ed, 2005.

[178] VEM Group, "Water-cooled three-phase asynchronous motors," ed, 2006.

[179] Rexroth Indramat, "Liquid Cooled Asynchronous Motors ADF Motor Line ADF1x4," ed, 2001.

[180] Parker, "Permanent Magnet (PMAC) Motors and Generators for Traction, Electro-Hydraulic Pumps (EHP) and Auxiliary Systems," ed, 2015.

[181] R. Shinnar, "The hydrogen economy, fuel cells, and electric cars," *Technology in Society,* vol. 25, pp. 455-476, 2003.

[182] M. Silverman. (2014, 10/7/2016). Projected size of the global market for 3D printing, materials & associated services in 2014 and 2018 (in billion U.S. dollars). *3D printing, materials & services.* Available: http://www.statista.com/statistics/315363/global-market-for-3d-priting-and-services/

[183] T. Maddox. (2014, 10/7/2016). Research: 60 percent of enterprises are using or evaluating 3D printing. *3D Printing: Building the Future.* Available: http://www.zdnet.com/article/research-60-percent-of-enterprises-are-using-or-evaluating-3d-printing/

[184] Z. Zhang, "Microsoft kinect sensor and its effect," *IEEE multimedia,* vol. 19, pp. 4-10, 2012.

[185] H. Lipson and M. Kurman, *Fabricated: The New World of 3D Printing*: Wiley, 2013.

[186] R. Smith. (2015, 12/4/2016). 7 Ways 3D Printing Is Already Disrupting Global Manufacturing. Available: http://www.forbes.com/sites/ricksmith/2015/06/29/7-ways-3d-printing-is-already-disrupting-global-manufacturing/#60a71f44158b

[187] C. Schubert, M. C. van Langeveld, and L. A. Donoso, "Innovations in 3D printing: a 3D overview from optics to organs," *British Journal of Ophthalmology,* pp. bjophthalmol-2013-304446, 2013.

[188] A. Anastasiou, C. Tsirmpas, A. Rompas, K. Giokas, and D. Koutsouris, "3D printing: Basic concepts mathematics and technologies," in *Bioinformatics and Bioengineering (BIBE), 2013 IEEE 13th International Conference on*, 2013, pp. 1-4.

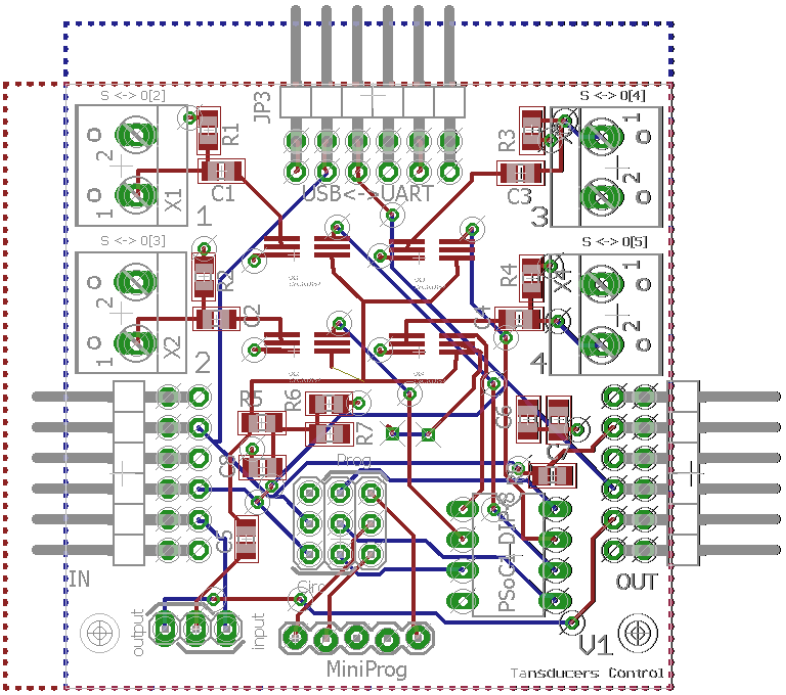
[189] A. Kingsley-Hughes. (2016, 10/5/2016). 3D Printers: From $179 to $4,000, the price is right to buy one now. Available: http://www.zdnet.com/article/3d-printers-from-179-to-4000-the-price-is-right-to-buy-one-now/

[190] D. Van Ess, "Cypress Application Note AN2283 - PSoC 1 Measuring Frequency," *Cypress Semiconductor,* 2007.

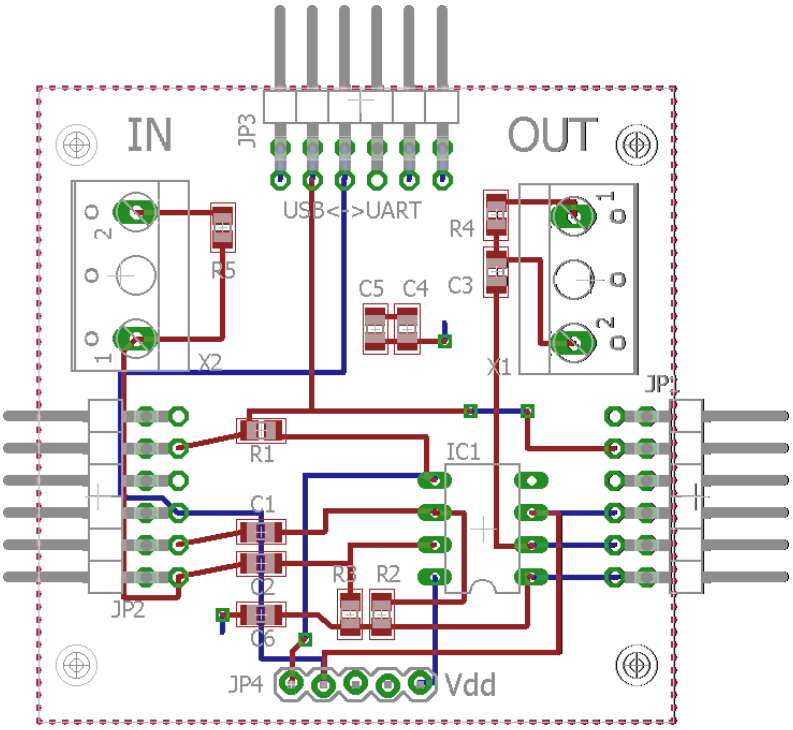
Appendices

Appendix A PCB layouts of modular system

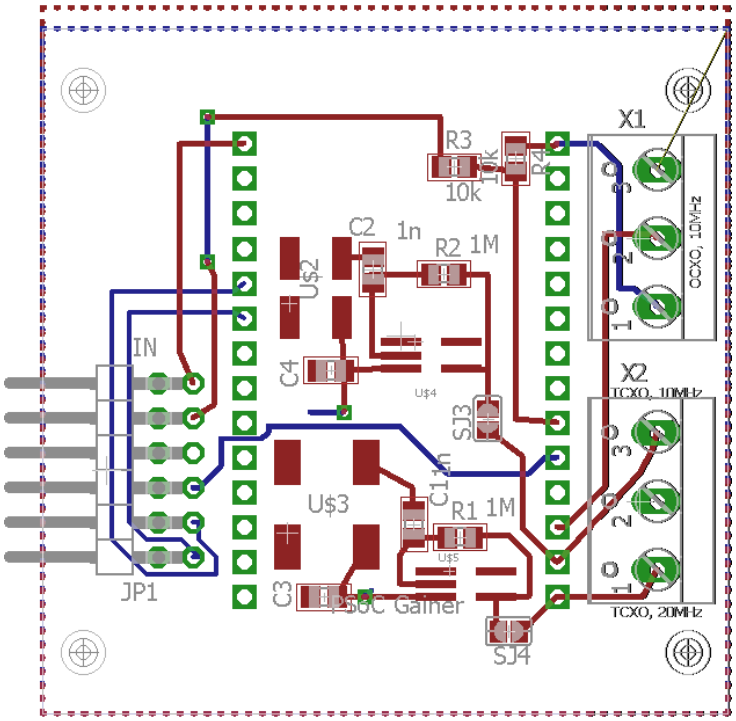
1) Signal multiplexer



2) Ultrasonic driver



3) Frequency meter



Appendix B C programs for modular system control

1) Signal multiplexer

```
#include <m8c.h>        // part specific constants and macros
#include "PSoCAPI.h"    // PSoC API definitions for all User Modules
#include "delay.h"
#include <stdlib.h>
#include <string.h>
#include <stdio.h>      //definitions for all standard io functions

void welcomeScreen(void);
//Declaration of the function that prints Welcome String on
Hyperterminal
int find_index(int a[], int num_elements, int value);
int str_cut(char *str, int begin, int len);
void copy_string(char *target, char *source);
void Newline(void);


void main(void)
{
    // Parameter pointer
  char *strPtr;
   char * pch;
   int index;
   int G1_value, G2_value, BPF_value;
   char *boardid, *parameter, *value;
   int G1_index, G2_index;
   int BPF_CA, BPF_CB, BPF_C1, BPF_C2, BPF_C3, BPF_C4;
   int BPFV[6];
```

```
   int i;
   char cBPF_CA[5]={0};
   char cBPF_CB[5]=[190];
   char cBPF_C1[5]={0};
   char cBPF_C2[5]={0};
   char cBPF_C3[5]={0};
   char cBPF_C4[5]={0};

    // Initialize receiver/cmd buffer
    UART_CmdReset();

    //Turn on interrupts
    M8C_EnableGInt ;

    //Enable RX interrupts
    UART_IntCntl(UART_ENABLE_RX_INT);
    //set parity as zero and start the UART
    UART_Start(UART_PARITY_NONE);

    //Clear the screen in Hyper terminal window
    UART_PutChar(12);

    // Print welcome screen
    welcomeScreen();

   while(1) {
      if (UART_bCmdCheck()) {            // Wait for command Terminator
         if(strPtr = UART_szGetParam()) {     // More than delimiter?
         }
         copy_string(boardid,strPtr);
         copy_string(parameter,strPtr);
         copy_string(value,strPtr);
         str_cut(parameter, 2, -1); //cut from 2 to end

         if (cstrcmp("B21", strPtr) == 0) {
            PRT0DR = 0x04;
         } else if (cstrcmp("B22", strPtr) == 0) {
            PRT0DR = 0x08;
         } else if (cstrcmp("B23", strPtr) == 0) {
            PRT0DR = 0x10;
         } else if (cstrcmp("B24", strPtr) == 0) {
            PRT0DR = 0x20;
         }
         //Reset command buffer and flags
          UART_CmdReset();
        }
    }
}

// Function to print the welcome screen
void welcomeScreen(void)
{
    UART_CPutString("\n\rThis is B2 - Tranducer Selection");
    UART_CPutString("\n\r");
}

int str_cut(char *str, int begin, int len)
{
    int l = strlen(str);
    if (len < 0) len = l - begin;
    if (begin + len > l) len = l - begin;
```

```
    memmove(str + begin, str + begin + len, l - len + 1);
    return len;
}

   int find_index(int a[], int num_elements, int value)
{
   int i;
   for (i=0; i<num_elements; i++)
   {
    if (a[i] == value)
    {
       return(i);  /* it was found */
    }
   }
   return(-1);  /* if it was not found */
}

void copy_string(char *target, char *source) {
   while (*source) {
      *target = *source;
      source++;
      target++;
   }
   *target = '\0';
}

void Newline(void)
{
   UART_CPutString("\r\n");
}
```

2) Ultrasonic driver

```
#include <m8c.h>        // part specific constants and macros
#include "PSoCAPI.h"    // PSoC API definitions for all User Modules
#include "delay.h"
#include <stdlib.h>
#include <string.h>
#include <stdio.h>      //definitions for all standard io functions

void welcomeScreen(void);
//Declaration of the function that prints Welcome String on
Hyperterminal
int find_index(int a[], int num_elements, int value);
int str_cut(char *str, int begin, int len);
void copy_string(char *target, char *source);
void Newline(void);

void main(void)
{
    // Parameter pointer
   char *strPtr;
   char * pch;
   int index;
   int G1_value, G2_value, BPF_value;
```

```
   char *boardid, *parameter, *value;
   int G1_index, G2_index;
   int BPF_CA, BPF_CB, BPF_C1, BPF_C2, BPF_C3, BPF_C4;
   int BPFV[6];
   int i;
   char cBPF_CA[5]={0};
   char cBPF_CB[5]={0};
   char cBPF_C1[5]={0};
   char cBPF_C2[5]={0};
   char cBPF_C3[5]={0};
   char cBPF_C4[5]={0};

   BYTE G1_gain[]={
PGA_1_G0_06,PGA_1_G0_12,PGA_1_G0_18,PGA_1_G0_25,PGA_1_G0_31,
PGA_1_G0_37,PGA_1_G0_43,PGA_1_G0_50,PGA_1_G0_56,PGA_1_G0_62,
PGA_1_G0_68,PGA_1_G0_75,PGA_1_G0_81,PGA_1_G0_87,PGA_1_G0_93,
PGA_1_G1_00,PGA_1_G1_06,PGA_1_G1_14,PGA_1_G1_23,PGA_1_G1_33,
PGA_1_G1_46,PGA_1_G1_60,PGA_1_G1_78,PGA_1_G2_00,PGA_1_G2_27,
PGA_1_G2_67,PGA_1_G3_20,PGA_1_G4_00,PGA_1_G5_33,PGA_1_G8_00,
PGA_1_G16_0,PGA_1_G24_0,PGA_1_G48_0};

   BYTE G2_gain[]={
PGA_2_G0_06,PGA_2_G0_12,PGA_2_G0_18,PGA_2_G0_25,PGA_2_G0_31,
PGA_2_G0_37,PGA_2_G0_43,PGA_2_G0_50,PGA_2_G0_56,PGA_2_G0_62,
PGA_2_G0_68,PGA_2_G0_75,PGA_2_G0_81,PGA_2_G0_87,PGA_2_G0_93,
PGA_2_G1_00,PGA_2_G1_06,PGA_2_G1_14,PGA_2_G1_23,PGA_2_G1_33,
PGA_2_G1_46,PGA_2_G1_60,PGA_2_G1_78,PGA_2_G2_00,PGA_2_G2_27,
PGA_2_G2_67,PGA_2_G3_20,PGA_2_G4_00,PGA_2_G5_33,PGA_2_G8_00,
PGA_2_G16_0,PGA_2_G24_0,PGA_2_G48_0};


   //M8C_EnableGInt;
   PGA_1_Start(PGA_1_HIGHPOWER);
   PGA_2_Start(PGA_2_HIGHPOWER);
   BPF2_1_Start(BPF2_1_HIGHPOWER);

   // Initialize receiver/cmd buffer
   UART_CmdReset();

   //Turn on interrupts
   M8C_EnableGInt ;

   //Enable RX interrupts
   UART_IntCntl(UART_ENABLE_RX_INT);
   //set parity as zero and start the UART
   UART_Start(UART_PARITY_NONE);


   //Clear the screen in Hyper terminal window
   UART_PutChar(12);

   // Print welcome screen
   welcomeScreen();

   G1_index = 1;
   G2_index = 1;

while(1) {
      if (UART_bCmdCheck()) {            // Wait for command Terminator
         if(strPtr = UART_szGetParam()) {     // More than delimiter?
         }
```

```
            copy_string(boardid,strPtr);
            copy_string(parameter,strPtr);
            copy_string(value,strPtr);
            str_cut(parameter, 2, -1); //cut from 2 to end

            if (cstrcmp("B11", strPtr) == 0) {
               PGA_1_SetGain(PGA_1_G1_00);
            } else if (cstrcmp("B12", strPtr) == 0) {
               PGA_1_SetGain(PGA_1_G2_27);
            } else if (cstrcmp("B13", strPtr) == 0) {
               PGA_1_SetGain(PGA_1_G4_00);
            } else if (cstrcmp("B14", strPtr) == 0) {
               PGA_1_SetGain(PGA_1_G16_0);
            }
            else if (cstrcmp("B15", strPtr) == 0) {
               PGA_1_SetGain(PGA_1_G0_06);
               PGA_2_SetGain(PGA_2_G0_06);
            }
            //Reset command buffer and flags
                UART_CmdReset();
           }
    }
}

// Function to print the welcome screen
void welcomeScreen(void)
{
    UART_CPutString("\n\rThis is B1 - Driver");
    UART_CPutString("\n\r");
}

int str_cut(char *str, int begin, int len)
{
    int l = strlen(str);
    if (len < 0) len = l - begin;
    if (begin + len > l) len = l - begin;
    memmove(str + begin, str + begin + len, l - len + 1);
    return len;
}

   int find_index(int a[], int num_elements, int value)
{
   int i;
   for (i=0; i<num_elements; i++)
   {
    if (a[i] == value)     return(i);  /* it was found */
   }
   return(-1);  /* if it was not found */
}

void copy_string(char *target, char *source) {
   while (*source) {
      *target = *source;
      source++;
      target++;
   }
   *target = '\0';
}

void Newline(void)
{
```

```
   UART_CPutString("\r\n");
}
```

3) Frequency meter

```
#include <m8c.h>        // part specific constants and macros
#include "PSoCAPI.h"    // PSoC API definitions for all User Modules
#include "delay.h"
#include <stdlib.h>
#include <string.h>

#define Aver 5

float MeasFreq(void);
void RepFreq(float);
BYTE IsOsc(void);

BYTE  cTemp,PRT1_Sha,gind1,gind2;
WORD  uiComCnt,uiTimOve;
DWORD   uiTimSta,uiTimFin,ucComCnt;
LONG  ulTimTot;
char*    pString, String1, String2;
float    fFreq, uFreq, SFreq;



void main(void)
{

   BYTE  tmp,i,i1,n,m,s,co,d;
   WORD  Ctr;
   float fFrAv;
   char  *strPtr;


   M8C_EnableGInt;                    /* enable global interrupts */
   Counter16_Start();                 /* start the counter        */
   DigBuf_Start();
   Counter16_WritePeriod(999);        /* set the period to 1000   */
   Counter16_WriteCompareValue(499);  /* generate a 50 duty cycle */
   Counter16_EnableInt();             /* disable the interrupt    */
   LED_1_Start();
   PGA_1_Start(PGA_1_LOWPOWER);

   for (i=0;i<5;i++)   {
      LED_1_Switch(1); Delay10msTimes(20);
      LED_1_Switch(0); Delay10msTimes(20);
   }

    UART_1_CmdReset();              // Initialize receiver/cmd buffer
    UART_1_IntCntl(UART_1_ENABLE_RX_INT); // Enable RX interrupts
    UART_1_Start(UART_1_PARITY_NONE);     // Enable UART
   Delay10msTimes(3);
   d=0;
```

```
   Delay10msTimes(30);
   COMP_1_Start(COMP_1_HIGHPOWER);
   Delay10msTimes(3);
   UART_1_CPutString("\r\n====================");
   Delay10msTimes(20);

while (1)   {
                  if ( IsOsc() ){
                        fFrAv=0;
                           for (Ctr=0;Ctr<Aver;Ctr++)
                              fFrAv += MeasFreq();
                           RepFreq(fFrAv/(float)Aver);
                     }
                     else  {
                        UART_1_CPutString("0.\n\r");
                        Delay10msTimes(5);}
                     }
}


#define Corr 0.5
//#define OscFreq ((float)(732*32768)/1.0043)
// internal 24 MHz clock with MiniProg connected
#define OscFreq ((float)(732*32768))
// clcok crystal operation - no MiniProg !
// setting for using interrupt of the comparator 0
#define IF_A1        (INT_CLR0 & 0b00000010)
#define IF_A1_CLR()    (INT_CLR0 &= (~0b00000010))
// setting for using Timer16 with output at DBB01
#define IF_DBB01       (INT_CLR1 & 0b00000100)
#define IF_DBB01_CLR() (INT_CLR1 &= (~0b00000100))

BYTE IsOsc(void) {

   ucComCnt=0;
   // reload period and start timer
   Timer24_1_Stop();
   Timer24_1_WritePeriod(2000000);
   Timer24_1_Start();     // clear IFs
   IF_DBB01_CLR();
   IF_A1_CLR();           // is there a pulse until Timer16 overflows

while ( ! IF_DBB01 )   {
      if ( IF_A1 )  {
         ucComCnt=1;
         break;
      }
   }
   // clear up
   Timer24_1_Stop();
   IF_DBB01_CLR();
   IF_A1_CLR();
   return ucComCnt;
}

float MeasFreq(void)   {
// FREQUENCY MEASUREMENT
   BYTE i;
   int Status;
   uiComCnt=0;
```

```
   ucComCnt=0;
   uiTimOve=0;

   // reload period and start timer
   Timer24_1_Stop();
   Timer24_1_WritePeriod(2000000);
   Timer24_1_Start();
   IF_DBB01_CLR();

   // get Timer16 reading on the first CMP pulse
   IF_A1_CLR();
   while ( ! IF_A1  );
   IF_A1_CLR();
   Timer24_1_ReadTimer(&uiTimSta);

   // count CMP pulses until Timer16 overflows
   while ( ! IF_DBB01 )   {
      if ( IF_A1 )  {
         Timer24_1_ReadTimer(&uiTimFin);
         IF_A1_CLR();
         ucComCnt++;
         if (uiTimFin<1000){
            break;
         }// do not wait until the Timer16 overflow
      }
   }

   if (ucComCnt>0) {
   // at least one period received within TIM period
      Timer24_1_Stop();
      IF_A1_CLR();
      IF_DBB01_CLR();
      ulTimTot = uiTimSta - uiTimFin;
      uiComCnt=ucComCnt;
      // ulTimTot (4 bytes) and uiComCnt (2 bytes) can be communicated
to the host instead
      fFreq= (float)uiComCnt*OscFreq / ((float)ulTimTot+Corr);
      fFreq = fFreq/2.3986176;
      return fFreq;
   }
   else  {
      // timeout
      //UART_1_CPutString("NoInp  ");
      return 0.;
   }
}

void RepFreq(float fFreq) {
   // reporting measurement
   int   iTemp;
   BYTE i;
   pString = ftoa(fFreq, &iTemp);
   UART_1_PutString(pString);
   Delay10msTimes(10);
   UART_1_PutChar('\n');
   Delay10msTimes(10);
   UART_1_PutChar('\r');
   Delay10msTimes(10);
   Delay10msTimes(20);

}
```